Journal of Chemistry

Water Remediation

Guest Editors: Reyna Natividad-Rangel, Manuel A. R. Rodrigo, Julie J. M. Mesa, and Rosa M. G. Espinosa

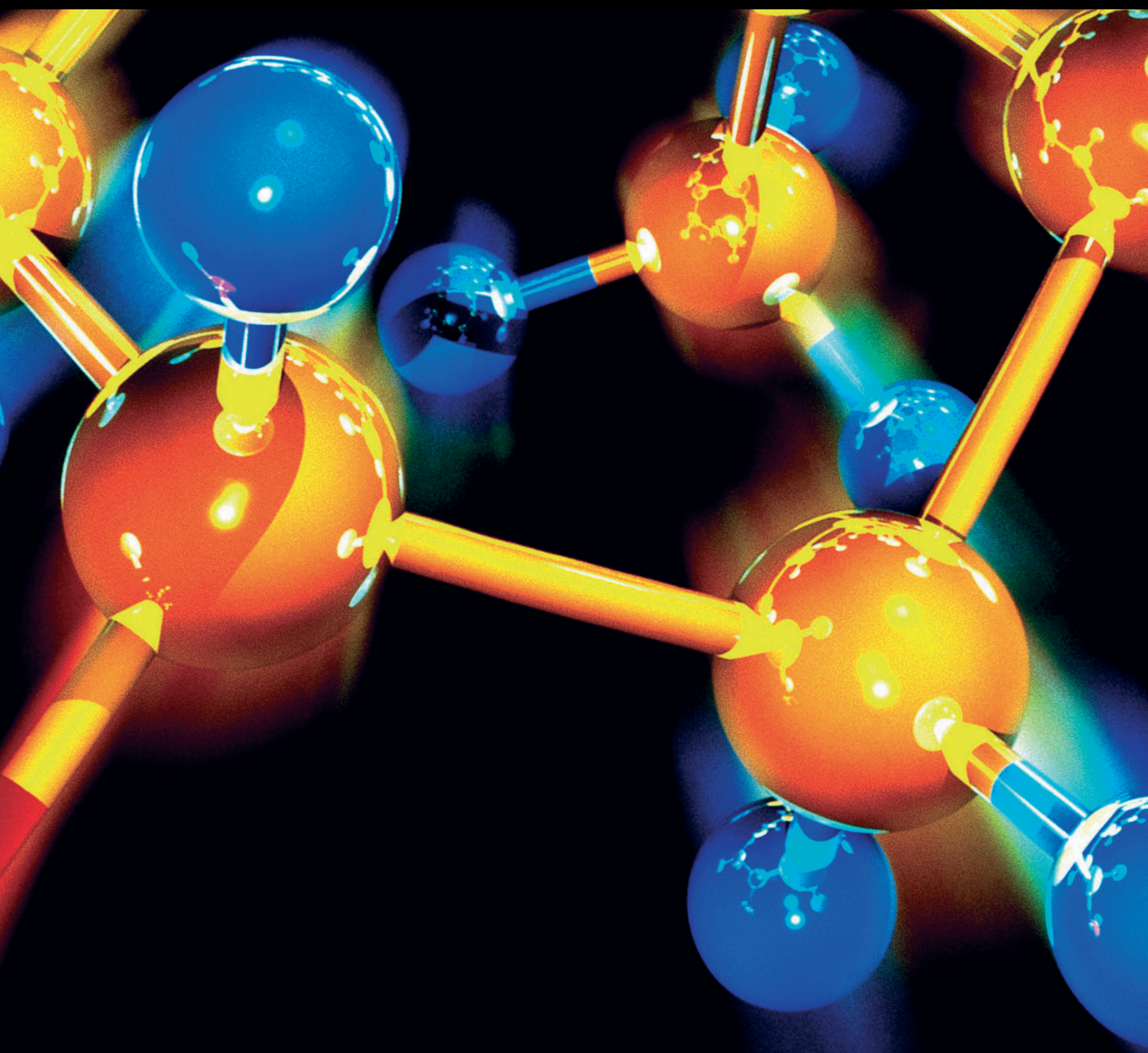

Water Remediation

Journal of Chemistry

Water Remediation

Guest Editors: Reyna Natividad-Rangel, Manuel A. R. Rodrigo, Julie J. M. Mesa, and Rosa M. G. Espinosa

Contents

Hindawi
Journal of Chemistry
Volume 2017, Article ID 9292306, 2 pages
https://doi.org/10.1155/2017/9292306

Editorial
Water Remediation

Reyna Natividad-Rangel,[1] Manuel A. R. Rodrigo,[2] Julie J. M. Mesa,[3] and Rosa M. G. Espinosa[1]

[1]*Centro Conjunto de Investigación en Química Sustentable UAEM-UNAM, Universidad Autónoma del Estado de México, km 14.5 Carr., Toluca-Atlacomulco, 50200 Toluca, MEX, Mexico*
[2]*Department of Chemical Engineering, Faculty of Chemical Sciences Technology, Universidad de Castilla-La Mancha, Edificio Enrique Costa Novella, Campus Universitario S/N, 13071 Ciudad Real, Spain*
[3]*Escuela de Ciencias Químicas, Universidad Pedagógica y Tecnológica de Colombia (UPTC), Avenida Central del Norte, Tunja, Boyacá, Colombia*

Correspondence should be addressed to Reyna Natividad-Rangel; reynanr@gmail.com, Manuel A. R. Rodrigo; manuel.rodrigo@uclm.es, Julie J. M. Mesa; jjuliejoseane@hotmail.com, and Rosa M. G. Espinosa; rosamarigo@gmail.com

Received 13 December 2016; Accepted 13 December 2016; Published 26 April 2017

The satisfaction of human needs has made past and current generations enroll in an unsustainable development because of the great negative effects that their activities exert on environment and therefore on the available natural resources. Consequently, this compromises the satisfaction of the needs of future human generations. In this context, pollution associated with anthropogenic species and heavy metals is becoming a serious environmental problem not only because of the important damage that causes to the environment, that includes among other aspects the loss of biodiversity and severe changes in the ecosystems, but also because it may prevent the use of water reservoirs to produce drinking water. Thus, both types of pollutants are associated with serious illnesses and their occurrence in water may be prevented. As for many other water treatment technologies, costs associated with their removal are directly related to the concentration of the species in the water matrix and the removal of highly polluted wastewater is much more cost-effective, where the concentrations can be even of hundreds of ppm rather than the treatment of drinking water reservoirs, where their concentrations are of only several ppb or even ppt (very low for an efficient treatment but high enough to produce health problems). For this reason, it is of paramount importance to develop technologies able to efficiently deplete this type of pollutants from their typical sources (frequently industrial wastes).

Through the fourteen papers contained in this special issue dedicated to water remediation, different and interesting approaches to improve the efficiency of a water treatment process are discussed and so cutting-edge technology to face this important problem is also presented. The approaches include either the novel modification of sorbents and catalysts or the integration of biological and physicochemical processes. In this sense, electrochemical, photochemical, adsorption, and ion exchange processes are evaluated alone and combined with biological and other physicochemical processes, like ozonation, in order to develop efficient water treatment technologies.

The adsorption related manuscripts indicate that currently the synthesis and application of sorbent materials is still useful and effective in the removal of heavy metals (Pb, Hg, Zn, and Cu), dyes, phenolic compounds, and other organic pollutants from water sources. It is worth noticing that an interesting trend can be observed on using biomass and agricultural waste as raw materials of sorbents, thus giving to this waste an added value. The sorbents' successful modifications reported are both physical and chemical, although the latter seems to exert a greater positive effect on adsorption capability than the former.

Photochemical processes (heterogeneous photocatalysis and photofenton) are also included in this issue mainly due to the important contribution of this technology in

environmental remediation. Different authors around the world have studied photocatalysis based on titania and other novel materials, showing that this treatment is efficient, suitable, and less expensive in water remediation. It is also important to note that this technology is not selective; it means that by photocatalysis different pollutants present in complex matrix samples can be removed, avoiding the use of additional treatments. An important challenge within photocatalysis, however, is to be able to conduct such a process under solar light and this depends mainly on the photocatalyst. In this sense, a manuscript related to the synthesis and application of a silver modified vanadia photocatalyst is included. Interestingly enough, such a material is demonstrated to be active under simulated solar light.

Generally speaking, the presented results range from lab to pilot scale and from synthetic to actual industrial wastewater (paraformaldehyde production chemical plant, truck wash water facility, and Hg contaminated groundwater) treatment.

Finally, it is worth pointing out that the results shown demonstrate that the assessed materials and technologies are efficient and, more important, that it is still possible to look for synergism between technologies looking for cheaper and more efficient water treatment technologies. Conclusions reached are sound and they indicate that despite the great achieved progress so far, this topic is still open for discussion in the next decades and may importantly contribute to the sustainability of processes.

Reyna Natividad-Rangel
Manuel A. R. Rodrigo
Julie J. M. Mesa
Rosa M. G. Espinosa

Hindawi
Journal of Chemistry
Volume 2017, Article ID 5849103, 10 pages
https://doi.org/10.1155/2017/5849103

Research Article

Synthesis and Characterization of Ag-Modified V_2O_5 Photocatalytic Materials

Dora Alicia Solis-Casados,[1] Luis Escobar-Alarcon,[2] Antonia Infantes-Molina,[3] Tatyana Klimova,[4] Lizbeth Serrato-Garcia,[1] Enrique Rodriguez-Castellon,[3] Susana Hernandez-Lopez,[5] and Alejandro Dorazco-Gonzalez[1]

[1] *Centro Conjunto de Investigación en Química Sustentable UAEM-UNAM, Km 14.5 Carretera Toluca-Atlacomulco, Unidad San Cayetano, 50200 Toluca, MEX, Mexico*
[2] *Departamento de Física, Instituto Nacional de Investigaciones Nucleares, P.O. Box 18-1027, 11801 Mexico City, Mexico*
[3] *Departamento de Quimica Inorganica, Facultad de Ciencias, Universidad de Malaga, 29071 Malaga, Spain*
[4] *Departamento de Ingenieria Quimica, UNAM, Mexico City, Mexico*
[5] *Facultad de Química, Universidad Autónoma del Estado de México, Paseo Colon esq Paseo Tollocan Col Nueva la Moderna, 50000 Toluca, MEX, Mexico*

Correspondence should be addressed to Dora Alicia Solis-Casados; solis_casados@yahoo.com.mx

Received 6 August 2016; Revised 29 October 2016; Accepted 10 November 2016; Published 14 February 2017

Academic Editor: Julie J. M. Mesa

V_2O_5 powders modified with different theoretical silver contents (1, 5, 10, 15, and 20 wt% as Ag_2O) were obtained with acicular morphologies observed by scanning electron microscopy (SEM). Shcherbinaite crystalline phase is transformed into the $Ag_{0.33}V_2O_5$ crystalline one with the incorporation and increase in silver content as was suggested by X-ray diffraction (XRD) and X-ray photoelectron spectroscopy (XPS) analysis. With further increase in silver contents the Ag_2O phase appears. Catalysts were active in photocatalytic degradation of malachite green dye under simulated solar light, which is one of the most remarkable facts of this work. It was found that V_2O_5-20Ag was the most active catalytic formulation and its activity was attributed to the mixture of coupled semiconductors that promotes the slight decrease in the rate of the electron-hole pair recombination.

1. Introduction

In recent years, wastewaters from domestic and industrial uses have contributed to the environmental problem because they arrive to the soil and aquifers mantles polluting clean water. In order to address this issue, the effort of many researchers from several scientific disciplines around the world [1, 2] has been focused on wastewater remediation. Heavy metals such as mercury, iron, cadmium, and chromium are included between the most dangerous pollutants in wastewaters as well as some organic compounds such as the phenols, dyes, pesticides, pharmaceutical, and fertilizers and in some cases solvents. All of them are extremely toxic to the humans and also living organisms, even if they are in a low concentration [3]. Several researchers have proposed solutions to reduce the most dangerous and toxic pollutants contained in wastewaters and also to improve water quality modifying the chemical processes, proposing new absorbent materials and some of the advanced oxidation processes as photocatalysis, which includes developing a photocatalytic material. The remotion of the most resilient organic compounds is among the most important topics concerning wastewater remediation and widely studied nowadays. In so many cases, one of the most extended methods is the photocatalytic degradation, whereby the catalyst is activated by using light. It is noteworthy that degradation of the resilient organic compounds dissolved in water occurs in a natural way by the photolysis process by using the cheapest

source energy such as that provided by the sun. The main disadvantage is its very low efficiency since the organic molecules degrade slowly, taking days and even months to achieve the complete mineralization of organic compounds into water and CO_2. The photocatalytic process increases the decomposition rate of organic compounds present in wastewaters. The photocatalyst employed is commonly a semiconductor material with desirable characteristics such as photoactivity, being chemically and biologically inert, photostability, nontoxicity, and low cost [4]. A photocatalyst could be employed in its pure, mixed, or doped form. An example of this is the TiO_2 in its anatase crystalline phase with a band gap energy around 3.2 eV and the rutile crystalline phase with a band gap energy of 3.0 eV [5, 6]. It has been reported that mixing different ratios of anatase : rutile results in higher catalytic activities, which can be attributed to the synergistic effect between both phases, as occurs in coupled semiconductors [7]. Titania in its anatase crystalline phase is in disadvantage for generating the electron-hole pair if the excitation source is sunlight [8, 9]. It is the reason to improve the photocatalytic performance of TiO_2 by doping and modification with metals and nonmetals [10, 11]. It is well known that, in order to obtain better catalytic performance, it is not enough that the photocatalytic material has a low band gap energy to be active under sunlight. Some unstable materials with reduced band gap energy are Fe_2O_3 (2.3 eV), GaP (2.23 eV), and GaAs (1.4 eV) that are not so good as photocatalysts to degrade organic compounds in aqueous solutions [12]. It has been reported before by some researchers that one of the materials with low band gap energy, of around 2.8 eV, and some stability in aqueous solutions is the V_2O_5-based photocatalysts [13], potentially active under irradiation with visible light and investigated in the last years [14–17]. The synthesis of V_2O_5 has been reported by using techniques as the hydrothermal synthesis [18], sol-gel technique [19], thermal decomposition of several precursors as ammonium metavanadate (NH_4VO_3) [20], flame-spray pyrolysis [21, 22] magnetron sputtering, electron-beam evaporation, and pulsed laser deposition [23, 24], obtaining several morphologies as nanobelts [18, 19], nanowires [18], nanoribbons, nanopowders [18, 21], and also thin films [19, 21–23]. Thin films and powders have been obtained with different textural and structural properties related in some cases with their photocatalytic activity [24–26]. It should be considered that the request of doped or coupled a V_2O_5 catalyst to another semiconductor to retarding the recombination of the electron-hole pair, improving catalytic activity [27], is due to the disadvantage of short migration distances for excited electron-hole pairs which increases the recombination rate and decreasing the photocatalytic activity. Other researchers to solve this fact in photocatalysts with low band gap energy have reported that adding a small amount of noble metals (such as Pt, Ag, and Pd) [28–30] could retard the recombination of the electron-hole pair and increase the photocatalytic activity of the V_2O_5. In this research work, the synthesis of Ag-modified V_2O_5 photocatalytic materials through the surfactant assisted technique by using the non-ionic surfactant molecule polyoxyethylene lauryl ether (Brij L23) is proposed. The main purpose was to obtain catalytic formulations based in V_2O_5-xAg that could be photoactive to degrade organic compounds contained in water under simulated solar light.

2. Experimental

2.1. Synthesis of V_2O_5 and Ag-Modified V_2O_5 Photocatalysts. V_2O_5 powders from Fermont were treated by the surfactant assisted technique. This technique uses a micellar solution prepared using polyoxyethylene (23) lauryl ether ($C_{12}E_{23}$, Brij L23 30% w/v solution from Sigma Aldrich), dibutyl ether ($[CH_3(CH_2)_3]_2O$, DBE-reagent plus ≥99% from Sigma Aldrich), and $AgNO_3$ (ACS Reagent, ≥99.0% from Sigma Aldrich). To obtain V_2O_5 photocatalyst, the commercial V_2O_5 was added to the micellar solution previously prepared with 30% Brij L23, 10% DBE, and 60% of water, solvothermally pressurized in a reactor at 60°C for 12 hours, with slow stirring. The obtained solids were filtered, washed with deionized water, and then thermally treated, raising temperature from room temperature to 400°C, at a heating rate of 5°C/min; afterwards, the temperature was isothermally maintained at 400°C for 3 hours in an air convection oven to eliminate the surfactant Brij L23; this sample was called hereinafter V_2O_5. The Ag-modified V_2O_5 photocatalysts were prepared by following the same synthesis procedure. Thus, the required amounts of V_2O_5 and $AgNO_3$ precursors were added to the micellar solution of Brij L23 to obtain a theoretical content of 1, 5, 10, 15, and 20 wt.% of Ag_2O. Photocatalysts will be referred hereinafter as V_2O_5-xAg, where x represents the percentage in weight of Ag_2O (1, 5, 10, 15, and 20 wt% Ag_2O) and for simplicity the Ag_2O content in some parts of the manuscript has been referred as the Ag load.

2.2. Physicochemical Characterization of V_2O_5-xAg. The temperature of surfactant elimination to obtain the photocatalytic formulation was determined from thermogravimetry and differential scanning calorimeter analysis (TGA-DSC), performed by using a Netzsch, STA 449 F3 Jupiter equipment. The weight loss and the heat flow during decomposition were measured in flowing air (20 mL/min) and heating from room temperature to 600°C at a heating rate of 3°C/min. Molecular structure was studied through the infrared spectra (IR) acquired in a Bruker tensor 27 IR spectrometer with ATR accessory. Surface morphology was observed with scanning electron microscopy (SEM) by using a JEOL JSM 6510 LV microscope; additionally, compositional analysis was carried out with an acceleration voltage of 15 kV, using an EDS probe coupled to the same microscope. Raman spectra (RS) were acquired using an HR LabRam 800 system equipped with an Olympus BX40 confocal microscope; a Nd:YAG laser beam (532 nm) was focused by a 100x objective onto the sample surface. A cooled CCD camera was used to record the spectra, usually averaged for 100 accumulations of 10 seconds in order to improve the signal-noise ratio. All spectra were calibrated using the 521 cm^{-1} line of monocrystalline silicon. X-ray diffraction (XRD) patterns were obtained with a X'Pert PRO MPD Philips diffractometer (PANanalytical), using monochromatic CuKα radiation ($\lambda = 1.5406$ Å). The Kα radiation was selected with a Ge (1 1 1) primary monochromator. The X-ray tube was set at 45 kV and 40 mA. X-ray diffraction (XRD) measurements were also performed on a

Rigaku D/MAX III B diffractometer with a copper target. X-ray line broadening analysis (XLBA) was performed using computer software supplied by Rigaku after measurement in the step scan mode. The textural properties (S_{BET}, Vp, and dp) were measured from the nitrogen adsorption-desorption isotherms at −196°C by an automatic ASAP 2020 system from Micromeritics. Prior to the measurements, samples were outgassed at 200°C and 10^{-4} mbar overnight. Surface areas were determined by using the Brunauer-Emmett-Teller (BET) equation and a nitrogen diatomic molecule cross section of 16.2 Å^2. The total pore volume was calculated from the adsorption isotherm at $P/P_0 = 0.996$. The optical band gap energy (E_g) values were determined using the Kubelka-Munk method; this was done by transforming the reflectance spectra of the samples with different Ag contents to the Kubelka-Munk function, $F(R)$, and then plotting $(F(R)E)^{1/2}$ versus E. The values of Eg were obtained by a linear fit at linear segments of the curve, determining its intersection with the photon energy axis [32]. It was mentioned in [33] that there are some discrepancies in opinion about the Kubelka-Munk method, but it is used with the sufficient accuracy required in photocatalytic applications. With the maximum absorbance in the UV-Vis spectra, it was observed the excitation wavelength of each sample to emit photoluminescence; this maximum has a slight shift; thus emission spectra were obtained with an excitation source fixed at $\lambda = 492$ nm in a FluoroMax-4, HORIBA, Jobin Yvon fluorometer. The intensity of the emission spectrum seems to be related to the rate of electron-hole recombination [34]. X-ray photoelectron spectra (XPS) were collected using a Physical Electronics PHI 5700 spectrometer with nonmonochromatic Mg Kα radiation (300 W, 15 kV, and 1256.6 eV) with a multichannel detector. Survey spectra were recorded from 0 to 1000 eV at constant pass energy of 100 eV, onto 720 μm diameter analysis area; narrow spectra of samples were recorded in the constant pass energy mode at 20 eV, using a 720 μm diameter analysis area and 10 scans at least. Charge correction was adjusted by using the carbon signal (C 1*s* at 285 eV). A PHI ACCESS ESCA-V6.0 F software package was used for acquisition and data analysis. A Shirley type background was subtracted from the spectra and then they were fitted using Gaussian-Lorentzian curves to determine the binding energies of the different element core levels more accurately. NIST database was used to identify the corresponding element to the measured binding energies.

2.3. Photocatalytic Activity Tests. The photocatalytic activity of the V_2O_5-*x*Ag photocatalysts was evaluated through the degradation reaction of a model molecule as the malachite green (MG) dye ($C_{23}H_{26}N_2O$) using an aqueous solution of 10 μmol/l. For this purpose, 0.05 g of catalyst was added to a batch reaction system and stirred in a dark room until reaching the adsorption equilibrium. Catalysts were activated by illumination with a solar simulator SF-150B class ABA from Sciencetech, emitting 6% of UV radiation. The light source was placed at a height of 40 cm from the solution surface. The degradation reaction was monitored by the decrease in intensity of the characteristic absorption band of the MG peaking at 619 nm in the UV-Vis spectra. Reaction was followed by 3 hours taking aliquots every 15 minutes. The obtained absorbances at each reaction time were correlated to MG concentrations through a calibration curve traced previously. The kinetic trace at 619 nm is related mainly to the MG concentration change. This trace could be fitted to a pseudo-first-order expression (exponential curve) with acceptable precision to determine the rate constant (k_{app}). Total organic carbon (TOC) was determined by the combustion method, for each solution at the end of the corresponding reaction as ppm of carbon. The mineralization degree was calculated taking as the percent from $[(T_{initial} - T_{final})/T_{initial}]$, where T_{final} and $T_{initial}$ are the TOC values at the end of the reaction and of the original solution, respectively.

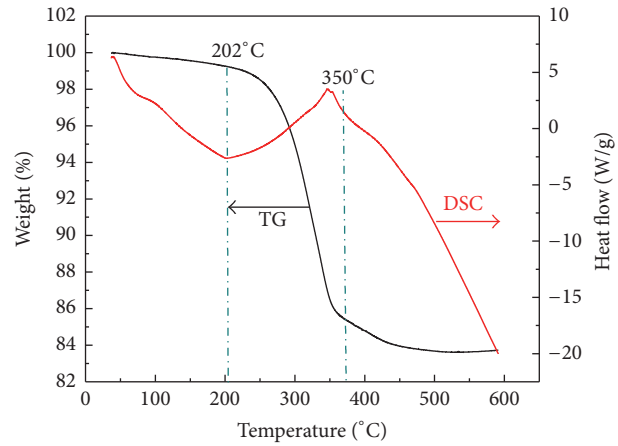

FIGURE 1: TGA-DSC curves of V_2O_5 catalyst precursor.

3. Results and Discussion

3.1. Surfactant Elimination

3.1.1. Thermal Analysis and Infrared Spectroscopy of V_2O_5 Precursors. From TGA-DSC curves shown in Figure 1, the temperature to eliminate the surfactant Brij L23 from V_2O_5 catalyst precursor was determined. The TGA curve shows a main weight loss starting at 200°C and finishing at 450°C, accompanied with an exothermic peak (DSC curve) at 350°C that can be attributed to the thermal decomposition of the surfactant [35]. The incorporation and further increase of Ag promotes a slight decrease in the exothermic peak temperature until 340°C. Therefore, the thermal treatment was carried out at 400°C for 3 hours, in order to achieve the elimination of the surfactant and to favor the thermal decomposition of the $AgNO_3$ into Ag_2O and also to induce the crystallization of the catalytic formulation. To confirm if the organic material was removed after the thermal treatment, IR spectra of V_2O_5-*x*Ag photocatalysts, before and after the thermal treatment, were compared; the results will be discussed later.

3.2. Surface Properties

3.2.1. Scanning Electron Microscopy. The morphology of the V_2O_5-*x*Ag photocatalysts was observed from the SEM images shown in Figures 2(a)–2(d). It is clear that silver

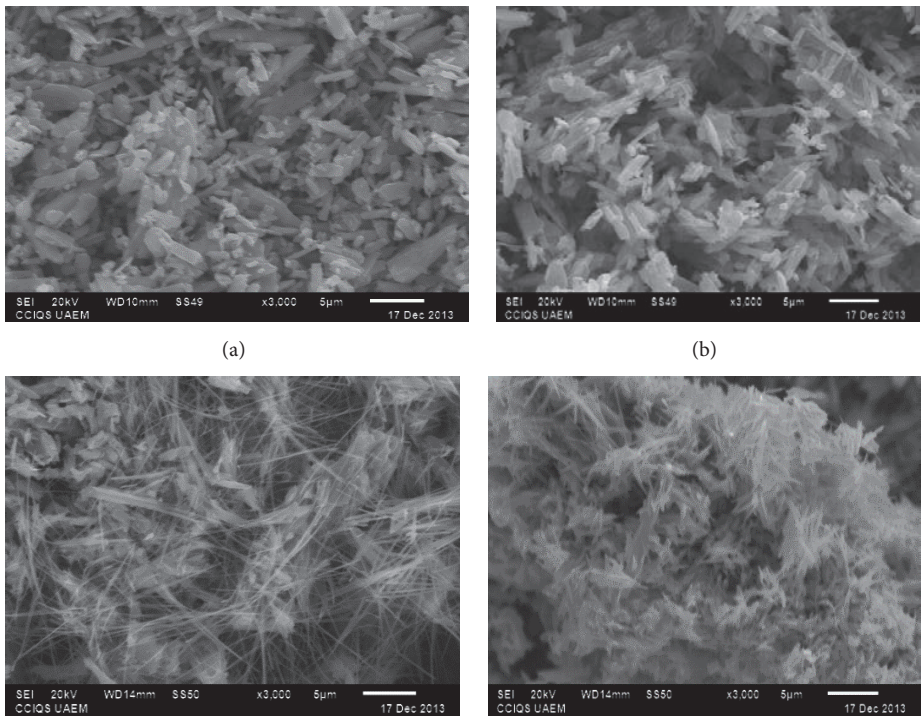

Figure 2: Scanning electron microscopy images at 3000x of (a) V_2O_5, (b) V_2O_5-5Ag, (c) V_2O_5-10Ag, and (d) V_2O_5-20Ag photocatalysts.

incorporation into the photocatalytic formulation changes morphology, obtaining acicular forms, which begin with the morphology bar-type with lengths about 2-3 microns as can be seen in Figures 2(a) and 2(b) for V_2O_5 and V_2O_5-5Ag photocatalysts. Further increase in silver content in the catalytic formulation promotes changes in the morphology, obtaining wires as can be seen in Figures 2(c) and 2(d) for V_2O_5-10Ag and some sharped bars in V_2O_5-20Ag photocatalysts. The catalytic performance observed for each formulation could be associated with the morphology as some changes are expected in textural properties related to morphology. It seems that nucleation process generates crystallites with different morphologies when silver is incorporated into the photocatalytic formulation. That process could be attributed to the solvothermal synthesis procedure mainly and to the increase in Ag_2O load to form different crystalline phases that have different crystallographic data. Elemental atomic composition % in the catalytic surface was determined by the EDS analysis, values shown in Table 1. The atomic % of Ag content increases as was expected with the increase in the theoretical Ag_2O content.

3.2.2. N_2-Physisorption Measurements. Textural properties, such as the specific surface area and total pore volume, were studied using the N_2 physisorption technique. This was done to estimate the effect of the changes observed in the morphology of the V_2O_5-xAg photocatalysts, on their surface properties. The specific surface area values, calculated using the BET model, are included in Table 2. These values increase with the Ag_2O content, from 5.3 to 14.6 m^2/g, which represent an increase close to 300%. These data indicate that Ag_2O incorporation increases the specific surface area and the porosity compared with pure V_2O_5. This result could be explained in terms of a higher amount of empty spaces between the formed particles with narrow dimensions as was observed in the SEM images. N_2-physisorption isotherms are shown in Figure 3, which according to IUPAC are type II, characteristic of low porous solids presenting meso- and macroporosity. An increase in the nitrogen adsorption volume with the increase of the silver content in the catalytic formulation is clear from the isotherms. A small hysteresis loop is observed, attributed to the empty spaces between particles with irregular forms and sizes.

Table 1: Comparison of atomic percent of silver in V_2O_5-xAg photocatalysts measured by XPS and EDS.

	Ag content (at.%) (XPS)	Ag content (at.%) (SEM)
V_2O_5	—	—
V_2O_5-1Ag	1.5	1.1
V_2O_5-5Ag	2.9	1.3
V_2O_5-10Ag	4.5	4.3
V_2O_5-15Ag	4.5	5.1
V_2O_5-20Ag	6.8	8.1

3.3. Crystalline and Molecular Structures

3.3.1. X-Ray Powder Diffraction. Figure 4 shows the diffractograms of the V_2O_5-xAg photocatalysts, where the main

Table 2: Specific surface area (S_{BET}) and pore volume (V_p) of pure V_2O_5 and V_2O_5-xAg photocatalysts.

Sample	S_{BET} (m^2/g)	V_p (cm^3/g)
V_2O_5*	3.3	0.005
V_2O_5**	3.4	0.010
V_2O_5-1Ag	5.3	0.020
V_2O_5-5Ag	11.0	0.023
V_2O_5-10Ag	10.6	0.030
V_2O_5-15Ag	11.9	0.025
V_2O_5-20Ag	14.6	0.026

*Commercial.
**Synthesized.

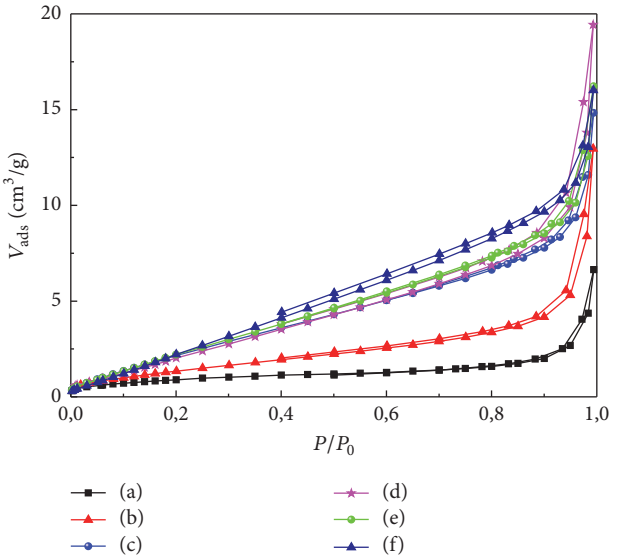

Figure 3: N_2 adsorption-desorption isotherms of (a) V_2O_5, (b) V_2O_5-1Ag, (c) V_2O_5-5Ag, (d) V_2O_5-10Ag, (e) V_2O_5-15Ag, and (f) V_2O_5-20Ag.

crystalline phases such as the Shcherbinaite V_2O_5, the $Ag_{0.33}V_2O_5$ bronze, and the Ag_2O oxide are observed. The intensity in the diffraction lines changes with the increase of the Ag load in the photocatalytic formulation. The diffractogram of the synthesized V_2O_5 catalyst (Figure 4(a)) shows diffraction lines at 2θ = 15.3, 20.2, 21.7, 26.1, 31.0, 32.3, 34.3, 41.2, and 47.3° that characterize unambiguously the Shcherbinaite crystalline phase of V_2O_5 (JCPDS 41-1426). After Ag incorporation, other diffraction lines become noticeable at 2θ = 29.2, 27.8, 30.6, 30.8, and 32.8° in the samples with the V_2O_5-1Ag and V_2O_5-5Ag catalysts. These new signals can be assigned to the called silver vanadium bronzes, specifically to the $Ag_{0.33}V_2O_5$ crystalline structure (JCPDS 81-1740). Further increase in silver load, samples V_2O_5-10Ag and V_2O_5-20Ag, gives rise to the appearance of new diffraction signals at 2θ = 32.9, 38.1, 54.9, and 65.7°, attributed to the Ag_2O crystalline phase (JCPDS 01-1041). These diffraction lines are very weak probably due to a dilution or dispersion effects and to a small crystallite size under 40 Å. It is clear that V_2O_5 crystalline phase almost disappears at the highest silver loads.

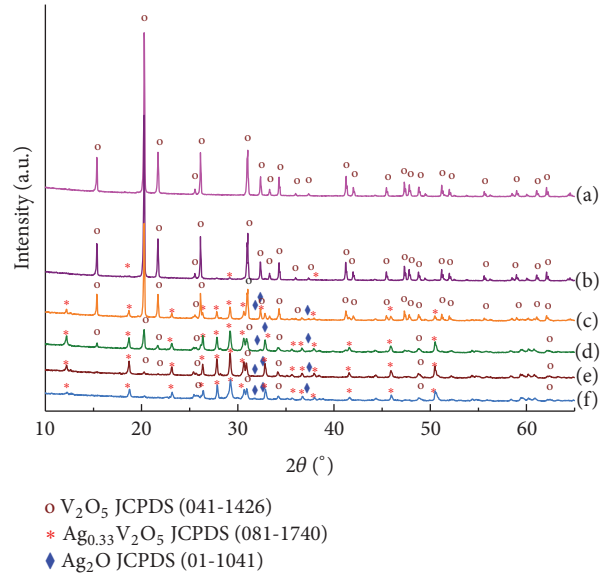

Figure 4: XRD diffraction patterns of (a) V_2O_5, (b) V_2O_5-1Ag, (c) V_2O_5-5Ag, (d) V_2O_5-10Ag, (e) V_2O_5-15Ag, and (f) V_2O_5-20Ag photocatalysts.

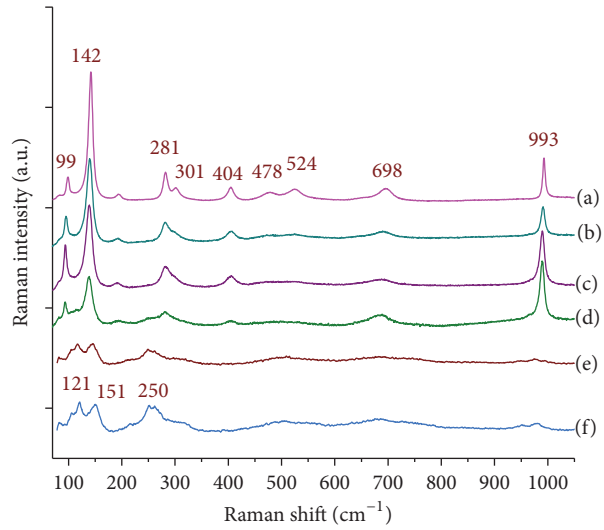

Figure 5: Raman spectra of samples (a) V_2O_5, (b) V_2O_5-1Ag, (c) V_2O_5-5Ag, (d) V_2O_5-10Ag, (e) V_2O_5-15Ag, and (f) V_2O_5-20Ag.

3.3.2. Raman Spectroscopy. To corroborate the microcrystalline structure observed by XRD, Raman spectra of unmodified and Ag-modified V_2O_5 photocatalysts were recorded. It can be seen in the spectra shown in Figure 5 that the Ag incorporation modifies some signals of the Raman spectra with respect to the synthesized V_2O_5 catalyst. The characteristic peaks of the V_2O_5, located at 99, 193, 281, 301, 404, 478, 524, 698, and 993 cm^{-1}, decrease and almost disappear by raising the amount of Ag_2O added during the synthesis along with the appearance of new peaks. The main peak located at 142 cm^{-1}, characteristic of the skeleton bend vibration, shifts from 142 cm^{-1} in V_2O_5 to 138 cm^{-1} in V_2O_5-10Ag photocatalyst, probably due to the distortion of the V_2O_5

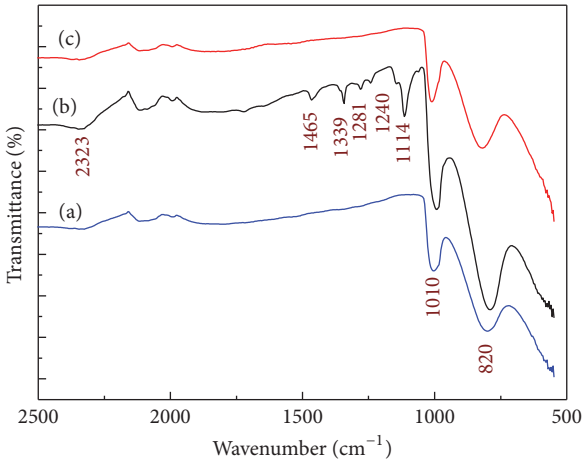

FIGURE 6: Infrared spectra of commercial V_2O_5 (a), V_2O_5 obtained through the surfactant assisted technique before calcination (b), and synthesized V_2O_5 after calcination (c).

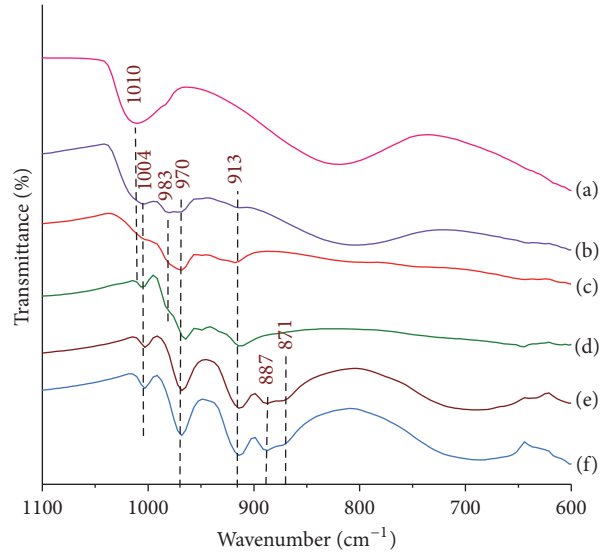

FIGURE 7: IR spectra of (a) V_2O_5, (b) V_2O_5-1Ag, (c) V_2O_5-5Ag, (d) V_2O_5-10Ag, (e) V_2O_5-15Ag, and (f) V_2O_5-20Ag photocatalysts.

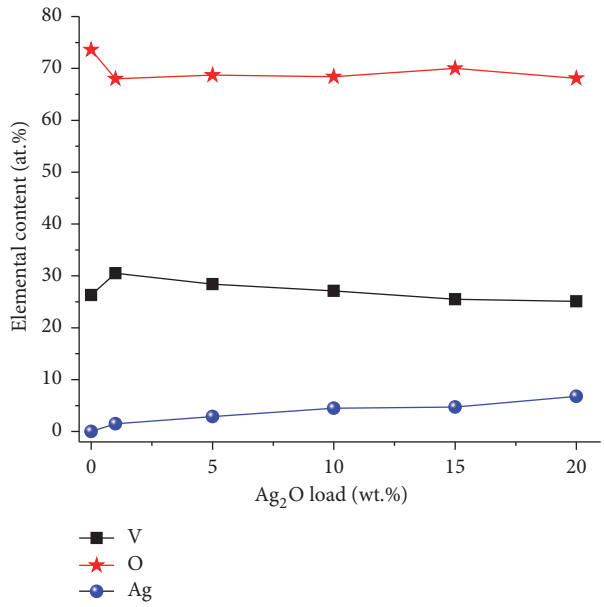

FIGURE 8: Elemental atomic contents for the V_2O_5-xAg photocatalysts.

structure caused by the Ag incorporation into the V_2O_5 lattice. New Raman bands at 121, 151, and 250 cm^{-1} appear for samples with the highest Ag_2O loads and V_2O_5-15Ag and V_2O_5-20Ag samples, which could be attributed to the formation of the $Ag_{0.33}V_2O_5$ bronze. It is noteworthy that no signals associated with Ag_2O were observed, contrary with the XRD results; this could be attributed to the small Raman section of this compound.

3.3.3. Infrared Spectroscopy. Infrared spectra were recorded with two main purposes: firstly, to corroborate the surfactant elimination from the photocatalytic preparation, as can be seen in Figure 6; secondly, to observe the bond vibration when silver is added at different Ag_2O loads. IR spectra of V_2O_5, commercial and as-synthetized, before and after thermal treatment, were compared. The IR spectrum of the commercial sample shows two bands at 1010 cm^{-1} and 820 cm^{-1} ascribed to the coupled vibration between V=O and V–O–V stretching vibrations [36, 37]. The infrared spectrum of the synthesized V_2O_5 before the thermal treatment also presents IR absorption bands characteristics of the surfactant at 1114, 1240, 1281, 1339, and 1465 cm^{-1} [38], attributed to the C-C and C-H bending in the alkyl groups of the surfactant Brij L23. After thermal treatment, these bands disappear confirming the surfactant elimination. IR spectra of the different V_2O_5-xAg photocatalysts are shown in Figure 7. The incorporation and further increase of the Ag_2O load promote the shift of the band at 1010 cm^{-1} to 1000 cm^{-1} and the disappearance of the band located at 820 cm^{-1} when the theoretical Ag_2O loading is higher than 5 wt.%. The observed shift has been assigned to disordered vacancies in the V_2O_5 lattice [39] due to the presence of Ag. The spectrum of the V_2O_5-1Ag sample shows bond vibrations located at 983 cm^{-1} and 970 cm^{-1}; the last one remains for samples with higher Ag_2O loads. The band at 983 cm^{-1} is related to the decrease of the bond strength of V=O stretch vibration by the incorporation of silver into the photocatalytic formulation as observed for Na-bronzes [40]. New infrared bands, at 917, 890 and 871 cm^{-1} and a broad band at 700 cm^{-1}, appear with the increase in Ag content. These could be ascribed to the presence of the $Ag_{0.33}V_2O_5$ bronze identified by XRD.

3.3.4. X-Ray Photoelectron Spectroscopy. Figure 8 shows the corresponding atomic contents of O, V, and Ag, determined from XPS, as a function of the Ag_2O load. From this figure, it is important to remark that the silver atomic content increases as the theoretical Ag_2O load increases. The spectrum region corresponding to V $2p_{3/2}$ has been only considered for the analysis. The corresponding V $2p_{3/2}$ core level spectra of vanadium pentoxide are depicted in Figure 9(a). The fitted

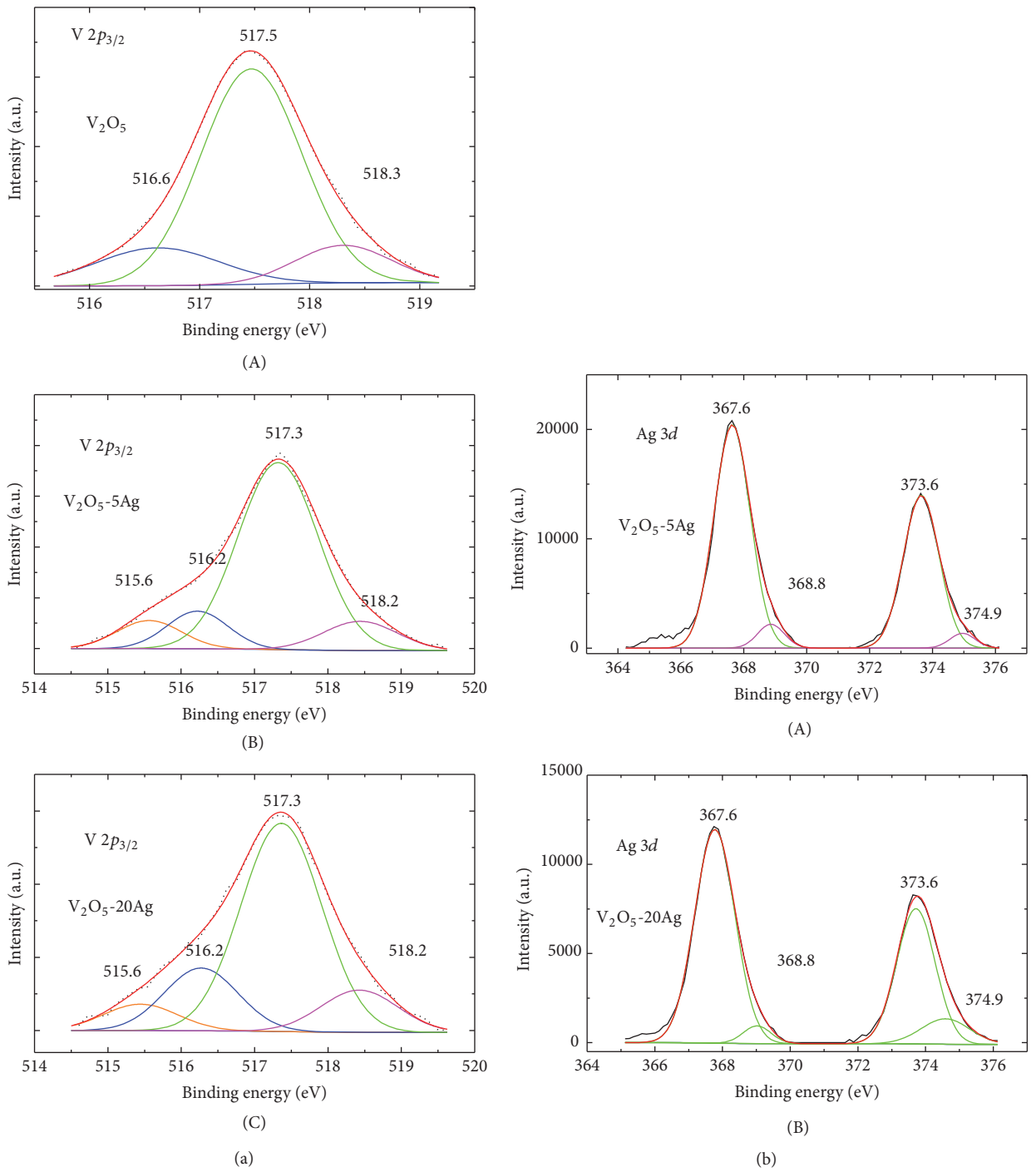

FIGURE 9: Core level spectra of (a) V $2p_{3/2}$ of (A) V_2O_5, (B) V_2O_5-5Ag, and (C) V_2O_5-20Ag and of (b) Ag $3d_{5/2}$ for (A) V_2O_5-5Ag and (B) V_2O_5-20Ag.

spectrum of the synthesized V_2O_5 shows binding energies at 515.6 and 517.5 eV. The peak at 515.6 eV is associated with V^{4+} species and the contribution at 517.5 eV corresponds to V^{5+} indicating the presence of V_2O_5 and confirming the Shcherbinaite crystalline structure observed by XRD. The incorporation of different Ag_2O loads into the photocatalytic formulation promotes the appearance of a new peak at binding energy of 516.2 eV, ascribed to the formation of the Ag-vanadium bronze ($Ag_{0.33}V_2O_5$) observed from XRD. Figures 9(a)(A)–(C) seem to indicate that the contribution at 516.2 eV increases with the Ag_2O loads. These results indicate that on the photocatalyst surfaces coexist mixed-valence vanadium oxides [41]. Concerning the fitting of the Ag $3d$ signal (Figure 9(b)), the contribution of two doublets is observed in all cases. One of them, centered at 367.7 and 373.6 eV, is attributed to the presence of Ag^+ species in the

Table 3: Band gap energy (E_g).

Catalyst	E_g (eV)	Wavelength (nm)
V_2O_5	2.3	564
V_2O_5-1Ag	2.2	566
V_2O_5-5Ag	1.6	765
V_2O_5-10Ag	1.4	867
V_2O_5-15Ag	1.2	1000
V_2O_5-20Ag	1.2	1033

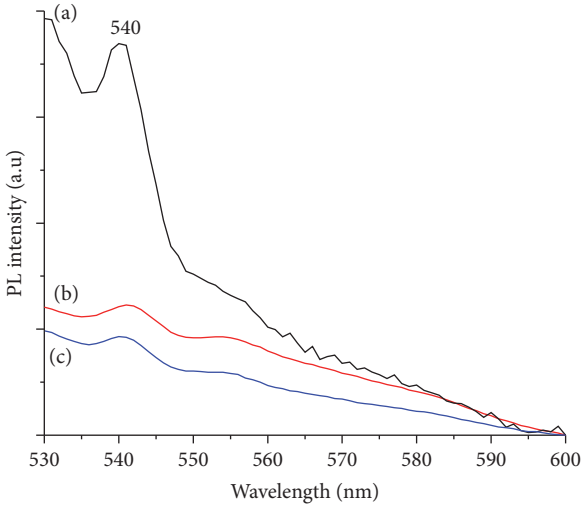

Figure 10: Photoluminescence spectra of (a) commercial V_2O_5, (b) synthesized V_2O_5, and (c) V_2O_5-20Ag.

$Ag_{0.33}V_2O_5$ oxide, while the other, centered at 368.8 and 374.9 eV, could be due to the presence of the Ag^+ species in Ag_2O, in agreement with the XRD results [41]. Finally, it should be mentioned that the O 1*s* spectra decrease slightly their intensity with the increase in atomic silver content and the characteristic peak is at 530.2 eV.

3.4. Band Gap Energy

3.4.1. Diffuse Reflectance Spectroscopy. It is well known that pentavalent vanadium has no d electrons and hence d-d transitions are not possible. Therefore, the observed bands in the electronic absorption spectrum are ascribed to charge transfer bands. The reflectance spectrum was processed with the Kubelka-Munk function and the optical band gap energy (E_g) was obtained as can be seen in Table 3. Results reveal that the increase in the Ag_2O load in photocatalytic formulation promotes narrowing of the band gap from 2.3 eV to values as low as 1.2 eV, remarking that this low band gap value makes this material potentially active under solar light.

3.4.2. Photoluminescence Spectroscopy. Figure 10 shows the photoluminescence spectra of the commercial and synthesized V_2O_5 as well as the V_2O_5-20Ag samples. The PL spectrum of the commercial V_2O_5 is characterized by an intense band peaking at 543. In contrast, the PL emission of the V_2O_5 obtained by the surfactant assisted technique shows

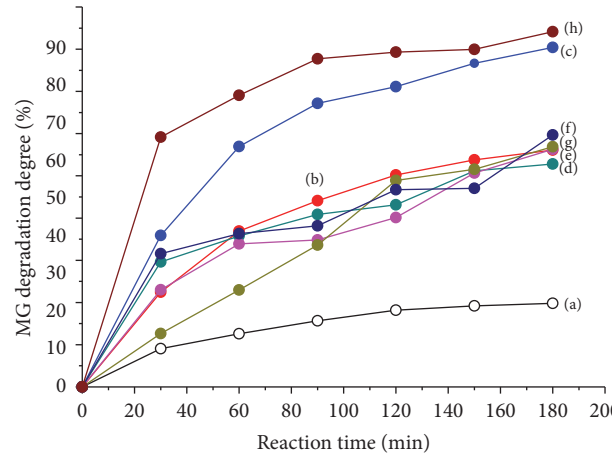

Figure 11: Photocatalytic degradation of malachite green dye during the first 180 minutes of reaction time (a) without catalyst (photolysis) and the photocatalytic process using (b) commercial V_2O_5, (c) synthesized V_2O_5, (d) V_2O_5-1Ag, (e) V_2O_5-5Ag, (f) V_2O_5-10Ag, (g) V_2O_5-15Ag, and (h) V_2O_5-20Ag photocatalysts.

the same band but with a lower intensity, almost three times less intensity. This can be interpreted as a higher electron-hole recombination rate in the commercial sample as the PL intensity is related directly to the recombination rate. An additional PL intensity decrease is also seen in the spectrum of the V_2O_5-20Ag photocatalyst, indicating that this sample exhibits the lowest recombination rate.

3.5. Photocatalytic Activity. Photocatalytic activity was evaluated in the degradation of the malachite green dye. Figure 11 shows that the photodegradation of the MG dye in the photolysis process is very low as can be seen in Figure 11(a). The use of the commercial V_2O_5 sample degrades 56% of the initial MG concentration after 180 min as is shown in Figure 11(b). The synthesized V_2O_5 catalyst (Figure 11(c)) reached a higher photocatalytic activity than the commercial sample, close to 80% of MG degradation. The Ag incorporation and further increase of the silver load in the photocatalyst decrease the photocatalytic activity in the range of 52–60% of MG degradation (Figures 11(d)–11(g)); however, the V_2O_5-20Ag photocatalyst exhibits the highest MG degradation reaching 84% (Figure 11(h)). It is worth noting that this is the best result found in this work, in which a photocatalyst that degrades organic molecules, as the MG dye, takes advantage of the cheapest illumination source as the sunlight. Moreover, a catalyst with high insolubility in water was obtained. This photocatalytic activity obtained was correlated with the acicular morphology of this material, which enhances the contact area in the reaction system. Also, the mixture of several semiconductors such as the V_2O_5, the $Ag_{0.33}V_2O_5$, and the small fraction of Ag_2O works as coupled conduction bands with electron transfer between them and decreases the recombination rate of the electron-hole pair, as was suggested by the photoluminescence results. Table 4 shows the reaction rate constant values k_{app} (min^{-1}) obtained from the fitting of the MG concentration at the early reaction times. Assuming a

Table 4: Kinetic rate constant (k_{app}) for photocatalytic formulations as a function of the silver load, determined using a nonlinear least squares data treatment [31].

Photocatalyst	% of degradation (UV-Vis)	% of degradation (TOC)	k_{app} (min^{-1})
V_2O_5	80.4	69.9	0.0081 ± 0.0001
V_2O_5-1Ag	52.8	67.5	0.0049 ± 0.0008
V_2O_5-5Ag	56.3	54.3	0.0056 ± 0.0007
V_2O_5-10Ag	56.9	56.0	0.0081 ± 0.0009
V_2O_5-15Ag	59.7	73.9	0.0053 ± 0.0001
V_2O_5-20Ag	84.2	74.4	0.0082 ± 0.0002

pseudo-first-order expression, a nonlinear least square fitting was used with an acceptable precision [31]. This reaction rate constant values agrees well with the degradation degree results. Additionally, the mineralization degree was followed by the quantification of the total organic carbon (TOC) through the reaction time; both results are quite similar as can be seen in Table 4, indicating that the photodegradation process follows the mineralization route of the organic dye tested.

4. Conclusions

Ag-modified photocatalysts were obtained in an easy way with acicular morphologies and enhanced specific surface areas. The changes in morphology and textural properties are associated with the appearance of new phases such as $Ag_{0.33}V_2O_5$ as well as Ag_2O coexisting at higher Ag loads as was suggested by XRD and XPS. These new phases have a strong influence in the photocatalytic response of these systems. It was observed that Ag incorporation into the photocatalytic formulation narrows the band gap energy making these materials photoactive under sunlight, a natural and cheaper irradiation source. The obtained photocatalytic formulations are conformed by a mixture of crystalline phases that work as coupled semiconductors. The V_2O_5-20Ag catalyst was the most active for the MG degradation using simulated sunlight.

Competing Interests

The authors declare that they have no competing interests.

Acknowledgments

The authors thank CONACyT for the financial support through CB-168827 and CB-240998 projects and CB-239648 project and also thank the academic staff of CCIQS Alejandra Núñez, Lizbeth Triana, Citlalit Martínez, and Dr. Uvaldo Hernández Balderas. E. Rodriguez Castellon and A. Infantes thank the financial support of the CTQ2015-68951-C3-3-R project (Ministerio de Economía y Competitividad) and FEDER funds.

References

[1] A. Fujishima and K. Honda, "Electrochemical photolysis of water at a semiconductor electrode," *Nature*, vol. 238, no. 5358, pp. 37–38, 1972.

[2] L. Di, H. Hajime, O. Naoki, H. Shunichi, and Y. Yukio, "Synthesis of nanosized nitrogen-containing MO_x-ZnO (M = W, V, Fe) composite powders by spray pyrolysis and their visible-light-driven photocatalysis in gas-phase acetaldehyde decomposition," *Catalysis Today*, vol. 93–95, pp. 895–901, 2004.

[3] I. N. M. Posada Velázquez, "Los compuestos orgánicos persistentes y su toxicidad a la salud humana," 2009, http://es.scribd.com/doc/16026795/Los-compuestos-organicos-persistentes-y-su-toxicidad-a-la-salud-humana.

[4] D. Dhananjay, S. Bhatkhande, V. G. Pangarkar, and A. Beenackers, "Photocatalytic degradation for environmental applications—a review," *Journal of Chemical Technology and Biotechnology*, vol. 77, no. 1, pp. 102–116, 2002.

[5] A. I. Martínez, D. Acosta, and A. López, "Efecto del contenido de Sn sobre las propiedades físicas de películas delgadas de TiO_2," *Superficies y Vacío*, vol. 16, pp. 5–9, 2003.

[6] K. Melghit, A. K. Mohammed, and I. Al-Amri, "Chimie douce preparation, characterization and photocatalytic activity of nanocrystalline SnO_2," *Materials Science and Engineering B: Solid-State Materials for Advanced Technology*, vol. 117, no. 3, pp. 302–306, 2005.

[7] H. T. Tran, H. Kosslick, M. F. Ibad et al., "Photocatalytic performance of highly active brookite in the degradation of hazardous organic compounds compared to anatase and rutile," *Applied Catalysis B: Environmental*, vol. 200, pp. 647–658, 2017.

[8] S. Chen, D. Li, Y. Liu, and W. Huang, "Morphology-dependent defect structures and photocatalytic performance of hydrogenated anatase TiO_2 nanocrystals," *Journal of Catalysis*, vol. 341, pp. 126–135, 2016.

[9] K. Nakata and A. Fujishima, "TiO_2 photocatalysis: design and applications," *Journal of Photochemistry and Photobiology C: Photochemistry Reviews*, vol. 13, no. 3, pp. 169–189, 2012.

[10] C. McManamon, J. O'Connell, P. Delaney, S. Rasappa, J. D. Holmes, and M. A. Morris, "A facile route to synthesis of S-doped TiO_2 nanoparticles for photocatalytic activity," *Journal of Molecular Catalysis A: Chemical*, vol. 406, pp. 51–57, 2015.

[11] H. Li, G. Zhao, G. Han, and B. Song, "Hydrophilicity and photocatalysis of $Ti_{1-x}V_xO_2$ films prepared by sol-gel method," *Surface and Coatings Technology*, vol. 201, no. 18, pp. 7615–7618, 2007.

[12] T. Bak, J. Nowotny, M. Rekas, and C. C. Sorrell, "Photo-electrochemical hydrogen generation from water using solar energy. Materials-related aspects," *International Journal of Hydrogen Energy*, vol. 27, no. 10, pp. 991–1022, 2002.

[13] X. Yong and M. A. A. Schoonen, "The absolute energy positions of conduction and valence bands of selected semiconducting minerals," *American Mineralogist*, vol. 85, no. 3-4, pp. 543–556, 2000.

[14] F. Amano, M. Tanaka, and B. Ohtani, "Alkali metal ion-modified vanadium mononuclear complex for photocatalytic mineralization of organic compounds," *Catalysis Letters*, vol. 140, no. 1, pp. 27–31, 2010.

[15] M. A. Rauf, S. B. Bukallah, A. Hamadi, A. Sulaiman, and F. Hammadi, "The effect of operational parameters on the photoinduced decoloration of dyes using a hybrid catalyst V_2O_5/TiO_2," *Chemical Engineering Journal*, vol. 129, no. 1-3, pp. 167–172, 2007.

[16] K. Teramura, T. Tanaka, M. Kani, T. Hosokawa, and T. Funabiki, "Selective photo-oxidation of neat cyclohexane in the liquid phase over V_2O_5/Al_2O_3," *Journal of Molecular Catalysis A: Chemical*, vol. 208, no. 1-2, pp. 299–305, 2004.

[17] C. Karunakaran and P. Anilkumar, "Photooxidation of iodide ion on immobilized semiconductor powders," *Solar Energy Materials and Solar Cells*, vol. 92, no. 4, pp. 490–494, 2008.

[18] X. Rui, Y. Tang, O. I. Malyi et al., "Ambient dissolution-recrystallization towards large-scale preparation of V_2O_5 nanobelts for high-energy battery applications," *Nano Energy*, vol. 22, pp. 583–593, 2016.

[19] J. Mu, J. Wang, J. Hao et al., "Hydrothermal synthesis and electrochemical properties of V_2O_5 nanomaterials with different dimensions," *Ceramics International*, vol. 41, no. 10, pp. 12626–12632, 2015.

[20] H. He, L. Zan, and Y. Zhang, "Effects of amorphous V_2O_5 coating on the electrochemical properties of $Li[Li_{0.2}Mn_{0.54}Ni_{0.13}Co_{0.13}]O_2$ as cathode material for Li-ion batteries," *Journal of Alloys and Compounds*, vol. 680, pp. 95–104, 2016.

[21] S. Sel, O. Duygulu, U. Kadiroglu, and N. E. Machin, "Synthesis and characterization of nano-V_2O_5 by flame spray pyrolysis, and its cathodic performance in Li-ion rechargeable batteries," *Applied Surface Science*, vol. 318, pp. 150–156, 2014.

[22] A. A. Mane, V. V. Ganbavle, M. A. Gaikwad, S. S. Nikam, K. Y. Rajpure, and A. V. Moholkar, "Physicochemical properties of sprayed V_2O_5 thin films: effect of substrate temperature," *Journal of Analytical and Applied Pyrolysis*, vol. 115, pp. 57–65, 2015.

[23] C. Julien, E. Haro-Poniatowski, M. A. Camacho-López, L. Escobar-Alarcón, and J. Jímenez-Jarquín, "Growth of V_2O_5 thin films by pulsed laser deposition and their applications in lithium microbatteries," *Materials Science and Engineering B*, vol. 65, no. 3, pp. 170–176, 1999.

[24] F. Gonzalez-Zavala, L. Escobar-Alarcón, D. A. Solís-Casados, C. Rivera-Rodríguez, R. Basurto, and E. Haro-Poniatowski, "Preparation of vanadium oxide thin films modified with Ag using a hybrid deposition configuration," *Applied Physics A: Materials Science and Processing*, vol. 122, no. 4, article 461, 2016.

[25] N. Serpone and E. Pelizzetti, *Photocatalysis: Fundamentals and Applications*, John Wiley & Sons, New York, NY, USA, 1989.

[26] D. Bahnemann, "Photocatalytic water treatment: solar energy applications," *Solar Energy*, vol. 77, no. 5, pp. 445–459, 2004.

[27] Y. He, Y. Wu, T. Sheng, and X. Wu, "Photodegradation of acetone over V-Gd-O composite catalysts under visible light," *Journal of Hazardous Materials*, vol. 180, no. 1-3, pp. 675–682, 2010.

[28] T. Ishihara, N. S. Baik, N. Ono, H. Nishiguchi, and Y. Takita, "Effects of crystal structure on photolysis of H_2O on K–Ta mixed oxide," *Journal of Photochemistry and Photobiology A: Chemistry*, vol. 167, no. 2-3, pp. 149–157, 2004.

[29] T. Ohno, S. Izumi, K. Fujihara, and M. Matsumura, "Electron-hole recombination via reactive intermediates formed on PdO-doped $SrTiO_3$ electrodes. Estimation from comparison of photoluminescence and photocurrent," *Journal of Photochemistry and Photobiology A: Chemistry*, vol. 129, no. 3, pp. 143–146, 1999.

[30] F. Han, V. S. R. Kambala, M. Srinivasan, D. Rajarathnam, and R. Naidu, "Tailored titanium dioxide photocatalysts for the degradation of organic dyes in wastewater treatment: a review," *Applied Catalysis A: General*, vol. 359, no. 1-2, pp. 25–40, 2009.

[31] G. Lente, *Deterministic Kinetics in Chemistry and Systems Biology*, Springer, 2015.

[32] A. B. Murphy, "Band-gap determination from diffuse reflectance measurements of semiconductor films, and application to photoelectrochemical water-splitting," *Solar Energy Materials and Solar Cells*, vol. 91, no. 14, pp. 1326–1337, 2007.

[33] R. López and R. Gómez, "Band-gap energy estimation from diffuse reflectance measurements on sol-gel and commercial TiO_2: A Comparative Study," *Journal of Sol-Gel Science and Technology*, vol. 61, no. 1, pp. 1–7, 2012.

[34] P. Malathy, K. Vignesh, M. Rajarajan, and A. Suganthi, "Enhanced photocatalytic performance of transition metal doped Bi_2O_3 nanoparticles under visible light irradiation," *Ceramics International*, vol. 40, no. 1, pp. 101–107, 2014.

[35] D. Solís, E. Vigueras-Santiago, S. Hernández-López, A. Gómez-Cortés, M. Aguilar-Franco, and M. A. Camacho-López, "Textural, structural and electrical properties of TiO_2 nanoparticles using Brij 35 and P123 as surfactants," *Science and Technology of Advanced Materials*, vol. 9, no. 2, 2008.

[36] J. M. Lee, H.-S. Hwang, W.-I. Cho, B.-W. Cho, and K. Y. Kim, "Effect of silver co-sputtering on amorphous V_2O_5 thin-films for microbatteries," *Journal of Power Sources*, vol. 136, no. 2, pp. 122–131, 2004.

[37] T. Ono, Y. Tanaka, T. Takeuchi, and K. Yamamoto, "Characterization of K-mixed V_2O_5 catalyst and oxidative dehydrogenation of propane on it," *Journal of Molecular Catalysis A: Chemical*, vol. 159, no. 2, pp. 293–300, 2000.

[38] Libro, "Tablas para la elucidación estructural de compuestos orgánicos por métodos espectroscópicos".

[39] M. D. Soriano, A. Vidal-Moya, E. Rodríguez-Castellón, F. V. Melo, M. T. Blasco, and J. M. López-Nieto, "Partial oxidation of hydrogen sulfide to sulfur over vanadium oxides bronzes," *Catalysis Today*, vol. 259, pp. 237–244, 2016.

[40] J. C. Badot, D. G. F. Bourdeau, N. Baffier, and A. Tabuteau, "Electronic Properties of $Na_{0.33}V_2O_5$ bronze obtained by sol-gel process," *Journal of Solid State Chemistry*, vol. 92, pp. 8–17, 1991.

[41] M. E. Tousley, A. W. Wren, M. R. Towler, and N. P. Mellott, "Processing, characterization, and bactericidal activity of undoped and silver-doped vanadium oxides," *Materials Chemistry and Physics*, vol. 137, no. 2, pp. 596–603, 2012.

Hindawi
Journal of Chemistry
Volume 2017, Article ID 4296515, 8 pages
https://doi.org/10.1155/2017/4296515

Research Article

Pb(II) Removal Process in a Packed Column System with Xanthation-Modified Deoiled Allspice Husk

Efrain Palma-Anaya,[1] Cheikh Fall,[2] Teresa Torres-Blancas,[1] Patricia Balderas-Hernández,[1] Julian Cruz-Olivares,[1] Carlos E. Barrera-Díaz,[1] and Gabriela Roa-Morales[1]

[1]*Centro Conjunto de Investigación en Química Sustentable (CCIQS), Universidad Autónoma del Estado de México (UAEMex), UAEM-UNAM, Carretera Toluca-Atlacomulco, km 14.5, 50200 Toluca, MEX, Mexico*
[2]*Centro Interamericano de Recursos del Agua (CIRA), UAEMex, Carretera Toluca-Atlacomulco, km 14.5, 50200 Toluca, MEX, Mexico*

Correspondence should be addressed to Gabriela Roa-Morales; gabyroam@gmail.com

Received 24 July 2016; Revised 19 October 2016; Accepted 25 October 2016; Published 29 January 2017

Academic Editor: Julie J. M. Mesa

The present research dealt with lead removal using modified *Pimenta dioica* L. Merrill as biosorbent in a batch and in continuous flow column systems, respectively. The allspice husk residues were modified first with a treatment through the xanthation reaction. For the adsorption tests, the atomic adsorption spectrophotometry method was used to determine the lead concentrations in the liquid samples. In the kinetic batch study (10 mg of sorbent in 10 mL of 25 mg L^{-1} lead solution), the removal efficiency was 99% (adsorption capacity of 25.8 mg g^{-1}). The kinetic data followed the pseudo-second-order model. The adsorption isotherm was fitted to the Freundlich model, where constants were K_f and $1/n$ (8.06 $mg^{(1-1/n)}$ g^{-1} $L^{1/n}$ and 0.52), corresponding to adsorption capacities of 8 and 62 mg g^{-1}, at liquid equilibrium concentration of 1 and 50 mg L^{-1}, respectively. In the continuous flow systems where lead solution of 50 mg L^{-1} was treated in 2 columns of 5 cm (4.45 g) and 10 cm (9.07 g) bed heights, the dynamic adsorption capacity obtained by fitting the Thomas model was 29.114 mg g^{-1} and 45.322 mg g^{-1}, respectively.

1. Introduction

Needless to say, water is the main environmental constituent comprised on earth, as well as being the essential electrolyte for all living organisms in this planet [1]. The pollution of this unique resource has increased in recent years because of heavy metals discharges; therefore it is of great interest to devise methods to detect, quantify, and remove these metals [2]. The dangerousness of heavy metals is even greater, considering that they are not biodegradable and are persistent. Once emitted, they can remain in the atmosphere for hundreds of years. Lead in particular is a highly toxic metal that causes neurological damage to humans. The main way of transporting lead from intestines to any other tissues is through red blood cells, followed by absorption through blood, liver, and kidney. Because of its toxicity, lead inhibits the enzymatic action; that is, it can be fixed in blood, bones, and so on [3] because it displaces calcium since they have similar atomic radius and because it has more affinity toward the functional groups present and produces alterations of the cell membrane [4, 5]. Recently, biosorption has been investigated as a very promising technology for the disposal of heavy metals especially in aqueous solution; it has the potential to do it efficiently, quickly, and at lower cost [6]. Therefore biosorption represents an alternative for conventional methods to dispose of metal ions. A broad range of biological materials, especially bacteria, algae, yeast, fungi, and agricultural industrial wastes, have received an increasing attention for the disposal of heavy metals, due to their good performance, low cost, and large quantities available [7, 8]. Previous studies indicate that biosorbents, in contrast to ion exchange functional resins, contain a variety of functional sites including imidazole, carboxyl, sulfhydryl, amino, phosphate, sulphate thioether, phenol, carbonyl, amide, and hydroxyl residues which allow us to obtain excellent results when using these materials [9, 10].

The development of new technologies for metal removal in aqueous solutions is convenient. This research work proposes a method of lead removal by biosorption as a conventional alternative to treat water polluted with this metal [11]. Chemical precipitation, oxidation, and ion exchange methods are expensive especially when the metal concentration is low; besides generation of sludge is high and its disposal becomes an environmental problem [12, 13].

In previous researches, the use of deoiled allspice husk residues for the Pb(II) removal in aqueous solution led to 78% removal in a batch system [14]. We have also used other biosorbents that were modified; for example, modified chitosan was used through a xanthation reaction to remove Pb(II) obtaining an 85% removal [15]. Another sort of biomass that can be used is orange peel, which likewise can be modified by a xanthation reaction, obtaining a Pb(II) removal of 95% [16]. Finally, residues chemically modified Lyocell for heavy metals treatment. The sorbent, which was prepared by a simple and concise method, was able to bind heavy metals such as Pb(II), Cu(II), and Cd(II), with very high efficiencies [17].

When doing chemical modifications to the used biosorbents, these increase their adsorption capacity because functional groups like amines, amides, thiols, imines, and phosphates become embedded. These create metal complexes or coordination complexes making the heavy metal adsorption process more efficient [18, 19]. The residues of *Pimenta dioica* L. Merrill, which belong to the Myrtaceae family, were used. Mexico exports about 4500 tons per year, and half of this production is processed domestically. In Mexico, 1500 tons of residues is produced annually as a result of the extraction of pepper essential oil. These residues contain 23.1% cellulose, 8.5% hemicellulose, and 26.8% lignin, among others. The pepper residues were modified by a xanthation reaction in a basic media, followed by a lead adsorption capacity test. Xanthation has been used before in pulp, sawdust, brown seaweed, and chitin; in every case an increase in the adsorption capacity was obtained [20]. Xanthates are created through the reaction of an organic substrate which contains hydroxyls with carbon disulphide; because of this, an increase of the biosorbent's affinity for Pb(II) is expected [21, 22].

2. Materials and Methods

2.1. Biosorbent Previous Treatment. 100 grammes of dry pepper residues with a particle size of 6 mm was vacuum-washed with 500 mL of a H_2O/CH_3OH (40% : 60%) mix using a Buchner flask and a Buchner funnel. The pepper residues were dried for 24 h in a heater at 70°C. Then, a second vacuum wash was performed in the same conditions; then they were dried in a heater for 48 h, at 70°C [14].

2.2. Modification of Pepper Residues by the Xanthation Reaction. This amount of 100 gr of pepper residues already dried was added with 800 mL of NaOH 3 N (ACS Fermont 98.9%) and was left to react for 3 hours of stirring; after that, 50 mL of CS_2 is added and left to react for 3 more hours [15]. Finally, we made a vacuum wash with deionized water to these pepper residues already modified which were let to dry at 70°C for 42 hours [21, 22].

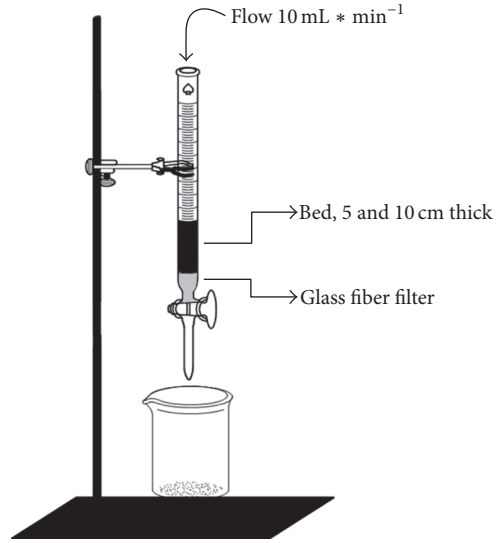

Figure 1: Column biosorbent with different thickness.

2.3. Pb(II) Solution Preparation. A 1000 mg L^{-1} lead stock solution was prepared, from which the following solutions were made: 0.05, 0.5, 1, 5, 10, 15, 20, 25, 30, 40, 50, 60, 70, and 80 mg L^{-1}, setting the dissolutions pH to 4 with a 0.001 M nitric acid solution.

2.4. Adsorption in Batch System. In order to study the adsorption kinetics of a 10 mL lead solution of 25 mg L^{-1} with a pH 4, 10 mg of biosorbent was continuously shaken at 30 rpm. The lead concentration in the system was established at 1, 5, 10, 15, 30, 45, 60, 75, 90, 105, and 120 minutes. To obtain the isotherms, solutions with different lead concentration levels were used that were 10, 20, 30, 40, and 50 mg L^{-1} at pH 4 and then mixed with a 10 mg biosorbent sample for 120 minutes at 200 rpm. In both processes several tubes were prepared using the same method as the ones stated, but assigning each of them to a different contact time. Once the latter had elapsed, the residual lead concentrations were determined in their liquid phase using an atomic absorption spectrophotometer.

2.5. Adsorption System in a Continuous Flow Column. A 40 cm length glass column with 2 cm diameter was assembled. A fiberglass filter was assembled at the bottom to prevent any obstructions because of the biosorbent settling thereat. Each column was packed with pepper. Three tests with different biosorbent thicknesses were used (5 and 10 cm) using a burette clamp and a universal support, as shown in Figure 1.

A 50 mg L^{-1} lead solution was passed through a packed column, by means of a fish tank pump and infusion instruments; the height was constantly regulated, just like the incoming and outgoing lead solution flow. Aliquots at the latter were gathered at different times; then, their lead

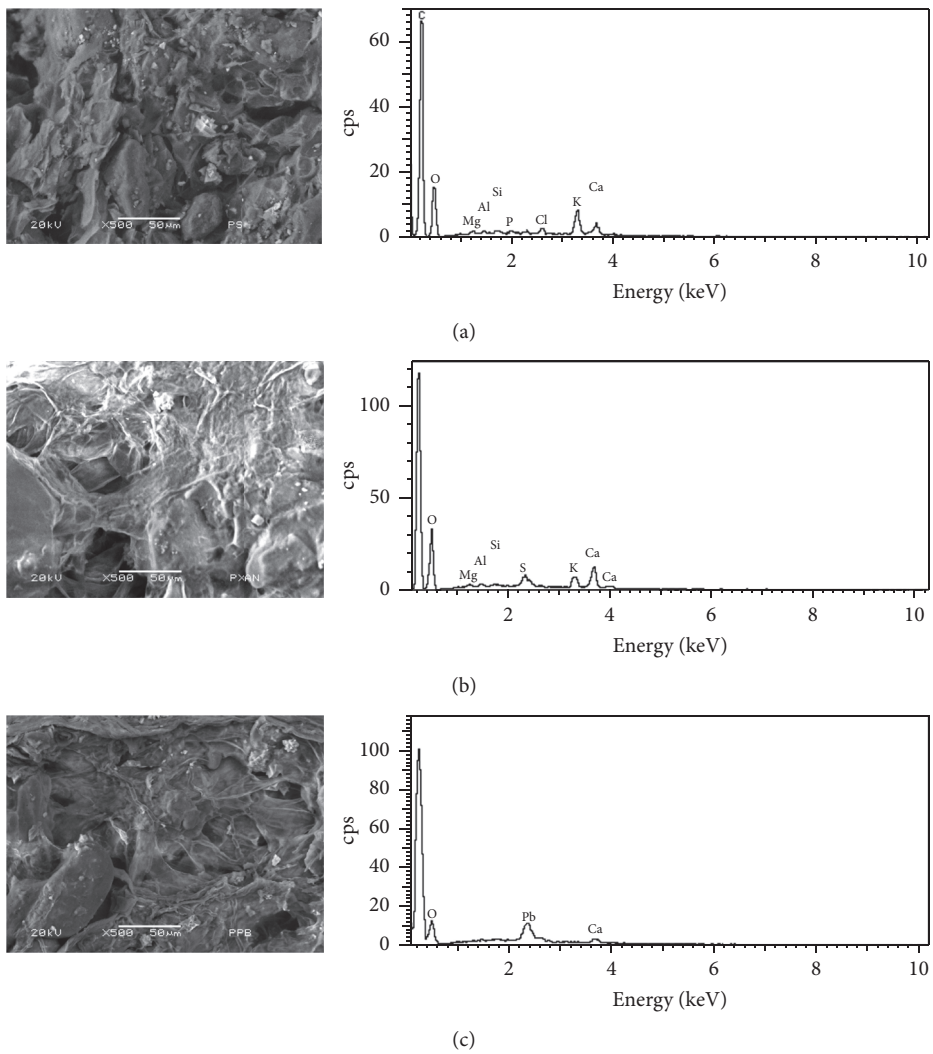

Figure 2: Micrographs pepper residues (a) unchanged, (b) modified, (c) after contact tests.

concentration was analyzed. This data was used to obtain the breakthrough curves.

2.6. Material Characterization

2.6.1. BET Analysis. The surface area and characteristics of the modified and unmodified pepper porosity were determined by means of N_2 BET gas method (GEMINI 2360 equipment) adsorbing nitrogen at 77 K. The respective adsorption isotherms were then recorded until attaining a 0.9 relative pressure in order to estimate the overall porosity volume: the porosity was determined using their volume and density.

2.6.2. Scanning Electron Microscope. The biosorbent images were obtained with a JEOL JSM 6510LV to 15 kV with 10 mm WD. The samples were covered with a 20 μm gold layer by means of sputtering with a Denton Vacuum DESK IV gold objective.

2.6.3. Infrared Spectroscopy. In order to identify the main functional groups involved in each process, the Fourier transform infrared (FTIR) spectroscopy was used, thus recording the infrared spectrum of the modified and unmodified pepper before and after the adsorption test in the batch system.

3. Results and Discussion

3.1. Biosorbent Characterization

3.1.1. MEB (SEM) Test. Figure 2 shows the MEB secondary electron images of pepper residues before modifying through the xanthation reaction, after the modification and after the adsorption test. Figure 2(a) shows the morphology of original material, comprising amorphous and irregular structures, though showing above all a large number of pores, with 50 μm length approximate particle size. The energy dispersion analysis gives the elemental composition of the

Table 1: Results of surface area.

	Specific surface area	Mean pore diameter
Unmodified pepper	1.65 $m^2 \cdot g^{-1}$	5.71 nm
Modified pepper	1.72 $m^2 \cdot g^{-1}$	3.02 nm

pepper residues, comprising at large carbon and oxygen, approximately representing 64.9% and 32.9%, respectively, of the total weight; small Mg, Al, Si, P, Cl, K, and Ca quantities are included. Figure 2(b) shows the pepper residues image after the xanthation modification. An amorphous and porous structure is visible, a particle size of 50 μm length in the magnified micrograph of 500x. For the elemental composition of the pepper residues after the modification through xanthation the majority elements are carbon and oxygen with the 60.509% and 36.817%, respectively, although sulphur is now present, which was expected because this group increases after modification. Figure 2(c) shows the image of the pepper residues already modified; after doing the adsorption tests, the resulting structure is amorphous and porous similar to the previous images: also, the particle size was 50 μm.

The elemental composition of the pepper residues after contact with the Pb(II) solution revealed that carbon and oxygen seem to be the majority with 67.636% and 28.642%, respectively, but now Pb(II) is present, which was expected though not in a higher percentage, because the particle size that was used was too large; thus there is a higher quantity of pores but there is also a smaller quantity of Ca.

3.1.2. BET Analysis. In Table 1 it is disclosed that the surface area of the biosorbent is 1.72 $m^2\ g^{-1}$ which is lower than that of the activated carbon with 500–1500 $m^2\ g^{-1}$, but that does not limit its adsorption capacity. Doing the modification did not increase considerably the material attributes [23].

3.1.3. Infrared Spectroscopy. Figure 3 shows the IR spectra that were obtained from the pepper residues before they were modified and after the contact tests, where the most important functional groups of each process are located and detailed. A characteristic -OH band was located at the 3000 cm^{-1} that reflects bond stretching; another band that was located at 1600 cm^{-1} comes from carbonyl vibration associated with the essential oil traces and the band located between 1300 cm^{-1} and 1500 cm^{-1} comes from the stretching vibrations of a C-O interaction associated with primary and secondary alcohols that are dissociated.

The band at 1100 cm^{-1} is due to the vibration between the C=S interaction and the band that at 1050 cm^{-1} is due to sulfoxides functional group C-S or O-C-S vibration, which demonstrate that the pepper modification was done, since the presence of S is observed.

3.2. Distribution Diagram of Lead Species. It has been stated that all tests of this study were made at pH 4, because the distribution diagram of the lead species shown in Figure 4 showed that any pH above 6 would involve lead precipitation;

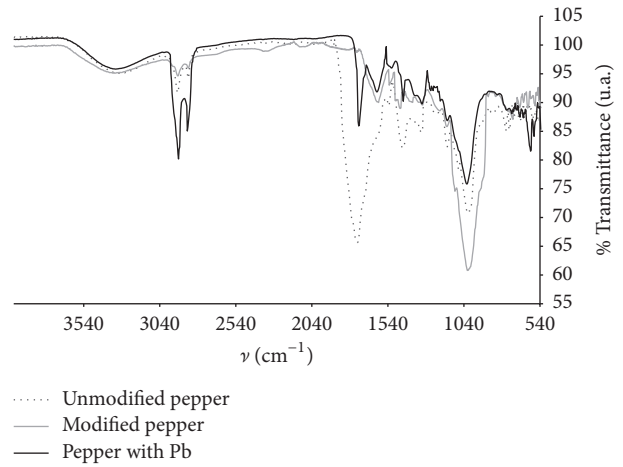

Figure 3: IR pepper residue unmodified and modified after contact tests.

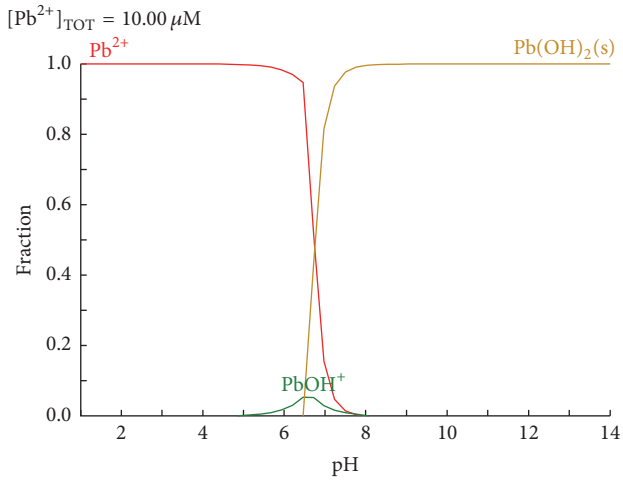

Figure 4: Diagram of distribution of lead species [I. Puigdomenech, Hydrochemical Equilibrium Constants Database (MEDUSA), Royal Institute of Technology, Stockholm, Sweden, 1997].

therefore the removal would not be through adsorption. Working in the pH < 6 zone would warrant that lead remained as Pb^{2+}. However, working with a pH 3 or smaller, a precipitation problem would not occur, although the working conditions would not be appropriate, considering that an acidic media prevailed, where the Pb^{2+} species would have to compete with H^+ for the biosorbent active place, thereby causing a protonation process of the biosorbent, affecting the lead removal process again [24, 25].

3.3. Batch Adsorption Kinetics. These tests were made with a 25 mg L^{-1} lead solution at pH 4 with constant stirring at 200 rpm and 10 mg of biosorbent. As shown in Figure 5, during the first 10 contact minutes, the concentration of Pb(II) in solution decreased almost to one-half, obtaining the acutest Pb(II) decrease during the first 5 minutes. Then, the Pb(II) concentration in solution decreased with increasing stirring time until reaching a quasi-equilibrium.

Table 2: Parameters from the pseudo-second-order kinetic model.

C_o (mg·L^{-1})	q_2 (mg·g^{-1})	q_{exp} (mg·g^{-1})	K_2 (g·mg^{-1} min^{-1})	R^2
25	27.03	25.8	4.67×10^{-3}	0.993

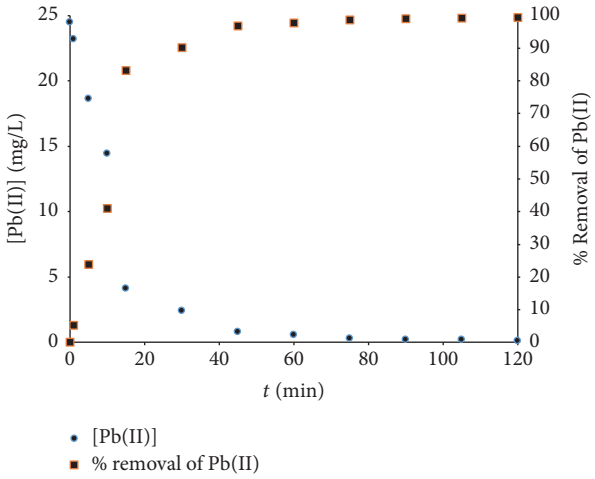

Figure 5: Concentration and lead removal percentage versus time at a pH value of 4 for the system Pb(II) and pepper modified with a particle size of 6 mm.

Figure 5 shows the removal percentage achieved after 120 contact minutes, reaching the 99%, which was very good, therefore confirming the efficiency of the modified biosorbent. The kinetic model with the best fitting was the pseudo-second-order model, with a correlation coefficient $R^2 = 0.99$, shown in Figure 6. The adsorption process kinetic was described by

$$\frac{1}{q_t} = \frac{1}{k_2 q_2^2} + \frac{1}{q_2} t, \quad (1)$$

where q_2 is the equilibrium adsorption capacity (mg g^{-1}) predicted by the pseudo-second-order (for a Co = 25 mg L^{-1}) adsorption when the initial q_t is the quantity of adsorbed metal at the time t (mg g^{-1}) and K_2 is the pseudo-second-order speed constant (mg g^{-1} min^{-1}) [26, 27]. Table 2 indicated that calculated q_2 is 27.03 mg g^{-1}, while K_2 was 4.67 × 10^{-3} g mg^{-1} min^{-1}. The q_2 value was estimated through mass balance with the last data of concentration in the liquid at 120 minutes giving a q_{exp} value of 25.8, which is comparable to the q_2 value obtained in the kinetic model [28, 29].

These results are similar to those obtained by [14] because in the previous study it was made with xanthated pepper with a particle size of 2.36 mm where they obtained a kinetic adsorption of pseudo-second order with a K_2 of 7.46 g mg^{-1} min^{-1} and a q_2 of 38.74 mg g^{-1}, which are values slightly higher than those obtained in this study but that agree with the particle size used in both studies. Based on the results shown, the studies to obtain the adsorption isotherm using different Pb(II) concentrations were made.

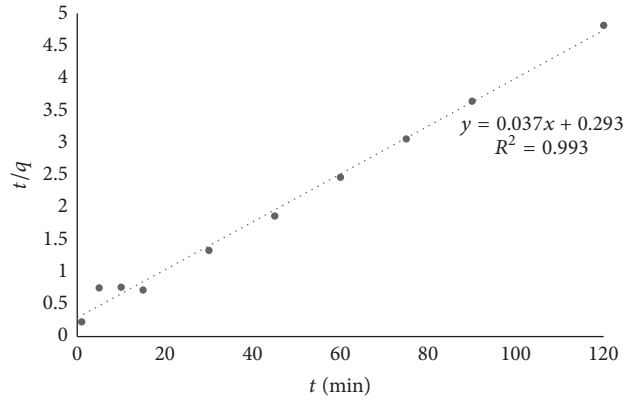

Figure 6: Kinetics of adsorption of pseudo-second-order q/t versus time, for the system of Pb(II) and pepper modified with a particle size of 6 mm.

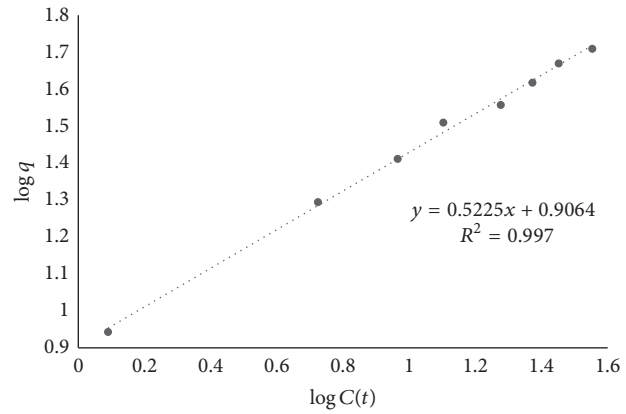

Figure 7: log q Freundlich isotherm according to the system log $C(t)$ of Pb(II) and pepper modified with a particle size of 6 mm.

3.3.1. Adsorption Isotherm. Figure 7 shows that the Freundlich isotherm model fitted well the data, giving a correlation coefficient $R^2 = 0.997$. The Freundlich isotherm fits well into the experimental data; consequently multilayer adsorption with heterogeneous distribution of active sites of the biosorbent is proposed [30, 31].

The values for Freundlich isotherm constants were K_f = 8.06 (mg g^{-1}) (mg$^{-1/n}$ L$^{1/n}$) and $1/n$ = 0.52, respectively [32, 33].

3.4. Continuous Flow Column System. Figure 8 shows the breakthrough curves that were obtained working with biosorbent beds of 5 cm and 10 cm height, with a flow of 10 mL min^{-1} and with a lead solution of 50 mg L^{-1}. With the

Table 3: Parameters of the Thomas model for the bed heights of 5 cm and 10 cm.

Bed height (cm)	Biosorbent used (g)	Flow of the Pb(II) solution (mL·min^{-1})	K_{TH} (L·min^{-1}·mg^{-1})	q_o (mg·g^{-1})	r^2
10	9.07	10	0.0026	45.322	0.98
5	4.45	10	0.0035	29.114	0.98

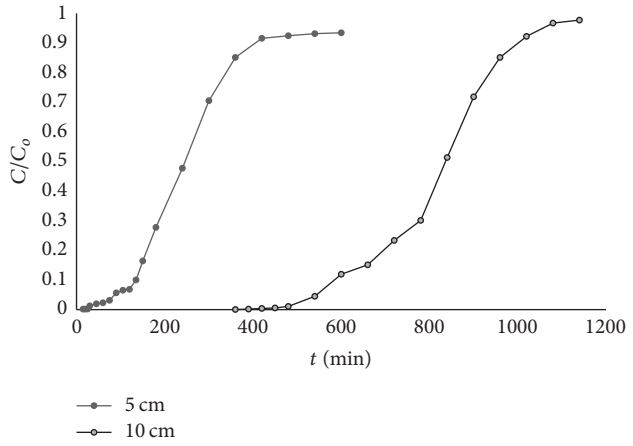

Figure 8: Breakthrough curves of the 5 and 10 cm columns packed with modified pepper (6 mm particle size).

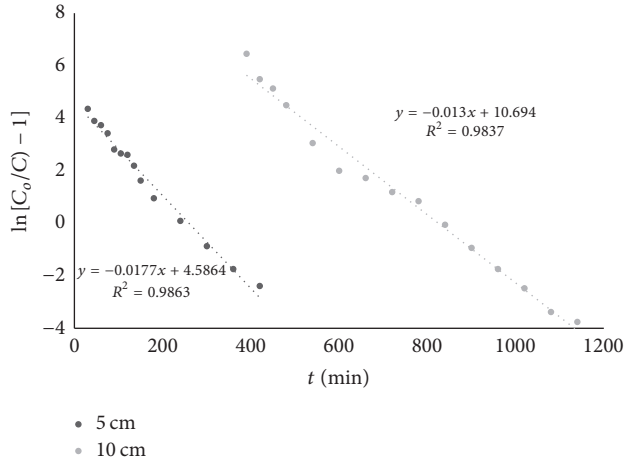

Figure 9: Fitting of the linearized Thomas model with data from the packed column of 5 and 10 cm (modified pepper adsorbent of 6 mm particle size).

10 cm height bed, 90% saturation occurs after 1000 minutes of operating time, although a complete saturation was not seen during the follow-up time.

Working with a biosorbent bed, 5 cm thick, saturation occurred after 300 minutes of operating time. The data obtained were analyzed mathematically using the Thomas model. The successful design of a sorption process in a column requires the prediction of the breakthrough curve for the effluent and the specification of the maximum sorption capacity of the sorbent. The linearized form of the equations is presented by the following Thomas equation:

$$\ln\left(\frac{C_o}{C} - 1\right) = \frac{K_{TH} q_o M}{Q} - K_{TH} C_o t, \quad (2)$$

where C is solute concentration in the affluent (mg·L^{-1}), C_o is solute concentration in the influent (mg L^{-1}), K is Thomas speed constant (mg min^{-1} mg^{-1}), q_o is maximum concentration of solute in the solid phase (mg g^{-1}), M is mass of sorbent (g), t is time (min), and Q is volumetric flow rate (mL min^{-1}).

Table 3 shows the results from the fitting of the Thomas model [33, 34]. By working with a xanthated pepper bed, 5 cm thick, a maximum adsorption capacity of 29.114 mg g^{-1} was obtained with a rate constant of 0.0035 L min^{-1} mg^{-1}, with a coefficient of determination (r^2) of 0.98, which is shown in Figure 9. With 10 cm bed, the maximum adsorption capacity was 45.322 mg g^{-1} while the Thomas kinetic constant was 0.0026 L min^{-1} mg^{-1} (r^2 = 0.98, also shown in Figure 9).

4. Conclusions

The removal percentage of Pb(II) in aqueous solution obtained was 99% at pH 4; the Pb(II) removal in aqueous solution was favoured by the modification done to the pepper residues, which increased the biosorbent affinity for Pb(II). The results from the batch kinetic studies showed a maximum adsorption capacity of 25.8 mg of Pb(II) per g of biosorbent, while the data were well fitted by the pseudo-second-order kinetic model. Pb(II) in aqueous solution was adsorbed through a multilayer process with heterogeneous distribution of the biosorbent's active sites. The infrared and scanning electron microscope studies verified that the sulphur insertion created the thiol group in the pepper structure, which was the aim of the biosorbent modification. The breakthrough curves of the continuous flow systems (colums) were adequately fitted with the Thomas model, which provided an estimation of the dynamic adsorption capacities of 29.114 mg g^{-1} and 45.322 mg g^{-1} (for the 5 and 10 cm bed height, resp.).

Competing Interests

The authors declare that they have no competing interests.

Acknowledgments

Efrain Palma-Anaya gratefully acknowledges the scholarship from CONACyT to pursue her postgraduate studies.

References

[1] T. H. Bakken, I. S. Modahl, K. Engeland, H. L. Raadal, and S. Arnøy, "The life-cycle water footprint of two hydropower projects in Norway," *Journal of Cleaner Production*, vol. 113, pp. 241–250, 2016.

[2] S. Chowdhury, M. A. J. Mazumder, O. Al-Attas, and T. Husain, "Heavy metals in drinking water: occurrences, implications, and future needs in developing countries," *Science of the Total Environment*, vol. 569-570, pp. 476–488, 2016.

[3] V. Geraldes, M. Carvalho, N. Goncalves-Rosa, C. Tavares, S. Laranjo, and I. Rocha, "Lead toxicity promotes autonomic dysfunction with increased chemoreceptor sensitivity," *Neuro-Toxicology*, vol. 54, pp. 170–177, 2016.

[4] M. Dörpinghaus, A. Brieger, O. Panichkina, L. Rink, and H. Haase, "Lead ions abrogate lipopolysaccharide-induced nitric monoxide toxicity by reducing the expression of STAT1 and iNOS," *Journal of Trace Elements in Medicine and Biology*, vol. 37, pp. 117–124, 2016.

[5] C. M. V. B. Almeida, M. A. Madureira, S. H. Bonilla, and B. F. Giannetti, "Assessing the replacement of lead in solders: effects on resource use and human health," *Journal of Cleaner Production*, vol. 47, pp. 457–464, 2013.

[6] H. T. Tran, N. D. Vu, M. Matsukawa et al., "Heavy metal biosorption from aqueous solutions by algae inhabiting rice paddies in Vietnam," *Journal of Environmental Chemical Engineering*, vol. 4, no. 2, pp. 2529–2535, 2016.

[7] A. K. Zeraatkar, H. Ahmadzadeh, A. F. Talebi, N. R. Moheimani, and M. P. McHenry, "Potential use of algae for heavy metal bioremediation, a critical review," *Journal of Environmental Management*, vol. 181, no. 1, pp. 817–831, 2016.

[8] J. Milojković, L. Pezo, M. Stojanović et al., "Selected heavy metal biosorption by compost of Myriophyllum spicatum—a chemometric approach," *Ecological Engineering*, vol. 93, pp. 112–119, 2016.

[9] N. K. Akunwa, M. N. Muhammad, and J. C. Akunna, "Treatment of metal-contaminated wastewater: a comparison of low-cost biosorbents," *Journal of Environmental Management*, vol. 146, pp. 517–523, 2014.

[10] R. K. Gautam, A. Mudhoo, G. Lofrano, and M. C. Chattopadhyaya, "Biomass-derived biosorbents for metal ions sequestration: adsorbent modification and activation methods and adsorbent regeneration," *Journal of Environmental Chemical Engineering*, vol. 2, no. 1, pp. 239–259, 2014.

[11] K. M. Al-Qahtani, "Water purification using different waste fruit cortexes for the removal of heavy metals," *Journal of Taibah University for Science*, vol. 10, no. 5, pp. 700–708, 2016.

[12] J. Zhao, J. Liu, N. Li et al., "Highly efficient removal of bivalent heavy metals from aqueous systems by magnetic porous Fe_3O_4-MnO_2: adsorption behavior and process study," *Chemical Engineering Journal*, vol. 304, pp. 737–746, 2016.

[13] J. Mehta, S. K. Bhardwaj, N. Bhardwaj et al., "Progress in the biosensing techniques for trace-level heavy metals," *Biotechnology Advances*, vol. 34, no. 1, pp. 47–60, 2016.

[14] T. Torres-Blancas, G. Roa-Morales, C. Fall, C. Barrera-Díaz, F. Ureña-Nuñez, and T. B. Pavón Silva, "Improving lead sorption through chemical modification of de-oiled allspice husk by xanthate," *Fuel*, vol. 110, pp. 4–11, 2013.

[15] D. Chauhan and N. Sankararamakrishnan, "Highly enhanced adsorption for decontamination of lead ions from battery wastewaters using chitosan functionalized with xanthate," *Bioresource Technology*, vol. 99, no. 18, pp. 9021–9024, 2008.

[16] N.-C. Feng and X.-Y. Guo, "Characterization of adsorptive capacity and mechanisms on adsorption of copper, lead and zinc by modified orange peel," *Transactions of Nonferrous Metals Society of China*, vol. 22, no. 5, pp. 1224–1231, 2012.

[17] J. K. Bediako, W. Wei, S. Kim, and Y.-S. Yun, "Removal of heavy metals from aqueous phases using chemically modified waste Lyocell fiber," *Journal of Hazardous Materials*, vol. 299, pp. 550–561, 2015.

[18] U. Farooq Umar, M. A. Khan, M. Athar, and J. A. Kozinski, "Effect of modification of environmentally friendly biosorbent wheat (Triticum aestivum) on the biosorptive removal of cadmium(II) ions from aqueous solution," *Chemical Engineering Journal*, vol. 171, no. 2, pp. 400–410, 2011.

[19] S. W. Won, P. Kotte, W. Wei, A. Lim, and Y.-S. Yun, "Biosorbents for recovery of precious metals," *Bioresource Technology*, vol. 160, pp. 203–212, 2014.

[20] K. Wang, L. Wang, M. Cao, and Q. Liu, "Xanthation-modified polyacrylamide and spectroscopic investigation of its adsorption onto mineral surfaces," *Minerals Engineering*, vol. 39, pp. 1–8, 2012.

[21] S. Liang, X. Guo, N. Feng, and Q. Tian, "Application of orange peel xanthate for the adsorption of Pb^{2+} from aqueous solutions," *Journal of Hazardous Materials*, vol. 170, no. 1, pp. 425–429, 2009.

[22] P. L. Homagai, K. N. Ghimire, and K. Inoue, "Adsorption behavior of heavy metals onto chemically modified sugarcane bagasse," *Bioresource Technology*, vol. 101, no. 6, pp. 2067–2069, 2010.

[23] M. T. Izquierdo, A. M. De Yuso, R. Valenciano, B. Rubio, and M. R. Pino, "Influence of activated carbon characteristics on toluene and hexane adsorption: application of surface response methodology," *Applied Surface Science*, vol. 264, pp. 335–343, 2013.

[24] A. Hammaini, F. González, A. Ballester, M. L. Blázquez, and J. A. Muñoz, "Biosorption of heavy metals by activated sludge and their desorption characteristics," *Journal of Environmental Management*, vol. 84, no. 4, pp. 419–426, 2007.

[25] B. F. Trueman and G. A. Gagnon, "A new analytical approach to understanding nanoscale lead-iron interactions in drinking water distribution systems," *Journal of Hazardous Materials*, vol. 311, pp. 151–157, 2016.

[26] L. Largitte and R. Pasquier, "A review of the kinetics adsorption models and their application to the adsorption of lead by an activated carbon," *Chemical Engineering Research and Design*, vol. 109, pp. 495–504, 2016.

[27] R. K. Anantha and S. Kota, "Removal of lead by adsorption with the renewable biopolymer composite of feather (*Dromaius novaehollandiae*) and chitosan (*Agaricus bisporus*)," *Environmental Technology and Innovation*, vol. 6, pp. 11–26, 2016.

[28] L. Largitte and R. Pasquier, "New models for kinetics and equilibrium homogeneous adsorption," *Chemical Engineering Research and Design*, vol. 112, pp. 289–297, 2016.

[29] M. M. Montazer-Rahmati, P. Rabbani, A. Abdolali, and A. R. Keshtkar, "Kinetics and equilibrium studies on biosorption of cadmium, lead, and nickel ions from aqueous solutions by intact and chemically modified brown algae," *Journal of Hazardous Materials*, vol. 185, no. 1, pp. 401–407, 2011.

[30] Y. P. Teoh, M. A. Khan, and T. S. Y. Choong, "Kinetic and isotherm studies for lead adsorption from aqueous phase on carbon coated monolith," *Chemical Engineering Journal*, vol. 217, pp. 248–255, 2013.

[31] S. Tunali Akar, S. Arslan, T. Alp, D. Arslan, and T. Akar, "Biosorption potential of the waste biomaterial obtained from Cucumis melo for the removal of Pb2+ ions from aqueous media: equilibrium, kinetic, thermodynamic and mechanism analysis," *Chemical Engineering Journal*, vol. 185-186, pp. 82–90, 2012.

[32] D. Bulgariu and L. Bulgariu, "Equilibrium and kinetics studies of heavy metal ions biosorption on green algae waste biomass," *Bioresource Technology*, vol. 103, no. 1, pp. 489–493, 2012.

[33] Q. Li, H. Lu, H. Xiao, K. Gao, and M. Diao, "Adsorption capacity of superabsorbent resin composite enhanced by non-thermal plasma and its adsorption kinetics and isotherms to lead ion in water," *Journal of Environmental Chemical Engineering*, vol. 1, no. 4, pp. 996–1003, 2013.

[34] S. Amirnia, M. B. Ray, and A. Margaritis, "Heavy metals removal from aqueous solutions using *Saccharomyces cerevisiae* in a novel continuous bioreactor–biosorption system," *Chemical Engineering Journal*, vol. 264, pp. 863–872, 2015.

Hindawi Publishing Corporation
Journal of Chemistry
Volume 2016, Article ID 4108587, 8 pages
http://dx.doi.org/10.1155/2016/4108587

Research Article

Comparison of AOPs Efficiencies on Phenolic Compounds Degradation

Lourdes Hurtado,[1] Deysi Amado-Piña,[1] Gabriela Roa-Morales,[1] Ever Peralta-Reyes,[2] Eduardo Martin del Campo,[3] and Reyna Natividad[1]

[1]*Chemical Engineering Lab, Centro Conjunto de Investigación en Química Sustentable, UAEMex-UNAM, Universidad Autónoma del Estado de México, km 14.5 Toluca-Atlacomulco Road, 50200 Toluca, MEX, Mexico*
[2]*Instituto de Ecología, Universidad del Mar, Ciudad Universitaria S/N, 70902 Puerto Ángel, OAX, Mexico*
[3]*Chemical Engineering Department, Faculty of Chemistry, Universidad Autónoma del Estado de México, Paseo Colon esq. Paseo Tollocan s/n, 50120 Toluca, MEX, Mexico*

Correspondence should be addressed to Reyna Natividad; reynanr@gmail.com

Received 23 July 2016; Revised 11 October 2016; Accepted 20 October 2016

Academic Editor: Sedat Yurdakal

In this work, a comparison of the performances of different AOPs in the phenol and 4-chlorophenol (4-CP) degradation at lab and pilot scale is presented. It was found that, in the degradation of phenol, the performance of a coupled electro-oxidation/ozonation process is superior to that observed by a photo-Fenton process. Phenol removal rate was determined to be 0.83 mg L^{-1} min^{-1} for the coupled process while the removal rate for photo-Fenton process was only 0.52 mg L^{-1} min^{-1}. Regarding 4-CP degradation, the complete disappearance of the molecule was achieved and the efficiency decreasing order was as follows: coupled electro-oxidation/ozonation > electro-Fenton-like process > photo-Fenton process > heterogeneous photocatalysis. Total organic carbon was completely removed by the coupled electro-oxidation/ozonation process. Also, it was found that oxalic acid is the most recalcitrant by-product and limits the mineralization degree attained by the technologies not applying ozone. In addition, an analysis on the energy consumption per removed gram of TOC was conducted and it was concluded that the less energy consumption is achieved by the coupled electro-oxidation/ozonation process.

1. Introduction

Water detoxification is an important issue that demands the immediate development and implementation of effective technologies able to abate pollutants in industrial wastewater. While no strict regulation about industrial wastewater could be applied to reduce the amounts of dangerous chemicals incorporated into water, the alternative is to follow the remedial route for degradation of pollutants and research needs to be done in this sense [1–3]. Among the numerous pollutant species, phenol and its derivatives deserve special attention due to its extended use, high toxicity, and its resistance to complete mineralization. Phenol (C_6H_6O) is employed as a raw material in the synthesis of innumerable chemical products as dyes, resins, and pharmaceuticals [4, 5]. One of the main phenol derivatives is 4-CP that is also widely employed in different industries [6, 7]. Phenolic compounds exposed to environment without any control can result in its transformation to more dangerous degradation products. The conventional wastewater treatment methods (i.e., filtration, centrifugation, sedimentation, coagulation, and aerobic or anaerobic processes) do not represent a real option to completely eliminate toxic aromatic compounds. As alternative, the advanced oxidation processes (AOPs) have emerged and received special attention due to the possibility to be helpful in the transformation of organic compounds into carbon dioxide and water at moderate operation conditions by means of potent oxidant agents and low cost and widely available reagents [8–11]. These processes have been successfully applied to water treatment for phenolic compounds removal and some of them are Fenton [12], photo-Fenton [13], electro-Fenton [4], electro-Fenton-like [14], anodic oxidation

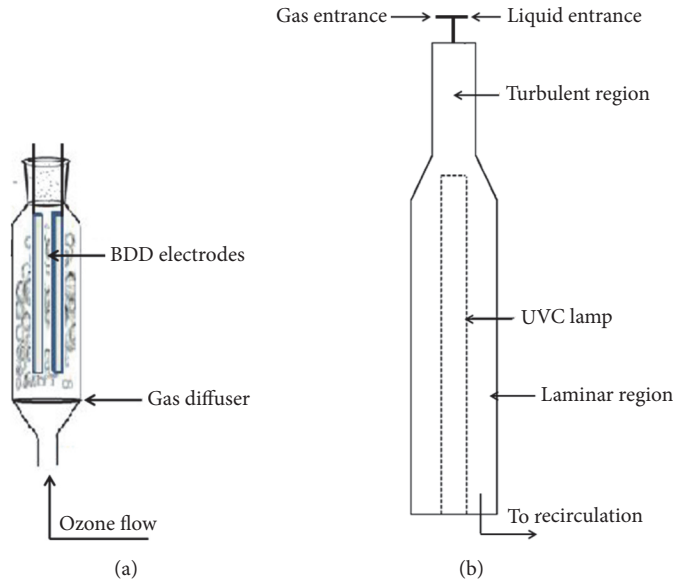

Figure 1: (a) Upflow bubble column reactor for coupled electro-oxidation/ozonation process. (b) Cocurrent downflow bubble column used for photocatalytic process for 4-CP degradation.

[15], photo-electro-Fenton [1], peroxicoagulation [16], H_2O_2 electrogenerated [17], photocatalysis [18], and ozonation [19] processes. Electrochemical oxidation is a promising clean technology that involves the production of hydroxyl radicals through anodic/cathodic reactions taking place at the electrodes [9, 11]. Ozonation process is also considered as a potent and clean technology to mineralize organic matter [20]. Ozone toxicity at the levels employed for organic degradation processes can be considered as low. A Fenton process involves the use of H_2O_2 which also is considered as a nontoxic reagent due to its decomposition gives inert compounds as oxygen and water [21]. Metallic reagents (Fe^{2+}/Fe^{3+}, Cu^{2+}/Cu^{+}) are also low cost and wide availability materials to conduct Fenton and Fenton-like processes [1]. Heterogeneous photocatalysis involves the activation of chemical reactions by light and implies the use of semiconductors as catalyst which normally are prepared from cheap metals [22]. All the aforementioned processes can be operated under mild conditions (room temperature and atmospheric pressure) reducing energy consumption cost and giving priority to environmental safety. Despite the variety of AOPs, in this work we focus on the degradation of phenolic compounds (phenol and 4-chlorophenol) by the following technologies: coupled electro-oxidation/ozonation, photo-Fenton, photocatalysis, and electro-Fenton-like processes performed at lab and pilot scale. It is worth clarifying that the results presented here for every treatment were chosen as the best ones in terms of phenolic compound mineralization from a set of experiments that have been reported elsewhere [23–26] by our group. Therefore, this work mainly aims to identify the most promising technology among the studied ones by comparing them in terms of mineralization efficiency and energy consumption per removed gram of total organic carbon at the best conditions previously reported for each process.

2. Materials and Methods

2.1. Reagents. Phenol (C_6H_5OH) was purchased from Merck. Reagent grade 4-CP (ClC_6H_4OH) and 4-aminoantipyrine ($C_{11}H_{13}N_3O$) were purchased from Sigma-Aldrich. Solutions of phenolic compounds at different concentrations were prepared with deionized water. Potassium ferrocyanide ($C_6N_6FeK_3$) was obtained from Baker. Hydrotalcite-like compound (MgAlZn 5%) used as photocatalyst was prepared according to the procedure described in a previous work [24]. H_2O_2 solution was provided by Fermont (30.2% purity).

2.2. Phenolic Compounds Oxidation

2.2.1. Coupled Electro-Oxidation/Ozonation. Oxidation of phenolic compounds by a coupled method was conducted in an upflow bubble column reactor adapted as electrochemical cell with two BDD (boron doped diamond) electrodes (20 cm × 2.5 cm) working as anode and cathode separated at a distance of 1 cm. Figure 1 depicts a schematic representation of the reaction system. Superficial area of electrodes was equal to 50 cm^2 and reaction volume was 1 L of solution. 0.1 M Na_2SO_4 was employed as support electrolyte and the initial concentration of phenol/4-CP to be degraded was 100 ppm. Ozone was produced in a Pacific Ozone Technology ozone generator by electric discharge. The ozone concentration in the gas stream at the inlet of the reactor was determined to be 5 ± 0.05 mg L^{-1}. Gas was fed at a flowrate of 0.05 L min^{-1} rate and was continuously supplied to the reactor through a porous gas-plate diffuser placed at the bottom of the reactor. In a typical experiment the reactor was operated in batch mode regarding the liquid phase and it was performed at room temperature. In the case of phenol degradation a current density of 60 mA/cm^2 was applied to the BDD

electrodes while 30 mA/cm^2 was the current density applied when 4-CP degradation was conducted. The applied potential value in this process was 11.25 V. The results presented here were obtained with experiments where the pH was initially adjusted at 7.0 by means of H_2SO_4 and/or NaOH analytical grade. This pH, in the range of 3 to 12, was found to be the one maximizing the mineralization of the phenolic compounds. For the same reason the applied densities were selected. The whole set of results are to be published elsewhere [26]. Samples were analysed by UV-vis spectroscopy, HPLC, and TOC.

2.2.2. Photo-Fenton Process. Degradation of phenolic compounds aqueous solutions (C_0 = 100 ppm) was also performed by Photo-Fenton process in a jacketed Pyrex glass vessel of 0.1 L coupled with a UVP Pen-Ray lamp (λ = 254 nm) located at its centre. Dimensions of the reactor were 2.5 cm internal diameter and 20 cm length. Iron reagent was provided through pillared iron clays at a catalyst concentration equal to 0.8 kg m^{-3}. Further details about pillared iron clays preparation and reaction system operation can be consulted in Martin del Campo et al. [23]. A typical experiment was performed at room temperature. The initial pH value was adjusted at 2.8 at all experiments by means of H_2SO_4 addition since it is well known that photo-Fenton process performs the best at acidic conditions. A stoichiometric amount of H_2O_2 was added to the system. A control experiment to elucidate the interaction of hydrogen peroxide with phenol and 4-CP was conducted. The change concentration was less than 2% after 120 min even when an amount of 20 times the stoichiometric amount of hydrogen peroxide was added to a 4-CP aqueous solution. After studying the effect of initial hydrogen peroxide concentration and pillared clay loading, it was concluded [23] that the highest mineralization degree was attained when using the stoichiometric amount of hydrogen peroxide and 0.8 g L^{-1} of pillared clay. Therefore, the calculations presented here are those obtained with the results at such conditions. Samples were periodically withdrawn and analysed by UV-vis spectroscopy and with the TOC analyser.

2.2.3. Heterogeneous Photocatalysis. Photooxidation of 4-CP (C_0 = 80 ppm) was conducted at pilot scale in a cocurrent downflow bubble column (CDBC) in which 14 L of a contaminated solution was treated. This reactor was coupled with a HITECH NNI 400/147 XL UVC lamp (λ = 254 nm) (Figure 1). A hydrotalcite-like compound (MgZnAl 5%) was used as photocatalyst at a concentration equal to 1.2 kg m^{-3}. According to the fabricant, the intensity of the light emitted by the employed lamp at a distance of 1 m is 1100 μW cm^{-2}. Temperature was kept constant during the entire experiment (298 K). pH was not adjusted at any moment of the experiment and basic conditions were observed at the end of it. In this case the effect of pH was not studied. Still, it is worth pointing out that hydrotalcites should not be used under acidic pH since get diluted. Further details about this device and its operation are available in Martin del Campo et al. [24]. The reaction was followed by UV-vis spectroscopy and TOC analysis.

2.2.4. Electro-Fenton-Like Process. This process was conducted in a cylindrical undivided electrochemical cell. Two pairs of electrodes were employed (the same material was used for anode and cathode). A pair of them made of graphite (superficial area: 50 cm^2) was adapted for H_2O_2 electrogeneration in situ and two copper electrodes (superficial area: 50 cm^2) were placed in order to provide, by applying pulses of current, metallic ions to catalyse the H_2O_2 dissociation (four 40 mA/cm^2 current pulses, 5 minutes each, every 30 minutes). Graphite electrodes were continuously energized with a current density of 4 mA/cm^2. The reaction volume was 0.85 L and consisted in a solution of Na_2SO_4 (0.05 M) and 4-CP (C_0 = 100 ppm). The applied potential value for this process was 8 V. At all experiments, pH was adjusted at 3.0 and temperature was kept constant during the entire experiment (291 K). These conditions were found to provide the highest mineralization degree in a comprehensive study previously conducted [25]. In such a report the effect of several variables on mineralization degree was studied. These variables were type of H_2O_2 dissociation catalyst (Fe or Cu), oxygen flowrate, number and length of current pulses applied to iron or copper electrodes, and current density. Chemical analysis included both, HPLC and TOC analysis.

2.3. Chemical Analysis. Phenol absorbance measurements were performed in a Perkin Elmer Lambda 25 UV-vis spectrophotometer (λ = 510 nm) by the reaction of phenol with 4-aminoantipyrine in the presence of potassium ferricyanide 4-CP concentration which was determined in the same device but the absorbance was taken at λ = 280 nm. Mineralization of phenol and 4-CP solutions treated by the coupled EO/O_3 and EFL was quantified in a Shimadzu TOC-L_{CPN} device. The samples from the PF and PC treatments were analysed in an Apollo Model 9000 TOC Analyser. The main reaction intermediates were identified and quantified by HPLC in a Waters 1015 equipment operating in isocratic mode. For the analysis of carboxylic acids, an Eclipse XDB C18 column was employed and the mobile phase (0.6 mL min^{-1}) was composed of water : acetonitrile : phosphoric acid in an 89.9 : 10 : 0.1 ratio. In the case of aromatic by-products, the chemical analysis required an Ascentis C18 column and a mobile phase (1 mL min^{-1}) composed of methanol : water in an 80 : 20 ratio acidified by 5 mM of H_2SO_4. The UV detector was configured at 210 nm to quantify carboxylic acids and at 280 nm to quantify aromatic compounds.

3. Results and Discussion

3.1. Phenol Degradation. Degradation of phenol was performed by two different AOPs: coupled electro-oxidation/ozonation process (EO/O_3) and photo-Fenton process (PF). These processes were evaluated after 60 min of treatment. It was found that the coupled treatment reached 100% of phenol degradation while by PF it was less efficient with only 36% of degradation of initial phenol and increased to 67% after 120 min. Furthermore, it is worth noticing that the reaction volume in the coupled EO/O_3 is about 10 times higher than that treated by photo-Fenton process.

The superior performance of the coupled process is expected since the synergetic effect of two coupled AOPs accelerates the degradation of the model compound. If the reaction time in photo-Fenton process was extended, probably the same degradation as that with the coupled process could be achieved.

The common element in the aforementioned processes is the oxidation of phenol molecule by means of hydroxyl radical according to (1)-(2) for EO [27], (3) for ozonation [27], and (4) for photo-Fenton process [11]. Oxidation through electrochemical process can follow two routes depending on the oxidizing agent: by hydroxyl radical produced by anodic oxidation (see (1)) or by hydrogen peroxide produced by cathodic reduction (see (2)). In ozonation two degradation routes can also be distinguished, direct oxidation of organic compounds due to the electrophilic character of O_3 and indirect oxidation by production of hydroxyl radicals (see (3)) although at a pH of 7 no preference for direct or indirect oxidation has been reported [27]. Finally, in photo-Fenton process the hydroxyl radical is produced by interaction of peroxide with light and iron reagent (see (4))

$$\mathrm{BDD} + \mathrm{H_2O} \longrightarrow \mathrm{BDD}\left(^{\bullet}\mathrm{OH}\right) + \mathrm{H^+} + \mathrm{e^-} \quad (1)$$

$$\mathrm{O_2} + 2\mathrm{H^+} + 2\mathrm{e^-} \longrightarrow \mathrm{H_2O_2} \quad (2)$$

$$2\mathrm{O_3} + \mathrm{H_2O} \longrightarrow 2\mathrm{HO^{\bullet}} + 2\mathrm{O_2} + \mathrm{HO_2^{\bullet}} \quad (3)$$

$$\mathrm{H_2O_2} + \mathrm{Fe^{2+}} + h\nu \longrightarrow \mathrm{Fe^{3+}} + \mathrm{HO^-} + \mathrm{HO^{\bullet}} \quad (4)$$

After hydrogen peroxide or hydroxyl radical is produced, this species reacts with phenol molecule oxidizing it towards intermediates or directly to carbon dioxide and water:

$$\mathrm{R} + \text{Phenol} \longrightarrow \text{Intermediates} \longrightarrow \mathrm{CO_2} + \mathrm{H_2O} \qquad \mathrm{R} = {}^{\bullet}\mathrm{OH} \text{ or } \mathrm{H_2O_2} \quad (5)$$

Due to the single or multiple possible degradation pathways for each treatment, differences in the concentration profiles as well as in the mineralization of the molecule were expected. This fact was confirmed and Figure 2 depicts normalized phenol concentration profiles of two representatives study cases: coupled EO/O_3 and photo-Fenton processes.

As expected, degradation routes of EO/O_3 and PF exhibit important differences. Degradation rate is considerably slower in the latter process which may require excessive reaction time to achieve competitive results against other technologies. Phenol degradation rate was determined as function of the total organic carbon (TOC) decay in the coupled EO/O_3. Thus, for this system,

$$-r_{\mathrm{TOC}} = 1.3501 \left(\mathrm{mg\,TOC/L\,min}\right). \quad (6)$$

The use of the Mineralization Current Efficiency for the comparison of the performances of electrochemical processes is widely accepted. In our case and on the basis of total organic carbon measurements, we also introduce this parameter according to the equation proposed by Professor Brillas' group [28] which is presented below:

$$\mathrm{MCE} = \frac{nFV\left(\text{Initial TOC} - \text{Final TOC}\right)}{4.23 * 10^7 mIt} * 100, \quad (7)$$

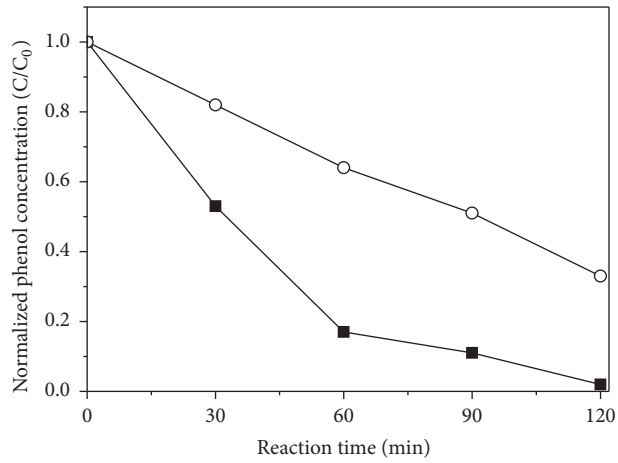

Figure 2: Phenol concentration temporal evolution obtained by EO/O_3 (■) and photo-Fenton (○) processes. Reaction conditions: EO (j = 60 mA cm^{-2}; pH = 7); photo-Fenton (C_{cat} = 0.8 kg m^{-3}; pH = 2.8).

where n is number of consumed electrons, F is Faraday constant (96487 C mol^{-1}), V is electrolyte volume (L), TOC is total organic carbon (mg L^{-1}), m is number of carbon atoms in the phenolic molecule (6), I is current (A), and t is time (h).

For phenol degradation (C_6H_6O), n = 28 according to the following chemical equation:

$$\mathrm{C_6H_6O} + 28\mathrm{OH^-} \longrightarrow 6\mathrm{CO_2} + 17\mathrm{H_2O} + 28\mathrm{e^-} \quad (8)$$

Finally, we calculate the MCE for the coupled EO/O_3 and results are presented in Table 1.

As the final step of the phenol degradation study, the by-products generated in the coupled EO/O_3 were identified. It was found that, in the first 10 min of treatment, aromatic compounds (hydroquinone, benzoquinone, and catechol) are formed and after 120 min practically they have disappeared by its degradation to carboxylic acids (oxalic, maleic, succinic, fumaric, and formic). Table 2 summarizes the identified by-products as well as its retention times and concentrations after 10 minutes (aromatic compounds) and 20 minutes (carboxylic acids) for the EO/O_3 coupled process.

3.2. 4-CP Degradation. The second phenolic compound to be degraded by AOPs was 4-CP. This molecule was elected to assess the performance of heterogeneous photocatalysis catalysed by MgAlZn 5% hydrotalcite-like compound (PC: MgAlZn 5%) and photo-Fenton process (PF) and Electro-Fenton-like process (EFL) in which H_2O_2 is also electro-generated in situ and coupled electro-oxidation/ozonation process (EO/O_3). The response variables for comparison among the four treatments were molecule degradation followed by UV-vis spectroscopy and mineralization degree by TOC analysis. For the former case the time evolution of 4-CP is presented in Figure 3 during a 180 min period.

From this concentration profiles comparison, we can observe important differences among AOPs. The total degradation of the model molecule is reached by both, EFL and

Table 1: MCE for the phenol degradation by coupled EO/O_3 process.

$TOC_{t=0}$ (mg TOC L^{-1})	$TOC_{t=2\,h}$ (mg TOC L^{-1})	j (mA cm^{-2})	MCE (%)
82.3	0.14	60	14.3

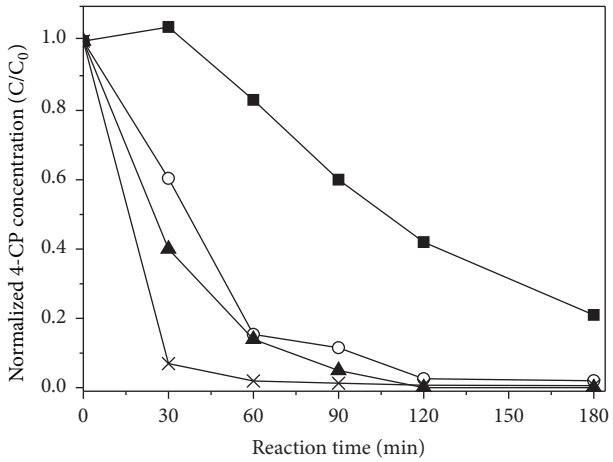

Figure 3: Temporal evolution of 4-CP concentration obtained by the following treatments: PC: MgZnAl 5% (■), PF (○), EFL (▲), and EO/O_3 (×). Reaction conditions: EFL (j at copper electrodes = 40 mA cm^{-2}, j at graphite electrodes = 4 mA cm^{-2}, and C_0 = 100 ppm); PC (C_{Cat} = 1.2 kg m^{-3}; C_0 = 80 ppm); PF (C_{Cat} = 0.8 kg m^{-3}; C_0 = 100 ppm); EO/O_3 (j = 30 mA cm^{-2}; C_0 = 100 ppm).

EO/O_3 treatments, and it can be observed that since 120 min no signal of 4-CP was detected. By means of PF almost the total degradation is attained. If we contrast these results with those obtained for phenol degradation, the Cl^- substituent present in 4-CP molecule appears to favour degradation process as has been reported by Pera-Titus and coworkers [11]. Photocatalytic process also was successfully applied to 4-CP degradation although no complete degradation was attained in 180 min. The perception that no degradation is occurring in PC process during the first 30 min can be explained by an electronic effect that modifies the UV absorbance spectrum and already has been reported in photocatalytic process as a photoinduced period associated with reactions that imply free-radicals formation [29]. It is beyond the scope of this work to explore the effect of variables like catalyst concentration or light intensity among others but further details of this process can be consulted in Martin del Campo et al. [24].

The following chemical reactions (see (9)–(15)) are intended to explain the different performance obtained by employing the referred processes in the 4-CP degradation. Coupled EO/O_3 involved reactions have been previously presented (see (1)–(3)). Regarding photocatalytic process, it starts with the excitation of a semiconductor, giving place to the generation of hole-electron pairs (see (9)) that are the precursors for hydroxyl radical formation (see (10)). This radical species can directly oxidize organic matter (see (5)) or also form hydrogen peroxide (see (11)) that also decomposes to hydroxyl radical (see (12)) [24, 30]. Hydroxyl radical formed by any pathway reacts with organic matter producing intermediates that could be finally oxidized to carbon dioxide and water. For EFL treatment, the reactions involved in the production of hydroxyl radical are given by (13)-(14) [25]. It must be noticed that in this case the hydrogen peroxide required in (14) is in situ produced. Finally, photo-Fenton process also requires the generation of hydroxyl radicals and (15) illustrates this interaction [11]

$$TiO_2 + h\nu \longrightarrow TiO_2\left(e^- + h^+\right) \quad (9)$$

$$TiO_2h^+ + OH^-_{ad} \longrightarrow TiO_2 + {}^\bullet OH \quad (10)$$

$$\left(HO^\bullet\right)_2 + \left(HO^\bullet\right)_2 \longrightarrow H_2O_2 + O_2 \quad (11)$$

$$H_2O_2 + e^- \longrightarrow {}^\bullet OH + OH^- \quad (12)$$

$$Cu^{2+} + e^- \longrightarrow Cu^+ \quad (13)$$

$$Cu^+ + H_2O_2 \longrightarrow Cu^{2+} + OH^- + {}^\bullet OH \quad (14)$$

$$H_2O_2 + Fe^{2+} + h\nu \longrightarrow Fe^{3+} + HO^- + HO^\bullet \quad (15)$$

If one compares the complexities of the hydroxyl radical production pathway by EO/O_3, EFL, PC, and PF, it is clear that, in EFL and PF, radical production is beneficiated by the continuous regeneration of copper and iron species, respectively. By coupling EO/O_3, the total degradation is quickly reached and may be ascribed to the different non-competitive pathways whereby hydroxyl radical is produced. In contrast, in the photocatalytic process, it is not possible to control the selectivity of hydroxyl radical to perform direct oxidation in addition to troubles related to hole-electron pair recombination.

As a complementary step of the comparison procedure, TOC analysis was conducted to establish the mineralization degree attained by the different methods as well as energy consumption required to mineralize one gram of total organic carbon. This parameter was calculated as follows [28]:

$$EC\left(kWh\,g^{-1}_{TOC}\right) = \frac{E_{cell}It}{V\,(\text{Initial TOC} - \text{Final TOC})}, \quad (16)$$

where E_{cell} is voltage applied to the cell, V is electrolyte volume (L), TOC is total organic carbon (mg L^{-1}), I is current (A), and t is time (h).

Figure 4 shows the results corresponding to mineralization rate and energy consumption on the basis of TOC removal by every assessed treatment, that is, EO/O_3, EFL, PC, and PF.

Total mineralization was only achieved by the coupled EO/O_3 after 100 min of treatment. In the studied treatment time, none of the other technologies were able to transform the whole organic matter to carbon dioxide and water which is a reminder of the well-known persistence of the 4-CP by-products generated through AOPs. In Figure 4, it is also worth noticing that interesting enough the process offering the less energy consumption is the coupled process EO/O_3. Furthermore, the calculated value suggests the process can

Table 2: Concentration and retention time of by-products of the phenol oxidation in a EO/O_3 coupled process.

	By-product	Retention time (min)	Concentration (ppm)
Aromatic by-products after 10 min of treatment	Benzoquinone	0.961	18
	Catechol	1.228	30
	Hydroquinone	4.988	1
Carboxylic by-products after 20 min of treatment	Oxalic	2.222	8.5
	Formic	2.638	6
	Maleic	3.121	7
	Succinic	3.332	5
	Fumaric	3.588	2

Table 3: Calculation of MCE for the 4-CP degradation by electrochemical processes.

Process	$TOC_{t=0}$ (mg TOC L^{-1})	$TOC_{t=2\,h}$ (mg TOC L^{-1})	t (h)	j (mA cm^{-2})	MCE (%)
Coupled EO/O_3	59.37	0	1.5	30	23
EFL	64	19.2	2	40	92

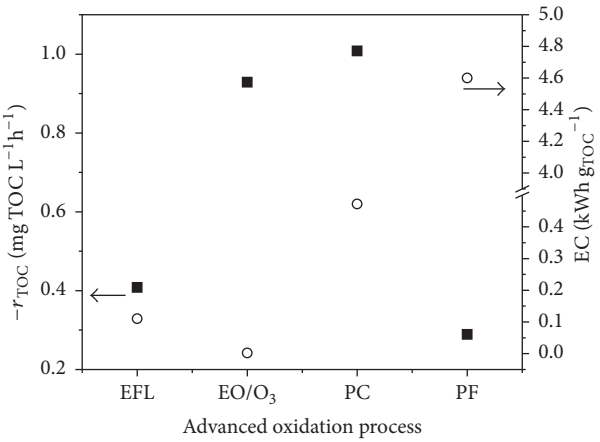

Figure 4: Mineralization rate of 4-CP molecule and energy consumption by EFL, EO/O_3, PC: MgZnAl 5%, and PF. Reaction conditions: EFL (j = 40 mA cm^{-2}; TOC_0 = 64 ppm); PC (C_{Cat} = 1.2 kg m^{-3}; TOC_0 = 56 ppm); PF (C_{Cat} = 0.8 kg m^{-3}; TOC_0 = 70 ppm); EO/O_3 (j = 30 mA cm^{-2}; TOC_0 = 59 ppm).

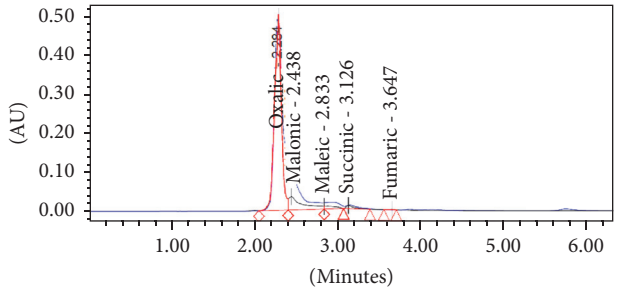

Figure 5: Chromatogram of 4-CP degradation by-products after 30 min of EFL treatment.

be conducted aided by solar cells which could considerably reduce the cost of the process. Also, from Figure 4, it can be concluded that the cocurrent downflow bubble column reactor is a promising technology that might be worthy to asses as electrochemical reactor to conduct the coupled process (EO/O_3) with the additional advantage of reducing the waste of ozone.

Analogous to phenol degradation, the MCE was determined for the electrochemical processes (coupled EO/O_3 and EFL) according to the following reaction:

$$ClC_6H_4OH + 27OH^- \longrightarrow 6CO_2 + Cl^- + 16H_2O + 26e^- \quad (17)$$

Results about MCE for electrochemical processes are presented in Table 3.

The efficiency of the coupled process is lower than the obtained for the EFL which almost reaches 100% of efficiency. It is worth clarifying that, in the case of EFL, the used current density to calculate MCE was the one applied to the graphite electrodes which was one order of magnitude lower than the one applied to the BDD in the coupled process.

Although by EFL and PF the model molecule was apparently destroyed (see Figure 3), it was only converted to smaller compounds that cannot be completely mineralized by the process and this implies the necessity to perform a post-treatment to reach a higher mineralization. Study of the recalcitrant by-products responsible of the partial mineralization was the final step of this work. This study was performed only for EFL. The side products of 4-CF degradation presents after 30 min of treatment were oxalic, malonic, maleic, succinic, and fumaric acids and Figure 5 exhibits a typical chromatograph in which all of them were identified at the referred time. Oxalic acid was present in higher amount and after 120 min was not possible to mineralize it by EFL. In contrast to phenol degradation, here only hydroquinone was detected as aromatic intermediate.

Stability of oxalic acid appears to be the major obstacle to perform a complete mineralization of a phenolic compound. Further research in this sense should be conducted. Still, it is expected that the results presented in this work help to improve the existing knowledge in degradation processes of phenolic compounds through different AOPs.

4. Conclusions

Phenol degradation and 4-CP degradation by different advanced oxidation processes were conducted and compared. Important differences in efficiency and in energy consumption were found. Among the studied AOPs, the process that fully mineralizes both phenolic compounds is the coupled electro-oxidation/ozonation process. By this treatment, 100% degradation of phenol is achieved in only 60 min while TOC is removed at a rate of 1.3501 mg TOC L^{-1} min^{-1}. A complete mineralization is achieved after 100 min. 4-CP is totally degraded and mineralized also by the coupled method although the highest TOC removal rate was found with the photocatalytic process (~1.0 mg TOC L^{-1} min^{-1}) performed at pilot scale. Photo-Fenton with pillared clays was found to be the less efficient process among the studied ones. In terms of energy consumption, the coupled process outperforms the other ones since it exhibited the lowest energy consumption level. Still, the cocurrent downflow contactor reactor emerges as a promising technology to conduct advanced oxidation processes.

Competing Interests

The authors declare that they have no competing interests.

Acknowledgments

The authors are grateful to CONACYT for financial support through Project 168305. Lourdes Hurtado is grateful to CONACYT for Scholarship no. 24012. The technical support of Citlalit Soto is also acknowledged.

References

[1] P. V. Nidheesh and R. Gandhimathi, "Trends in electro-Fenton process for water and wastewater treatment: an overview," *Desalination*, vol. 299, pp. 1–15, 2012.

[2] C. Comninellis, A. Kapalka, S. Malato, S. A. Parsons, I. Poulios, and D. Mantzavinos, "Advanced oxidation processes for water treatment: advances and trends for R&D," *Journal of Chemical Technology & Biotechnology*, vol. 83, no. 6, pp. 769–776, 2008.

[3] V. K. Gupta, I. Ali, T. A. Saleh, A. Nayak, and S. Agarwal, "Chemical treatment technologies for waste-water recycling—an overview," *RSC Advances*, vol. 2, no. 16, pp. 6380–6388, 2012.

[4] A. Babuponnusami and K. Muthukumar, "Advanced oxidation of phenol: a comparison between Fenton, electro-Fenton, sono-electro-Fenton and photo-electro-Fenton processes," *Chemical Engineering Journal*, vol. 183, pp. 1–9, 2012.

[5] G. Hurwitz, P. Pornwongthong, S. Mahendra, and E. M. V. Hoek, "Degradation of phenol by synergistic chlorine-enhanced photo-assisted electrochemical oxidation," *Chemical Engineering Journal*, vol. 240, pp. 235–243, 2014.

[6] X. Liu, J.-H. Fan, and L.-M. Ma, "Elimination of 4-chlorophenol in aqueous solution by the bimetallic Al-Fe/O_2 at normal temperature and pressure," *Chemical Engineering Journal*, vol. 236, pp. 274–284, 2014.

[7] A. Karci, "Degradation of chlorophenols and alkylphenol ethoxylates, two representative textile chemicals, in water by advanced oxidation processes: the state of the art on transformation products and toxicity," *Chemosphere*, vol. 99, pp. 1–18, 2014.

[8] M. A. Oturan and J.-J. Aaron, "Advanced oxidation processes in water/wastewater treatment: principles and applications. A review," *Critical Reviews in Environmental Science and Technology*, vol. 44, no. 23, pp. 2577–2641, 2014.

[9] C. A. Martínez-Huitle and S. Ferro, "Electrochemical oxidation of organic pollutants for the wastewater treatment: direct and indirect processes," *Chemical Society Reviews*, vol. 35, no. 12, pp. 1324–1340, 2006.

[10] J. M. Poyatos, M. M. Muñio, M. C. Almecija, J. C. Torres, E. Hontoria, and F. Osorio, "Advanced oxidation processes for wastewater treatment: state of the art," *Water, Air, and Soil Pollution*, vol. 205, no. 1–4, pp. 187–204, 2010.

[11] M. Pera-Titus, V. García-Molina, M. A. Baños, J. Giménez, and S. Esplugas, "Degradation of chlorophenols by means of advanced oxidation processes: A general review," *Applied Catalysis B: Environmental*, vol. 47, no. 4, pp. 219–256, 2004.

[12] A. Babuponnusami and K. Muthukumar, "A review on Fenton and improvements to the Fenton process for wastewater treatment," *Journal of Environmental Chemical Engineering*, vol. 2, no. 1, pp. 557–572, 2014.

[13] C. Catrinescu, D. Arsene, P. Apopei, and C. Teodosiu, "Degradation of 4-chlorophenol from wastewater through heterogeneous Fenton and photo-Fenton process, catalyzed by Al-Fe PILC," *Applied Clay Science*, vol. 58, pp. 96–101, 2012.

[14] M. Munoz, Z. M. De Pedro, G. Pliego, J. A. Casas, and J. J. Rodriguez, "Chlorinated byproducts from the fenton-like oxidation of polychlorinated phenols," *Industrial and Engineering Chemistry Research*, vol. 51, no. 40, pp. 13092–13099, 2012.

[15] E. Brillas, R. Sauleda, and J. Casado, "Degradation of 4-chlorophenol by anodic oxidation, electro-fenton, photoelectro-fenton, and peroxi-coagulation processes," *Journal of the Electrochemical Society*, vol. 145, no. 3, pp. 759–765, 1998.

[16] S. Vasudevan, "An efficient removal of phenol from water by peroxi-electrocoagulation processes," *Journal of Water Process Engineering*, vol. 2, pp. 53–57, 2014.

[17] S.-H. Cho, A. Jang, P. L. Bishop, and S.-H. Moon, "Kinetics determination of electrogenerated hydrogen peroxide (H_2O_2) using carbon fiber microelectrode in electroenzymatic degradation of phenolic compounds," *Journal of Hazardous Materials*, vol. 175, no. 1–3, pp. 253–257, 2010.

[18] K. Elghniji, O. Hentati, N. Mlaik, A. Mahfoudh, and M. Ksibi, "Photocatalytic degradation of 4-chlorophenol under P-modified TiO_2/UV system: kinetics, intermediates, phytotoxicity and acute toxicity," *Journal of Environmental Sciences*, vol. 24, no. 3, pp. 479–487, 2012.

[19] P. Van Aken, R. Van den Broeck, J. Degrève, and R. Dewil, "The effect of ozonation on the toxicity and biodegradability of 2,4-dichlorophenol-containing wastewater," *Chemical Engineering Journal*, vol. 280, pp. 728–736, 2015.

[20] W. H. Glaze, J.-W. Kang, and D. H. Chapin, "The chemistry of water treatment processes involving Ozone, hydrogen peroxide and ultraviolet radiation," *Ozone: Science & Engineering*, vol. 9, no. 4, pp. 335–352, 1987.

[21] R. Bauer, G. Waldner, H. Fallmann et al., "The photo-fenton reaction and the TiO_2/UV process for waste water treatment—novel developments," *Catalysis Today*, vol. 53, no. 1, pp. 131–144, 1999.

[22] A. Di Paola, E. García-López, G. Marcì, and L. Palmisano, "A survey of photocatalytic materials for environmental remediation," *Journal of Hazardous Materials*, vol. 211-212, pp. 3–29, 2012.

[23] E. Martin del Campo, R. Romero, G. Roa, E. Peralta-Reyes, J. Espino-Valencia, and R. Natividad, "Photo-Fenton oxidation of phenolic compounds catalyzed by iron-PILC," *Fuel*, vol. 138, pp. 149–155, 2014.

[24] E. Martín del Campo, J. S. Valente, T. Pavón, R. Romero, Á. Mantilla, and R. Natividad, "4-Chlorophenol oxidation photocatalyzed by a calcined Mg-Al-Zn layered double hydroxide in a co-current downflow bubble column," *Industrial & Engineering Chemistry Research*, vol. 50, no. 20, pp. 11544–11552, 2011.

[25] G. Santana-Martínez, G. Roa-Morales, E. Martin del Campo, R. Romero, B. A. Frontana-Uribe, and R. Natividad, "Electro-Fenton and Electro-Fenton-like with in situ electrogeneration of H_2O_2 and catalyst applied to 4-chlorophenol mineralization," *Electrochimica Acta*, vol. 195, pp. 246–256, 2016.

[26] D. Amado-Piña, G. Roa-Morales, C. Barrera-Díaz et al., "Synergic effect of ozonation and electrochemical methods on oxidation and toxicity reduction: phenol degradation," *Fuel*, 2015.

[27] C. Qiu, S. Yuan, X. Li et al., "Investigation of the synergistic effects for p-nitrophenol mineralization by a combined process of ozonation and electrolysis using a boron-doped diamond anode," *Journal of Hazardous Materials*, vol. 280, pp. 644–653, 2014.

[28] E. Brillas, I. Sirés, and M. A. Oturan, "Electro-fenton process and related electrochemical technologies based on fenton's reaction chemistry," *Chemical Reviews*, vol. 109, no. 12, pp. 6570–6631, 2009.

[29] J. S. Valente, F. Tzompantzi, and J. Prince, "Highly efficient photocatalytic elimination of phenol and chlorinated phenols by CeO_2/MgAl layered double hydroxides," *Applied Catalysis B: Environmental*, vol. 102, no. 1-2, pp. 276–285, 2011.

[30] J. C. Garcia, J. L. Oliveira, A. E. C. Silva, C. C. Oliveira, J. Nozaki, and N. E. de Souza, "Comparative study of the degradation of real textile effluents by photocatalytic reactions involving UV/TiO_2/H_2O_2 and UV/Fe^{2+}/H_2O_2 systems," *Journal of Hazardous Materials*, vol. 147, no. 1-2, pp. 105–110, 2007.

Hindawi Publishing Corporation
Journal of Chemistry
Volume 2016, Article ID 7296858, 13 pages
http://dx.doi.org/10.1155/2016/7296858

Research Article

Removal of Fluoride from Aqueous Solutions Using Chitosan Cryogels

Anete Jessica Arcos-Arévalo,[1] Rosa Elvira Zavala-Arce,[1] Pedro Ávila-Pérez,[2] Beatriz García-Gaitán,[1] José Luis García-Rivas,[1] and María de la Luz Jiménez-Núñez[1]

[1] *Tecnológico Nacional de México/Instituto Tecnológico de Toluca, Avenida Tecnológico S/N, Colonia Agrícola Bella Vista, 52149 Metepec, MEX, Mexico*
[2] *Dirección de Investigación Tecnológica, Instituto Nacional de Investigaciones Nucleares (ININ), Carretera México-Toluca S/N, La Marquesa, 52750 Ocoyoacac, MEX, Mexico*

Correspondence should be addressed to Rosa Elvira Zavala-Arce; rzavalaa@toluca.tecnm.mx

Received 22 July 2016; Accepted 21 November 2016

Academic Editor: Julie J. M. Mesa

In this study, crosslinked chitosan cryogels (QE) and chitosan's cryogels modified with iron (QEFe) were synthesized. They were characterized by BET, PZC, FTIR, and XPS spectroscopies. Results show a specific surface area of 36.67 and 29.17 $m^2 g^{-1}$ and 7.0 and 6.1 of PZC for the cryogels QE and QEFe, respectively. FTIR results show the characteristic bands of amino and hydroxyl groups, while in the XPS analysis, interactions between iron and oxygen with fluorine were observed. The removal of fluoride at temperatures of 303, 313, and 323 K in cryogels was tested. The Ho model is the best fit for the experimental data, suggesting that there is a chemisorption process involved in the removal of fluoride. The Langmuir-Freundlich model is the best to represent the behavior of the cryogels, and it is used to sorbents with heterogeneous surfaces. A maximum fluoride adsorption capacity of 280 and 295 mg F^-/g for QE and QEFe, respectively, at 303 K was obtained, showing that the removal of fluoride is favored by the iron incorporated in the polymer matrix of the cryogels. The thermodynamic parameters were obtained for both cryogels, where the values of ΔH° and ΔG° indicate that both systems are endothermic and nonspontaneous.

1. Introduction

The most abundant halogen in the Earth's crust is fluorine, with a concentration close to 0.3 g/kg. Diverse minerals contain fluorine in the form of fluorides [1, 2]. Aqueous solubilization of molecules containing fluorine occurs through geochemical processes. The regional geomorphic composition determines the amount of fluorine that reaches the aquifers [1–5]. The presence of fluorine affects the water quality for human consumption. Fluorine is highly reactive and therefore forms compounds with practically all the elements. Biologically active compounds are likely to incorporate fluorine when ingested in water for long periods. Epidemiological studies prove detrimental to the bone tissue (bones and teeth) and the spinal cord and brain. The degeneration of neurons and alteration of the metabolism of free radicals in the liver, kidney, and heart and lesions on the thyroid and the endocrine glands interfere with DNA synthesis, and metabolic disorders in soft tissues and some cancers are also associated with the exposure to fluorine [1–14]. The World Health Organization (WHO) classifies fluorine as a public health risk and recommends a maximum concentration of 1.5 mg/L of fluorine in drinking water. Globally, inhabitants in some regions of China, India, Mexico, and the United States are affected by higher concentrations [1, 2, 6–8, 12, 13].

In an effort to remove fluorine in water, diverse techniques have been studied, with absorption being the more versatile due to its high efficiency, sludge minimization, and regeneration of the sorbent material [6, 10, 15–18]. In recent years, biopolymers such as chitosan have proved to be effective for fluorine removal. Chitosan is a nontoxic, biodegradable, and biocompatible material [7]. Among the fluoride removal studies that have been used, sorbents from

chitosan inferred that these biosorbents offer satisfactory results in terms of fluoride elimination. In addition, chitosan is obtained from natural sources that are an ecologically low cost material [19–23]. The biopolymer structure consists of amino and hydroxyl groups which are mainly responsible for the adsorption of various ions [11, 16, 24, 25]. Also, limited swelling of chitosan in water causes low availability of its functional groups during sorption. Chemical and physical modifications improve the readiness of contact sites on chitosan [26, 27]. The cryogel synthesis route allows the structural transformations supplying adequate stability and strength to the material. Cryogels are porous materials that can provide a better contact surface between the functional groups of chitosan and different ions in aqueous solutions [28–33], so these materials are a suitable alternative for removal of fluoride ions in aqueous solutions.

The aim of this work was to synthesize chitosan's cryogels crosslinked with ethylene glycol diglycidyl ether (EGDE) and its modification with iron, in order to use them in the removal of fluoride from aqueous solutions prepared in the laboratory. A comparative assessment of the modified cryogels (QEFe) and unmodified cryogels (QE) was performed to determine the sorption capacity of each material and observe whether introducing Fe^{3+} into the chitosan polymeric matrix had a significant impact on the adsorption phenomenon.

2. Experimental

Industrial chitosan (América Alimentos) with 67% of deacetylation, ethylene glycol diglycidyl ether (TCI), $FeCl_3{\cdot}6H_2O$ (Sigma-Aldrich), ethanol (Meyer), and glacial acetic acid (Fermont) were used without further purification on cryogel synthesis. Sodium fluoride (Meyer) was used for preparing solutions in the sorption experiments.

2.1. Synthesis of Crosslinked Chitosan Cryogels (QE). Two solutions dissolving chitosan (Q) in 100 mL of acetic acid (3%) were prepared. Afterwards, the ethylene glycol diglycidyl ether as a cross-linking agent (E) was added at 1% relative to the chitosan weight under inert atmosphere and constant stirring during a 6-hour period. Each one of the solutions was dripped into liquid nitrogen and the obtained spheres were freeze-dried by using a lyophilizer CHRIST BETA 2-8 LD to 0018 mbar and 190 K for 17 hours. Finally, QE cryogels were washed with 1.5% acetic acid and then with deionized water until the rinse water's pH was equal to the pH of the deionized water.

2.2. Synthesis of Chitosan's Cryogels Modified with Iron (QEFe). The total QE cryogels obtained by one of the solutions in the synthesis of crosslinked chitosan cryogels were treated with 300 mL of solution 0.1 M $FeCl_3$ during a 24-hour period, with constant stirring at 303 K. Subsequently, the modified beads were washed with ethanol for removing the unreacted $FeCl_3$, followed by washing with deionized water until the rinse water pH was equal to the pH of the deionized water [26, 34].

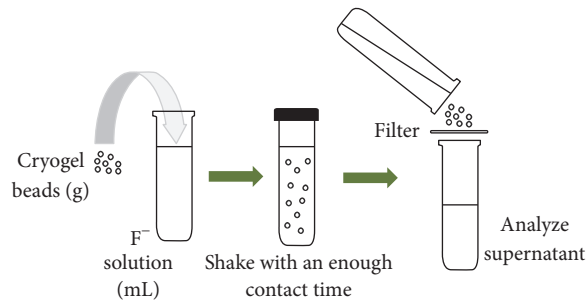

Figure 1: Experimental procedure for adsorption experiments.

2.3. Sorption Experiments. Sorption kinetics were performed in batch systems, putting a sample of each dried cryogel (0.002 g) in contact with 8 mL of a solution with an initial concentration of 10 mg/L of fluoride and pH = 6. Samples were placed at constant agitation of 200 rpm during a 24-hour period. Experiments were carried out at three constant temperatures (303 K, 313 K, and 323 K) to analyze the effect of this variable on sorption capacity (Figure 1). Furthermore, the effect of different fluoride initial concentrations was studied using 2 mg/L to 1000 mg/L at 303 K, 313 K, and 323 K. The adsorbent mass (0.002 g) was kept constant as well as pH value with a study solution volume of 8 mL. Fluoride ions in the solutions were quantified by using a Cole-Parmer 27504-14 selective ion electrode and a Thermo Scientific Orion 4-Star potentiometer. All experiments were triplicated under identical conditions. Finally, experimental data was fitted to mathematical models with nonlinear regression, using the Origin 8.1 program.

2.4. Characterization of Cryogels. The BET method was used with a Belsorp-max equipment to determine the specific surface area of cryogels. Before the analyses, the samples were subject to a degassing process in a Belprep II equipment, at a temperature of 373 K for 2 hours in order to remove impurities and water molecules contained in the material structure. Subsequently, each sample was weighed and placed in the Belsorp-max to carry out the determination of specific area through process of adsorption and desorption of N_2 gas at 77 K and 76.5 kPa.

The PZC was determined by means of contacting 0.5 g of the solid sample of cryogels (QE and QEFe) with 20 mL of NaCl solution 0.1 M at different pHs. The initial pH values of the solutions were adjusted using HCl or NaOH 0.1 M. The suspensions were then shaken for 24 hours (200 rpm and at 303 K), after which the pH value of the supernatant for each sample was measured. The difference between the final and initial pH ($\Delta pH = pH_f - pH_i$) was plotted versus pH_i and the point of intersection of the resulting curve at which $\Delta pH = 0$ was the pH_{PZC} value.

A FTIR spectrometer Variant 600 with an ATR-coupled device was used in order to identify the presence of the functional groups in chitosan-modified molecule by crosslinking in the adsorbent materials before (QEFe and QE) and after ($QEFe/F^-$ and QE/F^-) sorption. Sixteen scans were performed in a range of 4000–500 cm^{-1} with a resolution of 4 cm^{-1}.

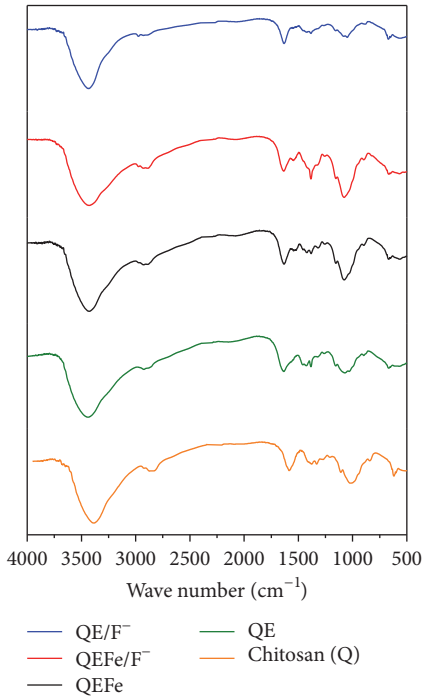

Figure 2: FTIR spectra.

An XPS spectrometer Thermo K-Alpha Scientific was also used to further verify the existence of study species in the materials, and the spectra were subjected to a mathematical deconvolution and an analysis of presented chemical interactions by using the Origin 8.1 program and the http://lasurface.com database.

3. Results and Discussion

3.1. Characterization of Cryogels. The specific surface area of cryogels was determined by the BET method. The specific surface areas for QE and QEFe cryogels were 36.67 m^2g^{-1} and 29.17 m^2g^{-1}, respectively.

In the infrared spectrum (Figure 2), vibrations of the different functional groups at the chitosan can be observed. In 3433 cm^{-1} band one is observed due to vibration of NH_2 and in 2922 cm^{-1} a band is observed due to vibration of OH; at 1633 cm^{-1} and 1420 cm^{-1} the vibration signals are present of NH_2 and OH, respectively. The spectra of the QE and QEFe cryogels have higher Q spectrum bands, virtually unchanged, showing that these functional groups are present in the cryogels. However, a decrease in signal intensity can be observed in the QEFe cryogel corresponding to the amino groups, which may indicate that the added iron is attached mainly by these functional groups. The cryogels spectra after fluoride sorption (QE/F^- and QEFe/F^-) show a decrease in the intensity of signal corresponding to the amino and hydroxyl groups. The hydroxyl group was the most decreased. This suggests that these groups are related to the removal of fluoride ions [35, 36].

The cryogels were analyzed by XPS before (QEFe and QE) and after (QEFe/F^- and QE/F^-) the sorption of fluoride ions. C, O, N, Fe, and F were identified in both samples. Figures 3 and 4 show the XPS results before and after the sorption of each material, where the predominant peaks C1s and O1s and a lower intensity peak N1s can be observed. These can be attributed to the amino groups of chitosan. In the case of QEFe cryogel, the presence of Fe2p can also be observed. After the sorption, the peak of F1s appears to show an average binding energy of about 690 eV, meaning that fluoride was adsorbed on the surface of both cryogels [37, 38].

Figures 5, 6, and 7 show the deconvolution of the O1s and Fe2p spectrums after the sorption with QE and QEFe cryogels. Here, it can be observed that fluoride ions are interacting with the atoms of iron and oxygen in the materials; that is, fluorine is showing bonds with the hydroxyl group of the cryogels, which can be hydrogen bonds. In the case of the QEFe cryogel, it is also forming links with the iron present in the modified cryogel. These interactions may be because the QEFe cryogel presents a higher sorption capacity than the cryogel QE [39, 40].

Figure 8 shows the PZC results. When the pH of the solution is lower than the PZC, the total charge of the solid surface is positive, while if the pH of the solution is greater than the PZC, the surface is negatively charged [41, 42]. The cryogel QEFe showed a less slightly acidic PZC compared to the cryogel QE (6.1 and 7.0, resp.), which can indicate that, in the first one, the content of total acid groups is greater than the content of basic groups.

The pH of the washing solution of cryogels (QE and QEFe) is pH 5 and according to the PZC, both cryogels have a positive charge on their surface; because of this, the removal mechanism of fluorine in the QE cryogel is mainly a physical adsorption by the formation of hydrogen bonds between fluoride and the hydroxyl group and in the QEFe cryogel is a physical and chemical adsorption mainly due to interactions between iron and fluoride (Figure 9) [21, 34, 43, 44].

3.2. Sorption Kinetics. The quality of the sorbent material is evaluated according to the capacity to retain certain species on its surface. For the purpose, it is customary to determine the amount of species removed per unit of solid phase (q) and the following equation is used:

$$q = \frac{\left(C_i - C_f\right) * V}{m}, \quad (1)$$

where C_i and C_f are the initial and final concentrations (mgL^{-1}), respectively, V is the total volume (L), and m is the amount of solid added (g).

In general, the removal of ions from aqueous solutions depends on the chemical mechanisms that involve the interaction of ions with the active groups present in the sorbent. Therefore, the kinetics show the steps through which the sorption takes place. In this paper, Lagergren, Elovich, and Ho models have been considered.

The mathematical expression for the kinetics of pseudo-first-order or Lagergren model is based on the assumption

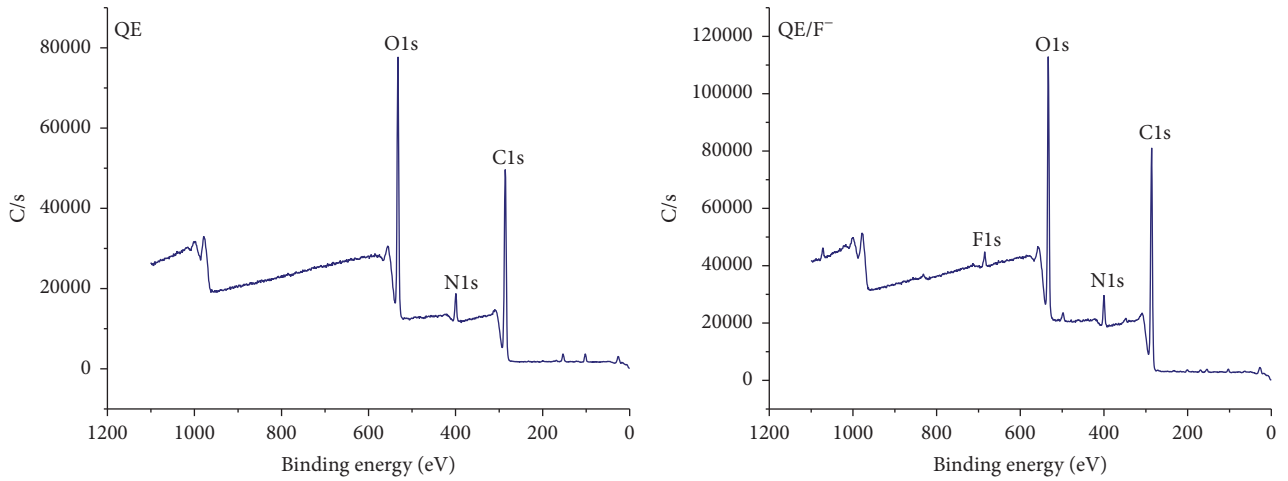

Figure 3: XPS spectrums of QE and QE/F⁻.

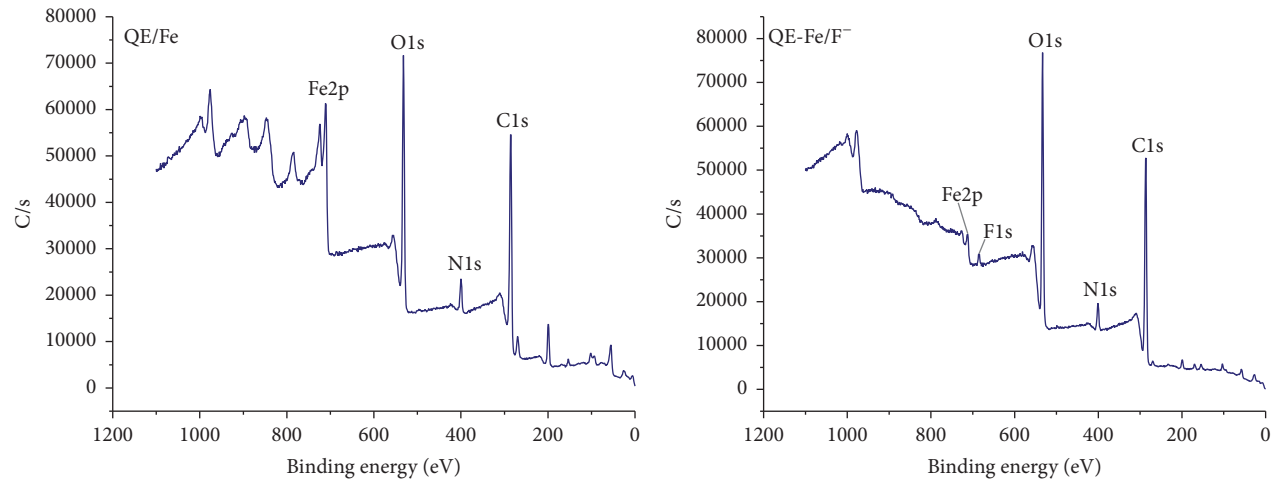

Figure 4: XPS spectrums of QEFe and QEFe/F⁻.

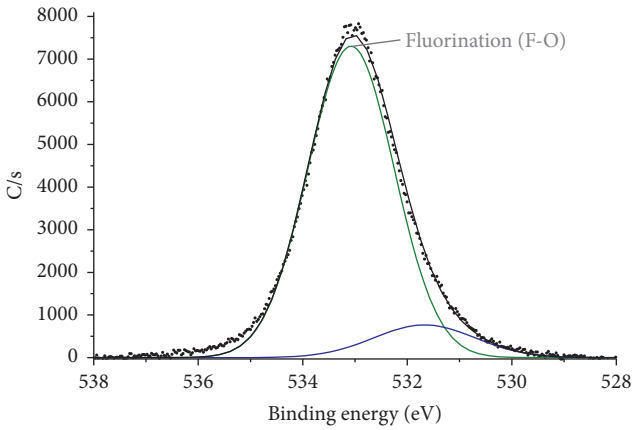

Figure 5: XPS spectrum to O1s of QE/F⁻.

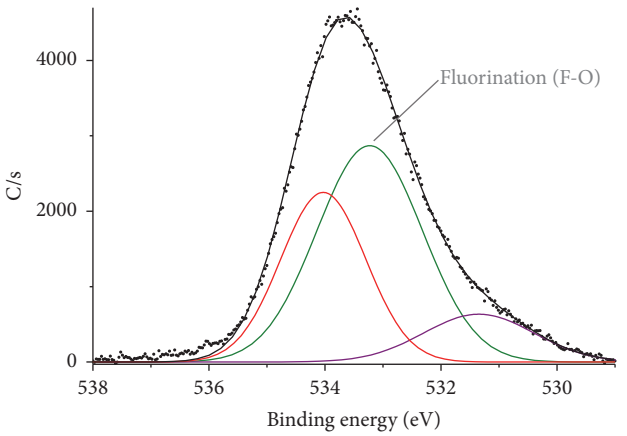

Figure 6: XPS spectrum to O1s of QEFe/F⁻.

Table 1: Summary of kinetics models.

T (K)	Cryogel	q_{exp} (mgg^{-1})	Lagergren			Ho		Elovich		
			R^2	K_1 (min^{-1})	q_e (mgg^{-1})	R^2	K_2 (gmg^{-1}min^{-1})	q_e (mgg^{-1})	R^2	α (mgg^{-1}h^{-1})	β (gmg^{-1})
303	QE	13.10	0.98	0.44	13.89	0.97	0.15	13.94	0.96	8.54×10^{44}	8.04
	QEFe	23.20	0.98	0.20	22.09	0.98	0.02	22.71	0.96	5.55×10^{5}	0.84
313	QE	15.80	0.88	0.26	14.20	0.94	2.30×10^{-2}	14.83	0.99	5.29×10^{3}	0.97
	QEFe	24.20	0.98	0.32	23.02	0.99	3.40×10^{-2}	23.37	0.98	4.65×10^{11}	1.42
323	QE	11.20	0.80	0.03	10.34	0.87	5.00×10^{-3}	10.81	0.94	6.977	0.76
	QEFe	14.50	0.99	0.20	14.62	0.97	0.03	14.91	0.91	1.32×10^{9}	1.88

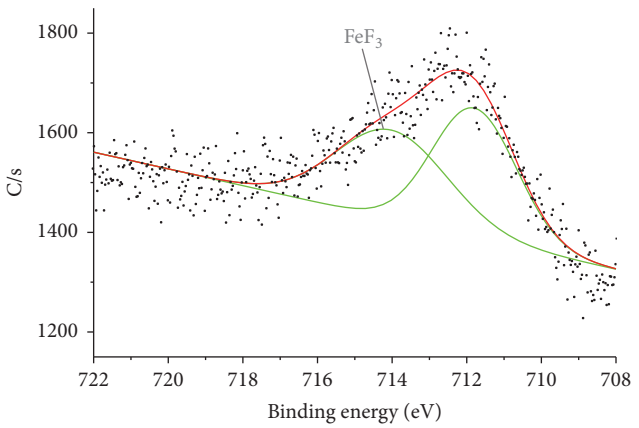

Figure 7: XPS spectrum to Fe2p of QEFe/F$^-$.

that each ion is assigned a sorption site of the sorbent material and it is represented [12, 45–47]:

$$q_t = q_e\left(1 - e^{-K_1 t}\right), \tag{2}$$

where K_1 is the sorption constant for pseudo-first-order model (min^{-1}), q_t is the mg of F$^-$ adsorbed/g of sorbent anytime, and q_e is the amount adsorbed on the equilibrium (mgg^{-1}).

The mathematical expression of Elovich model was developed for heterogeneous sorption processes of gas in solids. However, it has been successfully applied in processes of sorption for contaminants in solution, and the next equation describes this model [48–53]:

$$q_t = \frac{1}{\beta}\ln(\alpha\beta) + \frac{1}{\beta}\ln t, \tag{3}$$

where α is the initial sorption rate (mg g^{-1}h^{-1}), β is the desorption constant (gmg^{-1}), t is time (h), and q is the amount of solute sorbed (mgg^{-1}).

The Ho model was developed by Ho and McKay; it is assumed that the sorbate is adsorbed by two active sites in the sorbent. The next equation describes this model [45, 46, 52, 53]:

$$\frac{t}{q_t} = \frac{1}{(K_2)\,q_e^2} + \frac{t}{q_e}, \tag{4}$$

where K_2 is the pseudo-second-order constant (gmg^{-1} min^{-1}), q_t is the amount adsorbed anytime (or time, t) (mg g^{-1}), and q_e is the amount adsorbed on the equilibrium (mg g^{-1}).

The fluoride sorption occurs in the first 5 minutes of the test for both cryogels (Figure 10) and then begins to stabilize until equilibrium is reached. It was determined that the equilibrium time was reached approximately in 480 minutes for both cryogels. After reaching equilibrium, there were no significant changes in the quantity of fluorine captured by the materials. Furthermore, the QEFe cryogel exhibited a greater sorption capacity at the three temperatures studied than the QE cryogel.

After the sorption kinetics, an adjustment of the experimental data for the Lagergren, Elovich, and Ho models by means of nonlinear regression using the Origin 8.1 program was performed. Table 1 provides a summary of the obtained parameters.

The QE cryogel shows a higher R^2 coefficient in the Lagergren model at 303 K, whereas at 313 K and 323 K the coefficient is higher in the Elovich model. The QEFe cryogel shows a higher correlation coefficient for Ho model at 303 K and 313 K and for the Lagergren model at 323 K. According to Figure 11, the Ho model is what best fits the experimental data, suggesting that there is a chemisorption process involved in the removal of fluoride. As a result the model that best describes the behavior of the systems is the Ho model.

In other articles materials of chitosan have been used in order to remove fluoride and under similar conditions used in this study, such is the case of the chitosan beads modified by carboxylation followed by chelation with Fe^{3+} (4.23 mg F$^-$/g), the chitosan modified with a mixed of rare earths (3.72 mg F$^-$/g), a bioadsorbent of titanium(IV) hydrate based on chitosan template (11.44 mg F$^-$/g), and an Al-doping chitosan-Fe(III) hydrogel (3.9 mg F$^-$/g). The sorption capacity in equilibrium time is similar to or lower than sorption capacity obtained in this work: 13.10 mg F$^-$/g and 23.20 mg F$^-$/g at 303 K for the QE and QEFe cryogels, respectively [13, 34, 54, 55].

3.3. Sorption Isotherms. Over time, several mathematical models have been developed for the treatment of experimental data using the models of Langmuir, Freundlich, and Langmuir-Freundlich.

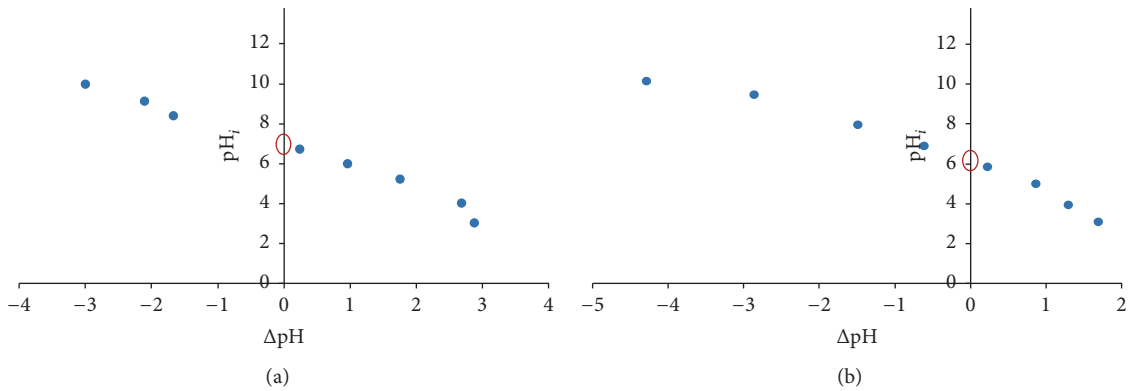

Figure 8: PZC of cryogels, 0.5 g cryogel mass, 20 mL NaCl solution at various pHs, 200 rpm, 303 K, a 24-hour period, closed atmosphere: (a) QE and (b) QEFe.

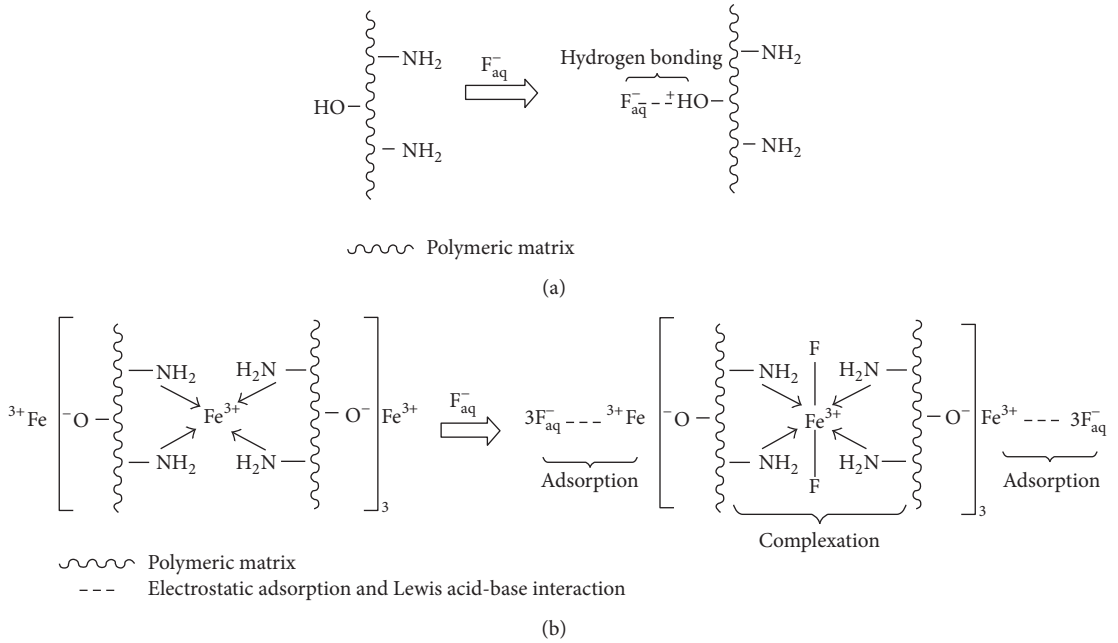

Figure 9: Fluoride removal mechanism (adapted from Viswanathan and Meenakshi [34]): (a) interaction with OH, (b) interaction with Fe.

The Freundlich model is an empirical model that can be applied to a nonideal adsorption in heterogeneous surfaces, as well as multilayer adsorption. The Freundlich model is expressed by the following equation [12, 13, 46–48]:

$$q_e = K_F C_e^{1/n}, \tag{5}$$

where q_e is the adsorption capacity at equilibrium (mgg^{-1}), K_F is the constant for Freundlich's isotherm (mgg^{-1}), C_e is the ion concentration in the solution at equilibrium (mgL^{-1}), $1/n$ is the quotient related to adsorption intensity, and n is the dimensionless exponent of the Freundlich isotherm.

The Langmuir model is probably the best-known and the most widely applied adsorption isotherm. This isotherm assumes that a solid has a limited adsorption capacity; the molecules are adsorbed on well-defined and energetically equivalent sites and are far enough away from each other to not allow interaction between the adsorbed molecules in adjacent sites. Each site can retain only one molecule of adsorbate and the sorption leads to the deposition of a layer of solute molecules on the surface of sorbent. The model can be represented by the following equation [46, 48–50, 56]:

$$q_e = \frac{q_m b C_e}{1 + b C_e}, \tag{6}$$

where q_e is the adsorption capacity at equilibrium (mgg^{-1}), q_m is the monolayer adsorption capacity (mgg^{-1}), b is the constant for Langmuir's isotherm (Lmg^{-1}), and C_e is the ion concentration in the solution at equilibrium (mgL^{-1}).

Langmuir also considered the case of a molecule occupying two sites and it produces the Sips or Langmuir-Freundlich isotherm. The Langmuir-Freundlich name is derived from

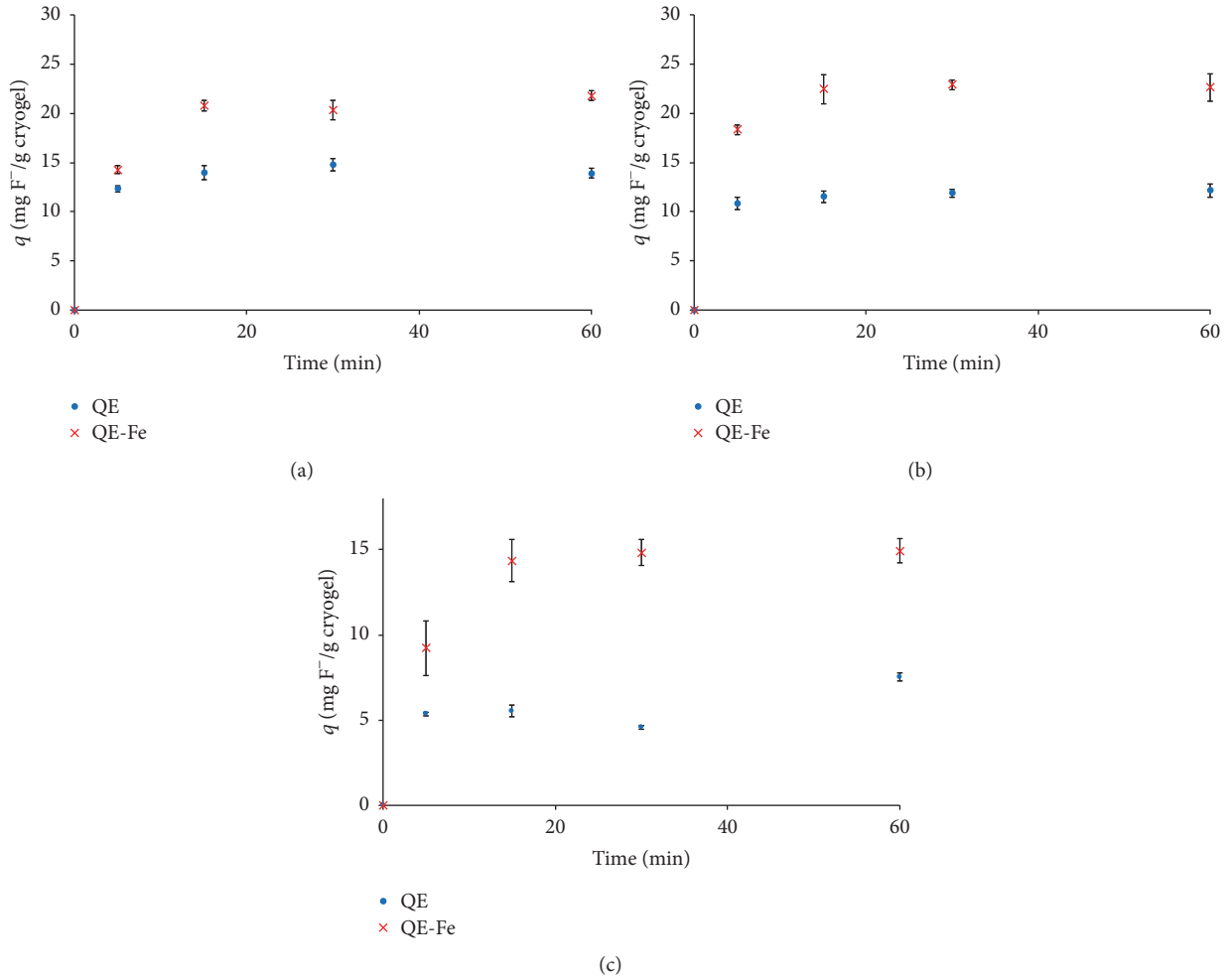

FIGURE 10: Sorption kinetics, 8 mL of 10 mgL^{-1}, 200 rpm, 0.002 g of cryogel mass, pH 6, closed atmosphere: (a) 303 K, (b) 313 K, and (c) 323 K.

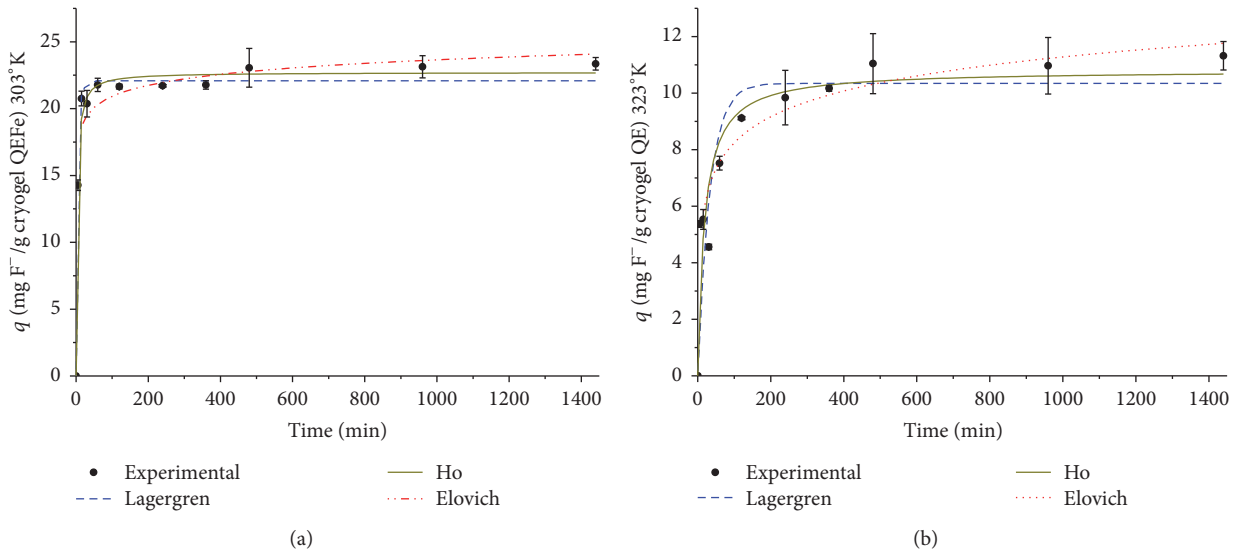

FIGURE 11: Adjustment to kinetics models, 8 mL of 10 mgL^{-1}, 200 rpm, 0.002 g cryogel mass, pH 6, closed atmosphere: (a) cryogel QEFe 303 K; (b) cryogel QE 323 K.

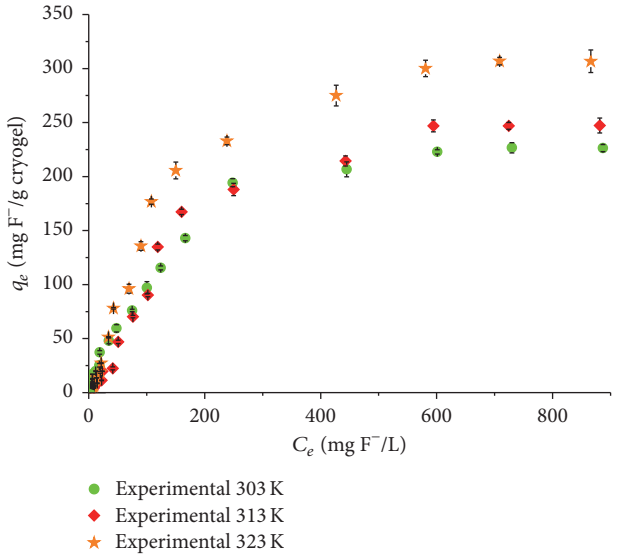

Figure 12: Sorption isotherms, cryogel QE, 8 mL, 24 hours of contact, 200 rpm, 0.002 g cryogel mass, pH 6, closed atmosphere.

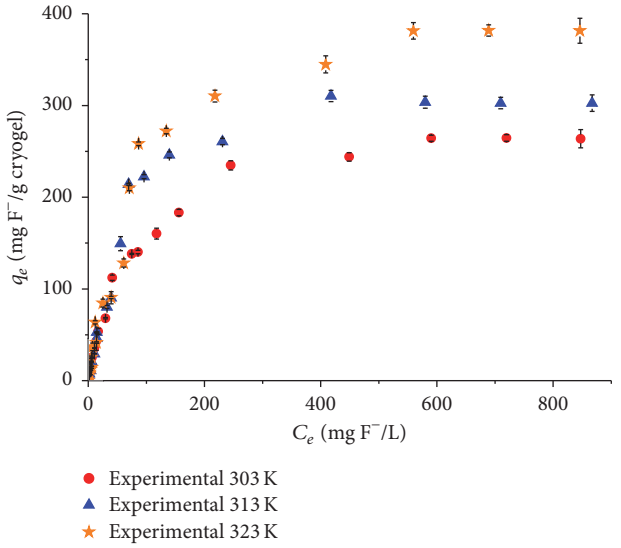

Figure 13: Sorption isotherms, cryogel QEFe, 8 mL, 24 hours of contact, 200 rpm, 0.002 g cryogel mass, pH 6, closed atmosphere.

the limiting behavior of the equation. At low sorbate concentrations it effectively reduces to a Freundlich isotherm. At high sorbate concentrations, it predicts the monolayer adsorption characteristic of the Langmuir isotherm [46, 57–60]. This isotherm can be determined by the following equation:

$$q_e = \frac{K_{LF}(C_e)^{n_{LF}}}{1 + (a_{LF}C_e)^{n_{LF}}}, \quad (7)$$

where q_e is the adsorption capacity at equilibrium (mgg^{-1}), a_{LF} is the constant of Langmuir-Freundlich's isotherm [(Lmg^{-1})$^{n_{LF}}$], C_e is the ion concentration in the solution at equilibrium (mgL^{-1}), K_{LF} is the constant of Langmuir-Freundlich's isotherm (mg$^{1-n_{LF}}$L$^{3n_{LF}}$g^{-1}), and n_{LF} is the dimensionless exponent of Langmuir-Freundlich's isotherm.

The isotherms do not show appreciable changes in adsorption capacity in a concentration of 500 mg/L of fluorine (Figures 12 and 13). In addition, it can be observed that the sorption capacities for both cryogels increase as the temperature increases; that is, the removal of fluoride ions was favored at higher temperatures, indicating an endothermic adsorption [15, 61].

Table 2 shows a summary of the values obtained after the adjustment of the experimental data to the models of Freundlich, Langmuir, and Langmuir-Freundlich, obtained by nonlinear regression and using the program Origin 8.1. Figures 14 and 15 show the data adjustment of these three models at the temperature of 323 K.

The identification of an adequate isotherm model can be carried out by means of the analysis of chi-square (χ^2), which uses the experimental data and the adjusted data by the isotherms models:

$$\chi^2 = \sum \left(\frac{(q_t - q_{tm})^2}{q_{tm}} \right), \quad (8)$$

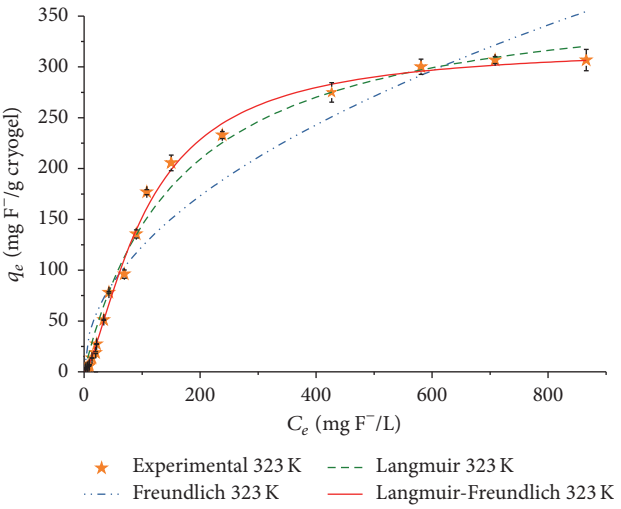

Figure 14: Sorption isotherms, cryogel QE fitted to Freundlich, Langmuir, and Langmuir-Freundlich models; 8 mL, 24 hours of contact, 200 rpm, 0.002 g cryogel mass, pH 6, T = 323 K, closed atmosphere.

where q_{tm} and q_t are the adsorption capacities obtained by the isotherm models and the experimental adsorption capacity (mgg^{-1}), respectively. When low values of χ^2 are observed, the experimental data has a good fit to the model used [15, 17, 34, 40, 44, 50, 53, 62].

A maximum fluoride adsorption capacity of 280 mg F$^-$/g for QE and 295 mg F$^-$/g for QEFe at 303 K was obtained, showing that the removal of fluoride is favored by the iron incorporated in the polymer matrix of the cryogels. The coefficients of determination are very similar in the Langmuir and Langmuir-Freundlich models (Table 2). The Chi-square test shows that the Langmuir and Langmuir-Freundlich models can adequately represent the experimental data because the

Table 2: Summary of isotherms.

T (K)	Cryogel	Freundlich					Langmuir				Langmuir-Freundlich				
		K_F [(mgg^{-1})(Lmg^{-1})$^{1/n}$]	n	$1/n$	R^2	χ^2	q_m (mgg^{-1})	b (Lmg^{-1})	R^2	χ^2	K_{LF} (mg^{1-n} L^{3n}g^{-1})	a	n	R^2	χ^2
303	QE	11.19	2.16	0.46	0.95	90.74	280.87	6×10^{-3}	0.99	17.23	1.13	4×10^{-3}	1.10	0.99	27.28
	QEFe	22.48	2.60	0.38	0.95	125.00	295.38	11×10^{-3}	0.99	10.33	4.13	14×10^{-3}	0.95	0.99	8.59
313	QE	7.56	1.86	0.54	0.93	194.89	330.35	4×10^{-3}	0.97	71.62	0.05	2×10^{-4}	1.76	0.99	41.57
	QEFe	23.86	2.66	0.37	0.94	133.97	291.19	13×10^{-3}	0.99	20.04	4.99	16×10^{-3}	0.92	0.99	17.41
323	QE	12.94	2.04	0.49	0.93	237.47	381.13	6×10^{-3}	0.99	66.71	0.35	1×10^{-3}	1.45	0.99	12.94
	QEFe	28.33	2.46	0.41	0.92	270.88	436.64	11×10^{-3}	0.98	54.53	2.11	5×10^{-3}	1.21	0.98	73.48

Table 3: Thermodynamic parameters.

Cryogel	ΔS° (J/Kmol)	ΔH° (J/mol)	$\Delta G^\circ_{303\,K}$ (J/mol)	$\Delta G^\circ_{313\,K}$ (J/mol)	$\Delta G^\circ_{323\,K}$ (J/mol)
QE	36.03	13472	2501	2287	1774
QEFe	49.41	17052	2024	1685	1029

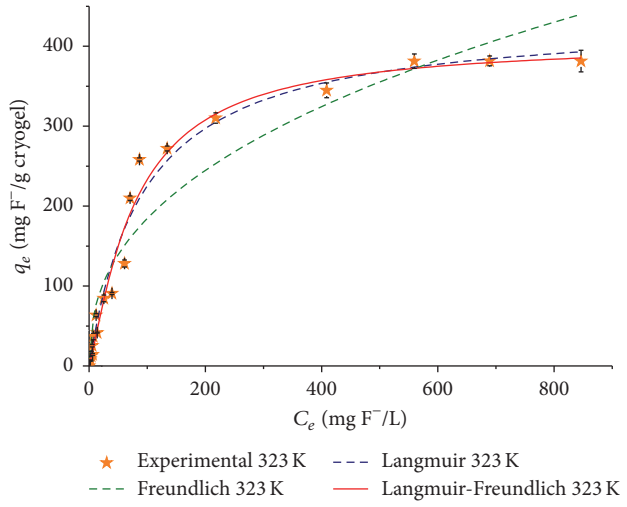

Figure 15: Sorption isotherms, cryogel QEFe fitted to Freundlich, Langmuir, and Langmuir-Freundlich models; 8 mL, 24 hours of contact, 200 rpm, 0.002 g cryogel mass, pH 6, T = 323 K, closed atmosphere.

lowest values of Chi-square are obtained by both models. However, the model that best represents the data obtained in terms of best fit to the experimental data is the Langmuir-Freundlich model, as shown in Figures 14 and 15. This model is applicable to adsorbents with heterogeneous surfaces. At low concentrations of sorbate, data is best adjusted by Freundlich's isotherm, while, at high concentrations of sorbate, data shows a monolayer adsorption and it is best adjusted by the Langmuir isotherm [47, 63]; this is consistent with the proposed removal mechanism in Section 3.1.

3.4. Thermodynamic Parameters. The thermodynamic parameters are used to estimate the feasibility of the adsorption process as well as the effect of temperature. The change in the standard Gibbs free energy (ΔG°) determines if a process is spontaneous or not.

The Van't Hoff equation is used to obtain graphically the values ΔH° and ΔS°. This equation arises from the equation of Gibbs free energy as follows:

$$\Delta G^\circ = -RT \ln K_C,$$
$$\ln K_C = \frac{-\Delta H^\circ}{RT} + \frac{\Delta S^\circ}{R}. \quad (9)$$

A plotting of $\ln K_C$ in the y-axis and T^{-1} on the x-axis should be lineal and the intercept would be equal to $\Delta S^\circ/R$, while the slope would be numerically equal to $-\Delta H^\circ/R$, where R (8.314 Jmol^{-1}K^{-1}) is the universal gas constant. Meanwhile K_C is determined as follows:

$$K_C = \frac{C_{Ae}}{C_{Se}}, \quad (10)$$

where C_{Ae} is equilibrium adsorbate concentration on the surface of the adsorbent and C_{Se} is the equilibrium concentration in the solution.

The standard enthalpy change (ΔH°) provides information about the exothermic or endothermic reaction, and finally the standard entropy change (ΔS°) predicts the magnitude of the changes on the adsorbent surface [15, 47, 49, 57, 61, 63–65].

Table 3 shows the results of the thermodynamic parameters. ΔS° suggests an increase in the disorder of the system and a more widespread disorder can be expected during sorption. The values of ΔH° indicate that these systems are endothermic, and because ΔH° is below 40 kJ/mol this suggests a coexistence of physical and chemical adsorption. Moreover, ΔG° suggest that the system is not spontaneous, so it is necessary to provide energy to the system [7, 13, 15, 16, 46, 52, 66, 67].

4. Conclusions

The X-ray photoelectron spectroscopy shows that fluoride groups interact with oxygen groups in the QE cryogel. Therefore, the fluoride presents links with the hydroxyl groups of the cryogels, which can be hydrogen bonds. Meanwhile, the QEFe cryogel shows interactions between iron and oxygen in the material, so the fluoride ions also form links with the iron by means of hydrogen bonds. The QEFe cryogel shows a higher sorption capacity for fluorides than the QE cryogel.

The QE and QEFe cryogels have a similar adsorption capacity. However, the QEFe cryogel shows the highest adsorption capacity. The sorption kinetics show that the Ho model fits the data better than the Elovich and Lagergren models, which suggests that the removal mechanism also involves chemical adsorption. The sorption isotherms show that the Langmuir-Freundlich model best represents the experimental data and the behavior of cryogels. The point of zero charge shows that on the surface of the cryogels it has predominantly positive charges; because of this, the removal mechanism of fluorine in the QE cryogel is mainly the physical adsorption type and in the QEFe cryogel is a physical and chemical adsorption. Finally, the thermodynamic parameters show that the systems are endothermic and nonspontaneous and there is a coexistence of physical and chemical adsorption.

Competing Interests

The authors declare that they have no competing interests.

Acknowledgments

The authors acknowledge sincerely Direction General of Technological Superior Education (DGEST) by the support (Code 5194.13-P), National Council for Science and Technology (CONACYT) for granting the fellowship of one of the authors, Miss Arcos-Arévalo, National Institute for Nuclear Research (ININ) for the facilities to perform this study, and also Mr. Rafael Basurto Sánchez of the physics department (ININ) and Mrs. Elvia Morales Moreno of the chemistry department (ININ) for their support in the XPS and FTIR analysis.

References

[1] Agencia para Sustancias Tóxicas y el Registro de Enfermedades (ATSDR), *Reseña Toxicológica del Cobre*, Departamento de Salud y Servicios Humanos de los EE.UU., Servicio de Salud Pública, Atlanta, Ga, USA, 2004.

[2] Organización Mundial de la Salud, *Guías para la Calidad del Agua Potable. Primer Apéndice a la Tercera Edición*, vol. 1, Organización Mundial de la Salud, Geneva, Switzerland, 2006.

[3] L. Galicia-Chacón, A. Molina-Frechero, A. Oropeza-Oropeza, E. Gaona, and L. Juárez-López, "Análisis de la concentración de fluoruro en agua potable de la delegación Tláhuac, Ciudad de México," *Revista Internacional de Contaminación Ambiental*, vol. 27, no. 4, 2011.

[4] R. Trejo-Vázquez, J. R. Treviño-Díaz, and E. García-Díaz, "Contaminación aguda por fluoruros en Aguascalientes," Conciencia Tecnológica 36, Instituto Tecnológico de Aguascalientes, Aguascalientes, México, 2008.

[5] S. Vega-Gleason, *Riesgo sanitario ambiental por la presencia de arsénico y fluoruros en los acuíferos de México*. Comisión Nacional del Agua, Gerencia de Saneamiento y Calidad del Agua, 2012.

[6] S. K. Swaina, T. Patnaik, P. C. Patnaik, U. Jha, and R. K. Dey, "Development of new alginate entrapped Fe(III)–Zr(IV) binary mixed oxide for removal of fluoride from water bodies," *Chemical Engineering Journal*, vol. 215-216, pp. 763–771, 2013.

[7] M. Karthikeyan, K. K. S. Kumar, and K. P. Elango, "Batch sorption studies on the removal of fluoride ions from water using eco-friendly conducting polymer/bio-polymer composites," *Desalination*, vol. 267, no. 1, pp. 49–56, 2011.

[8] N. Viswanathan and S. Meenakshi, "Selective fluoride adsorption by a hydrotalcite/chitosan composite," *Applied Clay Science*, vol. 48, no. 4, pp. 607–611, 2010.

[9] V. Tomar, S. Prasad, and D. Kumar, "Adsorptive removal of fluoride from water samples using Zr-Mn composite material," *Microchemical Journal*, vol. 111, pp. 116–124, 2013.

[10] V. Tomar, S. Prasad, and D. Kumar, "Adsorptive removal of fluoride from aqueous media using citrus limonum (lemon) leaf," *Microchemical Journal*, vol. 112, pp. 97–103, 2014.

[11] D. Thakre, S. Jagtap, A. Bansiwal, N. Labhsetwar, and S. Rayalu, "Synthesis of La-incorporated chitosan beads for fluoride removal from water," *Journal of Fluorine Chemistry*, vol. 131, no. 3, pp. 373–377, 2010.

[12] K. Biswas, K. Gupta, A. Goswami, and U. C. Ghosh, "Fluoride removal efficiency from aqueous solution by synthetic iron(III)-aluminum(III)-chromium(III) ternary mixed oxide," *Desalination*, vol. 255, no. 1–3, pp. 44–51, 2010.

[13] J. Liu, W.-Y. Li, Y. Liu, Q. Zeng, and S. Hong, "Titanium(IV) hydrate based on chitosan template for defluoridation from aqueous solution," *Applied Surface Science*, vol. 293, pp. 46–54, 2014.

[14] J. J. García-Sánchez, M. Solache-Ríos, V. Martínez-Miranda, and C. Solís Morelos, "Removal of fluoride ions from drinking water and fluoride solutions by aluminum modified iron oxides in a column system," *Journal of Colloid and Interface Science*, vol. 407, pp. 410–415, 2013.

[15] M. G. Sujana, A. Mishra, and B. C. Acharya, "Hydrous ferric oxide doped alginate beads for fluoride removal: adsorption kinetics and equilibrium studies," *Applied Surface Science*, vol. 270, pp. 767–776, 2013.

[16] S. Jagtap, D. Thakre, S. Wanjari, S. Kamble, N. Labhsetwar, and S. Rayalu, "New modified chitosan-based adsorbent for defluoridation of water," *Journal of Colloid and Interface Science*, vol. 332, no. 2, pp. 280–290, 2009.

[17] N. Viswanathan and S. Meenakshi, "Enriched fluoride sorption using alumina/chitosan composite," *Journal of Hazardous Materials*, vol. 178, no. 1-3, pp. 226–232, 2010.

[18] H. Paudyal, B. Pangeni, K. Inoue et al., "Adsorptive removal of trace concentration of fluoride ion from water by using dried orange juice residue," *Chemical Engineering Journal*, vol. 223, pp. 844–853, 2013.

[19] S. Annouar, M. Mountadar, A. Soufiane, A. Elmidaoui, and M. A. M. Sahli, "Defluoridation of underground water by adsorption on the chitosan and by electrodialysis," *Desalination*, vol. 165, p. 437, 2004.

[20] A. Bhatnagar, E. Kumar, and M. Sillanpää, "Fluoride removal from water by adsorption—a review," *Chemical Engineering Journal*, vol. 171, no. 3, pp. 811–840, 2011.

[21] P. Miretzky and A. Fernandez-Cirelli, "Fluoride removal from water by chitosan derivatives and composites: a review," *Journal of Fluorine Chemistry*, vol. 132, no. 4, pp. 231–240, 2011.

[22] N. Viswanathan, C. S. Sundaram, and S. Meenakshi, "Removal of fluoride from aqueous solution using protonated chitosan beads," *Journal of Hazardous Materials*, vol. 161, no. 1, pp. 423–430, 2009.

[23] R. Huang, B. Yang, Q. Liu, and K. Ding, "Removal of fluoride ions from aqueous solutions using protonated cross-linked chitosan particles," *Journal of Fluorine Chemistry*, vol. 141, pp. 29–34, 2012.

[24] S. Jagtap, M. K. Yenkie, S. Das, and S. Rayalu, "Synthesis and characterization of lanthanum impregnated chitosan flakes for fluoride removal in water," *Desalination*, vol. 273, no. 2-3, pp. 267–275, 2011.

[25] D. H. K. Reddy and S.-M. Lee, "Application of magnetic chitosan composites for the removal of toxic metal and dyes from aqueous solutions," *Advances in Colloid and Interface Science*, vol. 201-202, pp. 68–93, 2013.

[26] C. Jeon and W. H. Höll, "Chemical modification of chitosan and equilibrium study for mercury ion removal," *Water Research*, vol. 37, no. 19, pp. 4770–4780, 2003.

[27] C. Shen, H. Chen, S. Wu et al., "Highly efficient detoxification of Cr(VI) by chitosan-Fe(III) complex: process and mechanism studies," *Journal of Hazardous Materials*, vol. 244-245, pp. 689–697, 2013.

[28] X. Wang and B. G. Min, "Cadmium sorption properties of poly (vinyl alcohol)/hydroxyapatite cryogels: I. kinetic and isotherm studies," *Journal of Sol-Gel Science and Technology*, vol. 43, no. 1, pp. 99–104, 2007.

[29] X. Wang and B. G. Min, "Cadmium sorption properties of poly(vinyl alcohol)/hydroxyapatite cryogels: II. Effects of operating parameters," *Journal of Sol-Gel Science and Technology*, vol. 45, no. 1, pp. 17–22, 2008.

[30] I. E. Veleshko, V. V. Nikonorov, A. N. Veleshko et al., "Sorption of Eu(III) from solutions of covalently cross-linked chitosan cryogels," *Fibre Chemistry*, vol. 42, no. 6, pp. 364–369, 2011.

[31] V. V. Nikonorov, R. V. Ivanov, N. R. Kil'deeva, L. N. Bulatnikova, and V. I. Lozinskii, "Synthesis and characteristics of cryogels of chitosan crosslinked by glutaric aldehyde," *Polymer Science Series A*, vol. 52, no. 8, pp. 828–834, 2010.

[32] K. Tekin, L. Uzun, Ç. A. Şahin, S. Bektaş, and A. Denizli, "Preparation and characterization of composite cryogels containing imidazole group and use in heavy metal removal," *Reactive & Functional Polymers*, vol. 71, no. 10, pp. 985–993, 2011.

[33] R. Garcia-Gonzalez, R. R. E. Zavala-Arce, P. Avila-Perez et al., "Síntesis y caracterización de un material criogénico a partir de quitosano y celulosa," *Afinidad*, vol. 71, no. 567, 2014.

[34] N. Viswanathan and S. Meenakshi, "Selective sorption of fluoride using Fe(III) loaded carboxylated chitosan beads," *Journal of Fluorine Chemistry*, vol. 129, no. 6, pp. 503–509, 2008.

[35] C. J. Creswell, O. Runquist, and M. M. Campbell, Editorial Diana, México, 1972.

[36] G. Brust, *Espectroscopía Infrarroja*, Universidad del Sur de Mississippi, 1997.

[37] A. Bismarck, R. Tahhan, J. Springer et al., "Influence of fluorination on the properties of carbon fibres," *Journal of Fluorine Chemistry*, vol. 84, no. 2, pp. 127–134, 1997.

[38] C. D. Wagner, J. F. Moulder, L. E. David, and W. M. Riggs, *Handbook of X-Ray Photoelectron Spectroscopy*, Perkin-Elmer, Norwalk, Conn, USA, 1989.

[39] N. Viswanathan, C. Sairam Sundaram, and S. Meenakshi, "Development of multifunctional chitosan beads for fluoride removal," *Journal of Hazardous Materials*, vol. 167, no. 1-3, pp. 325–331, 2009.

[40] N. Viswanathan, C. Sairam Sundaram, and S. Meenakshi, "Removal of fluoride from aqueous solution using protonated chitosan beads," *Journal of Hazardous Materials*, vol. 161, no. 1, pp. 423–430, 2009.

[41] H. Valdés, M. Sánchez-Polo, and C. A. Zaror, "Impacto del tratamiento con ozono sobre las propiedades superficiales del carbón activado," *Ingeniare. Revista Chilena de Ingeniería*, vol. 19, no. 2, pp. 174–185, 2011.

[42] L. Giraldo and J. C. Moreno, "Relación entre la entalpía de inmersión de un carbón activado en soluciones acuosas de Pb^{2+} y los parámetros de adsorción," *Revista Colombiana de Química*, vol. 35, no. 1, pp. 41–49, 2006.

[43] N. Viswanathan, C. S. Sundaram, and S. Meenakshi, "Sorption behaviour of fluoride on carboxylated cross-linked chitosan beads," *Colloids and Surfaces B: Biointerfaces*, vol. 68, no. 1, pp. 48–54, 2009.

[44] N. Viswanathan, C. Sairam Sundaram, and S. Meenakshi, "Development of multifunctional chitosan beads for fluoride removal," *Journal of Hazardous Materials*, vol. 167, no. 1–3, pp. 325–331, 2009.

[45] Y. S. Ho, J. F. Porter, and G. McKay, "Equilibrium isotherm studies for the sorption of divalent metal ions onto peat: copper, nickel and lead single component systems," *Water, Air, and Soil Pollution*, vol. 141, no. 1–4, pp. 1–33, 2002.

[46] C. Gerente, V. K. C. Lee, P. Le Cloirec, and G. McKay, "Application of chitosan for the removal of metals from wastewaters by adsorption—mechanisms and models review," *Critical Reviews in Environmental Science and Technology*, vol. 37, no. 1, pp. 41–127, 2007.

[47] R. Bhattacharyya and S. K. Ray, "Removal of congo red and methyl violet from water using nano clay filled composite hydrogels of poly acrylic acid and polyethylene glycol," *Chemical Engineering Journal*, vol. 260, pp. 269–283, 2014.

[48] B. Kayranli, "Adsorption of textile dyes onto iron based waterworks sludge from aqueous solution; isotherm, kinetic and thermodynamic study," *Chemical Engineering Journal*, vol. 173, no. 3, pp. 782–791, 2011.

[49] Y. Liu and Y.-J. Liu, "Review: Biosorption isotherms, kinetics and thermodynamics," *Separation and Purification Technology*, vol. 61, no. 3, pp. 229–242, 2008.

[50] V. Vimonses, S. Lei, B. Jin, C. W. K. Chow, and C. Saint, "Kinetic study and equilibrium isotherm analysis of Congo Red adsorption by clay materials," *Chemical Engineering Journal*, vol. 148, no. 2-3, pp. 354–364, 2009.

[51] W. S. W. Ngah and S. Fatinathan, "Adsorption characterization of Pb(II) and Cu(II) ions onto chitosan-tripolyphosphate beads: kinetic, equilibrium and thermodynamic studies," *Journal of Environmental Management*, vol. 91, no. 4, pp. 958–969, 2010.

[52] M. Erşan, E. Baĝda, and E. Baĝda, "Investigation of kinetic and thermodynamic characteristics of removal of tetracycline with sponge like, tannin based cryogels," *Colloids and Surfaces B: Biointerfaces*, vol. 104, pp. 75–82, 2013.

[53] K. U. Ahamad and M. Jawed, "Kinetics, equilibrium and breakthrough studies for Fe(II) removal by wooden charcoal: a low-cost adsorbent," *Desalination*, vol. 251, no. 1-3, pp. 137–145, 2010.

[54] P. Liang, Y. Zhang, D. Wang, Y. Xu, and L. Luo, "Preparation of mixed rare earths modified chitosan for fluoride adsorption," *Journal of Rare Earths*, vol. 31, no. 8, pp. 817–822, 2013.

[55] J. Ma, Y. Shen, C. Shen, Y. Wen, and W. Liu, "Al-doping chitosan-Fe(III) hydrogel for the removal of fluoride from aqueous solutions," *Chemical Engineering Journal*, vol. 248, pp. 98–106, 2014.

[56] A. S. Elsherbiny, "Adsorption kinetics and mechanism of acid dye onto montmorillonite from aqueous solutions: stopped-flow measurements," *Applied Clay Science*, vol. 83-84, pp. 56–62, 2013.

[57] J. Thilagan, S. Gopalakrishnan, and T. Kannadasan, "Thermodynamic study on adsorption of Copper (II) ions in aqueous solution by Chitosan blended with Cellulose & cross linked by Formaldehyde, Chitosan immobilised on Red Soil, Chitosan reinforced by Banana stem fibre," *International Journal of Scientific Research Engineering & Technology*, vol. 2, no. 1, 2013.

[58] X. Li, Y. Li, S. Zhang, and Z. Ye, "Preparation and characterization of new foam adsorbents of poly(vinyl alcohol)/chitosan composites and their removal for dye and heavy metal from aqueous solution," *Chemical Engineering Journal*, vol. 183, pp. 88–97, 2012.

[59] R. Cortés-Martínez, M. T. Olguín, and M. Solache-Ríos, "Cesium sorption by clinoptilolite-rich tuffs in batch and fixed-bed systems," *Desalination*, vol. 258, no. 1–3, pp. 164–170, 2010.

[60] G. O. El Sayed and H. A. Dessouki, "Biosorption of Ni (II) And Cd (II) ions from aqueous solutions onto rice straw," *Chemical Sciences Journal*, vol. CSJ-9, pp. 1–11, 2010.

[61] M. Alkan, Ö. Demirbaş, and M. Doğan, "Adsorption kinetics and thermodynamics of an anionic dye onto sepiolite," *Microporous and Mesoporous Materials*, vol. 101, no. 3, pp. 388–396, 2007.

[62] N. Viswanathan and S. Meenakshi, "Synthesis of Zr(IV) entrapped chitosan polymeric matrix for selective fluoride sorption," *Colloids and Surfaces B: Biointerfaces*, vol. 72, no. 1, pp. 88–93, 2009.

[63] M. D. Burghardt, *Ingeniería Termodinámica*, 2nd edition, 1984.

[64] J. M. Smith, H. C. Van Ness, and M. M. Abbott, *Introducción a la Termodinámica en Ingeniería Química*, Mcgraw-Hill, Ciudad de México, México, 5th edition, 1997.

[65] M. Al-Ghouti, M. A. M. Khraisheh, M. N. M. Ahmad, and S. Allen, "Thermodynamic behaviour and the effect of temperature on the removal of dyes from aqueous solution using modified diatomite: A Kinetic Study," *Journal of Colloid and Interface Science*, vol. 287, no. 1, pp. 6–13, 2005.

[66] G. Crini and P.-M. Badot, "Application of chitosan, a natural aminopolysaccharide, for dye removal from aqueous solutions by adsorption processes using batch studies: a review of recent literature," *Progress in Polymer Science*, vol. 33, no. 4, pp. 399–447, 2008.

[67] N. Pérez, J. González, and L. A. Delgado, "Estudio termodinámico del proceso de adsorción de iones de Ni y V por parte de ligninas precipitadas del licor negro Kraft," *Revista Latinoamericana de Metalurgia y Materiales*, vol. 31, no. 2, pp. 168–181, 2011.

Hindawi Publishing Corporation
Journal of Chemistry
Volume 2016, Article ID 8105128, 9 pages
http://dx.doi.org/10.1155/2016/8105128

Research Article

A Comparative Electrochemical-Ozone Treatment for Removal of Phenolphthalein

V. M. García-Orozco,[1] C. E. Barrera-Díaz,[2] G. Roa-Morales,[2] and Ivonne Linares-Hernández[3]

[1]*Facultad de Química, Universidad Autónoma del Estado de México, Paseo Colón, Intersección Paseo Tollocan S/N, 50120 Toluca, MEX, Mexico*
[2]*Centro Conjunto de Investigación en Química Sustentable UAEM-UNAM, Carretera Toluca-Atlacomulco, Km 14.5, Campus San Cayetano, 50200 Toluca, MEX, Mexico*
[3]*Centro Interamericano de Recursos del Agua, Universidad Autónoma del Estado de México, C.P. 50091 Toluca, MEX, Mexico*

Correspondence should be addressed to C. E. Barrera-Díaz; cbd0044@gmail.com

Received 15 July 2016; Revised 15 September 2016; Accepted 21 September 2016

Academic Editor: Julie J. M. Mesa

The degradation of aqueous solutions containing phenolphthalein was carried out using ozone and electrochemical processes; the two different treatments were performed for 60 min at pH 3, pH 7, and pH 9. The electrochemical oxidation using boron-doped diamond electrodes processes was carried out using three current density values: 3.11 $mA{\cdot}cm^{-2}$, 6.22 $mA{\cdot}cm^{-2}$, and 9.33 $mA{\cdot}cm^{-2}$, whereas the ozone dose was constantly supplied at 5 ± 0.5 mgL^{-1}. An optimal degradation condition for the ozonation treatment is at alkaline pH, while the electrochemical treatment works better at acidic pH. The electrochemical process is twice better compared with ozonation.

1. Introduction

Water is one of the most valuable assets for a country; indeed, safe drinking water is a basic human right. Safe and reliable drinking water is vital to every community since human health has become expensive since inadequate water quality reduces work productivity [1, 2]. Water scarcity is an economic threat for developing countries in which a large amount is used in agricultural, industrial, and domestic purposes [3].

Wastewater treatment has become a priority since good quality treated wastewater can be reused in some activities. An effective approach for treating wastewater is to carry out treatments in well-located sources. In this sense, water and wastewater testing laboratories generate large amounts of residues. In particular, the analysis and test for alkalinity and acidity using phenolphthalein (PHPH) produce large amounts of wastewater containing PHPH. In industrial operations such as the flavour drinking water industry, the mixing reactors in which the water is prepared should be cleaned after the process; this is commonly done using an aqueous solution containing NaOH, and then rinsing water containing PHPH is used for checking that all NaOH has been eliminated.

PHPH was discovered by the German chemist Adolf von Baeyer in 1871. He prepared it by the fusion of phenol and phthalic anhydride in the presence of sulfuric acid or Zinc chloride [4, 5].

PHPH (1%) is used in alcoholic solutions in titration as a pH visual indicator to unveil information regarding other compounds that include some organic and mineral acids as well as most alkalis. When working as an indicator, it turns pink in basic solutions usually above pH 10 and colorless in acidic ones below pH 8 [6]. Furthermore, it is utilized to forecast depth of concrete carbonation. A different application for PHPH is in determination of diluted blood used for forensic evidences such as Kastle-Meyer test. Here, the color turns pink if the specimen analyzed contains haemoglobin. Likewise, PHPH is used as the staple ingredient to make disappearing dye in some toys [7]. PHPH can

be traced in an assortment of ingested products and in some scientific applications too. Furthermore, it could be incorporated in tablets, powders, and liquids because of its odourless and tasteless features. Additionally, it is employed as a laxative, in the form of a gum laxative product or chocolate [8]. In 1999 [9], PHPH was removed from Over-the-Counter medication (OTC) laxatives by the Food and Drug Administration (FDA). Recently, PHPH test indicates that it could cause neoplasia and ovary cancer [10–12].

The use of advanced oxidation processes (AOPs) allows producing hydroxyl radicals, which are strong oxidant agents, ready to react with organics [13–16]. Unlike many other radicals, hydroxyl radicals are nonselective and thus readily attack a big group of organic chemicals to transform them into less complex and damaging intermediate products that can degrade in an indiscriminate way of micropollutants [17]; these ones possess reaction rate constants around 10^9 $Lmol^{-1}$ s^{-1} [18].

Among others, electrooxidation and ozonation can produce hydroxyl radicals. Until now there are few studies in which both processes are used at the same time; indeed, PHPH degradation has not previously been reported.

2. Materials and Methods

2.1. Chemicals. Distilled water was used for the preparation of aqueous solutions, used as synthetic water prepared with PHPH (Técnical Química) at 5 mg/L. Na_2SO_4 (Fermont) at 0.05 M was selected as the support electrolyte in this work. The electrolytic medium was made basic, neutral, and acidic as required by the addition of aqueous $B(OH)_3$ (J. T. Baker at 0,04 M), H_3PO_4 (Merck at 0,04), and H_2SO_4 (Fermont at 1 M), where $B(OH)_3$ and H_3PO_4 (Merck) were used as buffer for maintaining the pH of 9 and 7 with the addition of NaOH (Merck at 5 M), respectively.

2.2. Electrooxidation Treatment. For this process a batch type reactor with cylindrical shape containing electrodes of boron-doped diamond (BDD) was used, where the electrodes were connected in parallel and each electrode is 20.6 cm large per 2.6 cm wide. Three electrodes were used as anodes and two as cathodes. The total anodic surface (Aa) was 321.36 cm^2. While the capacity of the reactor was 1.2 L, 1.0 L was used at all experiments. 1–3 A (3.11, 6.22, and 9.33 $mA{\cdot}cm^{-2}$) were supplied during all the process. Three different pH values were studied 3, 7, and 9. Aliquots were taken at different elapsed times (Figure 1(a)).

2.3. Ozonation Treatment. In this treatment ozone was supplied by a Pacific Ozone Technology generator number LAB212 with Serial Number 7646; ozone was produced using dry air. The reactor is 40 cm long and 8 cm in diameter, and one liter of contaminated solution was used for the test. The reactor was fed, with ozone, in the bottom part through a porous plate, with a constant concentration of 5 ± 0.5 mgL^{-1}. Ozonation experiments were carried out at the pH of 3, 7, and 9, and samples were taken at regular intervals to determine the chemical oxygen demand (COD).

Ozone not used in the reaction was collected in the upper part of the reactor and directed to a heated catalytic ozone destruct, PACIFIC OZONE, Model Number d42202, with Serial Number 1687 (Figure 1(b)).

2.4. Analytic Methods. The aliquots were characterized before and after the treatment. In this characterization, COD was measured in accordance with APHA/AWWA/WPCE.

The concentration of total organic carbon (TOC) of each sample was measured in a Shimadzu Total Organic Carbon Analyzer (model L_{CPH}) fitted with an autosampler [19].

The removal efficiency or percentage of COD removal (%RE) was then calculated as follows [20]:

$$\%\mathrm{RE} = \frac{\mathrm{COD}_0 - \mathrm{COD}_t}{\mathrm{COD}_0} \times 100\%. \tag{1}$$

The instantaneous current efficiency (ICE) can be used to calculate the apparent Faradic efficiency of COD removal by using the following formula [21]:

$$\mathrm{ICE} = \frac{\left[(\mathrm{COD})_t - (\mathrm{COD})_{t+\Delta t}\right] F * V * 100}{8 I \Delta t}. \tag{2}$$

The energy consumption (E_{C1}) per unit COD mass ($KWh\ mg^{-1}$ COD) was calculated using [22]

$$E_{C1} = \frac{IUt}{\left[(\mathrm{COD})_t - (\mathrm{COD})_{t+\Delta t}\right] V}; \tag{3}$$

then $(\mathrm{COD})_t$ and $(\mathrm{COD})_{t+\Delta t}$ are the COD values ($gO_2{\cdot}dm^{-3}$) at t and $t + \Delta t$ (s), respectively, I is the current intensity (A), F is the Faraday constant (96487 $Cmol^{-1}$), V is the electrolyte solution volume (L), the constant 8 is the oxygen equivalent mass (g $eq.^{-1}$), and U is the average cell voltage (V).

Converting m^3 to dm^3 considering 1000 dm^3 equals 1 m^3 and taking into account that the cost of electricity in US is \$0.15 (U.S. currency) per kWh, the monetary value required to demean a unit of volume effluent is given by the equation below [23]:

$$\mathrm{Cost}\left(\mathrm{US\$\ dm^{-3}}\right) = \mathrm{EC}\left(\mathrm{kWh\ dm^{-3}}\right) \times 0.15\ (\mathrm{US\$/kWh})\,. \tag{4}$$

3. Results and Discussions

3.1. UV-Vis Characterization. Figure 2(a) shows the ultraviolet-visible spectroscopy (UV-Vis) absorption spectra, of a 5 mgL^{-1} PHPH solution at pH 3, 7, and 9. All spectra present two absorption bands. At pH 3 and 7, however, they have an absorbance maximum in the wavelength (λ) of 229 nm, unlike at pH 9, where such a maximum is located in 234 nm. This is related to the protonated structure of the PHPH and agrees with the species distribution diagram found as described in Figure 2(b) (pka of PHPH is 9.7 [7, 24, 25]); the second of the three spectra is in 274 nm, which corresponds to the 100% of the acid specie at pH 3 and 7. At pH 9, a change in these bands is observed, because there are 84% of acidic species PHPH and 16% of basic

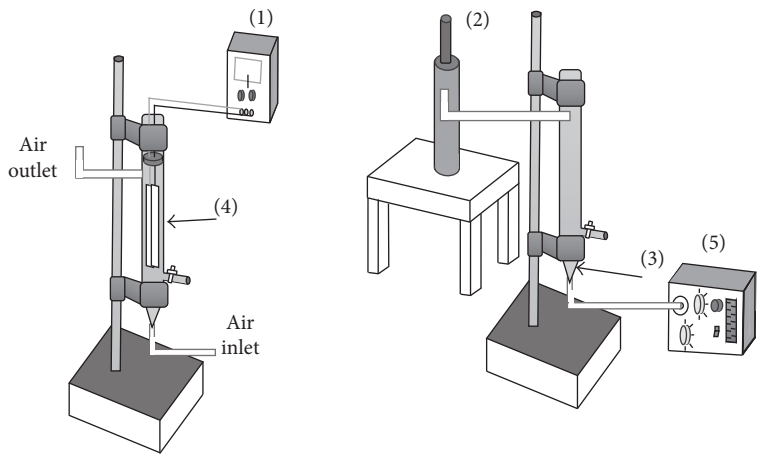

Figure 1: Schematic diagram: (a) electrooxidation treatment; (b) ozonation treatment.

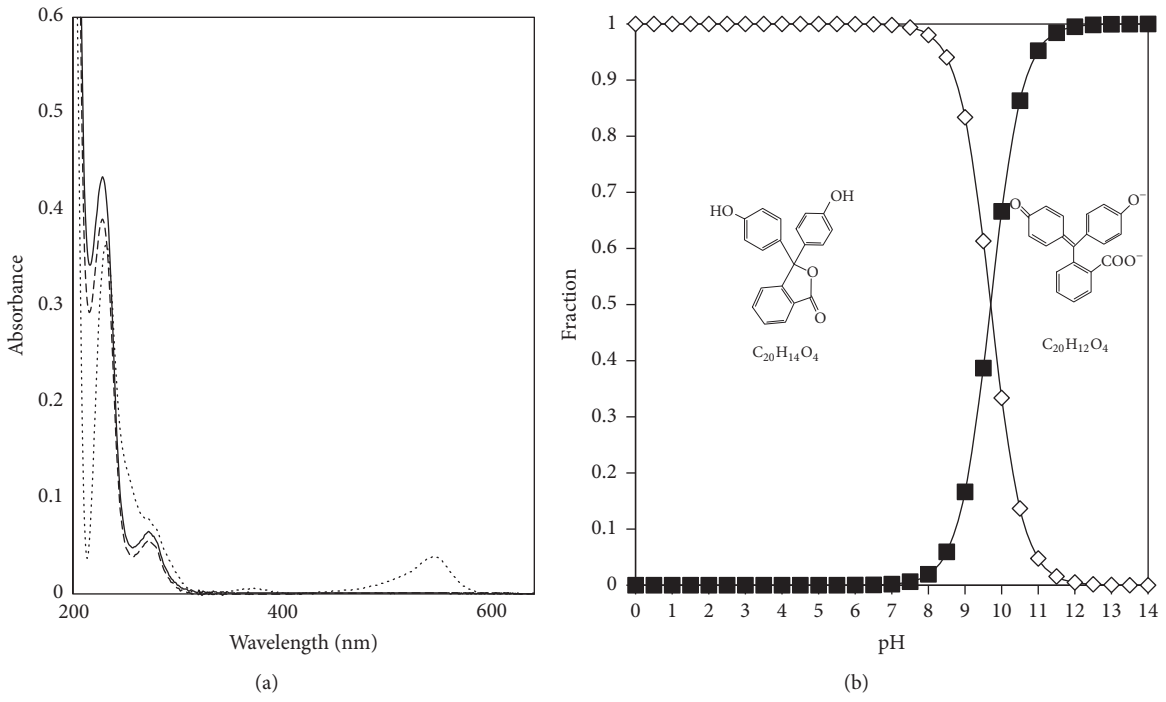

Figure 2: (a) UV-Vis PHPH peaks at different pH values: (. . .) 9, (—) 7, and (--) 3. (b) Chemical species distribution diagram, protonated and deprotonated: (◇) $C_{20}H_{14}O_4$ and (■) $C_{20}H_{12}O_4$.

species; additionally, an absorption band with an absorbance maximum of 554 nm is formed, which is associated with the pink color and is a consequence of the structure of the molecule formed in basic pH.

3.2. Effect of Current Density in Electrooxidation Treatment. The effect of current densities (J) (3.11 mA·cm^{-2}, 6.22 mA·cm^{-2}, and 9.33 mA·cm^{-2}) was studied to find the current density optimum value.

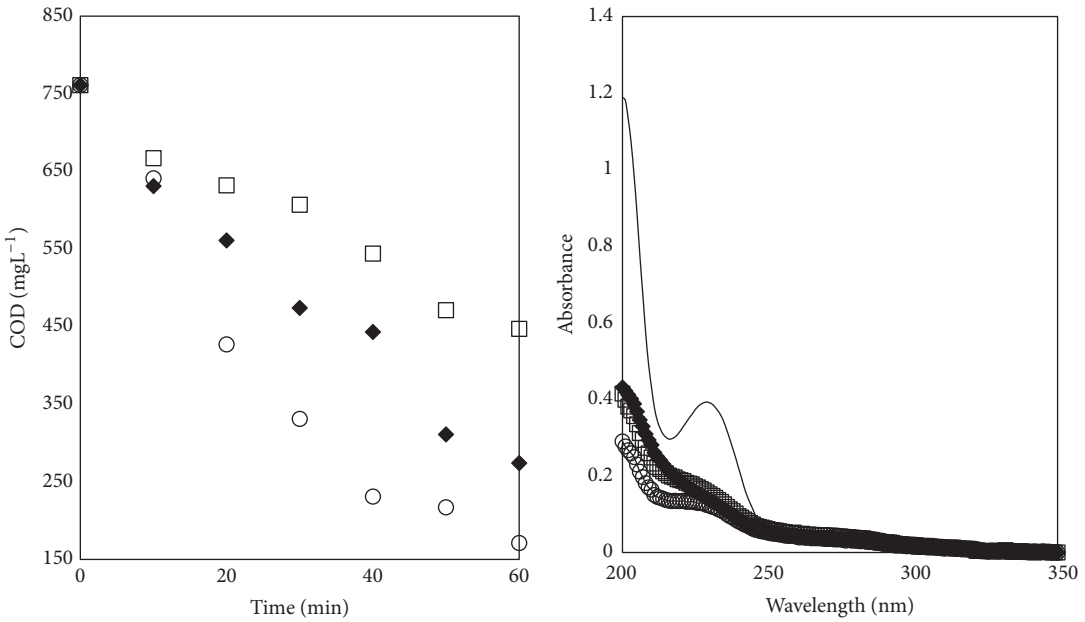

Figure 3: (a) Influence of the current density in the COD removal; (b) UV-Vis spectra: (▬) PHPH solution in the electrooxidation treatment to pH (□) 3.11, (⧫) 6.22, and (○) 9.33 mA·cm^{-2}.

Figure 3(a) shows the removal of the PHPH using the COD; the process was performed at 60 minutes; taking aliquots every 10 minutes, the initial concentration of the PHPH was 5 mgL^{-1}, at pH 3. The current density that shows a greater removal of the COD is 9.33 mA·cm^{-2} obtaining a 71% COD decrease.

In previous reports the treatment time is associated with pollutant and color removal [26].

Figure 3(b) depicts the absorption spectra acquired during the treatment at the three current densities previously mentioned. This technique confirms how the PHPH is eliminating. The pollutant removal occurs by the hydroxyl radical reactions formed in the electrooxidation treatment. Hydroxyl radical ($^{\bullet}$OH) formation occurs at the DDB surface [27]; its high oxidizing power oxidizes the organic material as shown in reaction (5) [28–31] and generates oxygen evolution. In this process it is possible to reach complete mineralization, where CO_2 and H_2O are formed according to Equations (6) and (7), and then CO_2 can be hydrolyzed to form carbonate ions [32, 33].

$$\text{BDD} + H_2O \longrightarrow \text{BDD}\left(^{\bullet}\text{OH}\right) + H^+ + e^- \quad (5)$$

$$\text{BDD}\left(^{\bullet}\text{OH}\right) + \text{PHPH} \longrightarrow \text{BDD} + mCO_2 + nH_2O \quad (6)$$

$$\text{BDD}\left(^{\bullet}\text{OH}\right) + \text{PHPH} \longrightarrow \text{BDD} + \text{Mineralization products} + H^+ + e^- \quad (7)$$

Reactions (6) and (7) compete with the secondary reaction of hydroxyl radical transformation to O_2 without any participation of the anode surface as indicated in the following equation [34]:

$$\text{BDD}\left(^{\bullet}\text{OH}\right) \longrightarrow \text{BDD} + \frac{1}{2}O_2 + H^+ + e^- \quad (8)$$

Table 1: Energy consumption to amperages and different pH.

pH	i, A	Kwh dm^{-3}	US $ m^{-3}
3	1	0.005	0.8
3	2	0.013	2.0
3	3	0.023	3.4
7	2	0.014	2.0
9	2	0.011	1.8

The energy consumption is shown in Table 1.

The optimal conditions for the electrooxidation treatment are presented in Figure 4(a); as shown, the acidic pH is more effective. The spectrum change after the treatment, as illustrated in Figure 4(b), which shows that the greater COD decreases is at pH 3. It can be concluded that the optimal conditions are a current density of 6.22 mA·cm^{-2} and using pH of 3.

Figure 5 shows the efficiency of the instantaneous current during the treatment of 6.22 mA·cm^{-2}, which also shows the lowest ICE (80%). This value indicates that almost all the energy is used in the degradation and there is little lost energy; this result agrees with previous works [35].

The better ICE percentage is found at the beginning stage of electrooxidation and it may be attributed to the presence of higher concentration of organics in the vicinity of the electrodes. This indicates that the electrooxidation is

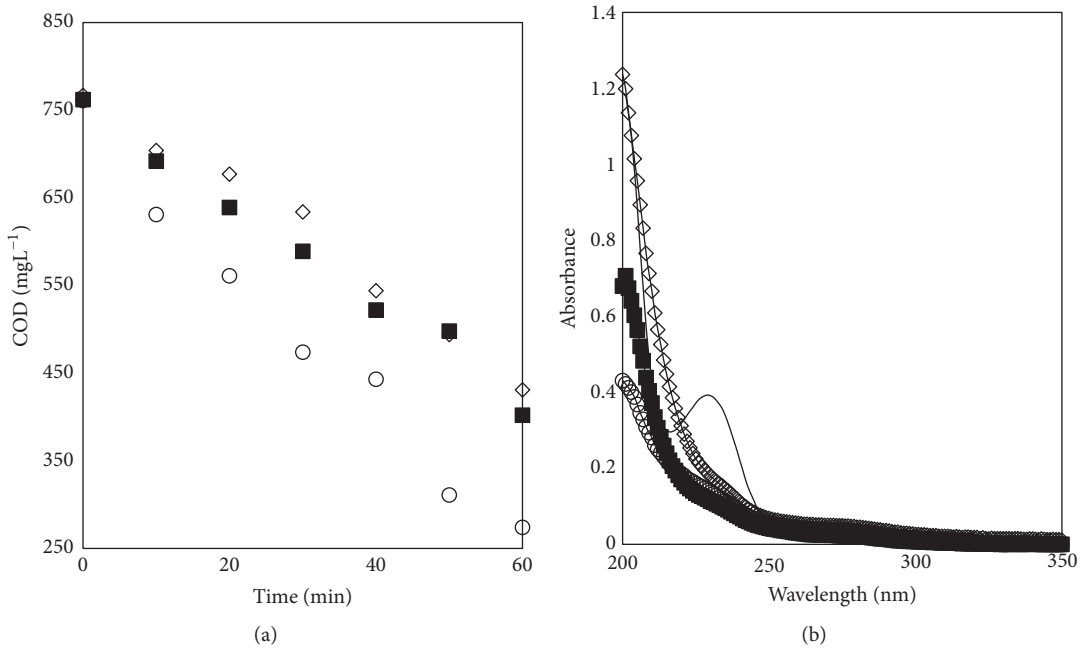

Figure 4: (a) Influence of the COD removal; (b) UV-Vis spectra: (▬) PHPH solution in the electrooxidation treatment to pH (◇) 9, (■) 7, and (○) 3.

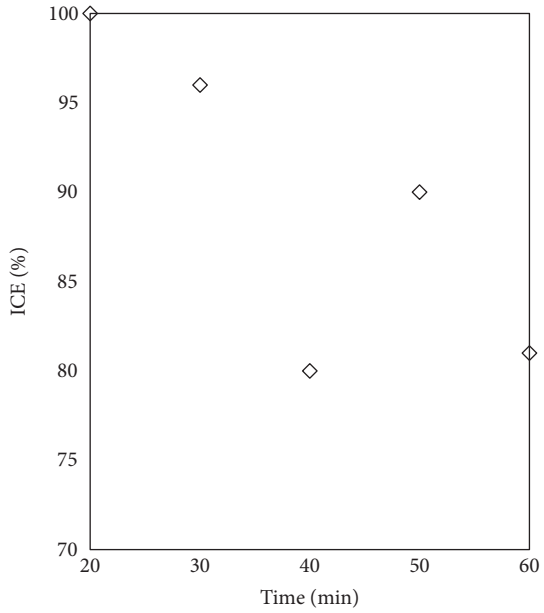

Figure 5: Instant Current Efficiency in the electrooxidation treatment to (◇) using a current density of 6.22 mA·cm^{-2}.

under current control regime at least in the middle stage of electrooxidation. It was observed that ICE decreased during the electrooxidation process. This may be explained due to the depletion of organics concentration in the vicinity of electrode surface [36].

3.3. Ozonation Treatment. The ozone was generated by an ozone generator (Equation (9)); the presence of ozone in the system generates the radicals (Equation (10)) that carry out the oxidation of the PHPH [37, 38]. Ozone has an oxidation potential of 2.07 v [39, 40]. Figure 6(a) shows a 26% COD removal at pH 9; in pH 7 only 11% is reached, but at pH 3 only 1% of the PHPH is removed after 60 minutes of treatment time. The main reactions (11)–(13) where hydroxyl radicals are formed are shown below: [41–44].

$$O_2 + O^{\bullet} \leftrightarrows O_3 \quad (9)$$

$$O^{\bullet} + H^{+} + e^{-} \longrightarrow {}^{\bullet}OH \quad (10)$$

The general stoichiometry occurs by the following equations, depending on whether the initiation is hydroxyl ions [41].

$$3O_3 + OH^{-} \longrightarrow {O_3}^{-} + O_2 \quad (11)$$

The hastened ozone decomposition resulted in the rapid production of $OH^{\bullet}$, leading to the higher removal of PHPH [43].

$$O_3 + OH^{-} \longrightarrow {HO_2}^{-} + O_2 \quad (12)$$

$$O_3 + {HO_2}^{-} \rightleftarrows {}^{\bullet}OH + {O_2}^{\bullet -} + O_2 \quad (13)$$

We present reactions that occur during the ozonation process in Equations (9)–(13); this indicates that fragmentation of the molecule PHPH is taking place and not a degradation.

3.4. TOC Removal Comparison between Electrooxidation and Ozone Treatment. In Figure 7 the TOC removal as a function of treatment time is shown, the removal is higher by using the electrooxidation treatment, and in the case of ozonation the removal is lower by 50 percent with respect to TOC.

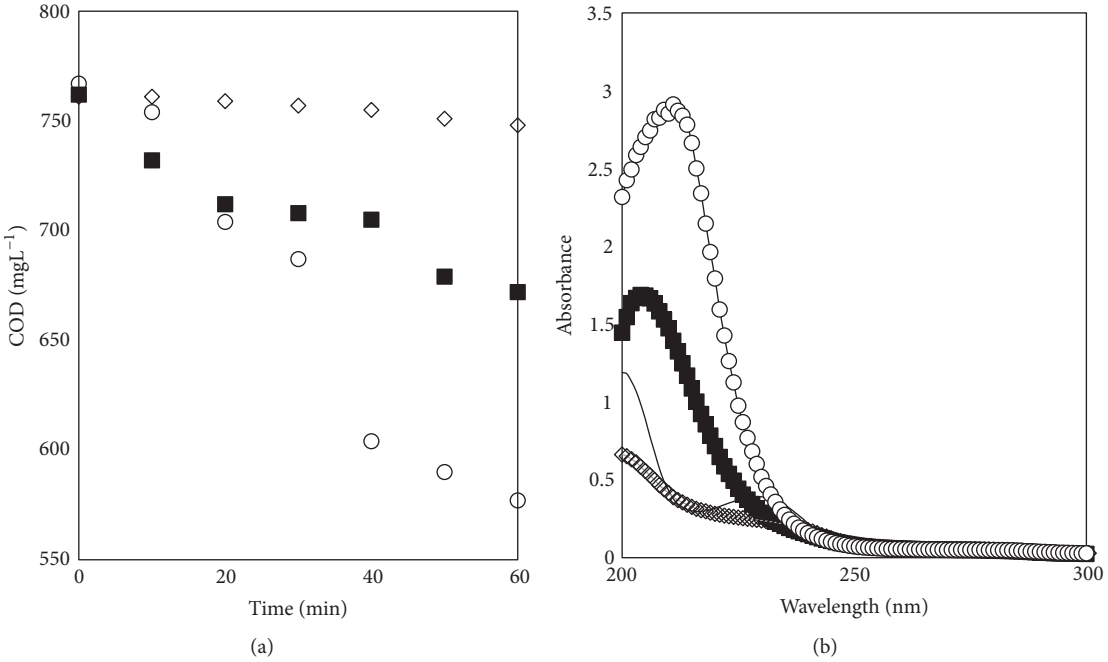

Figure 6: (a) Influence of the COD removal; (b) UV-Vis spectra: (▬) PHPH solution in the ozonation treatment to pH (◇) 3, (■) 7, and (○) 9.

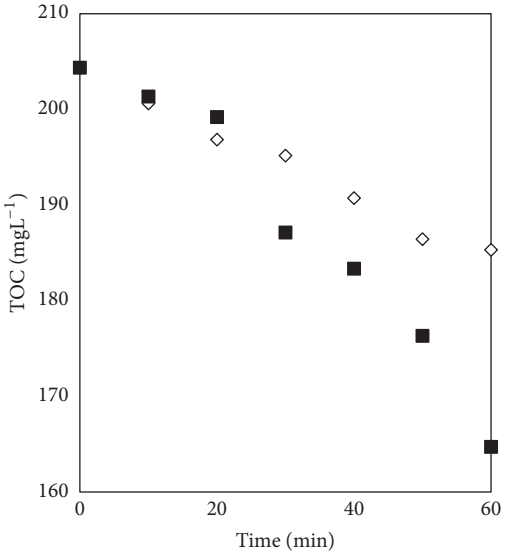

Figure 7: Influence of the TOC removal in the electrooxidation (■) and ozonation treatment (◇).

In the first minutes, the results are similar in both methods because in the two methods hydroxyl radicals are available to attack the PHPH; however, the electrochemical treatment requires less steps to produce the radicals (since they are produced directly on the electrode surface), while the ozone requires more steps to produce the radicals and also is limited by the gas-liquid mass transfer phenomena.

3.5. Mechanism. The PHPH degradation mechanism is presented in Figure 8.

4. Conclusions

In this work we present two methods for the degradation of PHPH present in an aqueous solution. The electrochemical method requires acidic conditions to reach a 71% COD removal, whereas the ozone method requires basic conditions to obtain a 25% COD removal. This fact relies on the hydroxyl radicals production, which is faster in the electrochemical methods since less steps are required and a large anodic area provides a good mass transfer. The production of hydroxyl

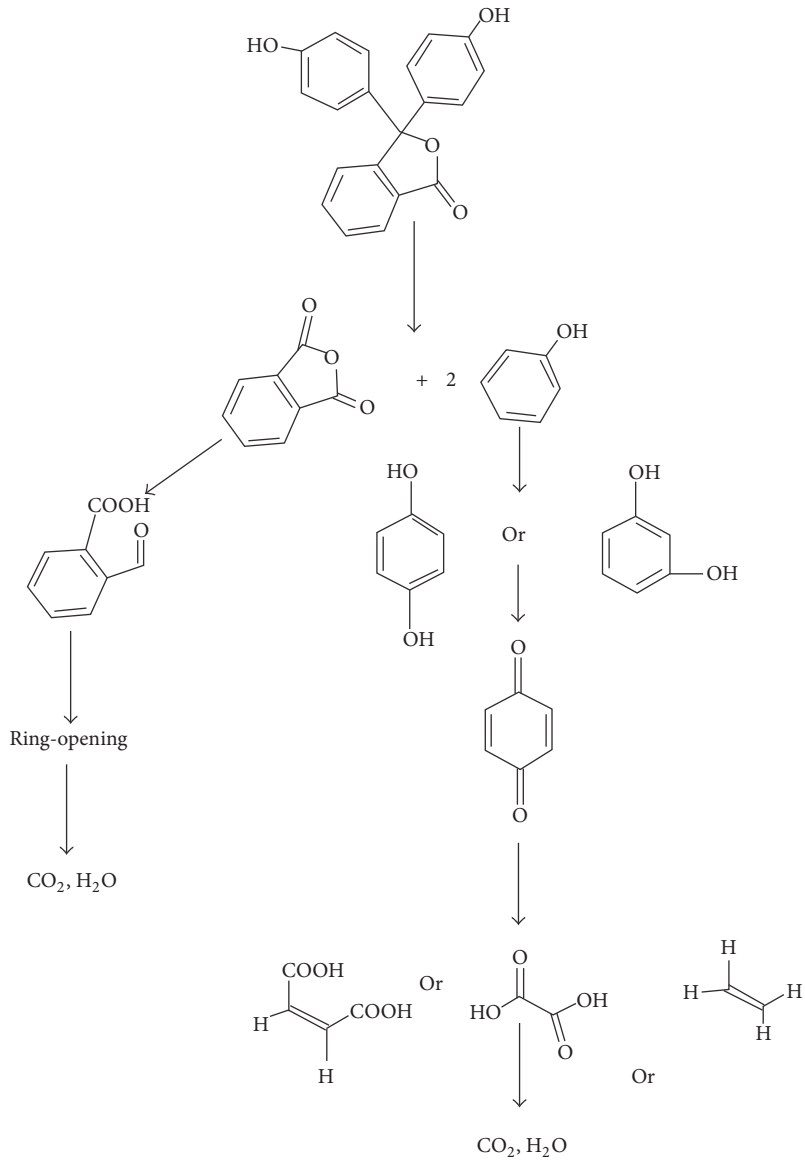

Figure 8: Proposed mechanism for the PHPH mineralization.

radicals using ozone involves more reactions and the mass transfer involves two phases: the gas and liquid.

Competing Interests

The authors declare that they have no competing interests.

Acknowledgments

The authors wish to acknowledge financial support from the CONACYT through the Project 153898, which is greatly appreciated.

References

[1] R. Mahanta, J. Chowdhury, and H. K. Nath, "Health costs of arsenic contamination of drinking water in Assam, India," *Economic Analysis and Policy*, vol. 49, pp. 30–42, 2016.

[2] A. Rasekh and K. Brumbelow, "A dynamic simulation-optimization model for adaptive management of urban water distribution system contamination threats," *Applied Soft Computing Journal*, vol. 32, pp. 59–71, 2015.

[3] B. Muchara, G. Ortmann, M. Mudhara, and E. Wale, "Irrigation water value for potato farmers in the Mooi River Irrigation Scheme of KwaZulu-Natal, South Africa: a residual value approach," *Agricultural Water Management*, vol. 164, pp. 243–252, 2014.

[4] S. CTR, "Hoja De Datos De Seguridad Iloxan®," 2014, http://www.ctr.com.mx/pdfcert/Fenolftaleina.pdf.

[5] B. J. F. MacFaddin, *Pruebas Bioquímicas para la Identificación de Bacterias de Importancia Clínica*, Edited by Tercera, Médica Panamericana S.A, Argentina, 2003.

[6] L. Liu, Y. Wang, D. Fan, and Y. Mi, "Using phenolphthalein as a promising indicator to monitor the vacuum freeze-drying process," *Materials Letters*, vol. 139, pp. 245–248, 2015.

[7] S. Saeidnia and A. Manayi, "Phenolphthalein," *Encyclopedia of Toxicology*, vol. 3, pp. 877–880, 2014.

[8] G. Y. Çiftçi, M. Durmuş, E. Şenkuytu, and A. Kiliç, "Structural and fluorescence properties of phenolphthalein bridged cyclotriphosphazatrienes," *Spectrochimica Acta Part A: Molecular and Biomolecular Spectroscopy*, vol. 74, no. 4, pp. 881–886, 2009.

[9] IARC, *Monograohs on the Evaluacion of Carcinogecic Risks to Humans. Carcinogenic Risks to Humans*, vol. 76, International Agency for Research on Cancer, World Health Organization, 2000, http://monographs.iarc.fr/ENG/Monographs/vol76/mono76-15.pdf.

[10] P. F. Coogan, L. Rosenberg, J. R. Palmer et al., "Phenolphthalein laxatives and risk of cancer," *Journal of the National Cancer Institute*, vol. 92, no. 23, pp. 1943–1944, 2000.

[11] G. S. Cooper, M. P. Longnecker, D. P. Sandler, and R. B. Ness, "Risk of ovarian cancer in relation to use of phenolphthalein-containing laxatives," *British Journal of Cancer*, vol. 83, no. 3, pp. 404–406, 2000.

[12] J. R. Bucher, "Toxicology and carcinogenesis studies of in F344/N rats and B6C3Fl mice (drinking water studies)," *National Toxicology Program*, no. 393, 1990.

[13] J. Brame, M. Long, Q. Li, and P. Alvarez, "Inhibitory effect of natural organic matter or other background constituents on photocatalytic advanced oxidation processes: mechanistic model development and validation," *Water Research*, vol. 84, pp. 362–371, 2015.

[14] M. Cheng, G. Zeng, D. Huang et al., "Hydroxyl radicals based advanced oxidation processes (AOPs) for remediation of soils contaminated with organic compounds: a review," *Chemical Engineering Journal*, vol. 284, pp. 582–598, 2016.

[15] S. O. Ganiyu, E. D. van Hullebusch, M. Cretin, G. Esposito, and M. A. Oturan, "Coupling of membrane filtration and advanced oxidation processes for removal of pharmaceutical residues: a critical review," *Separation and Purification Technology*, vol. 156, pp. 891–914, 2015.

[16] H. Suzuki, S. Araki, and H. Yamamoto, "Evaluation of advanced oxidation processes (AOP) using O_3, UV, and TiO_2 for the degradation of phenol in water," *Journal of Water Process Engineering*, vol. 7, pp. 54–60, 2015.

[17] K. Ayoub, E. D. van Hullebusch, M. Cassir, and A. Bermond, "Application of advanced oxidation processes for TNT removal: a review," *Journal of Hazardous Materials*, vol. 178, no. 1–3, pp. 10–28, 2010.

[18] A. R. Ribeiro, O. C. Nunes, M. F. R. Pereira, and A. M. T. Silva, "An overview on the advanced oxidation processes applied for the treatment of water pollutants defined in the recently launched directive 2013/39/EU," *Environment International*, vol. 75, pp. 33–51, 2015.

[19] L. Hurtado, R. Natividad, E. Torres-García, J. Farias, and G. Li Puma, "Correlating the photocatalytic activity and the optical properties of LiVMoO6 photocatalyst under the UV and the visible region of the solar radiation spectrum," *Chemical Engineering Journal*, vol. 262, pp. 1284–1291, 2015.

[20] P. Aravind, V. Subramanyan, S. Ferro, and R. Gopalakrishnan, "Eco-friendly and facile integrated biological-cum-photo assisted electrooxidation process for degradation of textile wastewater," *Water Research*, vol. 93, pp. 230–241, 2016.

[21] S. Ellouze, M. Panizza, A. Barbucci, G. Cerisola, T. Mhiri, and S. C. Elaoud, "Ferulic acid treatment by electrochemical oxidation using a BDD anode," *Journal of the Taiwan Institute of Chemical Engineers*, vol. 59, pp. 132–137, 2016.

[22] N. Abdessamad, H. Akrout, G. Hamdaoui, K. Elghniji, M. Ksibi, and L. Bousselmi, "Evaluation of the efficiency of monopolar and bipolar BDD electrodes for electrochemical oxidation of anthraquinone textile synthetic effluent for reuse," *Chemosphere*, vol. 93, no. 7, pp. 1309–1316, 2013.

[23] A. J. C. da Silva, E. V. dos Santos, C. C. de Oliveira Morais, C. A. Martínez-Huitle, and S. S. L. Castro, "Electrochemical treatment of fresh, brine and saline produced water generated by petrochemical industry using Ti/IrO2-Ta2O5 and BDD in flow reactor," *Chemical Engineering Journal*, vol. 233, pp. 47–55, 2013.

[24] S. Islam, N. Bidin, S. Riaz, and S. Naseem, "Sol-gel based phenolphthalein encapsulated heterogeneous silica-titania optochemical pH nanosensor," *Journal of Industrial and Engineering Chemistry*, vol. 34, pp. 258–268, 2016.

[25] A. V. Kachur, A. A. Popov, E. J. Delikatny, J. S. Karp, and A. V. Popov, "Synthesis of ^{18}F-labeled phenolphthalein and naphtholphthalein," *Journal of Fluorine Chemistry*, vol. 151, pp. 1–6, 2013.

[26] A. Thiam, I. Sirés, J. A. Garrido, R. M. Rodríguez, and E. Brillas, "Effect of anions on electrochemical degradation of azo dye Carmoisine (Acid Red 14) using a BDD anode and air-diffusion cathode," *Separation and Purification Technology*, vol. 140, pp. 43–52, 2015.

[27] C. Comninellis, *Electrochemistry for the Environment*, Primera, New York, NY, USA, Guohua Chen, Springer, London, USA, 2010.

[28] S. Garcia-Segura, Á. S. Lima, E. B. Cavalcanti, and E. Brillas, "Anodic oxidation, electro-Fenton and photoelectro-Fenton degradations of pyridinium- and imidazolium-based ionic liquids in waters using a BDD/air-diffusion cell," *Electrochimica Acta*, vol. 198, pp. 268–279, 2016.

[29] H. T. Madsen, E. G. Søgaard, and J. Muff, "Study of degradation intermediates formed during electrochemical oxidation of pesticide residue 2,6-dichlorobenzamide (BAM) at boron doped diamond (BDD) and platinum-iridium anodes," *Chemosphere*, vol. 109, pp. 84–91, 2014.

[30] I. Sirés, E. Brillas, G. Cerisola, and M. Panizza, "Comparative depollution of mecoprop aqueous solutions by electrochemical incineration using BDD and PbO_2 as high oxidation power anodes," *Journal of Electroanalytical Chemistry*, vol. 613, no. 2, pp. 151–159, 2008.

[31] C. Zhang, Y. Jiang, Y. Li, Z. Hu, L. Zhou, and M. Zhou, "Three-dimensional electrochemical process for wastewater treatment: a general review," *Chemical Engineering Journal*, vol. 228, pp. 455–467, 2013.

[32] M. A. García-Morales, G. Roa-Morales, C. Barrera-Díaz, B. Bilyeu, and M. A. Rodrigo, "Synergy of electrochemical oxidation using boron-doped diamond (BDD) electrodes and ozone (O_3) in industrial wastewater treatment," *Electrochemistry Communications*, vol. 27, pp. 34–37, 2013.

[33] S. A. Alves, T. C. R. Ferreira, N. S. Sabatini et al., "A comparative study of the electrochemical oxidation of the herbicide tebuthiuron using boron-doped diamond electrodes," *Chemosphere*, vol. 88, no. 2, pp. 155–160, 2012.

[34] I. Linares-Hernández, C. Barrera-Díaz, B. Bilyeu, P. Juárez-GarcíaRojas, and E. Campos-Medina, "A combined electrocoagulation-electrooxidation treatment for industrial wastewater," *Journal of Hazardous Materials*, vol. 175, no. 1–3, pp. 688–694, 2010.

[35] L. Yan, Y. Wang, J. Li et al., "Comparative study of different electrochemical methods for petroleum refinery wastewater treatment," *Desalination*, vol. 341, no. 1, pp. 87–93, 2014.

[36] G. B. Raju, M. T. Karuppiah, S. S. Latha, S. Parvathy, and S. Prabhakar, "Treatment of wastewater from synthetic textile industry by electrocoagulation-electrooxidation," *Chemical Engineering Journal*, vol. 144, no. 1, pp. 51–58, 2008.

[37] C.-W. Kan, H.-F. Cheung, and Q. Chan, "A study of plasma-induced ozone treatment on the colour fading of dyed cotton," *Journal of Cleaner Production*, vol. 112, pp. 3514–3524, 2016.

[38] S. Khuntia, S. K. Majumder, and P. Ghosh, "Quantitative prediction of generation of hydroxyl radicals from ozone microbubbles," *Chemical Engineering Research and Design*, vol. 98, pp. 231–239, 2015.

[39] G. Chen, "Electrochemical technologies in wastewater treatment," *Separation and Purification Technology*, vol. 38, no. 1, pp. 11–41, 2004.

[40] W. Hanni, A. Perret, M. Blaschke et al., "Electrochemical advanced oxidation process for water treatment using DiaChem® electrodes," *Diamond and Related Materials*, vol. 11, no. 3-6, pp. 640–645, 2002.

[41] M. A. Alsheyab and A. H. Muñoz, "Reducing the formation of trihalomethanes (THMs) by ozone combined with hydrogen peroxide (H_2O_2/O_3)," *Desalination*, vol. 194, no. 1–3, pp. 121–126, 2006.

[42] W. T. M. Audenaert, D. Vandierendonck, S. W. H. Van Hulle, and I. Nopens, "Comparison of ozone and $HO^{\bullet}$ radical dot induced conversion of effluent organic matter (EfOM) using ozonation and UV/H_2O_2 treatment," *Water Research*, vol. 47, no. 7, pp. 2387–2398, 2013.

[43] Z. Chen, J. Fang, C. Fan, and C. Shang, "Oxidative degradation of N-Nitrosopyrrolidine by the ozone/UV process: kinetics and pathways," *Chemosphere*, vol. 150, pp. 731–739, 2016.

[44] H.-W. Chen, Y.-L. Kuo, C.-S. Chiou, S.-W. You, C.-M. Ma, and C.-T. Chang, "Mineralization of reactive Black 5 in aqueous solution by ozone/H_2O_2 in the presence of a magnetic catalyst," *Journal of Hazardous Materials*, vol. 174, no. 1–3, pp. 795–800, 2010.

Hindawi Publishing Corporation
Journal of Chemistry
Volume 2016, Article ID 8782469, 7 pages
http://dx.doi.org/10.1155/2016/8782469

Research Article

Adsorption of Lead Ions from Aqueous Solutions Using Gamma Irradiated Minerals

Julián Cruz-Olivares,[1] Gonzalo Martínez-Barrera,[2] César Pérez-Alonso,[1] Carlos Eduardo Barrera-Díaz,[1] María del Carmen Chaparro-Mercado,[3] and Fernando Ureña-Núñez[4]

[1] *Facultad de Química, Universidad Autónoma del Estado de México, Paseo Colón Intersección Paseo Tollocan S/N, 50120 Toluca, MEX, Mexico*
[2] *Laboratorio de Investigación y Desarrollo de Materiales Avanzados (LIDMA), Facultad de Química, Universidad Autónoma del Estado de México, Km. 12 de la Carretera Toluca-Atlacomulco, 50200 San Cayetano, MEX, Mexico*
[3] *Departamento de Ingeniería y Ciencias Químicas, Universidad Iberoamericana, Prol. Paseo de la Reforma 880, Lomas de Santa Fe, Álvaro Obregón, 01210 Ciudad de México, Mexico*
[4] *Instituto Nacional de Investigaciones Nucleares, AP 18-1027, Col. Escandón, Delegación Miguel Hidalgo, 11801 Ciudad de México, Mexico*

Correspondence should be addressed to Julián Cruz-Olivares; jcruzo@uaemex.mx

Received 5 July 2016; Revised 7 September 2016; Accepted 20 October 2016

Academic Editor: Julie J. M. Mesa

For the first time, an irradiated mineral was used as a novel modified adsorbent for lead removal of aqueous solutions. The effects of gamma radiation doses and temperature on the lead adsorption capacity of an unknown mineral were evaluated. The results show that, in the chemisorption process, the highest adsorption capacity (9.91 mg/g) and the maximum percentage of lead removal (99.1%) were reached at 40°C when using an irradiated mineral at 150 kGy. The improvement on the lead adsorption speed was the most important feature of the irradiated mineral. The experimental results were successfully correlated with the pseudo second-order kinetic model. For all results, the average absolute relative deviations (AARD) were less than 13.20%, and the correlation factor (r^2) was higher than 0.998. Moreover, the average values of the thermodynamic parameters ($\Delta G_0 = -10612$ J/mol, $\Delta H_0 = -12360$ J/mol, and $\Delta S_0 = 171$ J/mol K) suggest the feasibility of the proposed process, in terms of the endothermic and irreversible chemisorption results; moreover, ion exchange was evaluated through the EDS results. The X-ray diffraction analysis showed that the unknown irradiated mineral is mainly composed of quartz (SiO_2), calcite ($CaCO_3$), and calcium magnesium silicate ($Ca_{0.15}Mg_{0.85}$) Mg (SiO_6).

1. Introduction

Despite the strict regulations on environmental issues imposed in many countries [1, 2], today, it is still possible to find some heavy metal ions in the wastewater because of industrial processes. However, true environmental damage may occur when such polluted water is unconsciously discharged into natural water flows. Not only aquatic animals and plants but also the human health is at risk [3–5]. Lead is one of the most dangerous metals for the human health, especially for children because their growing bodies can absorb a higher quantity than adults [6–8]. Although lead is prohibited in many products, it is still used in commercial products as automotive batteries, paints, cookware, and some Mexican potter glazes [9, 10]. At low concentrations of lead ions in the blood, some not dangerous diseases such as anemia, diarrhea, and headaches are observed, but, at a higher concentration (>10 μg/L), the liver, kidney, and neurological and reproductive systems can be severely affected [11, 12].

Many treatments for wastewater polluted with lead ions have been proposed, including an adsorption process which

does not have high effectiveness, unless the adsorbent material shows certain physicochemical and mechanical properties. In recent years, some physical, chemical, and biological treatments on natural raw minerals have been done in order to modify their structure, thus increasing the adsorption capacity or the selectivity [13, 14].

In this tenor, many works have been published; for example, the chemical surface modification of mesoporous silica with a tertiary aminosilane using supercritical carbon dioxide showed that the structural ordering of silica was preserved, but the grafting density increased, and the specific surface area and the average pore diameter decreased in the modified adsorbent material [15]. Specifically, for lead adsorption, a chemically modified adsorbent nanoparticle based on the treated low-value agricultural byproduct rice husk was used and it is reported that a maximum lead adsorption capacity of 93.45 mg/g was achieved [16]. Even the biological modification for mineral adsorbents has been done; such is the case of the functionalized cells with intracellular $CaCO_3$ mineral scaffolds in order to remove Pb(II) from the aqueous solution. The biosorption capacity of functionalized cells for Pb(II) was found to be 116.69 mg/g; compared with the pristine yeast cell, the adsorption capacity of the functionalized cells for metals ions was markedly increased [17].

Thermal treatments to obtain spherical mesoporous silica materials by pseudomorphic transformation of silica fume were used too; this modified adsorbent was employed as an effective adsorbent for removing Pb^{2+} and its capacity demonstrated great improvement [18].

A novel magnetic composite bioadsorbent, graphene oxide and magnetic chitosan-ionic liquids, for removing Pb(II) from water was developed. The mixture of ionic liquids and graphene oxide and magnetic chitosan resulted in a material to be applied in the adsorption of metal ions. The addition of ionic liquids can not only improve the dispersion of the adsorbent, but also increase the adsorption sites [19].

There is a reported study where gamma radiation was utilized to synthesize a modified adsorbent of chitosan grafted with acrylic acid. Grafting degree was evaluated as a function of a radiation dose, and the removal of Pb and Cd ions from aqueous solutions was investigated with both ungrafted and grafted chitosan adsorbents [20]. Gamma radiation was also used as a technique for inducing polymerization in the synthesis of some materials utilized in the removal of heavy metals from wastewater [13, 21].

Gamma radiation is a current tool that is used as a decontamination or sterilization process, as well as for modification of the physicochemical properties of materials. In this work, gamma radiation is used for the modification of physicochemical properties of a natural mineral and for improving its adsorption capacity for removing lead ions from industrial wastewater. The main novel aspects in the present work are the validation of the mechanism of the kinetic adsorption process and application of gamma irradiation as a technique to improve the lead adsorption capacity of a mineral.

2. Materials and Methods

2.1. Mineral. The natural mineral (from mines located in Oaxaca, Mexico) was provided by Lumogral S.A. de C.V. Enterprise (Iztapalapa, Mexico City), which has a particle size of 0.149 mm on average (100 Tyler mesh size).

2.2. Lead Adsorption Experiments. Aqueous solutions with 100 mg/L lead concentration were prepared by dissolving dried salt (159.8 mg) of lead nitrate $[Pb(NO_3)_2]$ in distilled water (1 L). Then, in 100 mL of such solution, 1.0 g of nonirradiated or irradiated mineral was added. These heterogeneous mixtures were heated at constant temperature (20, 30, and 40°C) and stirred with a shaker at 200 rpm (Lab-Line Incubator-Shaker, USA). Finally, separation of solid adsorbents was obtained by a filtration process, at different contact times (1, 15, 30, 60, 120, 180, 240, and 300 min).

2.3. Gamma Irradiation Treatment. The mineral was exposed at different gamma radiation doses using a ^{60}Co source. In this case, the mineral was placed into glass flasks and the applied doses were 10, 50, 100, and 150 kGy at the dose rate of 3.5 kGy/h. The experiments were performed in air at room temperature by using a Transelektro irradiator LGI-01 manufactured by IZOTOP Institute of Isotopes Co. Ltd., Budapest, Hungary, and located at the National Institute of Nuclear Research (ININ, Mexico).

2.4. Characterization of the Absorbent Material. The adsorbent material was dried and its morphological surface was characterized by using a scanning electron microscope (JEOL model JSM-6510LV) coupled with an energy dispersive X-ray probe (EDAX) for semiquantitative elemental analysis. The metal concentrations in the liquid solutions were analyzed by using Atomic Absorption Spectrophotometer (Perkin-Elmer model AA300), according to the standard method for lead detection [22].

Mineral samples were also characterized by X-ray diffraction (XRD), before and after irradiation. The analyses were carried out in a Siemens D5000 diffractometer with Cu Kα radiation. Data were collected in the radiation angle range from 2θ of 5° to 2θ of 75°.

3. Results and Discussion

Chemical composition of nonirradiated and irradiated minerals is shown in Table 1. As in many natural minerals, the most abundant component is oxygen followed by silicon and calcium. The received energy by the mineral after irradiation only modified its ratio of each chemical element. For instance, in the irradiated mineral at 10 kGy, concentrations of four of the seven chemical components decreased, when compared with nonirradiated mineral. To compensate it, the concentration of the others increased in the same ratio, such that the final concentration is always 100%. Therefore, each chemical element shows slight variation in the weight percentage after the irradiation process. As it is known, interactions of gamma irradiation with matter may cause different effects; one of them is breaking of chemical bonds, which may be combined and allow the formation of other chemical species. Another effect is the cross-linking of chemical bonds that cause changes in the morphology of matter [21, 23].

Table 1: EDS analysis of nonirradiated and irradiated minerals.

Element	Weight (%)				
	Nonirradiated	10 kGy	50 kGy	100 kGy	150 kGy
O	58.22	54.05	59.59	52.10	53.07
Mg	2.16	1.09	0.88	0.87	0.86
Al	2.22	2.90	2.63	2.13	2.17
Si	18.93	24.02	19.67	14.45	10.63
K	1.53	1.44	1.71	1.03	1.24
Ca	13.75	14.79	14.52	28.55	31.38
Fe	3.19	1.71	1.00	0.87	0.65
Total	100	100	100	100	100

Table 2: Diffraction peaks of each compound.

Compound	Diffraction peak (2θ)						
Quartz ◆	21.0	26.8	50.1				
Calcite ●	23.1	29.5	36.2	39.4	43.3	47.5	48.6
Calcium magnesium silicate ▼	26.8	27.9	30.9	35.0	42.3		

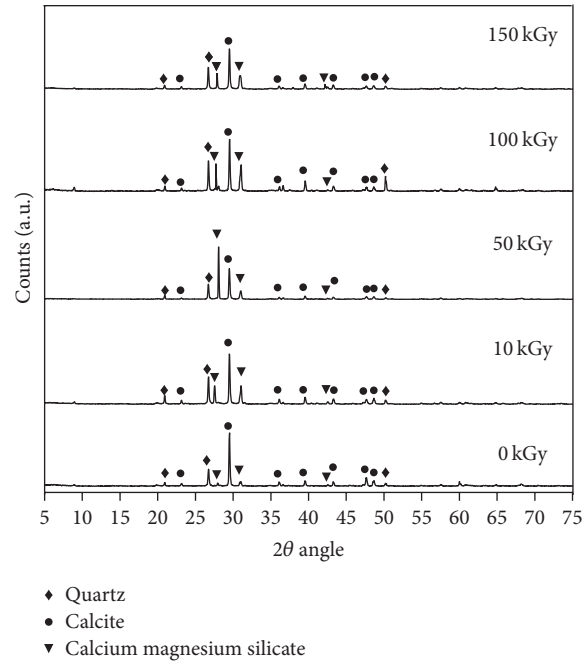

Figure 1: X-ray diffraction spectrum of nonirradiated and irradiated minerals.

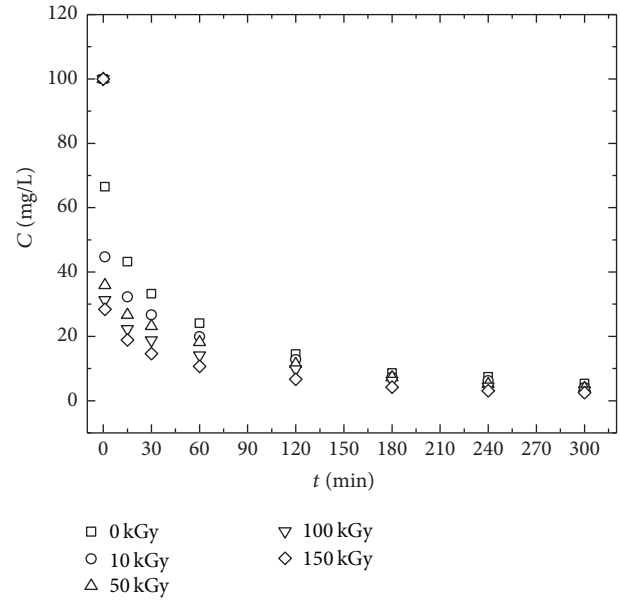

Figure 2: Kinetics of the lead adsorption process for nonirradiated and irradiated minerals (C_0 = 100 mg/L, T = 20°C, w = 1 g, and V = 0.1 L).

According to the literature, Si/Al ratio is an important parameter in such minerals [24, 25]. In this case, as it can be seen in the results of Table 1, for nonirradiated mineral, a value of 8.5 is obtained, with the lowest value of 4.9 for irradiated material at 150 kGy. Diminution of the Si/Al ratio is due to gamma irradiation; this result provides guidelines for future research as acid catalyst. It is observed that as the Si/Al ratio decreases, acidity increases [26, 27].

Chemical elements are part of three main compounds: quartz, calcite, and calcium magnesium silicate, as it is shown in the diffraction pattern of the nonirradiated and irradiated minerals (Figure 1). Diffraction peaks of each compound are summarized in Table 2. Moreover, calcium magnesium silicate compound gives the mineral interesting features as adsorbent material.

As it can be seen, at doses of 100 and 150 kGy, the most stable phase represented by the calcium magnesium silicate is highlighted, and probably at these highest radiation doses the porosity of the material was increased. So, it is inferred that the highest adsorption capacity is due to the highest radiation dose.

In Figure 2, the lead concentration in the aqueous solution versus time is shown. The values of the removal of lead are shown in Table 3. Such values are obtained by mass balance between the initial lead in the solution (C_0 = 100 mg/L) and the lead concentration at any time.

Faster lead adsorption on irradiated mineral was observed with respect to the nonirradiated one. The highest adsorption values were obtained for higher doses (150 kGy) with time less than 60 minutes. Moreover, according to the removal rate and adsorption capacity results, the highest adsorbent properties are developed for irradiated mineral at 150 kGy.

As it is observed in Table 3, during the first 15 minutes of contact, the adsorption rate is high, due to the high gradient of the lead concentration between the liquid and the adsorbent surface; this is a common behavior in the mass transfer phenomena as ion exchange and chemisorption processes. Moreover, 80% of lead is adsorbed for different combinations of contact time and irradiation dose: (a) 30 minutes and 100 kGy or (b) 60 minutes and 10 kGy. Thus, diminution of the irradiation dose requires more contact time. At the highest contact time (300 minutes), where the state of equilibrium

Table 3: Lead removal percentage of nonirradiated and irradiated minerals (C_0 = 100 mg/L, T = 20°C, w = 1 g, and V = 0.1 L).

t (min)	Lead removal (%)				
	Nonirradiated	10 kGy	50 kGy	100 kGy	150 kGy
1	33.5	55.3	64.1	68.7	71.6
15	56.8	67.7	73.3	77.7	81.1
30	66.8	73.3	76.8	81.2	85.4
60	75.9	80.1	81.8	85.9	89.3
120	85.5	87.2	88.6	90.2	93.3
180	91.4	92.7	92.7	93.8	95.8
240	92.6	93.8	94.8	95.6	96.9
300	94.7	95.9	96.1	96.8	97.5

happens, the adsorption capacity values are almost constant for nonirradiated and irradiated minerals, with only 3% difference between them. A similar behavior was observed for the other temperatures.

The experimental adsorption capacity was evaluated with the following equation:

$$q = \frac{(C_0 - C)V}{w}, \tag{1}$$

where q is the adsorption capacity (mg/g), C_0 is the initial lead concentration (mg/L), C is lead concentration of the filtered solution at any time (mg/L), V is sample volume (L), and w is adsorbent mass (g).

As it is known, kinetics of the adsorption process are related to the rate at which the adsorbent material retains a certain quantity of lead. By experimental data of the concentration and contact time, elucidation of the adsorption mechanism was done.

In the case of the adsorption of lead ions on nonirradiated and irradiated minerals, it was assumed that the adsorption rate is proportional to the square of the number of linking atoms. A lead ion [Pb^{2+}] present in the aqueous solution would be interacting with 2 oxygen atoms [-O-] in the chemical structure of the mineral surface [28]. Similar results have been found in other systems [3, 4].

According to the chemical equation

$$\left[Pb^{2+}\right] + 2\left[O^{2-}\right] \longrightarrow [\text{O-Pb-O}]^{\neq} \tag{2}$$

the kinetic equation is

$$\frac{dq}{dt} = k\left[Pb^{2+}\right]\left[O^{2-}\right]^2, \tag{3}$$

where

$$k\left[Pb^{2+}\right] = k_2$$
$$\left[O^{2-}\right] = (q_e - q)^2. \tag{4}$$

Then, the kinetic equation can be written as

$$\frac{dq}{dt} = k_2 (q_e - q)^2, \tag{5}$$

where q is the adsorption capacity (mg/g), q_e is the adsorption capacity at equilibrium (mg/g), and k_2 is the kinetic constant of the pseudo second order.

The differential equation is written in an integrated form:

$$\frac{t}{q} = \frac{1}{q_e}t + \frac{1}{k_2 q_e^2}. \tag{6}$$

The experimental results of the adsorption capacity were adjusted with (6), in order to obtain q_e and k_2 parameters; later, the calculated adsorption capacity was estimated and the results are shown in Tables 4 and 5. The comparison between experimental and calculated adsorption capacities was made considering the average absolute relative deviations (AARD), which were determined by

$$\text{AARD} = \frac{1}{n}\sum \frac{\left|q^{\text{cal}} - q^{\text{exp}}\right|}{q^{\text{exp}}}, \tag{7}$$

where n is the number of data, q^{exp} is the experimental adsorption capacity obtained with (1), and q^{cal} is the calculated adsorption capacity through (6).

According to the AARD and r^2 results shown in Tables 4 and 5, the pseudo second-order kinetic model represents satisfactorily the adsorption capacity process of lead ions on nonirradiated and irradiated mineral, regardless of the irradiation dose or temperature. The AARD values were lower than 14%, and r^2 was higher than 0.998.

Determination of the main thermodynamic parameters of the adsorption process allows knowing the feasibility of the separation process as well as deciding whether it is controlled by physisorption or chemisorption. Such parameters include free energy (ΔG_0), enthalpy (ΔH_0), and entropy (ΔS_0), which are evaluated by using the equilibrium constant (K_{eq}) value, as follows:

$$K_{\text{eq}} = \frac{C_{\text{ads}}}{C_t}, \tag{8}$$

where C_{ads} is the concentration of adsorbed lead by the mineral and C_t is the concentration of lead in the supernatant solution.

The relation between K_{eq} and the free energy is given by

$$\Delta G_0 = -RT \ln K_{\text{eq}}, \tag{9}$$

where T (K) is the absolute temperature and R is the universal gas constant.

The dependence of K_{eq} on the temperature is expressed by

$$\ln K_{\text{eq}} = \frac{\Delta H_0}{R}\left(\frac{1}{T}\right) + \frac{\Delta S_0}{R}. \tag{10}$$

Since (10) represents a straight line, plotting $\ln K_{\text{eq}}$ versus $(1/T)$, it is possible to obtain both ΔH_0 and ΔS_0 from the slope and intercept, respectively.

Although the adsorption process is a natural phenomenon, in order to get the highest adsorption capacity, it is necessary to work at higher temperatures. In this case,

Table 4: Experimental and calculated lead adsorption capacity of nonirradiated and irradiated minerals (C_0 = 100 mg/L, T = 20°C, w = 1 g, and V = 0.1 L).

t (min)	Adsorption capacity (mg/g)									
	Nonirradiated		10 kGy		50 kGy		100 kGy		150 kGy	
	Exp.	Cal.	Exp.	Cal.	Exp.	Cal.	Exp.	Cal.	Exp.	Cal.
1	3.35	0.80	5.53	1.06	6.41	1.24	6.87	1.55	7.16	2.03
15	5.68	5.56	6.77	6.29	7.33	6.68	7.77	7.21	8.11	7.82
30	6.68	7.07	7.33	7.64	7.68	7.92	8.12	8.29	8.54	8.71
60	7.59	8.18	8.01	8.56	8.18	8.73	8.59	8.97	8.93	9.23
120	8.55	8.88	8.72	9.10	8.86	9.20	9.02	9.34	9.33	9.52
180	9.14	9.14	9.27	9.30	9.27	9.36	9.38	9.48	9.58	9.62
240	9.26	9.28	9.38	9.40	9.48	9.45	9.56	9.55	9.69	9.67
300	9.47	9.36	9.59	9.46	9.61	9.50	9.68	9.59	9.75	9.70
AARD (%)	12.15		13.13		13.19		12.11		10.46	
r^2	0.9981		0.9985		0.9988		0.9992		0.9997	

Table 5: Experimental and calculated lead adsorption capacity of irradiated mineral at different temperatures (150 kGy, C_0 = 100 mg/L, w = 1 g, and V = 0.1 L).

t (min)	Adsorption capacity (mg/g)					
	20°C		30°C		40°C	
	Exp.	Cal.	Exp.	Cal.	Exp.	Cal.
1	7.16	2.03	7.46	2.27	7.73	2.81
15	8.11	7.82	8.39	8.09	8.67	8.51
30	8.54	8.71	8.74	8.9	9.04	9.17
60	8.93	9.23	9.15	9.38	9.37	9.55
120	9.33	9.52	9.47	9.63	9.66	9.74
180	9.58	9.62	9.63	9.72	9.74	9.81
240	9.69	9.67	9.78	9.76	9.86	9.85
300	9.75	9.7	9.85	9.79	9.91	9.87
AARD (%)	10.46		10.11		8.89	
r^2	0.9997		0.9997		0.9989	

Table 6: Thermodynamic parameters of the lead adsorption process (150 kGy, C_0 = 100 mg/L, w = 1 g, and V = 0.1 L).

ΔG_0 (J/mol)			ΔH_0 (J/mol)	ΔS_0 (J/mol K)
20°C	30°C	40°C	41326.4	171.3
−8929.0	−10546.8	−12359.8		

the higher the temperature, the greater the spontaneity, as an endothermic process (Table 6). Furthermore, a higher value of ΔH_0 suggests a chemisorption mechanism for the process. According to the results, it is possible to establish a set of process variables and the conditions to scale up the process to an industrial wastewater treatment plant.

According to the EDS results, a great capacity to adsorb lead ions is observed in Table 1. The ion interchange is present; the Mg and Fe ions were substituted by Pb ions as it is shown in Table 7 by comparing with the results shown in Table 1.

Morphological changes are observed in nonirradiated and irradiated minerals after the lead adsorption process, as it is shown in Figure 3. At higher radiation doses (50, 100, and 150 kGy), the porosity of this material increased because the size of the particle decreased drastically; this is most evident at 150 kGy which corresponds to the XRD results. On the other hand, as mentioned earlier, one of the effects of gamma irradiation is the cross-linking of chemical bonds, which produces morphological changes, with an increment on the porosity between them.

Table 7: EDS analysis of nonirradiated and irradiated minerals after the lead adsorption process.

Element	Weight (%)	
	Nonirradiated	150 kGy
O	65.56	63.29
Si	25.13	25.72
Al	4.38	4.64
Pb	2.29	3.15
Ca	1.38	1.57
K	1.27	1.62

4. Conclusions

A novel natural mineral adsorbent was obtained, through its structural modification by gamma radiation, in order to increase the adsorption capacity and the percentage of removal of lead from aqueous solutions. The ionizing energy submitted by gamma rays on the mineral allows a high crystallinity degree as well as high chemical stability. The effects of gamma radiation doses and the temperature on the lead adsorption capacity of the mineral were evaluated. The highest adsorption capacity (9.91 mg/g) and the maximum percentage of lead removal (99.1%) were reached at 150 kGy and 40°C, for industrial wastewater with a content of lead of 100 mg/L. The improvement on the lead adsorption speed was the most important feature of the irradiated mineral. The experimental results were successfully correlated with the pseudo second-order kinetic model. In all cases, the average absolute relative deviations (AARD) were lower than 13.20%, and the correlation factor (r^2) was higher than 0.998.

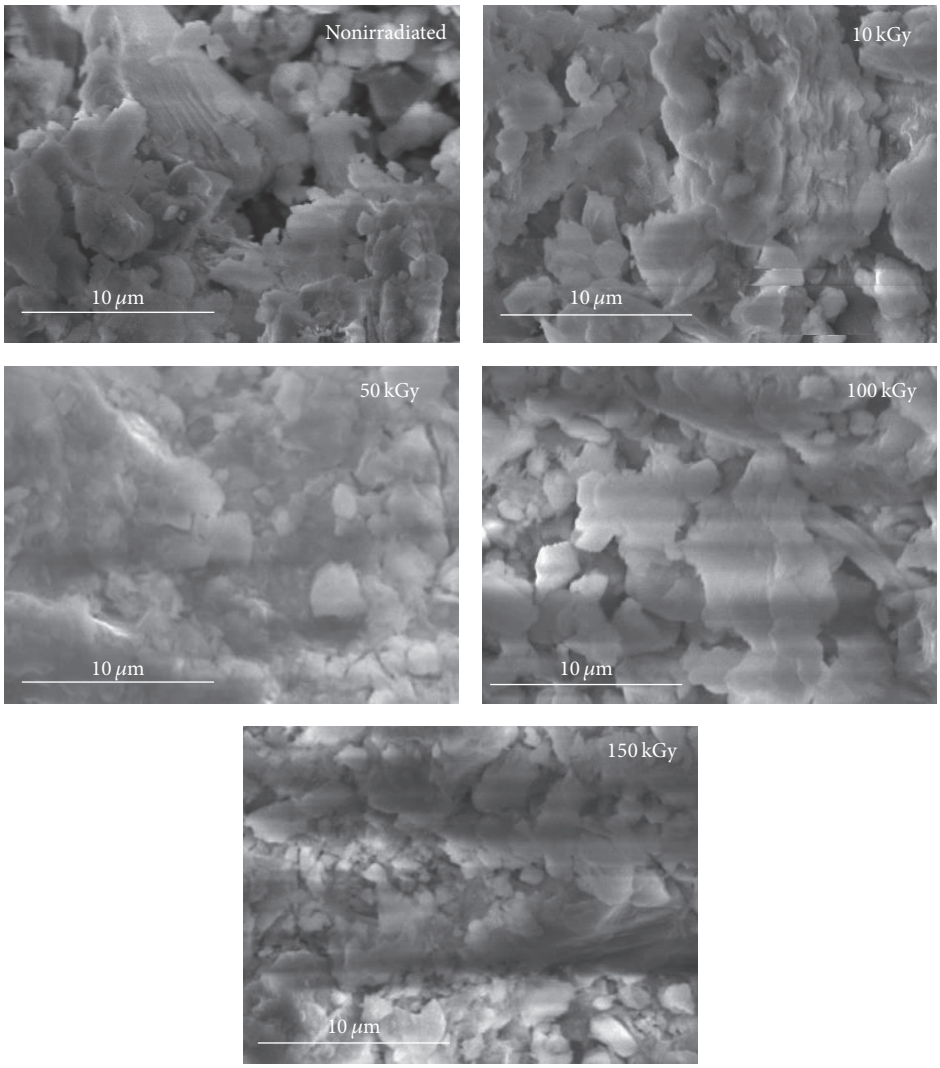

Figure 3: SEM images of nonirradiated and irradiated minerals.

Moreover, the thermodynamic parameters values (ΔG_0, ΔH_0, and ΔS_0) revealed a feasible, endothermic, and irreversible process, where lead ions are mainly chemisorbed or ion-exchanged. The mineral showed specific characteristics: (a) its adsorption capacity is not too high compared with the bioadsorbents, (b) it was insoluble in water, and (c) it had high mechanical strength; thus, the proposed adsorbent can be regenerated and reused, mainly in large-scale processes such as adsorption columns, where large pressure drops are present.

Additional Points

Highlights. More than 95% of lead ions contained in industrial wastewater were removed by using an irradiated mineral. The lead adsorption kinetic process was successfully correlated with the pseudo second-order model. The lead adsorption is a spontaneous and endothermic process that achieved higher adsorption capacity at 40°C. The highest values for lead adsorption capacity were obtained for irradiated mineral at 150 kGy, which were 17.5% higher than that obtained by the nonirradiated one.

Competing Interests

The authors declare that they have no competing interests.

References

[1] E. Cordero Arroyo, F. Arroyo Vieyra, R. A. Diaz Lizama, E. Peña Nieto, and M. A. Osorio Chong, "Ley Federal de Responsabilidad Ambiental," *Diario Oficial de la Federación. México*, vol. 7, article 6, 2013.

[2] M. Greenstone and R. Hanna, "Environmental regulations, air and water pollution, and infant mortality in India," *American Economic Review*, vol. 104, no. 10, pp. 3038–3072, 2014.

[3] S. Demim, N. Drouiche, A. Aouabed, and S. Semsari, "CCD study on the ecophysiological effects of heavy metals on *Lemna gibba*," *Ecological Engineering*, vol. 57, pp. 302–313, 2013.

[4] S. Demim, N. Drouiche, A. Aouabed, T. Benayad, O. Dendene-Badache, and S. Semsari, "Cadmium and nickel: assessment of the physiological effects and heavy metal removal using a response surface approach by *L. gibba*," *Ecological Engineering*, vol. 61, pp. 426–435, 2013.

[5] M. Jaishankar, T. Tseten, N. Anbalagan, B. B. Mathew, and K. N. Beeregowda, "Toxicity, mechanism and health effects of some heavy metals," *Interdisciplinary Toxicology*, vol. 7, no. 2, pp. 60–72, 2014.

[6] R. L. Canfield, C. R. Henderson Jr., D. A. Cory-Slechta, C. Cox, T. A. Jusko, and B. P. Lanphear, "Intellectual impairment in children with blood lead concentrations below 10 μg per deciliter," *The New England Journal of Medicine*, vol. 348, no. 16, pp. 1517–1526, 2003.

[7] A. Chen, K. N. Dietrich, J. H. Ware, J. Radcliffe, and W. J. Rogan, "IQ and blood lead from 2 to 7 years of age: are the effects in older children the residual of high blood lead concentrations in 2-year-olds?" *Environmental Health Perspectives*, vol. 113, no. 5, pp. 597–601, 2005.

[8] S. Wang and J. Zhang, "Blood lead levels in children, China," *Environmental Research*, vol. 101, no. 3, pp. 412–418, 2006.

[9] J. D. Weidenhamer, P. A. Kobunski, G. Kuepouo, R. W. Corbin, and P. Gottesfeld, "Lead exposure from aluminum cookware in Cameroon," *Science of the Total Environment*, vol. 496, pp. 339–347, 2014.

[10] P. Gottesfeld, "Time to ban lead in industrial paints and coatings," *Frontiers in Public Health*, vol. 3, no. 144, pp. 1–4, 2015.

[11] L. Charlet, Y. Chapron, P. Faller, R. Kirsch, A. T. Stone, and P. C. Baveye, "Neurodegenerative diseases and exposure to the environmental metals Mn, Pb, and Hg," *Coordination Chemistry Reviews*, vol. 256, no. 19-20, pp. 2147–2163, 2012.

[12] N. Arancibia-Miranda, S. E. Baltazar, A. García et al., "Nanoscale zero valent supported by Zeolite and Montmorillonite: template effect of the removal of lead ion from an aqueous solution," *Journal of Hazardous Materials*, vol. 301, no. 1, pp. 371–380, 2016.

[13] F. Ureña-Nuñez, C. Barrera-Díaz, and B. Bilyeu, "Gamma radiation-polymerized Zn(II) methacrylate as a sorbent for removal of Pb(II) ions from wastewater," *Industrial and Engineering Chemistry Research*, vol. 46, no. 10, pp. 3382–3389, 2007.

[14] S. Kadouche, H. Lounici, K. Benaoumeur, N. Drouiche, M. Hadioui, and P. Sharrock, "Enhancement of sedimentation velocity of heavy metals loaded hydroxyapatite using chitosan extracted from shrimp waste," *Journal of Polymers and the Environment*, vol. 20, no. 3, pp. 848–857, 2012.

[15] Y. Sánchez-Vicente, C. Pando, M. Cortijo, and A. Cabañas, "Chemical surface modification of mesoporous silica SBA-15 with a tertiary aminosilane using supercritical carbon dioxide," *Microporous and Mesoporous Materials*, vol. 193, pp. 145–153, 2014.

[16] A. Masoumi, K. Hemmati, and M. Ghaemy, "Low-cost nanoparticles sorbent from modified rice husk and a copolymer for efficient removal of Pb(II) and crystal violet from water," *Chemosphere*, vol. 146, no. 2, pp. 253–262, 2016.

[17] X. Ma, W. Cui, L. Yang, Y. Yang, H. Chen, and K. Wang, "Efficient biosorption of lead(II) and cadmium(II) ions from aqueous solutions by functionalized cell with intracellular $CaCO_3$ mineral scaffolds," *Bioresource Technology*, vol. 185, no. 1, pp. 70–78, 2015.

[18] W. Zhu, X. Li, D. Wu et al., "Synthesis of spherical mesoporous silica materials by pseudomorphic transformation of silica fume and its Pb2+ removal properties," *Microporous and Mesoporous Materials*, vol. 222, no. 1, pp. 192–201, 2016.

[19] W. Sun, L. Li, Ch. Luo, and L. Fan, "Synthesis of magnetic graphene nanocomposites decorated with ionic liquids for fast lead ion removal," *International Journal of Biological Macromolecules*, vol. 85, no. 1, pp. 246–251, 2016.

[20] S. Benamer, M. Mahlous, D. Tahtat et al., "Radiation synthesis of chitosan beads grafted with acrylic acid for metal ions sorption," *Radiation Physics and Chemistry*, vol. 80, no. 12, pp. 1391–1397, 2011.

[21] F. Ureña-Nuñez, P. Díaz-Jiménez, C. Barrera-Díaz, M. Romero-Romo, and M. Palomar-Pardavé, "Gamma radiation-induced polymerization of Fe(II) and Fe(III) methacrylates for Cr(VI) removal from wastewater," *Radiation Physics and Chemistry*, vol. 68, no. 5, pp. 819–825, 2003.

[22] APHA, *A.W.W.A. Standard Methods for the Examination of Water and Wastewater*, American Public Health Association, Washington, DC, USA, 19th edition, 1998.

[23] C. Barrera-Díaz, M. Palomar-Pardavé, M. Romero-Romo, and F. Ureña-Nuñez, "Lead removal from wastewater using Cu(II) polymethacrylate formed by gamma radiation," *Journal of Polymer Research*, vol. 12, no. 5, pp. 421–428, 2005.

[24] M. A. Elsheikh, N. Matsue, and T. Henrni, "Effect of Si/AI ratio of allophane on competitive adsorption of phosphate and Oxalate," *International Journal of Soil Science*, vol. 4, no. 1, pp. 1–13, 2009.

[25] S. S. A. Talesh, S. Fatemi, S. J. Hashemi, and M. Ghasemi, "Effect of Si/Al ratio on CO_2–CH_4 adsorption and selectivity in synthesized SAPO-34," *Separation Science and Technology*, vol. 45, no. 9, pp. 1295–1301, 2010.

[26] D. Coster, A. L. Blumenfeld, and J. J. Fripiat, "Lewis acid sites and surface aluminum in aluminas and zeolites: a high-resolution NMR study," *The Journal of Physical Chemistry*, vol. 98, no. 24, pp. 6201–6211, 1994.

[27] J. Huang, Y. Jiang, V. R. R. Marthala, B. Thomas, E. Romanova, and M. Hunger, "Characterization and acidic properties of aluminum-exchanged zeolites X and Y," *The Journal of Physical Chemistry C*, vol. 112, no. 10, pp. 3811–3818, 2008.

[28] J. Cruz-Olivares, C. Pérez-Alonso, C. E. Barrera-Díaz, R. Natividad, and M. C. Chaparro-Mercado, "Thermodynamical and analytical evidence of lead ions chemisorption onto *Pimenta dioica*," *Chemical Engineering Journal*, vol. 166, no. 3, pp. 814–821, 2011.

Hindawi Publishing Corporation
Journal of Chemistry
Volume 2016, Article ID 2746715, 7 pages
http://dx.doi.org/10.1155/2016/2746715

Research Article

Multistage A-O Activated Sludge Process for Paraformaldehyde Wastewater Treatment and Microbial Community Structure Analysis

Danyang Zheng,[1] Yujiao Sun,[1] Huijuan Li,[2] Sidan Lu,[1] Mingjun Shan,[1] and Shangwei Xu[1]

[1]*College of Water Science, Beijing Normal University, Beijing 100875, China*
[2]*Beijing Water Business Doctor CO. Ltd., Beijing 100875, China*

Correspondence should be addressed to Yujiao Sun; sun201405@163.com

Received 21 July 2016; Accepted 9 October 2016

Academic Editor: Reyna Natividad

In recent years, the effect of formaldehyde on microorganisms and body had become a global public health issue. The multistage combination of anaerobic and aerobic process was adopted to treat paraformaldehyde wastewater. Microbial community structure in different reaction stages was analyzed through high-throughput sequencing. Results showed that multistage A-O activated sludge process positively influenced polyformaldehyde wastewater. The removal rates of formaldehyde were basically stable at more than 99% and those of COD were about 89%. Analysis of the microbial diversity index indicated that the microbial diversity of the reactor was high, and the treatment effect was good. Moreover, microbial community had certain similarity in the same system. Microbial communities in different units also showed typical representative characteristics affected by working conditions and influent concentrations. Proteobacteria, Firmicutes, and Bacteroidetes were the dominant fungal genera in the phylum level of community composition. As to family and genus levels, Peptostreptococcaceae was distributed at various stages and the dominant in this system. This bacterium also played an important role in organic matter removal, particularly decomposition of the acidified middle metabolites. In addition, Rhodobacteraceae and Rhodocyclaceae were the formaldehyde-degrading bacteria found in the reactor.

1. Introduction

Formaldehyde is a basic chemical raw material widely used in plastics, chemical, leather, resin, and other production processes. Formaldehyde is soluble in water; the emissions of aqueous solution of this compound can bring serious pollution to water and even kill water creatures. Meanwhile, formaldehyde can produce irritating effect on human body, damage the immune system, and cause cancer. Therefore, China has launched a series of emission regulatory controls for formaldehyde wastewater. For example, the secondary emission standard of formaldehyde must not exceed 2 mg/L in the standard of integrated wastewater discharge, and the formaldehyde content of centralized surface water for domestic and drinking water must not exceed 0.9 mg/L in the standard of surface water environment quality [1, 2]. The large source and quantity of formaldehyde wastewater cause certain difficulties to wastewater treatment. But considering economic or reality reasons, we cannot ban the application of formaldehyde on the whole. Therefore, we need to treat formaldehyde wastewater from industrial production properly. Physical, chemical, and biological methods are mainly used for wastewater treatment. Physical methods include steam blow-off and adsorption. Blowing can be used as a pretreatment process. The effect of formaldehyde wastewater treatment on adsorption is satisfactory but presents limitations in adsorbent recycling. Chemical methods, including advanced oxidation and condensation/precipitation, are expensive. Biological methods are characterized by low cost, simple operation, and low pollution. Most microbes can use formaldehyde as carbon source and degrade wastewater [3]. Hidalgo [4] used *Rhodococcus erythropolis* UPV-1 in formaldehyde wastewater treatment. Both continuous dosing and intermittent dosing can form stable colony. The formaldehyde and chemical oxygen demand (COD) removal rates are 90% and 56%, respectively. Wang et al. [5] used

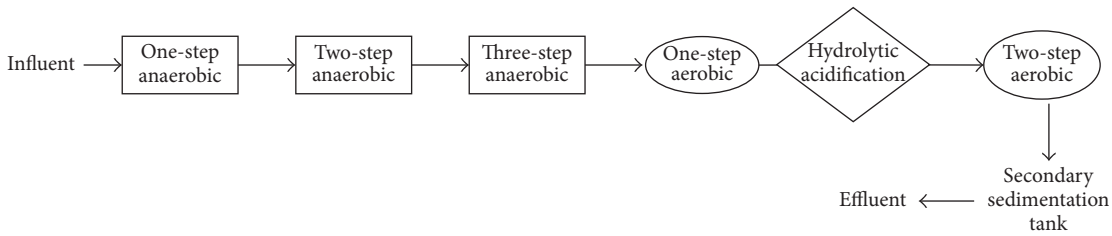

Figure 1: Process flow diagram in the field.

Table 1: Flooding water quality and sludge properties in the field.

Index	HCHO (mg/L)	COD (mg/L)	pH	MLSS (mg/L)	DO (mg/L)	SV_{30} (%)	SVI (mL/g)	SS (mg/L)
Content	650~1200	4000~5800	3.55~3.80	5900~15000	3.40~4.75	90~98	124~683	200~440

activated sludge process in the treatment of formaldehyde wastewater. The results showed that the initial concentration of formaldehyde is 400 mg/L and the sludge concentration is 4 g/L after 10 h; in addition, the removal rates of formaldehyde and COD reach more than 99% and 83%, respectively. *Methylobacillus flagellatus* [6], *Pseudomonas putida* [7], *Ralstonia eutropha* [8], and *Candida maltose* [9] have been reported in formaldehyde degradation. Nevertheless, the degradation effect of these strains shows differences. Most of the strains can only degrade low formaldehyde concentration. Suitable degradation strains should still be determined for high-concentration formaldehyde produced in industrial process. The present study adopted multistage A-O activated sludge process in the treatment of polyformaldehyde wastewater; microbes in the sludge can use formaldehyde as carbon source and degrade wastewater. The process was complex, and the hydraulic retention time was short. This in-depth process can be reproducible in view of high concentration and complex wastewater. We used high-throughput sequencing technology to analyze the change in microbial community, ecological information of colony, and degradation function relationship in different reaction steps in depth. We hoped that our work can provide certain technical and theoretical support for the actual project. Therefore, we can treat formaldehyde wastewater better and reduce its harm to environment and human body.

2. Materials and Methods

2.1. Overview of the Reactor. This study was based on the polyformaldehyde wastewater treatment in the production process in a chemical plant. The experiment process is as follows: raw water → iron and carbon microelectrolysis → one-step anaerobic (A1) → two-step anaerobic (A2) → three-step anaerobic (A3) → one-step aerobic (O1) → hydrolytic acidification → two-step aerobic (O2). The process flow diagram and the flooding water quality and sludge properties in the field are shown in Figure 1 and Table 1.

2.2. Sample Collection. The collection date was June 8, 2015, and the sludge samples were obtained from A1, A2, A3, O1, hydrolysis acidification, and O2. We collected the samples in the reactor when it was starting. The sludge sample number information is shown in Table 2.

Table 2: Sludge sample number information in the reactor.

Sample number	Sampling stage
A1D	One-step anaerobic
A2D	Two-step anaerobic
A3D	Three-step anaerobic
O1D	One-step aerobic
BD	Hydrolytic acidification
O2D	Two-step aerobic

Table 3: Testing index and method of activated sludge.

Testing index	Testing method
SS	Dry weight
SV_{30}	Sedimentation method
SVI	Settlement of weighing
MLSS	Weight method

2.3. Chemical Analysis. Conventional water quality indicators, such as pH, temperature, and COD, were analyzed using the national standard method [10]. The dissolved oxygen (DO) and formaldehyde concentration were analyzed using the DO instrument. Table 3 shows the testing index and method of activated sludge.

2.4. DNA Extraction and High-Throughput Sequencing. DNA was extracted via phenol–chloroform extraction and was purified by purification kit (TIANquick Midi Purification Kit, Tiangen). DNA samples were detected of fragment length through agarose gel electrophoresis detection after purification. The concentration and purity were determined by Nanodrop. PCR (Polymerase Chain Reaction) amplification was carried out, and the amplification products were used for DNA sequencing [11]. The library of sequencing DNA was constructed by TruSeq kit (Illumina, USA) and was determined by Illumina Miseq2500 high-throughput sequencing machine for sequencing.

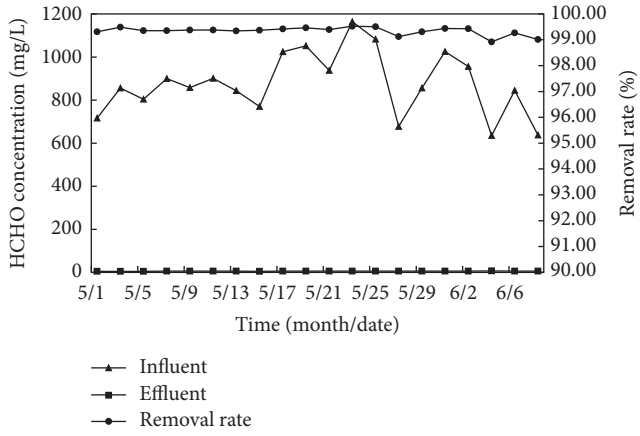

Figure 2: Formaldehyde removal from the reactor.

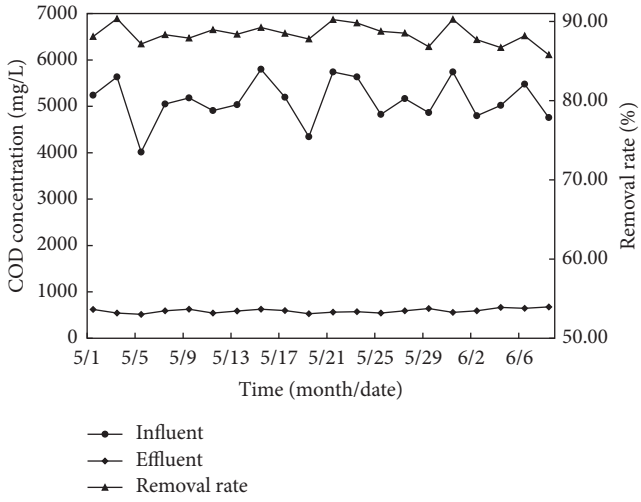

Figure 3: COD removal from the reactor.

3. Results and Discussion

3.1. HCHO Removal Performance of the Reactor. Figure 2 shows the formaldehyde removal from the reactor.

Figure 2 shows that influent formaldehyde concentration is 635–1164 mg/L, and the effluent formaldehyde concentration in secondary sedimentation tank is about 5 mg/L. The fluctuation of influent formaldehyde concentration is large because of the complex working conditions in the field. However, the removal rate is basically stable at more than 99%, with the highest at 99.5%. This rate shows that the performance of the technology is ideal, and such technology can respond to the change in external conditions.

3.2. COD Removal Performance of the Reactor. Figure 3 shows the COD removal from the reactor.

Figure 3 shows that influent COD concentration is 4000–5800 mg/L, and the effluent COD concentration in secondary sedimentation tank is 510–670 mg/L. The removal rate of COD is about 89%, and the highest can reach 90.36%. The different removal rates of formaldehyde and COD show that formaldehyde degradation and its degradation products are not completely synchronous [12, 13]. Longer time is needed before it becomes fully biodegradable.

The system has a total of six units of series reactor, which includes three stages of anaerobic reaction, two stages of aerobic reaction, and a hydrolysis acidification phase. This process is relatively complicated, which can be carried out in in-depth degradation processing in the view of high COD concentration and complex wastewater. Table 4 presents the quality index of polyformaldehyde wastewater.

First, high-concentration wastewater underwent three continuous anaerobic reaction systems with long anaerobic reaction time. Both the flora in graded response and the differentiation of ecological level are abundant. At this stage, most of the carbon sources that can be used are degraded by anaerobic microbes. Thus, most of the reactor formaldehyde and COD are removed during the anaerobic phase, and the removal rate reaches 62.6% and 73.3%, respectively. The biochemical substance content in the effluent water at anaerobic phase is relatively small. Most of these substances are materials that are difficult to use via anaerobic microbes. The organic matter is degraded and mineralized in depth in aerobic phase. Macromolecular organic matter and intermediate metabolites are decomposed sequentially in the hydrolysis acidification phase; these materials are then translated thoroughly into harmless substance and discharged after secondary aerobic phase.

3.3. Sludge Ecology Analysis in the Reactor

3.3.1. Microbial Numbers and Diversity. The results of operational taxonomic unit (OTU), abundance (Chao 1), and diversity (Shannon) index of microbial community were obtained by high-through sequencing. The microbial community diversity in the sludge sample of the reactor is shown in Table 5. The Shannon index of the sediment samples changes in the range of 5.44–6.74. Shannon index is low at the three-step anaerobic, hydrolysis, and acidification stages. Such low value may be attributed to that as the reaction continues; the bacteria, which are not adapted to the environment, gradually lose activity, age, and die because of the continuous change of DO and nutrition matrix. When the hydrolysis acidification phase is reached, the sludge activity is reduced because the life cycle of anaerobic microbes is longer than those of aerobic ones, and the sludge accumulated in the bottom causes inadequate contact with wastewater and poor microbial diversity [14].

Chao 1 and OTU index had a similar change rule with Shannon index. These three indicators describe the microbial diversity and its relationship with the effect of wastewater treatment. The results also reflect that the microbial diversity is high, and the treatment effect is relatively good in the reaction pool [15].

3.3.2. Phylum Level of Community Composition in Sludge Samples. The microbial classification in sludge samples according to phylum is shown in Figure 4. Comparing with sequence in the library construction, we can determine the kinds of microbial communities. Proteobacteria, Firmicutes,

Table 4: Quality index of polyformaldehyde wastewater.

	Raw water	Effluent water of iron and carbon microelectrolysis	A1	A2	A3	O1	Hydrolytic acidification	O2
HCHO (mg/L)	638	511	191	9.81	—	10.3	8.6	10.5
COD (mg/L)	4957.2	3772.2	1006.4	920.0	654.0	303.0	283.0	276.4
pH	3.5	5.0	7.0	7.2	7.5	7.5	7.5	8.0
Temperature (°C)	—	—	35.0	36.0	35.0	35.0	36.0	31.0

Table 5: Microbial community diversity in the sludge sample of the reactor.

Samples number	Chao 1	Shannon index	OTU number
A1D	1458.35	6.74	1053
A2D	1281.31	6.42	903
A3D	1351.01	5.84	856
O1D	1815.04	6.65	1219
BD	911.64	5.44	663
O2D	1608.42	6.14	991

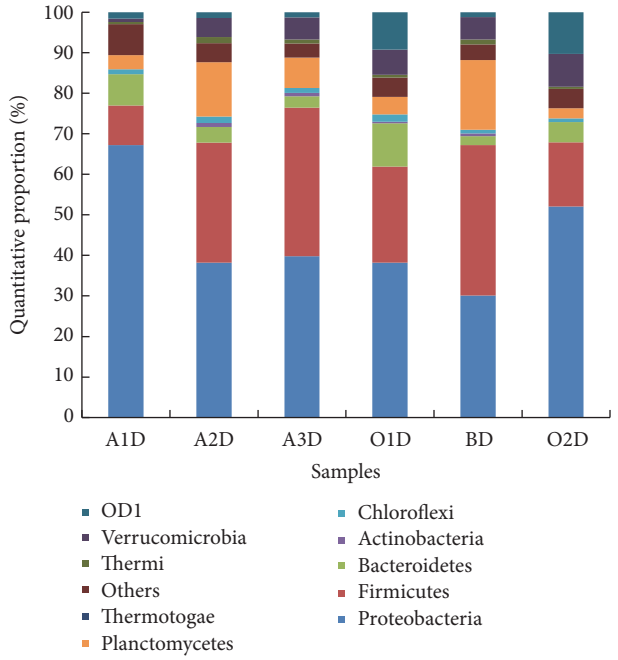

Figure 4: Classification of microbes in sludge samples according to phylum.

Bacteroidetes, Actinobacteria, Chloroflexi, Planctomycetes, and Thermotogae are the dominant bacterial communities in the samples.

Proteobacteria (30.1%–67.2%) are dominant in all of the samples [16]. Proteobacteria are one of the largest bacterial categories, which belong to gram-negative bacteria. Their outer membrane is mainly composed of lipopolysaccharide. The metabolic type is different among different members, and most of them is facultative or obligate anaerobic. Proteobacteria are the main groups of bacteria in the wastewater treatment system and plays an important role in the removal of organic matter from wastewater [17, 18]. In wastewater treatment process, the amount of Proteobacteria decreases from 67.2% to 30.1% of hydrolysis acidification phase and subsequently increases to 52.1%. This result might be because Firmicutes and Bacteroidetes begin to multiply and occupy some ecological niches of Proteobacteria [19] through anaerobic fermentation.

Firmicutes is gram-positive bacteria. The peptidoglycan content accounts for 50%–80% of the total quality of cell walls. Firmicutes is absolutely dominant in hydrolysis acidification phase [20, 21]. Its proportion gradually increases from 9.8% to 37.1% of hydrolysis acidification phase in the reactor.

Bacteroidetes is autotrophic bacteria that can translate macromolecular organic matter (protein, starch, and lipid) into small molecules through hydrolysis and fermentation. Bacteroidetes includes some nitrogen-fixing bacteria, which play a part in the denitrification process [22, 23].

3.3.3. Family and Genus Levels of Community Composition in Sludge Samples. The microbial classification in sludge samples according to family and genus is shown in Figure 5. The distribution of family and genus levels can reflect detailed microbial functional information in the system. Microbial community has certain similarity in the same system. The dominant microflora slightly changes and has certain regularity. Peptostreptococcaceae (3.3%–27.2%), Phycisphaerales (0.9%–14.2%), Rhodobacteraceae (5.0%–15.2%), *Azospirillum* (2.1%–11.9%), Rhodocyclaceae (0.6%–8.8%), *Alphaproteobacteria_BD7-3* (0.2%–6.2%), Piscirickettsiaceae (0.9%–3.5%), and *Candidatus Xiphinematobacter* (0.7%–8.1%) are the dominant bacterial communities in the samples. Most of these communities belong to Proteobacteria.

This process system is further complicated. Different processing units have different functions in the system. The anaerobic phase is relatively different between aerobic phases. Microbial communities in different units show typical representative characteristic affected with working conditions and influent concentration.

Rhodobacteraceae is the dominant microbes in the one-step anaerobic process. These bacteria can accumulate phosphorus in denitrification [24–26]. Rhodobacteraceae and Rhodocyclaceae play an important role in organic matter

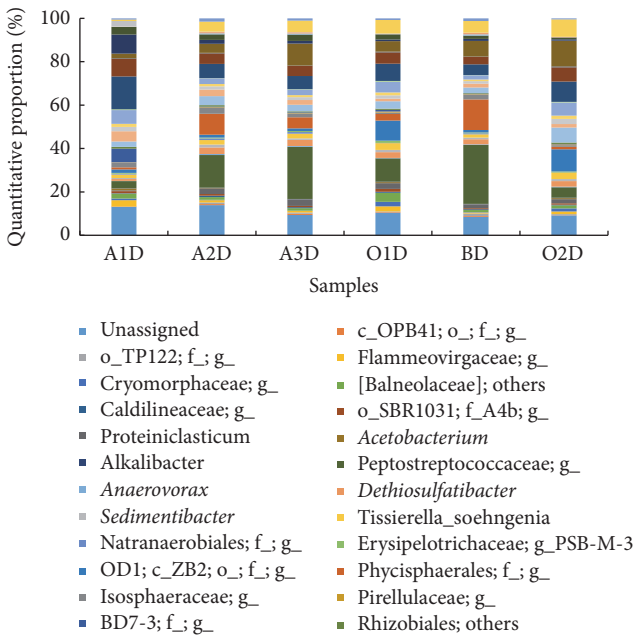

Figure 5: Microbial classification in the sludge samples according to family and genus.

degradation [27]. Approximately 60% of the formaldehyde is decomposed during the one-step anaerobic process (Figure 4). Both the numbers of Rhodobacteraceae and Rhodocyclaceae obviously decline with formaldehyde degradation. Therefore, Rhodobacteraceae and Rhodocyclaceae should be the main formaldehyde degradation bacteria in the reactor.

Most of formaldehyde and COD have been degraded in the one-step anaerobic process, and thus two- and three-step anaerobic processes are the main procedures of in-depth anaerobic treatment. The microbial community structures of these two processes are relatively similar, and Peptostreptococcaceae and Phycisphaerales are the dominant bacteria in the system. Phycisphaerales belongs to Planctomycetes and is the anaerobic ammonia oxidation bacterium. These bacteria can create nitrite-oxidizing ammonium and produce nitrogen under anoxic conditions, which contribute to denitrification [28, 29].

After entering the aerobic reaction stage, the diversity of microbial community structure increases in the reactor because the bacterial aerobic metabolism grows quickly, including the increase of nitrifying bacteria, which has high DO demand.

Peptostreptococcaceae is the dominant microbes during hydrolysis acidification. This microbe belongs to Firmicutes and typically uses little or no sugar. It can decompose protein to produce acetic acid [19]. Peptostreptococcaceae reaches about 27.2% in this process, which illustrates that it has already reached the vigorous stage of acid production. Peptostreptococcaceae is also distributed at all stages in the system and has an obvious advantage in the middle of four stages. This microbe is a facultative aerobic bacterium and plays an important role in the removal of organic matter, specifically the acidification decomposition of middle metabolites.

In addition, *Azospirillum* is distributed at all stages in the system; these nitrogen-fixing microbes belong to Proteobacteria and can fix nitrogen with cereals and Gramineae [30]. *Azospirillum* is also part of the denitrifying bacteria groups and can translate nitrate into N_2O or N_2 under enzyme catalysis. This microbe also has a role in the nitrogen cycle [31].

Candidatus Xiphinematobacter grows with the reaction and belongs to Thermotogae. This microbe is a kind of nitrifying bacteria, and little information is available regarding it.

3.3.4. RDA (Redundancy Analysis) of Dominant Bacterium in Sludge Samples. Figure 6 shows the RDA of dominant bacterium and major environmental factor in sludge samples. Rhodobacteraceae and Rhodocyclaceae have a high correlation with formaldehyde removal rate, which is consistent with the conclusions mentioned above.

Piscirickettsiaceae and *Alphaproteobacteria_BD7-3* also have a high correlation with COD removal rate. Piscirickettsiaceae belongs to γ-Proteobacteria and uses organic matter as the main carbon source. It also plays an important role in COD removal process [28]. *Alphaproteobacteria_BD7-3* belongs to α-Proteobacteria and has not been named. Most of α-Proteobacteria is saprophytic heterotrophic bacteria, and their main carbon source is the organic matter. Therefore, these bacteria are important in the removal process of COD [30].

4. Conclusions

(1) Multistage A-O-activated sludge process has good treatment effect on polyformaldehyde wastewater. Under the initial formaldehyde concentration of 635–1164 mg/L and COD concentration of 4000–5800 mg/L, the removal rates of formaldehyde are basically stable at more than 99% and those of COD are about 89%. This method can remove pollutant effectively. We hoped that our work can provide certain technical support for the actual project.

(2) The ecology of activated sludge in different reaction stages through high-throughput sequencing was analyzed. The analysis results of microbial diversity indices (Shannon, Chao 1, and OTU) indicated that the microbial diversity of the reactor is high, and the treatment effect is good. Microbial community has certain similarity in the same system. Microbial communities in different units show typical representative characteristic affected with working conditions and influent concentration.

(3) The microbial community structure of the sludge samples was also analyzed. Proteobacteria, Firmicutes, and Bacteroidetes are dominant fungal genera in the phylum level of community composition. Peptostreptococcaceae, Phycisphaerales, and Rhodobacteraceae are dominant fungal genera in the family and genus levels of community composition. Peptostreptococcaceae is distributed at various stages and dominant in this system. This bacterium also plays an important role in organic matter removal, particularly the decomposition in middle metabolite acidification. Rhodobacteraceae and Rhodocyclaceae are formaldehyde-degrading bacteria in the reactor.

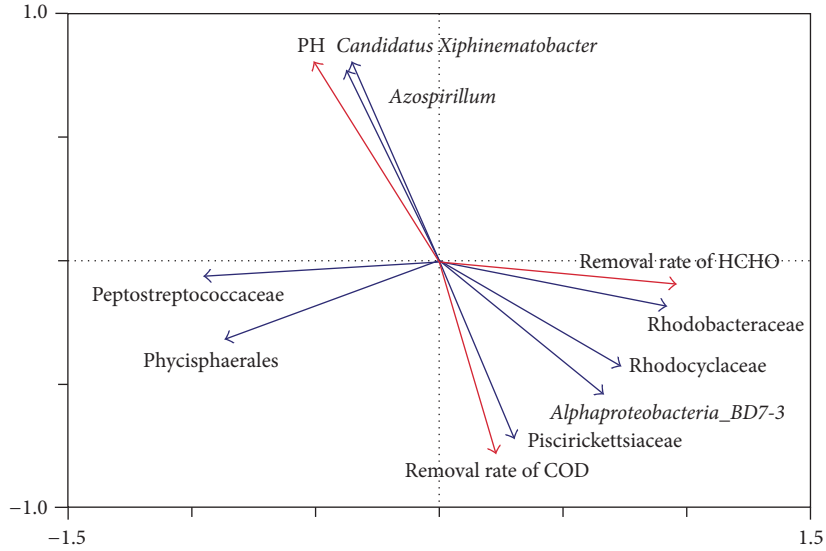

Figure 6: RDA of advantage bacterium in sludge samples.

Competing Interests

The authors declare that they have no competing interests.

Acknowledgments

This study was supported by the National Natural Science Foundation of China (Grants nos. 51178048 and 51378064) and the Fundamental Research Funds for the Central Universities (Grant no. 2014KJJCB22).

References

[1] Q. Cao, "Advances in formaldehyde wastewater treatment," *Pollution Control Technology*, vol. 22, no. 4, pp. 55–58, 2009.

[2] Z. J. Xu, Z. F. Cheng, A. J. Lin, J. G. Wang, and H. Tong, "Removal of formaldehyde from wastewater by activated sludge," *Chinese Journal of Environmental Engineering*, vol. 2, no. 9, pp. 1173–1176, 2008.

[3] H. X. Yang, *The Study on Biodegradation of Industrial Formaldehyde Wastewater Using Sequencing Batch Reactor Processing*, Nanjing University of Science & Technology, 2013.

[4] A. Hidalgo, A. Lopategi, M. Prieto, J. L. Serra, and M. J. Llama, "Formaldehyde removal in synthetic and industrial wastewater by Rhodococcus erythropolis UPV-1," *Applied Microbiology and Biotechnology*, vol. 58, no. 2, pp. 260–263, 2002.

[5] Z. H. Wang, H. B. Wei, Z. Y. Jia, Y. M. Lu, X. Liu, and P. Zou, "Activated sludge process for treatment of formaldehyde wastewater," *China Water & Wastewater*, vol. 25, no. 1, pp. 86–87, 2009.

[6] S. Mirdamadi, A. Rajabi, P. Khalilzadeh, D. Norozian, A. Akbarzadeh, and F. A. Mohseni, "Isolation of bacteria able to metabolize high concentrations of formaldehyde," *World Journal of Microbiology and Biotechnology*, vol. 21, no. 6-7, pp. 1299–1301, 2005.

[7] N. Kato, H. Kobayashi, M. Shimao, and C. Sakazawa, "Properties of formaldehyde dismutation catalyzing enzyme of *Pseudomonas-putida* F61," *Agricultural and Biological Chemistry*, vol. 48, no. 8, pp. 2017–2023, 1984.

[8] A. Habibi and F. Vahabzadeh, "Degradation of formaldehyde at high concentrations by phenol-adapted Ralstonia eutropha closely related to pink-pigmented facultative methylotrophs," *Journal of Environmental Science and Health—Part A Toxic/Hazardous Substances and Environmental Engineering*, vol. 48, no. 3, pp. 279–292, 2013.

[9] N. N. Maidan, M. V. Gonchar, and A. A. Sibirny, "Oxidation of exogenous formaldehyde in methylotrophic and nonmethylotrophic yeast cells," *Biochemistry*, vol. 62, no. 6, pp. 636–640, 1997.

[10] SEPA, *The Editorial Committee of Water and Waste Water Monitoring and Analysis Methods*, Environmental Science Press, Beijing, China, 4th edition, 2002.

[11] Y. Qu, X. Zhang, W. Shen et al., "Illumina MiSeq sequencing reveals long-term impacts of single-walled carbon nanotubes on microbial communities of wastewater treatment systems," *Bioresource Technology*, vol. 211, pp. 209–215, 2016.

[12] P. Kaszycki, M. Tyszka, P. Malec, and H. Kołoczek, "Formaldehyde and methanol biodegradation with the methylotrophic yeast *Hansenula polymorpha*. An application to real wastewater treatment," *Biodegradation*, vol. 12, no. 3, pp. 169–177, 2001.

[13] A. Habibi and F. Vahabzadeh, "Degradation of formaldehyde in packed-bed bioreactor by kissiris-immobilized *Ralstonia eutropha*," *Biotechnology and Bioprocess Engineering*, vol. 18, no. 3, pp. 455–464, 2013.

[14] S. Y. He, J. X. Li, Y. T. Xu, Z. T. Hu, and Y. G. Wang, "The microbial community structure of brewery wastewater treatment system by hydrolytic acidification and SBR technics," *Technology of Water Treatment*, vol. 34, no. 3, pp. 35–38, 2008.

[15] D. Cui, *Microbial Community Analysis of Bioaugmented Biological Wastewater Treatment Systems at Low Temperature*, Harbin Institute of Technology, 2014.

[16] Z. Wang, Y. Yang, Y. Dai, and S. Xie, "Anaerobic biodegradation of nonylphenol in river sediment under nitrate- or sulfate-reducing conditions and associated bacterial community," *Journal of Hazardous Materials*, vol. 286, pp. 306–314, 2015.

[17] M. Madigan and J. Martinko, *Brock Biology of Microorganisms*, Prentice Hall, New York, NY, USA, 11th edition, 2005.

[18] Y. Xu, *Evolution of the Structures and Functions of the Microbial Community during Adapting to Different Wastewater Treatment Systems*, Henan Normal University, Xinxiang, China, 2013.

[19] G. G. Liu, *Microbial Community Succession of Excess Sludge Acidification Process Contral in Bench Scale*, Harbin Institute of Technology, Harbin, China, 2015.

[20] D. Zhang, Y. Chen, Y. Zhao, and X. Zhu, "New sludge pretreatment method to improve methane production in waste activated sludge digestion," *Environmental Science and Technology*, vol. 44, no. 12, pp. 4802–4808, 2010.

[21] H. Zhang, J. E. Banaszak, P. Parameswaran, J. Alder, R. Krajmalnik-Brown, and B. E. Rittmann, "Focused-Pulsed sludge pre-treatment increases the bacterial diversity and relative abundance of acetoclastic methanogens in a full-scale anaerobic digester," *Water Research*, vol. 43, no. 18, pp. 4517–4526, 2009.

[22] F. Y. Shi, B. B. Song, and S. Z. Fu, "Pilot study on ammonium removal efficiency and nitrifying bacteria variety in marine biofilter charged with bamboo substrate," *Progress in Fishery Sciences*, vol. 3, no. 1, pp. 92–96, 2009.

[23] V. R. Hill, A. M. Kahler, N. Jothikumar, T. B. Johnson, D. Hahn, and T. L. Cromeans, "Multistate evaluation of an ultrafiltration-based procedure for simultaneous recovery of enteric microbes in 100-liter tap water samples," *Applied and Environmental Microbiology*, vol. 73, no. 13, pp. 4218–4225, 2007.

[24] X. X. Jiang, *Research on the Nitrogen and Phosphorous Removal Efficiency and Microbial Properties of SBR Process Operated in the Mode of A/O/A*, Harbin Institute of Technology, 2011.

[25] H. Y. Wang, Y. X. Zhou, and J. Y. Jiang, "Microbial populations and community structure characterization technologies of the enhanced biological phosphate removal system," *Microbiology*, vol. 32, no. 1, pp. 118–122, 2005.

[26] C. J. Sun, *Efficiency of Denitrifying Phosphorus Removal and Community Structure in Two Stage Biological Filters Operated by Alternative Aeration*, University of Jinan, 2015.

[27] X. Hong, B. B. Liu, and X. J. Zhang, "Comparison of microbial community structure of quinoline and in dole acclimated denitrifying bioreactor," *Acta Microbiologica Sinica*, vol. 48, no. 4, pp. 503–507, 2008.

[28] D. Weissbrodt, S. Lochmatter, and T. R. Neu, "Isolation and physiological characteristics on strictly anaerobic hydrogen-producing bacteria (Thermopirellula anaerlimosa) of *Planctomycetes*," *Acta Microbiologeca Sinica*, vol. 52, no. 8, pp. 994–1001, 2012.

[29] C. Peng, *Study on Biological Denitrification Efficiency and Microbial Diversity of Composite Iron Enzymatic Biofilm Technology*, Qingdao University of Technology, Qingdao, China, 2015.

[30] P. M. Yan, H. P. Qiao, and W. J. Zhao, "Effects of methyl bromide fumigation on community structure of denitrifying bacteria with nitrousoxide reductase gene (*nosZ*) in soil," *Acta Microbiologica Sinica*, vol. 55, no. 1, pp. 73–79, 2015.

[31] Y. Y. Xu, X. H. Xu, G. M. Ren, Y. Sun, and H. T. Li, "Effect of microbial inoculum on denitrifying bacterial communities in cow manure compost," *Journal of Agro-Environment Science*, vol. 34, no. 3, pp. 570–577, 2015.

Hindawi Publishing Corporation
Journal of Chemistry
Volume 2016, Article ID 9863408, 13 pages
http://dx.doi.org/10.1155/2016/9863408

Research Article

Bench-Scale Flushing Experiments for Remediation of Hg-Contaminated Groundwater

Sung-Wook Jeen

Department of Earth and Environmental Sciences and The Earth and Environmental Science System Research Center, Chonbuk National University, Jeonju-si, Jeollabuk-do 561-756, Republic of Korea

Correspondence should be addressed to Sung-Wook Jeen; sjeen@jbnu.ac.kr

Received 21 July 2016; Accepted 12 October 2016

Academic Editor: Julie J. M. Mesa

Bench-scale laboratory column experiments were conducted to determine the desorption characteristics of Hg in the aquifer material from an area of known elevated Hg concentrations in groundwater under flushing conditions. The experimental results showed that columns packed with perched aquifer material (PA) showed flushing of Hg, with the general decline of effluent Hg concentrations over time (from 0.05–0.1 mg/L in the beginning to 0.0001–0.003 mg/L at the end of the experiment). Columns with lower aquifer material (LA) showed nondetectable level of effluent Hg throughout the experiment. Possibility of redissolution/desorption of Hg after static condition (for the duration of 18 days) was tested, showing only slight rebound of Hg concentrations after equilibration. The results suggest that removal of up to 20% of Hg inventory in the sediment could be achievable for the duration of the experiments (about 10 pore volumes). The results also indicate that the treated water from the water treatment plant was more effective compared to deionized water, probably due to complexing agents contained in the treated water.

1. Introduction

Mercury is one of the most toxic contaminants released by gold mining and operation of industrial facilities and elevated mercury concentration down gradient of the mine tailings has been a primary concern for many mining projects [1–5]. Hg contamination in mining impacting aquatic environments is historically due to gold extraction by amalgamation techniques [6]. Extraction with sodium cyanide has also been widely used and caused mercury contamination in the environment [7]. In the extraction, gold is leached from the ores during gold-cyanide process (GCP) [8, 9]. In addition to forming gold complexes, cyanide also coordinates other metals such as iron, zinc, copper, and mercury, forming soluble metal-cyano complexes in leachate solution, causing a serious environmental problem [10].

The fate and transport of mercury in the contaminated systems are controlled by the interaction between aqueous speciation and sediment-water partitioning [11–13]. The aqueous speciation of Hg is strongly affected by chemical conditions such as pH, redox, and concentrations of organic and inorganic ligands [14, 15]. While environmental impact of mine drainage, which is often acidic and containing elevated levels of mercury, is assessed at some mines, successful remediation measures are not fully implemented [16].

Recent efforts for remediating Hg-contaminated water include methods using zerovalent iron (ZVI) [17–19], elemental Cu and S, granular activated carbon (GAC), attapulgite clay (ATP) [18], and biochars [20]. However, in situ technologies to remediate Hg-contaminated groundwater yet need to be developed. In this regard, only a few studies have been conducted to investigate the controls on Hg mobility and leaching persistence originated from mine tailings [21, 22].

In this study, bench-scale column flushing experiments were conducted to mitigate elevated dissolved mercury concentrations down gradient from the mine tailings at a gold and silver mine. The flushing experiments evaluated whether injected water can flush redissoved/desorbed Hg in the aquifer under the ideal conditions in the laboratory, from which determination can be drawn with regard to the actual remedial performance in the field.

Little is known about the geochemical characteristics of the aquifer matrix at the site with respect to adsorption/desorption properties for contaminants and in particular

mercury in solution. Understanding these characteristics is integral to developing the most efficient remedial strategy and to constraining the estimates for completion of aquifer remediation. The bench-scale laboratory column experiments were conducted to augment the pilot aquifer flushing test to determine the desorption characteristics of Hg in the aquifer material from an area of known elevated Hg concentrations in groundwater. Key objectives of the study were (1) to determine maximum achievable removal of Hg from aquifer solids using potential flushing water, including water sourced from the water treatment plant, which is located downgradient from the tailings, and deionized water and (2) to determine Hg desorption behavior in aquifer solids and to determine the potential for postflushing desorption of Hg from aquifer solids.

The experiments were performed in small columns, measured Hg concentrations overtime, and provided empirical information on the number of pore volumes required for successful flushing. In addition, following initial flushing, columns were permitted to equilibrate and residual Hg concentrations in pore water were measured to evaluate the potential for postflushing desorption and whether this geochemical process could contribute to unacceptable residual Hg concentrations in groundwater. The results will help to define the threshold of reasonably achievable remediation of Hg from the aquifer.

2. Materials and Methods

2.1. Sediments and Source Water. The mining of gold and silver ore at the mine site began in early 1990s. The tailings are dry-filtered and placed in an adjacent mountain slope. Cyanide used in the milling process is discharged with the tailings. Typically, the tailings are disposed with a maximum moisture content of 15 wt.%. Although the tailings have low moisture content, monitoring identified an extensive plume of groundwater contaminated with Hg in the unconfined aquifer. The mercury treatment plant and the planned remedial system site are located approximately 5 km downgradient from the tailings.

Aquifer materials for filling the columns were collected from the drilled cores at the pilot test remedial system site. Three sediment cores were collected at the site and sent to the laboratory. One core represents perched aquifer sediment and was collected from depth of 17.5 to 18.5 m. This depth of the core contains poorly graded sand and gravel with maximum particle size of 60 mm. Particles are subrounded to rounded and have brownish color with black patches. Sediment has some moisture content and is odorless. Two other cores were from the lower aquifer and represent samples from 35 to 36.5 m and from 41 to 42.5 m. The core from depth of 35 to 36.5 m contains soft silty sand and is very wet. The core from depth of 41 to 42.5 m also contains silt to sandy silt with orange mottling and is moist. These two cores were treated essentially as the same material and thus were mixed together during the column packing. For characterization of the sediments, paste pH, particle size distribution, total organic and inorganic carbons, metals, and total sulfur were analyzed and the results are presented in Table 1. Of note, mercury (Hg) content in sediment samples was 0.196 mg/kg for perched aquifer material and 0.0287 mg/kg for lower aquifer material.

A total of 20 liters of treated water from the water treatment plant at the site were sent to the laboratory. The pH, alkalinity, electrical conductivity (EC), total cyanide, and dissolved metals including mercury were analyzed for the received water, as the results presented in Table 2. Deionized water was also used for the experiments to test the performance in comparison to the treated water.

2.2. Column Setup. A total of six flow-through columns were manufactured and the column experiments were conducted simultaneously. Two columns were packed with the sediment from perched aquifer (PA): one received deionized water (DI) and another received treated water from the treatment plant (TW). Three columns were packed with the sediment from lower aquifer (LA). One column received the treated water, while two other columns received deionized water. The latter two columns (LA-DI1 and LA-DI2) were set up as duplicates to test reproducibility of the experiments. The sixth column contained only silica sand (SS) and received deionized water as the influent. It served as a control column.

For all of the columns, except the control column (SS-DI), approximately 2.5 cm of clean silica sand was layered at the influent and effluent ends of the columns to improve the distribution of flow in the columns and to filter coarse solids out of the effluent. Silica sand was washed with 5% HNO_3 solution overnight and then rinsed with plenty of deionized water until pH is back to normal (>pH 5). The control column was about half filled only with silica sand and thus pore volume was less than other columns. Characteristics of each column are summarized in Table 3.

Each column consisted of a clear acrylic tube, 21.5 cm length and 15 cm internal diameter, and was fitted with end plates. Column dimensions have been selected to optimize the flow rate to allow for a low velocity flow representative of typical field conditions in the aquifer sediments and also to accommodate representative volume of aquifer materials.

Aquifer sediments were retrieved from the cores inside a N_2 glove bag to minimize disturbance of redox conditions in the sediments. The glove bag was fully inflated with N_2 gas and then deflated three times after a core was located inside the bag. Sediments were retrieved under positive pressure of N_2 and thus oxygen intrusion was minimized. After all of the sediments were retrieved from the cores, each of aquifer materials (PA or LA) was mixed by hands to homogenize the sediments as much as possible. This was to ensure that sediments in the columns should have representative samples for each aquifer material. Some large particles such as gravel were excluded from the packing materials.

The retrieved sediments (within the glove bag) were relocated into another glove bag. At this point, the column with ~2.5 cm of silica sand at the bottom was put into the same bag. After that, the outer glove bag was once again purged with N_2 gas three times before column packing started. The sediment was packed into the column over the silica sand

Table 1: Characteristics of aquifer materials.

Sample	Perched aquifer (PA)	Lower aquifer (LA)	Detection limit
pH (1 : 2 soil : water)	4.24	6.35	0.01
Particle size			
% gravel (>2 mm)	8.97	5.78	0.10
% sand (2.00 mm–1.00 mm)	18.3	14.8	0.10
% sand (1.00 mm–0.50 mm)	21.9	18.3	0.10
% sand (0.50 mm–0.25 mm)	11.2	9.76	0.10
% sand (0.25 mm–0.125 mm)	10.7	10.7	0.10
% sand (0.125 mm–0.063 mm)	5.23	6.86	0.10
% silt (0.063 mm–0.0312 mm)	7.17	8.37	0.10
% silt (0.0312 mm–0.004 mm)	10.6	14.8	0.10
% clay (<4 μm)	6.04	10.7	0.10
Texture	Sandy loam/loamy sand	Sandy loam	
Organic/inorganic carbon			
$CaCO_3$ equivalent (%)	<0.80	<0.80	0.80
Inorganic carbon (%)	<0.10	<0.10	0.10
Total carbon (%)	0.1	<0.1	0.1
Total organic carbon (%)	0.10	<0.10	0.10
Metals			
Aluminum (Al) (mg/kg)	31900	54100	50
Antimony (Sb) (mg/kg)	2.48	1.91	0.10
Arsenic (As) (mg/kg)	282	178	0.050
Barium (Ba) (mg/kg)	157	146	0.50
Beryllium (Be) (mg/kg)	0.61	1.34	0.20
Bismuth (Bi) (mg/kg)	<0.20	0.26	0.20
Cadmium (Cd) (mg/kg)	2.07	0.227	0.050
Calcium (Ca) (mg/kg)	1060	2430	50
Chromium (Cr) (mg/kg)	8.77	11.3	0.50
Cobalt (Co) (mg/kg)	50.1	12.8	0.10
Copper (Cu) (mg/kg)	85.9	52.9	0.50
Iron (Fe) (mg/kg)	35000	33900	50
Lead (Pb) (mg/kg)	47.1	27.1	0.50
Lithium (Li) (mg/kg)	55.6	25.6	5.0
Magnesium (Mg) (mg/kg)	2610	3010	20
Manganese (Mn) (mg/kg)	7790	2330	1.0
Mercury (Hg) (mg/kg)	0.196	0.0287	0.0050
Molybdenum (Mo) (mg/kg)	2.00	2.16	0.50
Nickel (Ni) (mg/kg)	13.9	8.70	0.50
Phosphorus (P) (mg/kg)	537	509	50
Potassium (K) (mg/kg)	1370	1520	100
Selenium (Se) (mg/kg)	<0.20	<0.20	0.20
Silver (Ag) (mg/kg)	0.38	0.18	0.10
Sodium (Na) (mg/kg)	270	250	100
Strontium (Sr) (mg/kg)	80.1	133	0.50
Sulfur (S), total (mg/kg)	1100	1400	500
Thallium (Tl) (mg/kg)	2.61	0.830	0.050
Tin (Sn) (mg/kg)	<2.0	<2.0	2.0
Titanium (Ti) (mg/kg)	774	787	1.0
Uranium (U) (mg/kg)	0.543	1.18	0.050
Vanadium (V) (mg/kg)	70.6	90.7	0.20
Zinc (Zn) (mg/kg)	358	407	1.0

Table 2: Composition of the treated water collected from the water treatment plant.

Parameter	Unit	Concentration	Detection limit
Alkalinity	mg/L as $CaCO_3$	14	0.10
pH	—	3.85	0.01
Electrical conductivity (EC)	μS/cm	2950	0.10
Total cyanide	mg/L	0.0231	0.0050
Aluminum (Al)	mg/L	28.2	0.0025
Antimony (Sb)	mg/L	<0.00010	0.00010
Arsenic (As)	mg/L	0.00407	0.00010
Barium (Ba)	mg/L	0.00948	0.00010
Beryllium (Be)	mg/L	0.0147	0.000050
Bismuth (Bi)	mg/L	<0.000025	0.000025
Boron (B)	mg/L	0.917	0.025
Cadmium (Cd)	mg/L	0.00692	0.000025
Calcium (Ca)	mg/L	432	0.10
Chromium (Cr)	mg/L	0.00065	0.00050
Cobalt (Co)	mg/L	0.0764	0.000025
Copper (Cu)	mg/L	0.213	0.00050
Iron (Fe)	mg/L	0.207	0.0050
Lead (Pb)	mg/L	0.000065	0.000025
Lithium (Li)	mg/L	0.712	0.0025
Magnesium (Mg)	mg/L	61.6	0.025
Manganese (Mn)	mg/L	16.6	0.00025
Mercury (Hg)	mg/L	0.000038	0.000010
Molybdenum (Mo)	mg/L	<0.00025	0.00025
Nickel (Ni)	mg/L	0.0430	0.00025
Phosphorus (P)	mg/L	<1.5	1.5
Potassium (K)	mg/L	7.22	0.25
Selenium (Se)	mg/L	0.00054	0.00020
Silicon (Si)	mg/L	47.4	0.25
Silver (Ag)	mg/L	<0.000025	0.000025
Sodium (Na)	mg/L	112	0.050
Strontium (Sr)	mg/L	1.05	0.00025
Thallium (Tl)	mg/L	0.000011	0.000010
Tin (Sn)	mg/L	<0.000050	0.000050
Titanium (Ti)	mg/L	<0.0025	0.0025
Uranium (U)	mg/L	0.00118	0.000010
Vanadium (V)	mg/L	0.00041	0.00025
Zinc (Zn)	mg/L	10.2	0.0025
Zirconium (Zr)	mg/L	<0.00050	0.00050

layer by an increment of about 2.5 cm at each step, after which the column wall was gently tapped by hand to homogenize the sediment inside the column. This step continued until the column was packed leaving only about 2.5 cm at the top. The column packing was completed by filling with silica sand to the remaining portion of the column at the top. Once column packing was completed, columns were saturated with deionized water before the desired source solutions for each column were introduced. Column weights were measured at each step of the column packing and saturated pore volume (PV) and porosity were calculated from the column weights before and after saturation (Table 3). The column experiments were conducted for a total of 44 days at room temperature.

2.3. Column Operation. Figure 1 shows the schematic of the column experiment. The column experiment was designed so that water enters from the bottom of the column and flows upward discharging from the top of the columns; thus, the bottom of the column is effectively upgradient and the top of the column is downgradient. This was done to ensure consistent and even flow throughout the columns, eliminating the risk of uncontrolled gravity-driven drainage and preferential flow paths.

The nominal residence time in the aquifer layer (excluding ~2.5 cm layer of silica sand at each end of the column) was calculated with the target flow rate of 400 mL/day and the average porosity of 0.3. The actual flow rates in the columns during the experiments were slightly variable, but generally the flow ranged between 350 and 390 mL/day. This corresponded to 0.40–0.45 PV/day, with an exception of the control column. Because of the smaller pore volume, the control column had the flow rates ranging from 0.62 to 0.67 PV/day. With these flow rates, water velocity through the columns was 6.5–7.3 cm/day and residence time was between 2.2 and 2.5 days, indicating that residence time for water in each of the columns is quite similar. By end of the experiment, 9.0–9.5 L of source water had flushed through the columns (Figure 2(a)). With respective to the cumulative PV flushed through the columns, approximately 16 PV flowed through the control column (SS-DI) and 10-11 PV flowed through the other columns (Figure 2(b)).

Following the initial flushing for 16 days, columns were allowed to equilibrate for a period of 18 days without the movement of flushing water through the columns. After the equilibration period, flushing of the columns recommenced and samples were immediately collected from the equilibrated aquifer pore water to determine if postflushing desorption had occurred. This equilibration period is indicated by discontinuities between elapsed days of 16 and 17 in the cumulative effluent volumes and cumulative pore volumes in Figure 2.

2.4. Sample Collection and Analysis. A total of 11 samplings were conducted for each of the columns every two to four days during the total operation period of 44 days. Between elapsed days 16 and 17, pumping was stopped for the duration of 18 days to evaluate if Hg concentration is rebounded due to redissolution/desorption in static conditions; thus, the total elapsed days for the flow-through period, excluding the 18 days of static conditions, were 26 days by the end of the experiment.

For each sampling event, approximately 80 mL of sample was collected from each of the column effluents (40 mL for metals, 15 mL for total cyanide, and 25 mL for pH/

Table 3: Column properties.

Column	SS-DI	PA-DI	PA-TW	LA-DI1	LA-DI2	LA-TW
Sediment	Silica sand (SS)	Perched aquifer (PA)	Perched aquifer (PA)	Lower aquifer (LA)	Lower aquifer (LA)	Lower aquifer (LA)
Source water	Deionized water (DI)	Deionized water (DI)	Treated water (TW)	Deionized water (DI)	Deionized water (DI)	Treated water (TW)
Mass of sediment (kg)	3.52	5.35	5.73	5.26	5.43	5.70
Estimated pore water volume (cm^3)	556[a]	1000	800	835	835	835
Porosity	0.30	0.34	0.27	0.29	0.29	0.29
Elapsed days[b]	26	26	26	26	26	26
Cumulative pore volume (PV) flushed	16.30	10.72	10.63	10.96	10.94	10.51

[a]SS-DI was only half filled with silica sand; thus pore volume is less than other columns.

[b]Between elapsed days 16 and 17, pumping was stopped for the duration of 18 days. Thus, the total column operation period was 26 + 18 = 44 days.

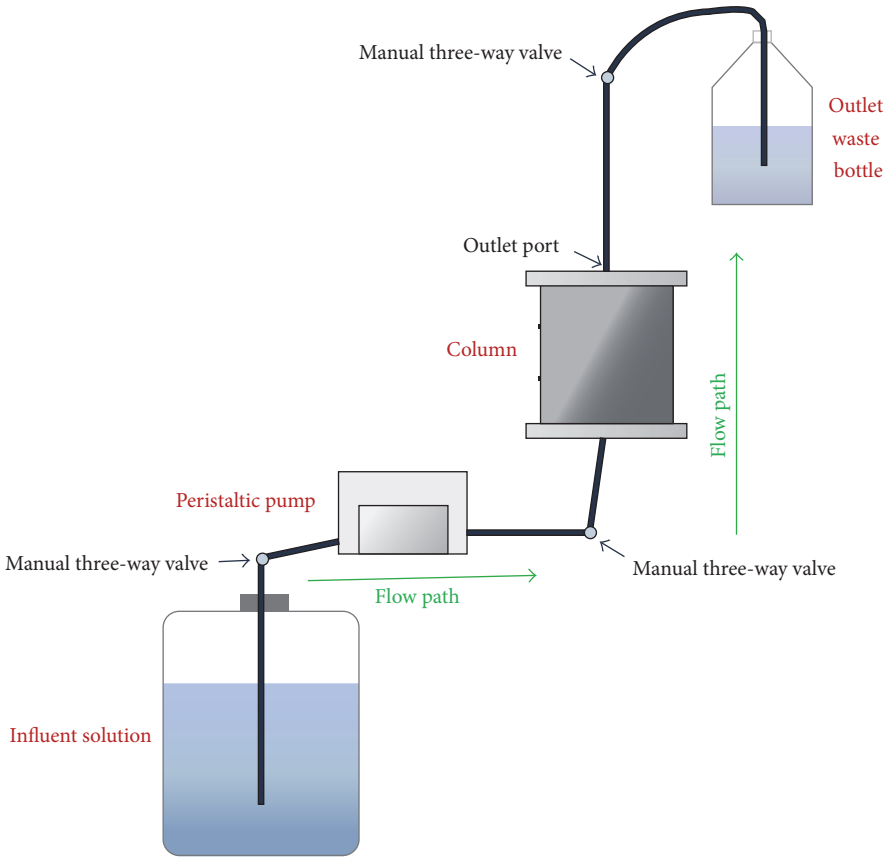

Figure 1: Schematic of the column experiment.

alkalinity/EC). To preserve the redox state during sampling, the sampling bottle was purged with nitrogen gas before each of sampling events. Outlet tubing from the sampling bottle was submersed under water to prevent oxygen ingress into the sampling bottle during sampling. Sample was passed through an in-line syringe filter (0.45 μm) so that analyses of dissolved components can be done without interference potentially induced by sampling procedures.

Samples for dissolved metals including Hg were acidified with concentrated, ultrapure nitric acid after filtration. Samples for total cyanide were prepared by adding 100 μL of 6 N NaOH to a 15 mL of filtered sample. Samples for metals and total cyanide analyses were refrigerated immediately after collection and were analyzed using inductively coupled plasma-mass spectrometry (ICP-MS) and colorimetric analysis (ISO 14403:2002), respectively.

pH, alkalinity, and EC were determined immediately after each sampling event. For pH measurement, a three-point calibration was carried out for the pH meter each time using pH 4.01, 7.00, and 10.01 buffers. Total alkalinity was determined by colorimetric titration with 0.01 M hydrochloric acid. EC

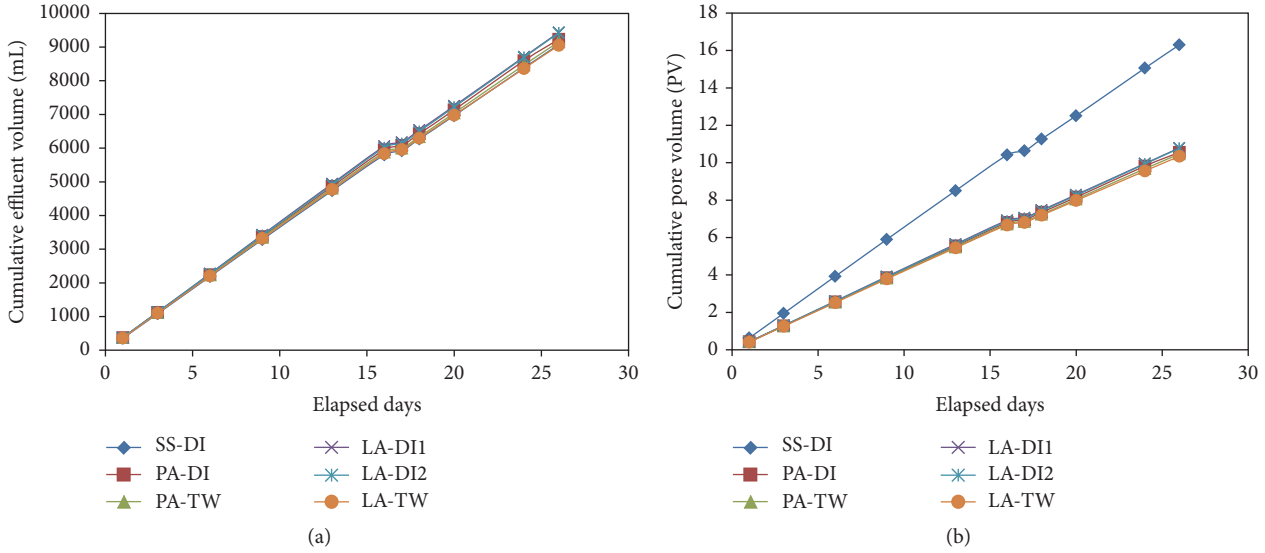

Figure 2: (a) Cumulative effluent volume (mL) and (b) cumulative pore volume (PV) for each column.

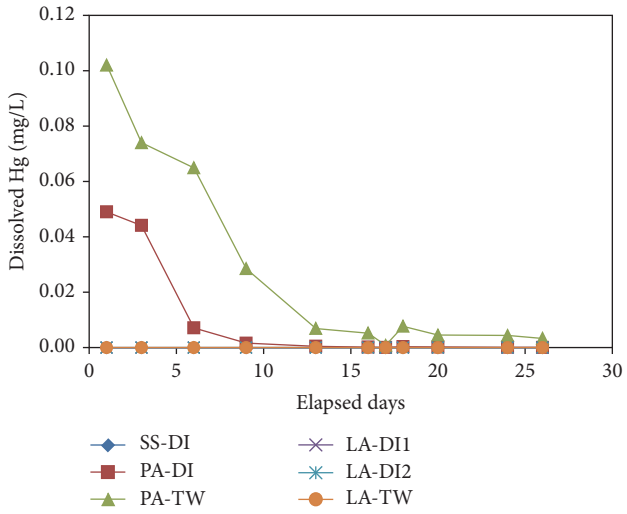

Figure 3: Dissolved Hg concentrations measured over time for each column.

was measured by a Thermo Scientific/Orion 5 Star conductivity meter with an Orion 013010MD conductivity cell after calibration with a 1413 μS/cm conductivity standard solution. Total organic and inorganic carbons, metals, and total sulfur for the sediments were analyzed using gravimetric method [23], ICP-MS, and combustion method (ISO 15178:2000), respectively. Detection limits for the analyses are provided in Tables 1 and 2. Replicate analyses showed little differences.

3. Results and Discussion

3.1. Mercury (Hg). Figure 3 shows the dissolved Hg concentrations for each of column effluents measured over time. Elevated concentrations of dissolved Hg at the effluents were only observed for the columns containing the sediment from perched aquifer (PA). Column effluents from lower aquifer material (LA) showed nondetectable level of dissolved Hg throughout the column operation the same as the control column (SS-DI). The duplicate columns for LA receiving deionized water (DI) showed the similar behaviors with regard to effluent water chemistry (also for other parameters), suggesting that the sediments were relatively homogeneous between the columns and thus column results are representative at least for the sediments collected in the cores.

The highest dissolved Hg concentration was 0.102 mg/L for PA-TW at day 1 (0.43 PV), while the highest concentration for PA-DI was 0.049 mg/L at day 1 (0.43 PV). The difference in Hg concentrations for the two columns is believed to be due to different complexing abilities of the influent water, primarily represented by total cyanide concentrations (see Figure 4). It is also possible that other complexing agents in the treated water, such as dissolved organic matter (DOM), are responsible for the enhanced Hg recovery. Hg forms strong complexes with organic matter due to its high binding affinity [24, 25]. Also, common complexing ligands, such as chloride and sulfate, can affect the sorption of Hg on the mineral surfaces [26]. Chloride can form aqueous $HgCl_2$ and Hg_2Cl_2 complexes reducing sorption of Hg. Concentrations of dissolved organic carbon (DOC) and chloride at the effluent water were not measured in this study; however, total organic carbon content in the sediment is higher in the PA than LA (Table 1) and chloride concentration up to 170 mg/L is reported in the downgradient aquifer from the field monitoring data, partially supporting this possibility.

The dissolved Hg concentrations at the effluents continuously decreased to 3.33 μg/L for PA-TW and 0.079 μg/L for PA-DI by the end of the experiments. Most of the decline was observed before day 13 (5.58 PV) for PA-TW and day 9 (3.91 PV) for PA-DI. The experimental results indicate that flushing of aquifer by injection of water may achieve decreased level of Hg in the field.

Table 4: Hg removal efficiency by flushing.

Column	PA-DI	PA-TW	LA-DI1	LA-DI2	LA-TW
Hg in sediment (mg)	1.048	1.123	0.151	0.156	0.163
Maximum concentration expected in pore water (mg/L)	1.05	1.40	0.18	0.19	0.20
Hg removal by flushing (mg)	0.063	0.22	N/A[a]	N/A[a]	N/A[a]
% Hg removal	6.0	20.3	N/A[a]	N/A[a]	N/A[a]

[a]N/A: not applicable.

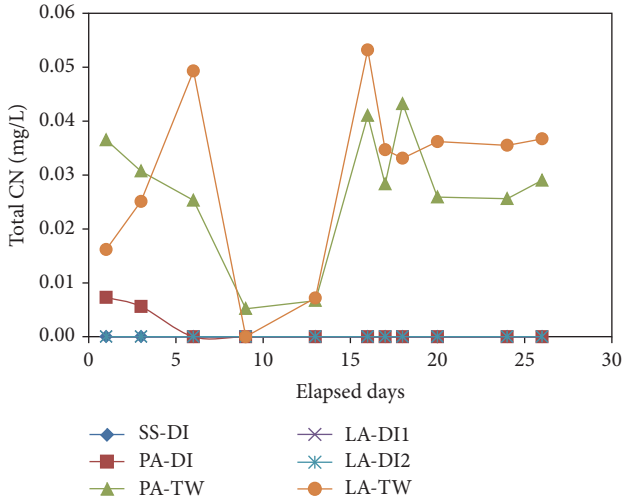

Figure 4: Total cyanide (CN) concentrations measured over time for each column.

In the field site, it is reported that almost all of the dissolved mercury in the aquifer pore water is in the form of cyanide complexes and the neutrally charged $Hg(CN)_2$ complex predominates over other dissolved mercury species at the aquifer pH values. Attenuation of Hg in the main part of the aquifer is only a minor control on dissolved Hg concentrations in the aquifer and the predominance of Hg as a neutrally charged cyanide complex may be responsible for its apparent high mobility in the aquifer. Therefore, the Hg in the sediment cores for this column experiment, which were drilled down gradient of the tailings, can also be present in the form of cyanide complexes.

As explained in Section 2.3, pumping of influent water was stopped for the duration of 18 days between elapsed days 16 and 17, to evaluate if Hg concentration is rebounded due to redissolution/desorption in static conditions. As shown in Figure 3, after the equilibration period, only slight rebound of dissolved Hg concentration was observed only for PA-TW, showing Hg concentration of 7.70 μg/L at elapsed day 18 from 0.81 μg/L at elapsed day 17 (there is one day of lag time for sampling that has representative effluent water sample from the column). It is not certain whether or not further rebound could be observed over longer period of static condition.

Based on the Hg content in the solid samples (0.196 mg/kg for PA and 0.0287 mg/kg for LA) and sediment masses and pore volumes in each column, the maximum Hg concentrations expected in water, if all of Hg is dissolved into pore water, were calculated to be 1.05–1.40 mg/L for PA and 0.18–0.20 mg/L for LA (Table 4). The highest Hg concentration observed in the effluent of PA was 0.102 mg/L, only 7–10% of the maximum concentration expected from complete dissolution. The amounts of water passed through the columns between two adjacent sampling events and the effluent Hg concentrations at each sampling event provide masses of Hg flushed out between the two sampling events. By summing up the masses of Hg flushed out for the entire sampling period, Hg removal by flushing was calculated to be 0.063 mg for PA-DI and 0.227 mg for PA-TW. These values correspond to 6.0 and 20.3% of removal of Hg inventory in the sediments of PA-DI and PA-TW, respectively. The results indicate that flushing of aquifer by injecting water, particularly the treated water, can achieve significant amount of Hg removal from the sediment under the conditions similar to this experiment.

3.2. Total Cyanide (CN). Figure 4 shows the total cyanide (CN) concentrations measured over time for each column. The total CN concentrations at the column effluents were generally low (0.026–0.053 mg/L for PA-TW and LA-TW and nondetectable level (<0.005 mg/L) for the rest of the columns, except for early times in PA-DI). The effluent total CN concentrations for PA-TW and LA-TW were roughly comparable to the total CN concentration in the treated water (0.0231 mg/L, Table 2). It is also possible that some cyanide was released from the sediments. The lower values for two sampling events at elapsed days 9 and 13 could be experimental artifacts. It appears that the total CN initially present in PA-DI column was flushed out as the deionized source water continued to be supplied to the column.

Cyanide is a strong complexing agent and it may enhance the mobility of many dissolved metals, including Hg, in the tailings pore water. Dissolved mercury cyanide complexes may exist in the forms of $Hg(CN)_2$, $Hg(CN)_3^-$, and $Hg(CN)_4^{2-}$. In the acidic pH conditions in the tailings, anionic mercury cyanide complexes are adsorbed onto clays, iron and aluminum oxides, and oxyhydroxides due to the positive surface charge of these materials [27, 28]. The dissociation of surface cyanide complexes may occur upon geochemical changes [21, 29], which might be the case for the conditions in the flushing column experiments. The pH values of the column effluents (pH ~ 4 for PA and ~5 to 6 for LA, Figure 5(a)) were in the range where HCN is the predominant form of free cyanide.

3.3. pH, Alkalinity, and Electrical Conductivity (EC). Figure 5(a) shows the effluent pH values measured over time for

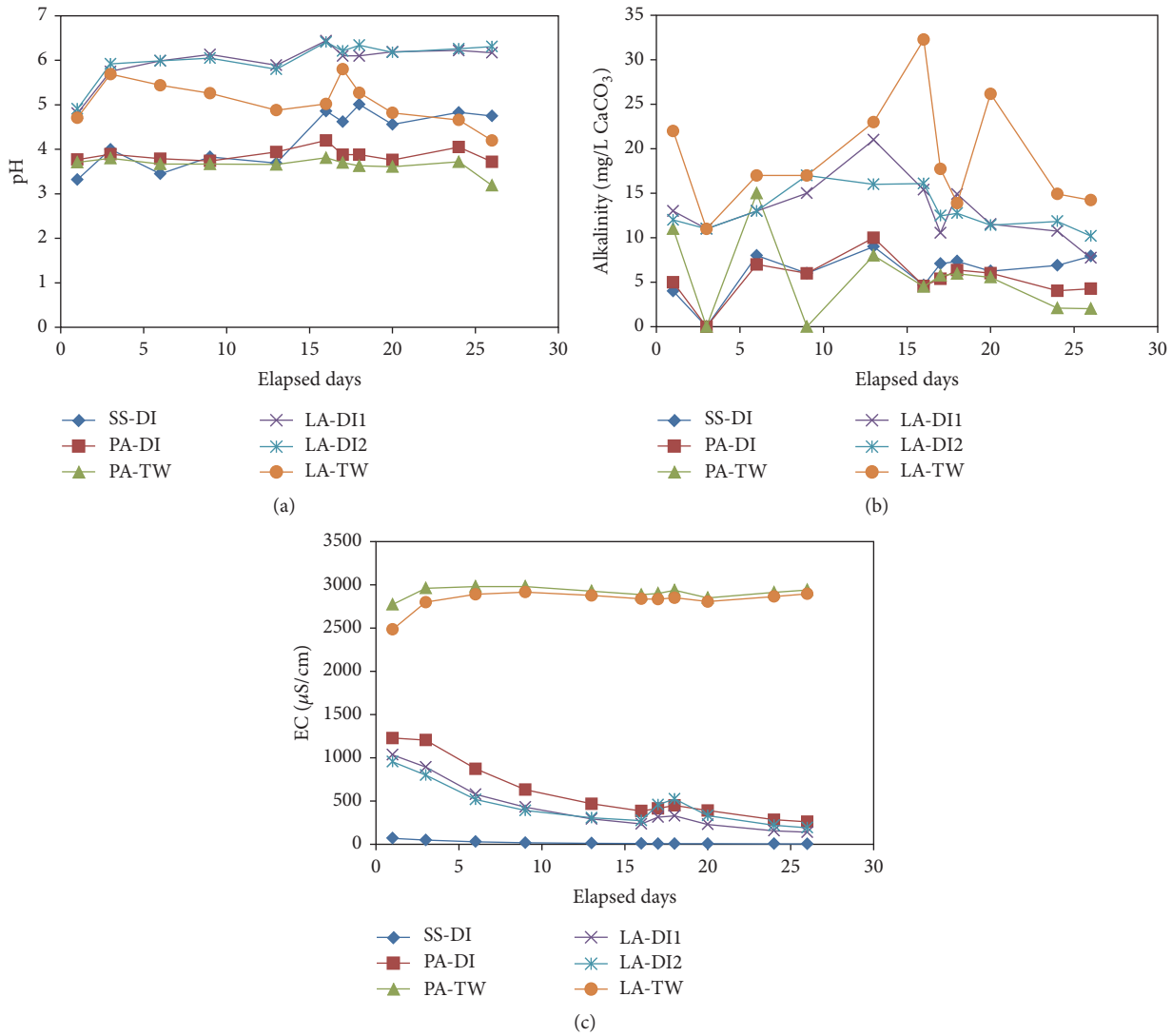

Figure 5: (a) pH, (b) alkalinity, and (c) EC measured over time for each column.

each column. Generally, higher pH values for LA columns are observed compared to those for PA columns, which is consistent with the paste pHs for the sediments (4.24 and 6.35 for PA and LA, resp., for 1 : 2 solid : water, Table 1). This indicates that naturally acidic pH values are present in the perched aquifer due to occurrences of sulfur mineralization in the area. Gradual decline in pH observed for LA-TW could be due to dissolution of alumino-silicate minerals in this column (see Figure 7).

It is not certain why pH for the control column (SS-DI) showed low pH (<4) until day 16. One possible cause is the remnant of acidic pore water that was initially present because of acid washing. As explained in Section 2.2, silica sand was washed with 5% HNO_3 solution overnight and rinsed with deionized water. Although the measured pH for the top water after rinsing was back to normal, some remnant of acidic water might be present in the pore spaces because more silica sand was used for the control column. This potential effect may be minimal for the other columns because only bottom and top ~ 2.5 cm ends were filled with silica sand for the other columns, while almost half was filled with silica sand for the control column.

Figure 5(b) shows the total alkalinities measured over time for each column. Alkalinities for PA columns were 4–15 mg/L as $CaCO_3$, while they were 8–32 mg/L as $CaCO_3$ for LA columns. For comparison, the influent TW water had alkalinity of 14–17 mg/L as $CaCO_3$. The higher alkalinity values for LA columns compared to PA columns are probably due to dissolution of carbonate minerals in LA. The Ca contents in the sediments were 1060 and 2430 mg/kg for PA and LA, respectively, and Mg contents were 2610 and 3010 mg/kg for PA and LA, respectively, supporting this explanation. This is consistent with the dissolved Ca and Mg concentrations at the effluents (see Figures 7(a) and 7(b)) and also consistent with the effluent pH values (Figure 5(a)).

The trends of EC (Figure 5(c)) show that dissolved components in the columns receiving deionized water are generally flushed out, while the columns receiving treated

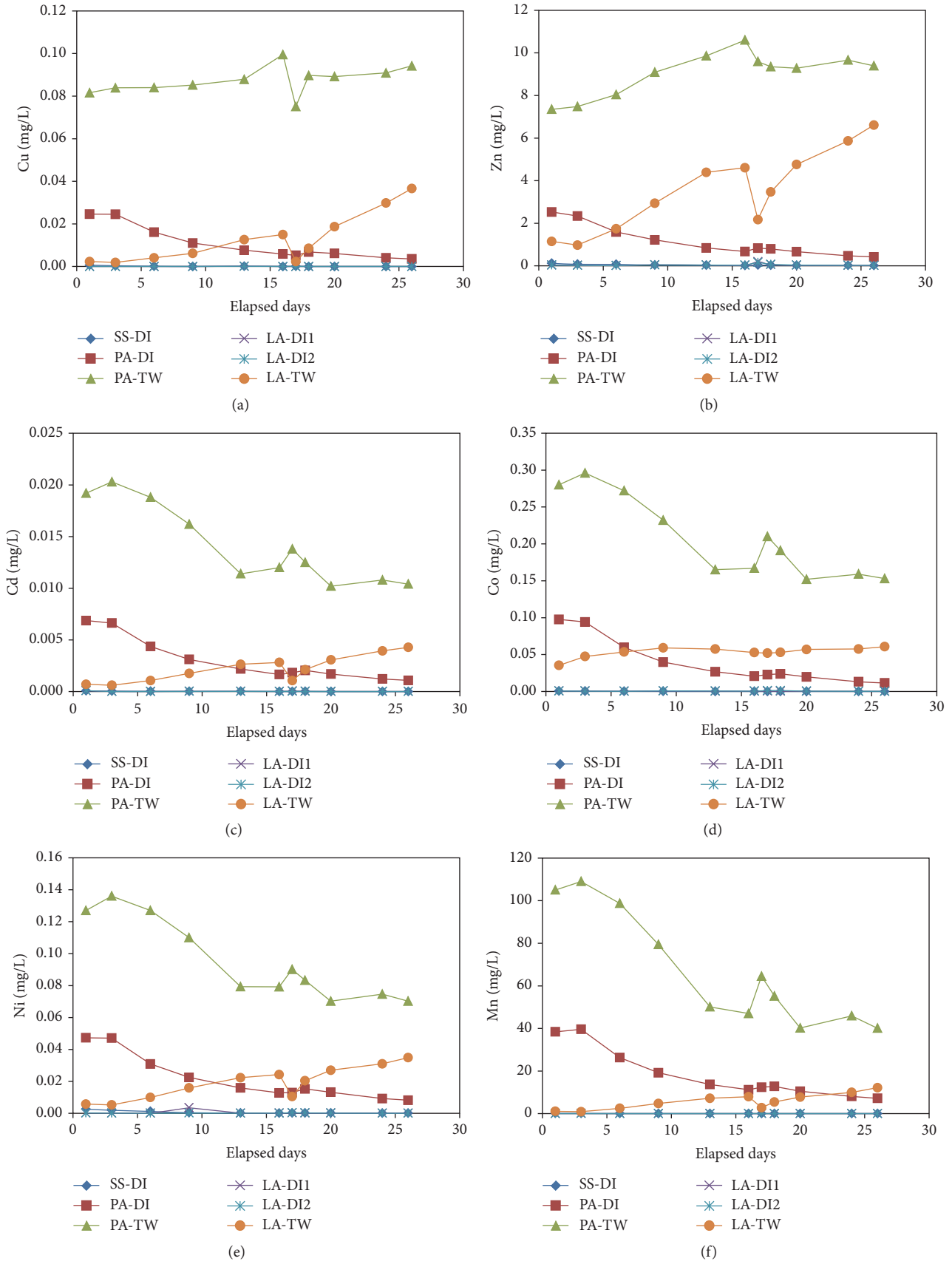

Figure 6: Continued.

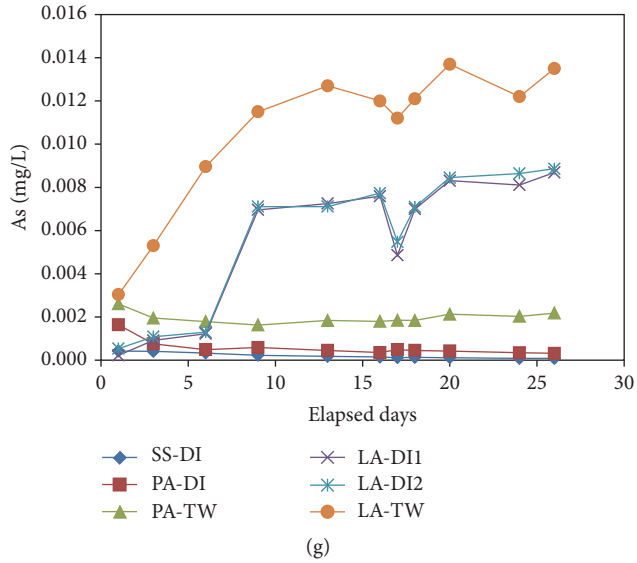

Figure 6: (a) Cu, (b) Zn, (c) Cd, (d) Co, (e) Ni, (f) Mn, and (g) As concentrations measured over time for each column.

water show more or less consistent EC over the course of the experiments, primarily due to already high total dissolved solids (TDS) in the treated water.

3.4. Other Metals and Cations. Considering similar complexation behaviors of Hg, Cu, and Zn with cyanide, it was expected that the trends of Cu and Zn concentrations are similar to those of Hg. It was the case for the columns receiving deionized water (Figures 6(a) and 6(b)); however, for the columns receiving the treated water, Cu and Zn concentrations generally increased as the experiment progressed, except for the elapsed days 16 and 17 when the static conditions were tested. This may be partly due to the fact that the sediments contained higher Cu and Zn contents (Cu content of 85.9 and 52.9 mg/kg and Zn content of 358 and 407 mg/kg for PA and LA, resp.) relative to Hg (0.196 mg/kg for PA and 0.0287 mg/kg for LA). While complexation of Cu and Zn with cyanide could explain the elevated Cu and Zn concentrations for PA-TW and LA-TW, the total cyanide concentrations at the effluents were low (0.026–0.053 mg/L for PA-TW and LA-TW), suggesting the presence of other complexing agents in the treated water other than cyanide, similar to the case for Hg.

The trends for Cd, Co, Ni, and Mn (Figures 6(c)–6(f)) were similar to those for Cu and Zn; however, PA-TW showed general decreases in concentrations as the experiment progressed, suggesting flushing of these elements out of the sediments instead of increases in concentrations due to dissolution/desorption or complexation. Dissolved As concentrations at the column effluents were higher for LA than for PA (Figure 6(g)), although the solid sample analyses showed higher value for PA than LA (282 and 178 mg/kg for PA and LA, resp.). Dissolved As, which is not complexed with cyanide, is attenuated due to adsorption onto and coprecipitation with secondary metal oxides and (oxy)hydroxides under neutral or acidic pH conditions [30]. Thus, the release of As in LA columns could be related to desorption of As associated with dissolution of oxides and (oxy)hydroxides that was previously precipitated in this sediment. It may also be caused by reductive dissolution of As-bearing oxyhydroxides such as ferrihydrite [31].

The effluent Ca and Mg concentrations (Figures 7(a) and 7(b)) suggest that dissolution of carbonate minerals could be the source of Ca and Mg in most of the columns, while flushing is predominant in PA-DI. The releases of Al, K, Na, and Si (Figures 7(c)–7(f)) may indicate dissolution of aluminosilicate minerals, such as feldspar, in the sediments. It is shown that the aquifer materials consist primarily of quartz and feldspar, with lesser amounts of clay, mica, and iron oxides and oxyhydroxides. The trends for Al (Figure 7(c)) are different from other elements (K, Na, and Si, Figures 7(d)–7(f)), indicating the precipitation and dissolution of other Al-containing minerals, such as amorphous $Al(OH)_3$, gibbsite, and alunite, or Al-complexation may also be controlling Al concentrations.

4. Conclusions

The column experiments evaluated removal of Hg from the aquifer sediments using potential flushing waters including the treated water from the water treatment plant and deionized water. The results showed that columns packed with perched aquifer material had flushing of Hg, with the general decline of effluent Hg concentrations over time (from 0.05–0.1 mg/L in the beginning of the experiment to 0.0001–0.003 mg/L at the completion of the experiment). About 5–20% Hg had been flushed out from the sediment during the experiments (about 10 pore volumes), while most of flushing occurred within 5 pore volumes.

The results suggest that flushing of Hg in the aquifer materials by injection of water has the potential to be effective at reducing Hg concentrations in the aquifer. Removal of

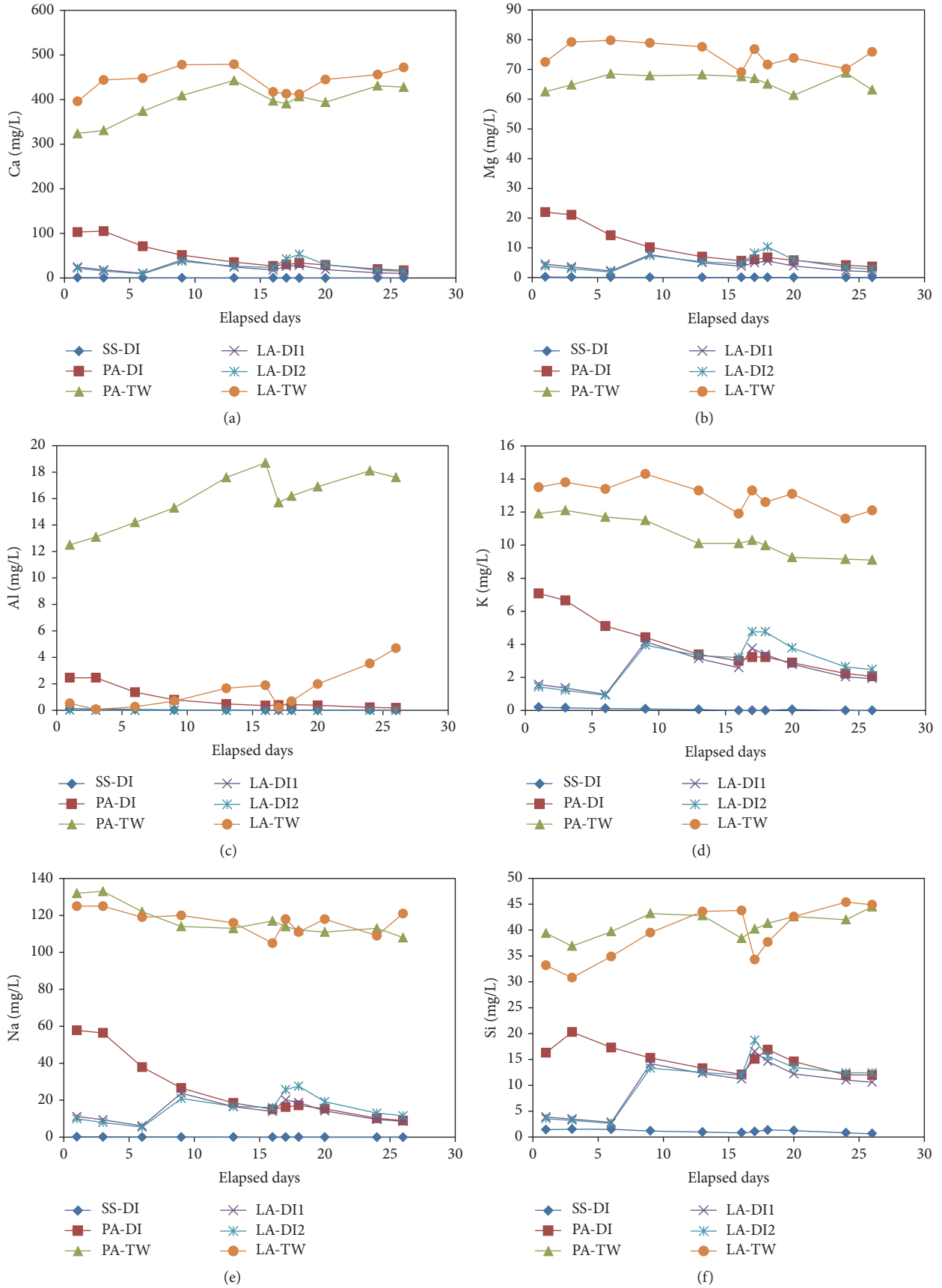

Figure 7: (a) Ca, (b) Mg, (c) Al, (d) K, (e) Na, and (f) Si concentrations measured over time for each column.

up to 20% of the Hg inventory in the sediment could be achievable. The results also indicate that the treated water from the water treatment plant is a reasonable flushing solution, probably due to complexing agents contained in the treated water.

It should be noted, however, that the field condition can be different from the experimental conditions. For example, the flow velocity in the column was 6.5–7.3 cm/day, while the groundwater velocity during the injection could be as high as 2 m/day in the field. The difference in contact time may affect dissolved Hg concentrations in the flushed water. Also, the actual field injection may deliver up to 3 pore volumes for a period of 3 months, indicating that extended period of injection may be required to obtain desirable results.

The solid-phase analyses, as well as the results of the column experiments, showed that the perched aquifer contained more Hg compared to lower aquifer and only the perched aquifer showed flushing of Hg out of the sediment. Perched aquifer material has more Hg than lower aquifer material (0.196 mg/kg versus 0.0287 mg/kg). This result indicates heterogeneity of aquifer geochemistry that needs to be considered in the field practice.

Possibility of redissolution/desorption of Hg after static conditions (for the duration of 18 days) was tested, showing only slight rebound of Hg concentrations. However, because of the limited time frame for this study, it is not certain whether or not further rebound could be observed over longer periods of static conditions. Additional testing for longer periods of static conditions could confirm this behavior.

As shown in the experiments, complexation of Hg with complexing agents can enhance removal of Hg by flushing. Testing of water containing added complexing agents, such as ethylenediaminetetraacetic acid (EDTA) and ethylenediamine-*N*,*N*′-disuccinic acid (EDDS), a biodegradable alternative to EDTA, can be used to evaluate the enhanced removal of Hg by complexation and its potential benefits.

Competing Interests

The author declares that they have no competing interests.

Acknowledgments

Funding for this research was provided by the Basic Science Research Program through the National Research Foundation of Korea (NRF) funded by the Ministry of Education (NRF-2014R1A1A2058040) and by the "R&D Project on Environmental Management of Geologic CO_2 Storage" from the KEITI (Project no. 2014001810003).

References

[1] W. Salomons, "Environmental impact of metals derived from mining activities: processes, predictions, prevention," *Journal of Geochemical Exploration*, vol. 52, no. 1-2, pp. 5–23, 1995.

[2] J. J. Rytuba, "Mercury from mineral deposits and potential environmental impact," *Environmental Geology*, vol. 43, no. 3, pp. 326–338, 2003.

[3] United Nations Environmental Programme, "Technical and economical criteria for processing mercury-containing tailings," Final Report, nited Nations Environmental Programme, Division of Technology, Industry, and Economics, 2010.

[4] S. C. Brooks and G. R. Southworth, "History of mercury use and environmental contamination at the Oak Ridge Y-12 Plant," *Environmental Pollution*, vol. 159, no. 1, pp. 219–228, 2011.

[5] D. Watson, C. Miller, B. Lester et al., "Mercury source zone identification using soil vapor sampling and analysis," *Frontiers of Environmental Science and Engineering*, vol. 9, no. 4, pp. 596–604, 2015.

[6] J.-C. J. Bonzongo, B. W. Nemer, and W. B. Lyons, "Hydrological controls on water chemistry and mercury biotransformation in a closed river system: the Carson River, Nevada," *Applied Geochemistry*, vol. 21, no. 11, pp. 1999–2009, 2006.

[7] M. M. Matlock, B. S. Howerton, M. A. van Aelstyn, F. L. Nordstrom, and D. A. Atwood, "Advanced mercury removal from gold leachate solutions prior to gold and silver extraction: a field study from an active gold mine in Peru," *Environmental Science and Technology*, vol. 36, no. 7, pp. 1636–1639, 2002.

[8] A. Tadjeddine and A. Le Rille, "Adsorption of cyanide on gold single crystal investigated by in situ visible-infrared difference frequency generation," *Electrochimica Acta*, vol. 45, no. 4-5, pp. 601–609, 1999.

[9] M. A. Rawashdeh-Omary, M. A. Omary, and H. H. Patterson, "Oligomerization of $Au(CN)_2^-$ and $Ag(CN)_2^-$ ions in solution via ground-state aurophilic and argentophilic bonding," *Journal of the American Chemical Society*, vol. 122, no. 42, pp. 10371–10380, 2000.

[10] K. L. Rees and J. S. J. van Deventer, "The role of metal-cyanide species in leaching gold from a copper concentrate," *Minerals Engineering*, vol. 12, no. 8, pp. 877–892, 1999.

[11] C. S. Kim, G. E. Brown Jr., and J. J. Rytuba, "Characterization and speciation of mercury-bearing mine wastes using X-ray absorption spectroscopy," *The Science of the Total Environment*, vol. 261, no. 1–3, pp. 157–168, 2000.

[12] C. S. Kim, J. J. Rytuba, and G. E. Brown Jr., "Geological and anthropogenic factors influencing mercury speciation in mine wastes: an EXAFS spectroscopy study," *Applied Geochemistry*, vol. 19, no. 3, pp. 379–393, 2004.

[13] T. A. Al, M. I. Leybourne, A. C. Maprani et al., "Effects of acid-sulfate weathering and cyanide-containing gold tailings on the transport and fate of mercury and other metals in Gossan Creek: Murray Brook mine, New Brunswick, Canada," *Applied Geochemistry*, vol. 21, no. 11, pp. 1969–1985, 2006.

[14] G. A. Gill and K. W. Bruland, "Mercury speciation in surface freshwater systems in California and other areas," *Environmental Science and Technology*, vol. 24, no. 9, pp. 1392–1400, 1990.

[15] A. J. Slowey, S. B. Johnson, J. J. Rytuba, and G. E. Brown Jr., "Role of organic acids in promoting colloidal transport of mercury from mine tailings," *Environmental Science and Technology*, vol. 39, no. 20, pp. 7869–7874, 2005.

[16] J. J. Rytuba, "Mercury mine drainage and processes that control its environmental impact," *The Science of the Total Environment*, vol. 260, no. 1–3, pp. 57–71, 2000.

[17] C. G. Weisener, K. S. Sale, D. J. A. Smyth, and D. W. Blowes, "Field column study using zerovalent iron for mercury removal

from contaminated groundwater," *Environmental Science and Technology*, vol. 39, no. 16, pp. 6306–6312, 2005.

[18] B. D. Gibson, C. J. Ptacek, M. B. J. Lindsay, and D. W. Blowes, "Examining mechanisms of groundwater Hg(II) treatment by reactive materials: an EXAFS study," *Environmental Science and Technology*, vol. 45, no. 24, pp. 10415–10421, 2011.

[19] J. D. Vernon and J.-C. J. Bonzongo, "Volatilization and sorption of dissolved mercury by metallic iron of different particle sizes: implications for treatment of mercury contaminated water effluents," *Journal of Hazardous Materials*, vol. 276, pp. 408–414, 2014.

[20] P. Liu, C. J. Ptacek, D. W. Blowes, and R. C. Landis, "Mechanisms of mercury removal by biochars produced from different feedstocks determined using X-ray absorption spectroscopy," *Journal of Hazardous Materials*, vol. 308, pp. 233–242, 2016.

[21] S. A. Shaw, T. A. Al, and K. T. B. MacQuarrie, "Mercury mobility in unsaturated gold mine tailings, Murray Brook mine, New Brunswick, Canada," *Applied Geochemistry*, vol. 21, no. 11, pp. 1986–1998, 2006.

[22] A. Navarro, E. Cardellach, and M. Corbella, "Mercury mobility in mine waste from Hg-mining areas in Almería, Andalusia (Se Spain)," *Journal of Geochemical Exploration*, vol. 101, no. 3, pp. 236–246, 2009.

[23] R. H. Loeppert and D. L. Suarez, "Gravimetric method for loss of carbon dioxide," in *Methods of Soil Analysis: Part 3. Chemical Methods*, J. M. Bartels and J. M. Bigham, Eds., Book Series No. 5, ASA and SSSA, Madison, Wis, USA, 3rd edition, 1996.

[24] C. H. Lamborg, C.-M. Tseng, W. F. Fitzgerald, P. H. Balcom, and C. R. Hammerschmidt, "Determination of the mercury complexation characteristics of dissolved organic matter in natural waters with 'reducible Hg' titrations," *Environmental Science and Technology*, vol. 37, no. 15, pp. 3316–3322, 2003.

[25] C. L. Miller, L. Liang, and B. Gu, "Competitive ligand exchange reveals time dependant changes in the reactivity of Hg-dissolved organic matter complexes," *Environmental Chemistry*, vol. 9, no. 6, pp. 495–501, 2012.

[26] C. S. Kim, J. J. Rytuba, and G. E. Brown Jr., "EXAFS study of mercury(II) sorption to Fe- and Al-(hydr)oxides: II. Effects of chloride and sulfate," *Journal of Colloid and Interface Science*, vol. 270, no. 1, pp. 9–20, 2004.

[27] A. Smith and T. Mudder, *The Chemistry and Treatment of Cyanidation Wastes*, Mining Journal Books Limited, London, UK, 1991.

[28] T. Rennert and T. Mansfeldt, "Sorption of iron-cyanide complexes in soils," *Soil Science Society of America Journal*, vol. 66, no. 2, pp. 437–444, 2002.

[29] G. J. Zagury, K. Oudjehani, and L. Deschênes, "Characterization and availability of cyanide in solid mine tailings from gold extraction plants," *Science of the Total Environment*, vol. 320, no. 2-3, pp. 211–224, 2004.

[30] P. L. Smedley and D. G. Kinniburgh, "A review of the source, behaviour and distribution of arsenic in natural waters," *Applied Geochemistry*, vol. 17, no. 5, pp. 517–568, 2002.

[31] J. J. Erbs, T. S. Berquó, B. C. Reinsch, G. V. Lowry, S. K. Banerjee, and R. L. Penn, "Reductive dissolution of arsenic-bearing ferrihydrite," *Geochimica et Cosmochimica Acta*, vol. 74, no. 12, pp. 3382–3395, 2010.

Hindawi Publishing Corporation
Journal of Chemistry
Volume 2016, Article ID 6701828, 8 pages
http://dx.doi.org/10.1155/2016/6701828

Research Article

Adsorbability Enhancement of Macroporous Resin by Dielectric Barrier Discharge Plasma Treatment to Phenol in Water

Shoufeng Tang, Deling Yuan, and Jun He

Key Laboratory of Applied Chemistry, School of Environmental and Chemical Engineering, Yanshan University, Qinhuangdao 066004, China

Correspondence should be addressed to Deling Yuan; yuandeling83@126.com

Received 22 July 2016; Revised 2 October 2016; Accepted 9 October 2016

Academic Editor: Reyna Natividad

In order to enhance the adsorption efficiency and economize the use of macroporous resin, we have treated it with the dielectric barrier discharge (DBD) plasma to improve its adsorbing capacity for phenol. The effects of operation conditions, for instance, applied voltage, treated time, and air flow rate on resin, were investigated by adsorption kinetics and isotherms. Results showed that the adsorption data were in good agreement with the pseudo-second-order and Freundlich equation. Experimental results showed that the modified resin was 156.5 mg/g and 39.2% higher than the untreated sample, when the modified conditions were conducted for discharge voltage 20 kV, treatment time 45 min, and air flow rate 1.2 L/min. The resin was characterized by FTIR and nitrogen adsorption isotherms before and after the DBD processes. It was found that the reason for the enhancement of resin adsorbability was attributed to the DBD plasma changing the surface physical and chemical structure.

1. Introduction

Adsorption on resin is a simple technology that has found widespread application in the treatment of industrial effluents [1, 2]. In order to improve the adsorption efficiency and economize the use of macroporous resins, many studies on surface modifications have been carried out, and they mainly focus on chemical modifications [3–6].

Recently, nonthermal plasma technology for material modification becomes one of the most active fields [7–9]. Nonthermal plasma surface treatment has lots of features, including no change to the thermal and mechanical properties of the adsorbents, but altering the various interfacial characteristics, such as the surface chemical and physical structure properties [10, 11].

Dielectric barrier discharge (DBD) could produce spatially uniform and stable plasma under atmospheric pressure easily [12, 13]. Using oxygen as gas source in DBD plasma, various kinds of active species including high-energy electron, ozone, and many other strong oxidized free radicals have been generated [12, 13], which could be beneficial to the material surface modification. However, to our knowledge, systematic studies on surface modification of resin by DBD plasma are still limited.

Phenol is a kind of highly toxic and refractory pollutant commonly emitted from industrial effluents. This paper presents a new approach that macroporous resin is modified in a double dielectric barriers discharge reactor. The effects of operation parameters for phenol removal, including applied voltage, treatment time, and gas flow rate on adsorption kinetics and adsorption isotherms, have been investigated. FTIR and N_2 adsorption isotherms were employed to evaluate the surface chemical and physical characteristics of macroporous resin treated with DBD plasma. The obtained experimental data demonstrate the DBD could enhance the phenol adsorption of resin effectively.

2. Experimental

2.1. Materials. Macroporous resin (XDA-1, diameter 0.3–1.2 mm) was acquired from Xi'an Sunresin and Technology Co. Ltd. (Shanxi province, China). Before adsorption, the resins were under extraction filtration process using ethanol for at least 8 hours and then dried in an oven at 333 K

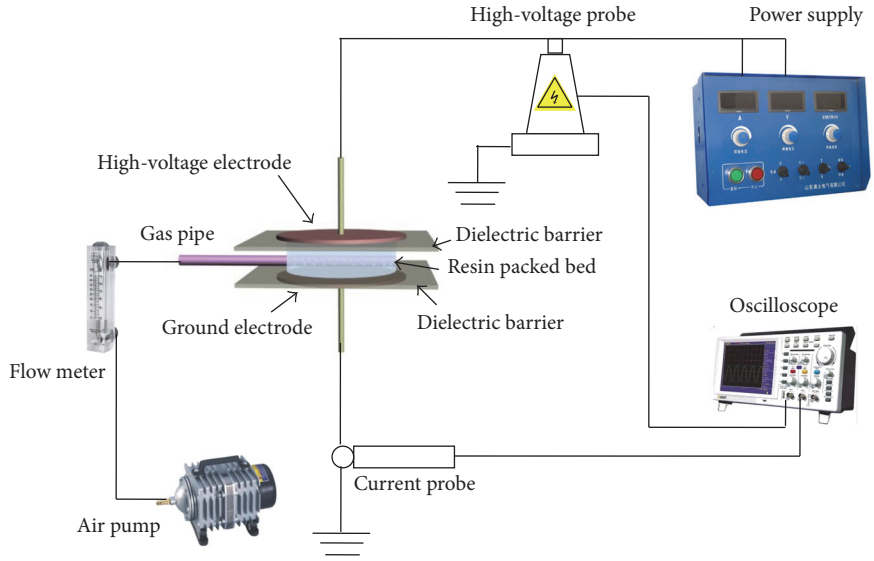

Figure 1: Schematics of the experimental system.

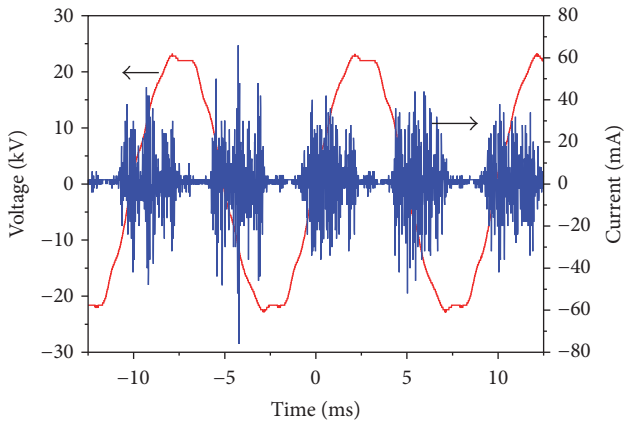

Figure 2: Typical voltage and current waveforms of the DBD reactor.

overnight. Phenol and other chemical reagents were of analytical grade and purchased from the Tianjin Kermel Co., Ltd. (Tianjin, China). The phenol solution was prepared with deionized water.

2.2. Experimental System. Figure 1 illustrated the DBD treatment system. The DBD reactor was driven by an alternating current (AC) high-voltage power. The reactor was comprised of two parallel-plate stainless steel electrodes as the high-voltage and ground electrodes, respectively, and each electrode was covered by one quartz glass dielectric, and the detailed dimensions were given in our previous articles [14]. The AC power frequency was 100 Hz, and the peak voltage was adjustable in a range of 0–50 kV. In every batch experiment, before the DBD treatment began, 2.0 g resin was filled in the packed bed of the reactor. Typical voltage and current waveforms of the DBD reactor were shown in Figure 2, which were recorded by a digital oscilloscope (Tektronix TDS2014, USA) equipped with a voltage probe (Tektronix P6015A, USA) and a current probe (Tektronix P6021, USA).

2.3. Adsorption Experiments. After the DBD plasma treatment, 0.05, 0.1, 0.2, 0.3, and 0.4 g of resins were added into the phenol solution (50 mL, 100 mg/L) in a series of sealed flasks. These flasks were placed in the water bath shaker with a 150 rpm of agitation speed.

The concentrations of phenol were determined by a UV-vis spectrophotometer (UV-2102C, Unico (Shanghai, China) Instrument Co., Ltd.). The equilibrium adsorption capacity of phenol onto the adsorbent (q_e, mg/g) was calculated from the following equation:

$$q_e = (C_o - C_e)\frac{V}{m}, \tag{1}$$

where C_o and C_e (mg/L) are the initial and equilibrium concentration of phenol in solution, q_e is the adsorption capacity of resin, V (L) is the volume of solution, and m (g) is the adsorbent mass.

Langmuir isotherm is used to describe a type of monolayer adsorption, which has a finite number of identical localized sites:

$$q_e = \frac{Q_o K_L C_e}{1 + K_L C_e}, \tag{2}$$

where Q_o (mg/g) is the initial amount of adsorbate and K_L (L/g) is a Langmuir constant related to the affinity of the binding site.

Freundlich sorption isotherm is the most widely used equation describing the nonideal and reversible adsorption, and the equation has the form:

$$q_e = K_F C_e^{1/n}, \tag{3}$$

Table 1: Effect of applied voltage on adsorption kinetic parameters of virgin and DBD treated resins.

Sample	Exp $q_{e,\exp}$ (mg/g)	Lagergren first-order			Pseudo-second-order		
		k_1 (1/h)	$q_{e,\text{cal}}$ (mg/g)	R^2	k_2 (g/mg/h)	$q_{e,\text{cal}}$ (mg/g)	R^2
Untreated	112.4	0.510	102.3	0.923	0.002348	117.2	0.984
16 kV	123.4	0.453	111.1	0.976	0.004471	126.4	0.995
20 kV	133.1	0.443	124.2	0.961	0.004788	137.8	0.996
24 kV	114.7	0.429	101.3	0.893	0.002669	117.8	0.988
28 kV	109.0	0.461	94.5	0.942	0.002567	112.1	0.986

Table 2: Effect of applied voltage on Freundlich and Langmuir parameters of virgin and DBD treated resins.

Adsorbents	Freundlich parameters			Langmuir parameters		
	$1/n$	K_F ($\text{mg}^{(1-1/n)}\text{L}^{1/n}/\text{g}$)	R^2	q_m (mg/g)	K_L (L/mg)	R^2
Untreated	0.7681	1.966	0.977	115.3	0.01053	0.926
16 kV	0.7766	2.174	0.978	126.0	0.01106	0.936
20 kV	0.7778	2.318	0.989	133.8	0.01119	0.934
24 kV	0.7736	2.035	0.980	119.0	0.0108	0.928
28 kV	0.7913	1.581	0.986	114.0	0.00884	0.937

where K_F ($\text{mg}^{(1-1/n)}\text{L}^{1/n}/\text{g}$) is a Freundlich constant related to adsorption amount and n is also a Freundlich constant to measure the adsorption intensity.

For the purpose of comparison the adsorption capacity before and after DBD plasma treatment, the same method was used to determine the adsorption kinetic of the virgin resin.

2.4. Analysis Method. The surface characteristics of virgin and DBD treated resins were measured from the N_2 adsorption at 77 K by NOVA 1200 (Quanta Chrome) equipment. Surface areas were identified according to the BET method. FTIR spectroscopy (EQUINOX5 spectrophotometer) was applied to characterize the chemical properties of the resin samples.

3. Results and Discussion

3.1. DBD Modified Resins Adsorption. In this study, the comparison of adsorption dynamics and isotherms of the resins has been done before and after DBD treatment under different operation parameters, including applied voltage, treatment time, and air flow rate, which allow us to obtain valuable information for the adsorption process of these resin samples.

Adsorption kinetic is an important physical characterization of adsorption rate, because it could indicate the removal rate of the pollutant in aqueous solutions and provide valuable data for a good understanding of the sorption reactions mechanism. Therefore, Lagergren first-order and pseudo-second-order kinetic models were utilized in the analysis of the experimental data in this study.

Analysis of isotherm data is very important for predicting adsorption capacity and adsorption behavior of adsorbent. Several models have appeared in the literature to evaluate adsorption isotherm. The Langmuir and Freundlich [15] models are the models often used. In the Langmuir model it is assumed that the adsorption is totally homogeneous in the surface of adsorbent, whereas it is a highly heterogeneous surface for Freundlich model. Thus, Langmuir and Freundlich isotherm models were tested and made the comparison of the goodness of fit based on the experimental data.

3.1.1. Effect of Applied Voltage. The strength of electric field obviously affects the generation of active species (such as O_3, ·OH, etc.) in DBD plasma and thus can influence the resin modification. The other viable run parameters were included below: treatment time 30 min and air flow rate 0.8 L/min. Figure 3 presented the adsorption kinetics of virgin and DBD treated resins under different applied voltages. For both samples, phenol adsorption was quick in the initial 7 h, and the equilibrium plateau was achieved in 12 h. After that time point, the adsorption amount kept constant.

The fast adsorption is probably because the pore structure of the resins offered sufficient available adsorption sites in the early stage of the adsorption. Thereafter the active sites reduced with increasing contact time, and then the observed plateau appeared.

Table 1 showed the kinetics of phenol adsorption on the resin samples. The Lagergren first-order and pseudo-second-order models were used to investigate the adsorption mechanisms. Clearly, the correlation coefficients of the pseudo-second-order model were much closer to 1, and the calculated q_e accorded well with the experimental data, proving that this model could be adopted for the simulation of the resins adsorption to phenol.

The fitting results of the Freundlich and Langmuir models were presented in Table 2 and Figure 4. The contrasted results showed that the theoretical calculations of Freundlich model could be better fitted to the experimental data than Langmuir.

In summary, as shown in Figures 3 and 4 and Tables 1 and 2, the DBD treated resins adsorption capacities upgraded firstly and then decreased with the rising peak voltages. When the applied voltage was 20 kV, the optimal adsorption

Table 3: Effect of treatment time on adsorption kinetic parameters of virgin and DBD treated resins.

Sample	Exp $q_{e,\exp}$ (mg/g)	Lagergren first-order			Pseudo-second-order		
		k_1 (1/h)	$q_{e,\text{cal}}$ (mg/g)	R^2	k_2 (g/mg/h)	$q_{e,\text{cal}}$ (mg/g)	R^2
Untreated	112.4	0.510	102.3	0.923	0.002348	117.2	0.984
15 min	113.6	0.431	101.7	0.898	0.002545	116.4	0.986
30 min	133.1	0.443	124.2	0.961	0.004788	137.8	0.996
45 min	145.8	0.430	134.5	0.877	0.005135	147.1	0.997
65 min	103.2	0.374	97.5	0.906	0.002077	104.6	0.966

Table 4: Effect of applied voltage on Freundlich and Langmuir parameters of virgin and DBD treated resins.

Adsorbents	Freundlich parameters			Langmuir parameters		
	$1/n$	K_F (mg$^{(1-1/n)}$L$^{1/n}$/g)	R^2	q_m (mg/g)	K_L (L/mg)	R^2
Untreated	0.7681	1.966	0.987	115.3	0.01053	0.923
15 min	0.7657	2.093	0.975	117.4	0.01107	0.912
30 min	0.7778	2.318	0.982	133.8	0.01119	0.934
45 min	0.7864	2.485	0.974	148.9	0.01103	0.901
60 min	0.7599	1.822	0.982	106.5	0.01018	0.945

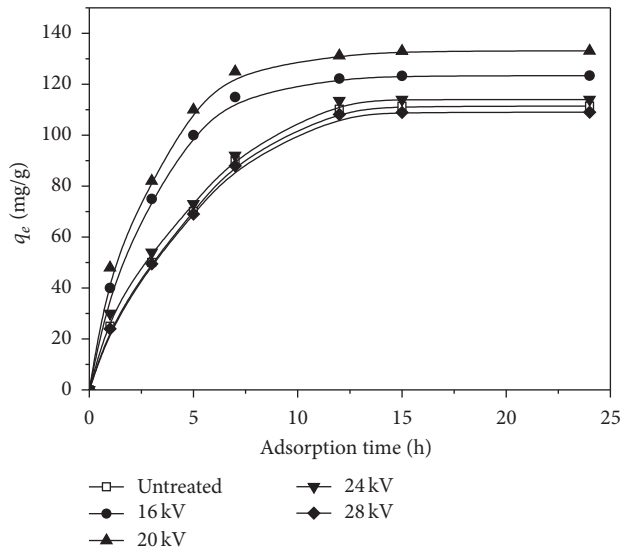

Figure 3: Effect of applied voltage on adsorption kinetics of virgin and DBD treated resins.

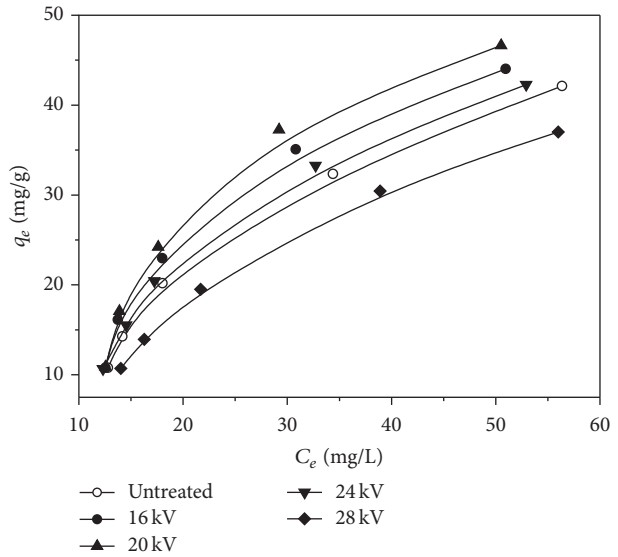

Figure 4: Effect of applied voltage on adsorption isotherm of virgin and DBD treated resins.

capability was 133.1 mg/g and increased 19.4% than untreated one. In contrast, the adsorption capability of 28 kV was 109.0 mg/g and lower than virgin one. It is generally believed that the excessive voltage produces more active species in plasma, which could affect the surface properties of resins, resulting in the fact that their hydrophilicity was enhanced. Under this circumstance, it was helpful for the adsorption of resin for phenol. However, the energetic species could also collapse the adsorption channels and framework of resin under higher voltage, leading to the decline of adsorption capacity of resin.

3.1.2. Effect of Treatment Time. The DBD plasma treatment time would also directly affect the generation of active species and the influence of the modification of the resins, so the effects of treatment time on resin adsorption should be clarified. The other practical run parameters included applied voltage 20 kV and air flow rate 0.8 L/min. Figure 5 indicated the adsorption kinetics of virgin and DBD treated resins under different treatment times. Combining the determination coefficient in Table 3, it is obvious that the pseudo-second-order model can imitate the phenol adsorption on resins more accurately than the Lagergren first-order.

The fitting results of the Freundlich and Langmuir isotherms were shown in Table 4 and Figure 6. By analysis and comparison, the Freundlich model could be better used to simulate the phenol adsorption onto virgin resin and DBD

Table 5: Effect of air flow rate on adsorption kinetic parameters of virgin and DBD treated resins.

Sample	Exp $q_{e,exp}$ (mg/g)	Lagergren first-order			Pseudo-second-order		
		k_1 (1/h)	$q_{e,cal}$ (mg/g)	R^2	k_2 (g/mg/h)	$q_{e,cal}$ (mg/g)	R^2
Untreated	112.4	0.510	102.3	0.923	0.002348	117.2	0.984
0.4 L/min	111.4	0.454	101.7	0.937	0.002592	115.6	0.985
0.8 L/min	145.8	0.430	134.5	0.877	0.005135	147.1	0.997
1.2 L/min	156.5	0.410	144.9	0.984	0.004462	157.8	0.997
1.6 L/min	127.1	0.387	117.4	0.931	0.002796	130.5	0.987

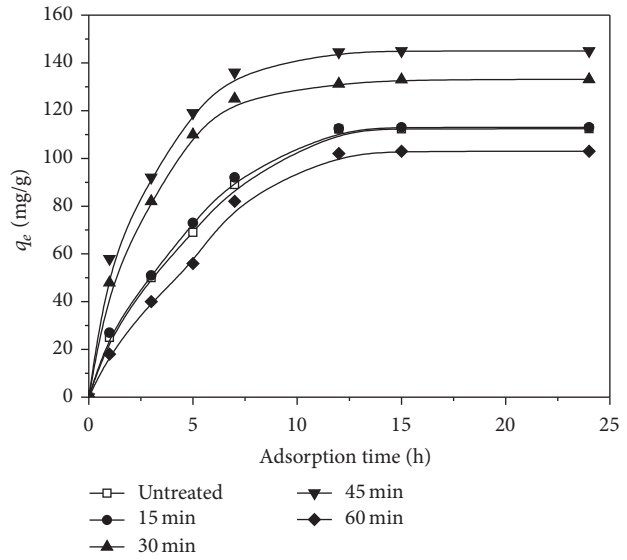

Figure 5: Effect of treatment time on adsorption kinetics of virgin and DBD treated resins.

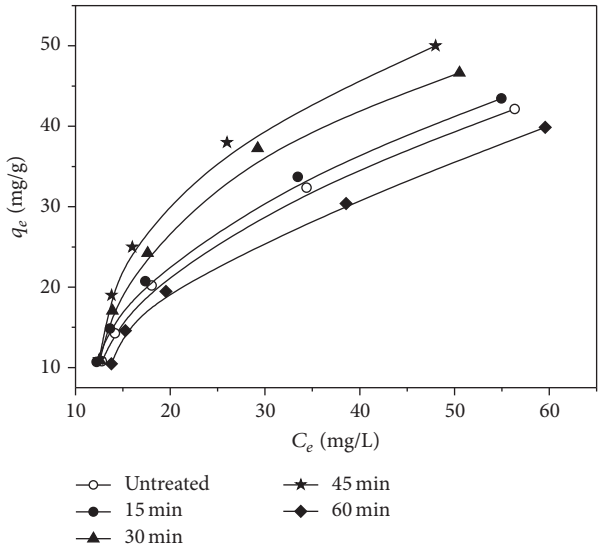

Figure 6: Effect of treatment time on adsorption isotherm of virgin and DBD treated resins.

treated resins under different treatment times than Langmuir model.

The adsorption quantity of phenol firstly rose and then decreased with increasing treatment time (as shown in Figure 5 and Table 3). When the discharge time increased to 45 min, the corresponding adsorption amount was 145.8 mg/g, which was enhanced to 29.0% compared to the untreated sample, whereas when discharge time extended to 60 min, the adsorption capability was 8.4% lower than virgin one. This phenomenon may be attributed to the following reasons: the increase of the treatment time resulted in the increase in the collision and even reacting probabilities between the active species and the resin, which was favorable to enhance the variety of oxygen-containing functional groups on the resin surface, strengthening the electrostatic and hydrogen bonding interactions during the phenol adsorption process. On the contrary, prolonging the reaction time would oxidize the surface structure of resin, resulting in the fact that its textural structure collapses. So it could be suggested that a longer treatment time is harmful to the adsorption of resin.

3.1.3. Effect of Air Flow Rate. Gas source is essential for non-thermal plasma production. In this research, we employed air as the gas source for the DBD reactor. Other experimental conditions included applied voltage 20 kV and treatment time 45 min.

Figure 7 shows the sorption kinetics of virgin and DBD treated resins under different air flow rates. Combining Table 5, it is obvious that the pseudo-second-order model has higher goodness of fit than the Lagergren first-order. Moreover, combining Figure 8 and Table 6, it can be inferred that the Freundlich model can fit better the phenol adsorption data for virgin resin and DBD treated resins.

From these figures and tables, it can be seen that the adsorption was increased with air flow rate. However, the improvement of the adsorption at 0.4 L/min was not so promoted compared with the untreated one. The maximal adsorption was achieved 156.5 mg/g when air flow rate was 1.2 L/min, which was 39.2% higher than the untreated one. It could be suggested that, with the increase of air flow, the amount of active species produced by DBD plasma is increased, which is benefit to improve the surface chemical properties. Conversely, when the air flow rate is too high (1.6 L/min), the residence time of active species in DBD reactor is shortened and their utilization efficiencies are correspondingly decreased. Hence, the combined effects of above

Table 6: Effect of air flow rate on Freundlich and Langmuir parameters of virgin and DBD treated resins.

Adsorbents	Freundlich parameters			Langmuir parameters		
	$1/n$	K_F ($mg^{(1-1/n)}L^{1/n}/g$)	R^2	q_m (mg/g)	K_L (L/mg)	R^2
Untreated	0.7681	1.966	0.977	115.3	0.01053	0.936
0.4 L/min	0.7597	2.123	0.974	114.2	0.01140	0.924
0.8 L/min	0.7864	2.485	0.964	148.9	0.01103	0.909
1.2 L/min	0.7918	2.574	0.953	156.1	0.01108	0.887
1.6 L/min	0.7549	2.615	0.965	127.2	0.01273	0.895

Table 7: Structural properties of the virgin and DBD treated resin.

Resin samples	S_{BET} (m^2/g)	$S_{Micropore}$ (m^2/g)	$V_{Micropore}$ (m^3/g)	$V_{Total\ pore}$ (m^3/g)	Average pore diameter (nm)
Untreated	944.6	715.8	0.377	0.586	1.428
DBD 1	1056.4	838.9	0.593	0.658	1.428
DBD 2	937.7	605.1	0.301	0.610	1.418

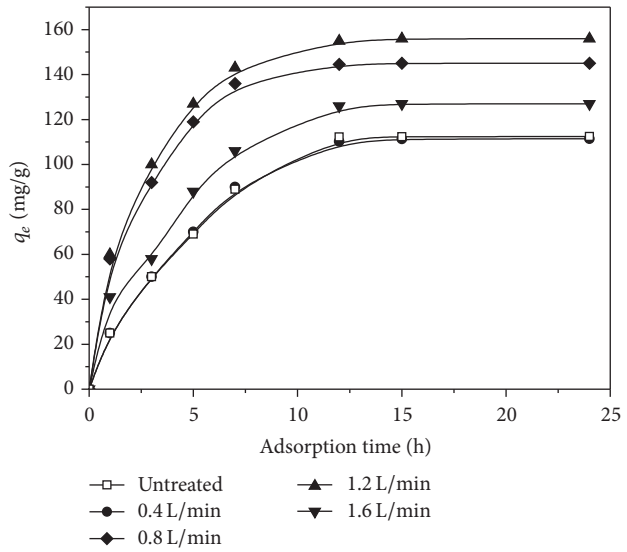

Figure 7: Effect of air flow rate on adsorption kinetics of virgin and DBD treated resins.

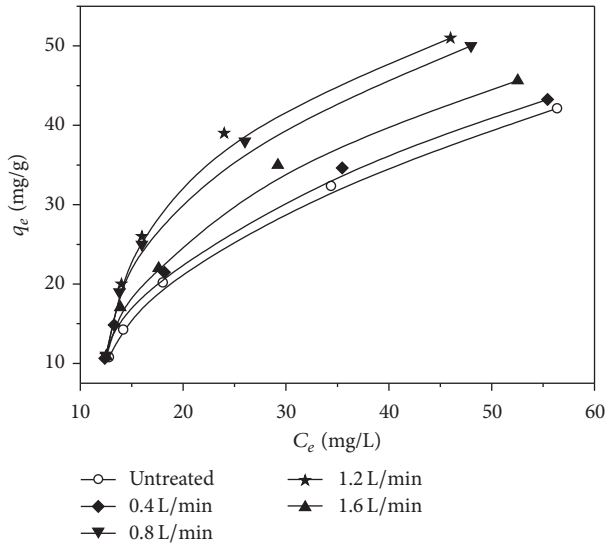

Figure 8: Effect of air flow rate on adsorption isotherm of virgin and DBD treated resins.

two aspects resulted in the best adsorption performance achieved when the air flow rate was 1.2 L/min.

3.2. FTIR Spectra Analysis. Figure 9 illustrates the FTIR spectra obtained from the virgin and DBD plasma treated resins. The sample presenting the highest adsorption capacity, which was treated under the condition of applied voltage 20 kV, treatment time 45 min, and air flow rate 1.2 L/min, was named as DBD 1. In contrast, DBD 2 was the lowest result at applied voltage 20 kV, treatment time 60 min, and air flow rate 0.8 L/min. From Figure 9, DBD 1 and DBD 2 had two strong representative peaks at 1604 and 2922 cm^{-1} similar to untreated one but were both greatly weakened. DBD also results in some new changes for the IR spectrum of treated samples. Firstly, a moderate C-O stretching band involving hydroxyl groups came back at 1105 cm^{-1}, and appearance of this band might result from DBD treatment [16]. Secondly, the peak at 3600 cm^{-1} disappeared through DBD treatment, which could be assigned to O-H [4].

3.3. Surface Textural Properties. Table 7 mainly generalized the relevant surface structural properties of virgin and DBD treated resin. Based on the information observed in Table 7, it could be noticed that the various data of the DBD treated samples were considerable different from the virgin one. Compared with the untreated resin, DBD 1 resin had a bigger BET surface area, micropore area, micropore volume, and total pore volume. Conversely, all data of DBD 2 has little change compared to the virgin resin. It can be indicated that the surface area and pore volume of DBD 1 were upgraded by the suitable plasma treatment. It is generally believed that the surface textural properties of resin were improved under conditions of DBD 1; at the same time, along with the DBD

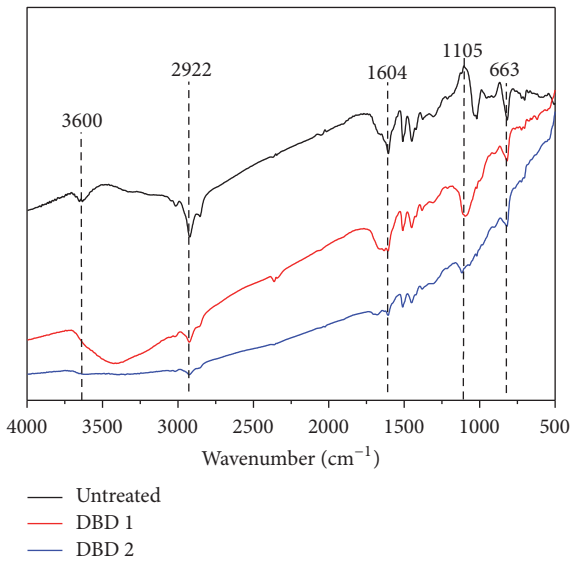

Figure 9: FTIR spectra of untreated and DBD treated resin.

chemical effects, such as electrostatic and hydrogen bonding interactions, the enhancement of adsorption capacity reached.

4. Conclusions

The DBD treatment for surface modification of macroporous resin had been performed for improving its adsorbability for phenol. Significant influences of applied voltage, treatment time, and air flow rate on resin adsorption capacity were observed. The experimental results show that the adsorbability of DBD treated resin was 156.5 mg/g and 39.2% higher than the untreated resin when the treatment was conducted in these conditions, such as discharge voltage 20 kV, treatment time 45 min, and air flow rate 1.2 L/min. The phenol adsorption on resins was fitted well with the pseudo-second-order and Freundlich model, indicating the homogeneity of the resin surface. At the optimum conditions, the DBD treatment increased the surface area and pore volume of the resin but slightly changed the surface chemical properties. The obtained experimental data has demonstrated that the DBD could enhance the phenol adsorption of resin effectively.

Competing Interests

The authors declare that there is no conflict of interests regarding the publication of this paper.

Acknowledgments

The authors acknowledge the financial support supplied by the Natural Science Foundation of Hebei Province, China (Project nos. B2015203303 and B2015203300), the China Postdoctoral Science Foundation (Project no. 2015M580216), the Youth Teacher Independent Research Program of Yanshan University (Project nos. 15LGA013 and 14LGB021), and the Doctoral Foundation Program of Yanshan University (Project nos. B849 and B878).

References

[1] S.-H. Lin and R.-S. Juang, "Adsorption of phenol and its derivatives from water using synthetic resins and low-cost natural adsorbents: a review," *Journal of Environmental Management*, vol. 90, no. 3, pp. 1336–1349, 2009.

[2] I. Turku and T. Sainio, "Modeling of adsorptive removal of benzalkonium chloride from water with a polymeric adsorbent," *Separation and Purification Technology*, vol. 69, no. 2, pp. 185–194, 2009.

[3] G. Li, X. Wei, W. Wang, T. He, and X. Li, "Modification of unsaturated polyester resins (UP) and reinforced UP resins via plasma treatment," *Applied Surface Science*, vol. 257, no. 1, pp. 290–295, 2010.

[4] X. Wang, J. Huang, and K. Huang, "Surface chemical modification on hyper-cross-linked resin by hydrophilic carbonyl and hydroxyl groups to be employed as a polymeric adsorbent for adsorption of p-aminobenzoic acid from aqueous solution," *Chemical Engineering Journal*, vol. 162, no. 1, pp. 158–163, 2010.

[5] T. Acsente, M. D. Ionita, M. Teodorescu, V. Marascu, and G. Dinescu, "Surface modification of polymethylmethacrylate foils using an atmospheric pressure plasma jet in presence of water vapors," *Thin Solid Films*, vol. 614, pp. 25–30, 2016.

[6] K. Chen, H. Lyu, S. Hao, G. Luo, S. Zhang, and J. Chen, "Separation of phenolic compounds with modified adsorption resin from aqueous phase products of hydrothermal liquefaction of rice straw," *Bioresource Technology*, vol. 182, pp. 160–168, 2015.

[7] J. Huang, L. Yang, X. Wu, M. Xu, Y.-N. Liu, and S. Deng, "Phenol adsorption on $\alpha,\alpha\prime$-dichloro-p-xylene (DCX) and 4,4′-bis(chloromethyl)-1,1′-biphenyl (BCMBP) modified XAD-4 resins from aqueous solutions," *Chemical Engineering Journal*, vol. 222, pp. 1–8, 2013.

[8] L. Karam, M. Casetta, N. E. Chihib, F. Bentiss, U. Maschke, and C. Jama, "Optimization of cold nitrogen plasma surface modification process for setting up antimicrobial low density polyethylene films," *Journal of the Taiwan Institute of Chemical Engineers*, vol. 64, pp. 299–305, 2016.

[9] Q. Li, H. Lu, H. Xiao, K. Gao, and M. Diao, "Adsorption capacity of superabsorbent resin composite enhanced by non-thermal plasma and its adsorption kinetics and isotherms to lead ion in water," *Journal of Environmental Chemical Engineering*, vol. 1, no. 4, pp. 996–1003, 2013.

[10] S. Kodama, H. Habaki, H. Sekiguchi, and J. Kawasaki, "Surface modification of adsorbents by dielectric barrier discharge," *Thin Solid Films*, vol. 407, no. 1-2, pp. 151–155, 2002.

[11] S. Marais, M. Métayer, M. Labbé et al., "Surface modification by low-pressure glow discharge plasma of an unsaturated polyester resin: effect on water diffusivity and permeability," *Surface and Coatings Technology*, vol. 122, no. 2-3, pp. 247–259, 1999.

[12] L. Xin, Y. Sun, J. Feng, J. Wang, and D. He, "Degradation of triclosan in aqueous solution by dielectric barrier discharge plasma combined with activated carbon fibers," *Chemosphere*, vol. 144, pp. 855–863, 2016.

[13] C. A. Aggelopoulos, P. Svarnas, M. I. Klapa, and C. D. Tsakiroglou, "Dielectric barrier discharge plasma used as a means for the remediation of soils contaminated by non-aqueous phase liquids," *Chemical Engineering Journal*, vol. 270, pp. 428–436, 2015.

[14] S. Tang, N. Lu, J. Li, K. Shang, and Y. Wu, "Improved phenol decomposition and simultaneous regeneration of granular activated carbon by the addition of a titanium dioxide catalyst under a dielectric barrier discharge plasma," *Carbon*, vol. 53, pp. 380–390, 2013.

[15] B. J. Pan, B. C. Pan, W. M. Zhang, L. Lv, Q. X. Zhang, and S. R. Zheng, "Development of polymeric and polymer-based hybrid adsorbents for pollutants removal from waters," *Chemical Engineering Journal*, vol. 151, no. 1–3, pp. 19–29, 2009.

[16] G. C. Pratt, C. Y. Wu, D. Bock et al., "Comparing air dispersion model predictions with measured concentrations of VOCs in urban communities," *Environmental Science and Technology*, vol. 38, no. 7, pp. 1949–1959, 2004.

Hindawi Publishing Corporation
Journal of Chemistry
Volume 2016, Article ID 9378460, 11 pages
http://dx.doi.org/10.1155/2016/9378460

Research Article

Performance Investigation of O-Ring Vacuum Membrane Distillation Module for Water Desalination

Adnan Alhathal Alanezi,[1] H. Abdallah,[2] E. El-Zanati,[2] Adnan Ahmad,[3] and Adel O. Sharif[4]

[1]*Department of Chemical Engineering Technology, College of Technological Studies, The Public Authority for Applied Education and Training (PAAET), P.O. Box 117, 44010 Sabah Al-Salem, Kuwait*
[2]*Chemical Engineering and Pilot Plant Department, Engineering Research Division, National Research Centre, Dokki, Giza, Egypt*
[3]*Department of Polymer Engineering and Technology, University of the Punjab, Quaid-e-Azam Campus, P.O. Box 54590, Lahore, Pakistan*
[4]*Qatar Environment and Energy Research Institute, HBKU, Qatar Foundation, Doha, Qatar*

Correspondence should be addressed to Adnan Alhathal Alanezi; aa.alanezi@paaet.edu.kw

Received 14 July 2016; Revised 9 September 2016; Accepted 15 September 2016

Academic Editor: Rosa Maria Gomez Espinosa

A new O-ring flat sheet membrane module design was used to investigate the performance of Vacuum Membrane Distillation (VMD) for water desalination using two commercial polytetrafluoroethylene (PTFE) and polyvinylidene fluoride (PVDF) flat sheet hydrophobic membranes. The design of the membrane module proved its applicability for achieving a high heat transfer coefficient of the order of 10^3 (W/m^2 K) and a high Reynolds number (Re). VMD experiments were conducted to measure the heat and mass transfer coefficients within the membrane module. The effects of the process parameters, such as the feed temperature, feed flow rate, vacuum degree, and feed concentration, on the permeate flux have been investigated. The feed temperature, feed flow rate, and vacuum degree play an important role in enhancing the performance of the VMD process; therefore, optimizing all of these parameters is the best way to achieve a high permeate flux. The PTFE membrane showed better performance than the PVDF membrane in VMD desalination. The obtained water flux is relatively high compared to that reported in the literature, reaching 43.8 and 52.6 (kg/m^2 h) for PVDF and PTFE, respectively. The salt rejection of NaCl was higher than 99% for both membranes.

1. Introduction

Fresh water shortages and water scarcity are major global issues, especially in the arid and semiarid regions of the world, where fresh water can be obtained through different techniques, such as the desalination of seawater. Desalination is one of the earliest methods known to man of obtaining salt-free water. In nature, it forms the source of the hydrological cycle. Desalination usually refers to the process of reducing the concentration of salt and dissolved substances in seawater or brackish water to make it palatable and suitable for consumption. In addition to salt removal, some desalination techniques also remove suspended material, organic matter, bacteria, and viruses [1–5]. Desalination has great potential for supplying fresh water for the 2.4 billion people living in coastal areas, which is equivalent to 39% of the world population. As a result, over the past 15 years, the daily water production has increased from approximately 13 million m^3/day to the current 48 million m^3/day in the 17,000 desalination plants operating worldwide [6]. Globally, more than 80% of the world's desalination capacity is provided by two processes: multistage flash (MSF) and reverse osmosis (RO) [7]. However, these technologies are energy intensive, with the energy mainly supplied by fossil fuel sources, and are not linked to renewable energy sources. Among the recent technologies, membrane distillation (MD) has the advantage of performing at moderate temperatures and pressure [2, 3, 8, 9]. MD process is an emerging thermally driven membrane process and can be applied successfully in desalination [10, 11]. The MD process is economical in terms of energy because the heat source for the process can be low grade and/or alternative energy sources such as solar and geothermal energy and because energy is continuously recovered [2, 8, 9, 12]. During the MD process, a hot saline solution is brought

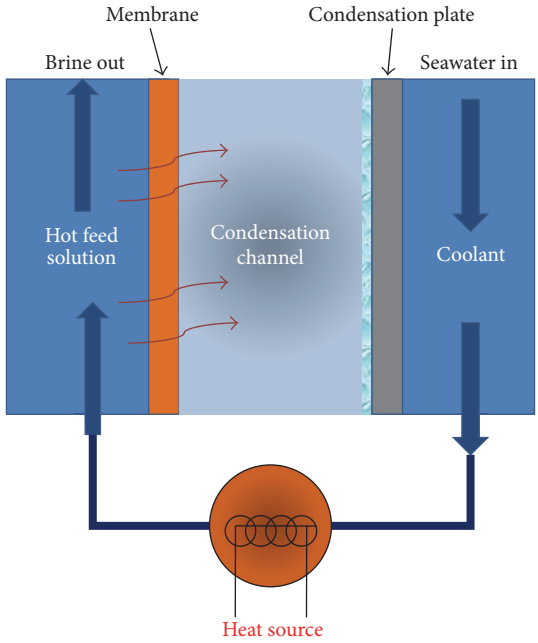

Figure 1: Principle of the membrane distillation (MD) process.

in contact with a hydrophobic membrane, which allows water vapor to diffuse through the membrane, restricting the flow of liquid and hence dissolved salts through its pores [13, 14]. The mass transfer of water vapor through the membrane pores is facilitated by the vapor pressure difference, as well as the temperature difference between the two sides of the hydrophobic membrane, that is, the feed side and the permeate side, as shown in Figure 1 [2, 3, 8, 14–16]. MD can be divided into four configurations (Figure 2) such as (a) Direct Contact Membrane Distillation (DCMD), where the membrane is in direct contact with the cold and hot fluids, (b) Air Gap Membrane Distillation (AGMD), where an air gap is introduced between the membrane and the condensation surface, (c) Sweeping Gas Membrane Distillation (SGMD), where a cold inert gas is employed to sweep the water vapor at the permeate side to condense outside the membrane module, and (d) Vacuum Membrane Distillation (VMD), where the vacuum is applied to the permeate side by means of a vacuum pump to condense the water vapor outside of the membrane module [2, 9, 10, 17]. The difference between these configurations depends on the way in which the vapor is condensed and/or removed from the membrane module [2]. All four configurations have advantages and disadvantages, depending on their applications with the feed solution to be treated [2, 3, 16, 18]. VMD process has many attractive features compared to other MD configurations, where one of the greatest advantages of the VMD process is that heat conduction across the membrane is negligible due to the very low pressure (i.e., a high vacuum degree) on the permeate side; therefore VMD is highly efficient in terms of energy [2, 19]. Additionally, the low pressure enables the VMD process to achieve the best performance in terms of permeate flux compared to other MD configurations [2, 20]. The mechanism makes the VMD process appropriate for separation of various volatile compounds from their aqueous solutions or a mixture of the same and it is only recently that it was applied for seawater desalination and treatment of RO brines [21, 22] However, VMD process has attracted less attention compared to other MD processes and few papers have focused on the fabrication of membranes modules for VMD applications [22–33]. Therefore, in our previous study, new asymmetric PES/TiO_2NTs (polyethersulfone blends with titanium dioxide nanotubes) blend membranes were successfully fabricated by the phase inversion method. The results showed a significant improvement in the performance of the new membrane compared to the commercial membrane, where the permeate flux and salt rejection reached 5.5 (kg/m^2 h) and 96.7% at 35,000 ppm, respectively [34]. Due to the advantages of the VMD process, the new O-ring membrane module was designed and developed. Therefore, the main objective of this paper is to investigate the effect of the operating conditions such as feed temperature, feed flow rate, vacuum degree, and feed concentration using the O-ring membrane module on the performance of VMD process for two commercial PTFE and PVDF hydrophobic membranes.

2. Experimental Work

2.1. Flat Sheet Membrane Modules. A flat sheet O-ring membrane module was designed and specially manufactured to apply Vacuum Membrane Distillation to seawater desalination (Figure 3). The O-ring membrane module consists of three opening holes, one for controlling the vacuum on the permeate side and the other two for feed and water recycling to the feed tank, where the membrane module was constructed to provide better mixing, which increases the heat and mass transfer coefficients and consequently enhances the performance of the VMD process.

2.2. Experimental Set-Up. The experiments were carried out on a bench scale unit, as shown in Figure 4. The feed solution was continuously fed into the membrane module from the feed tank using a peristaltic feed pump. The feed solution was heated using a hot plate, and the feed temperature T_f (28–65°C) was controlled by a hot plate thermostat and recorded using a thermometer. The flow rates used (27.7, 58.7, 97.2, and 110.2 L/h) were measured by a flow meter connected to the feed pump. Vacuum or low pressure on the permeate side P_p (Pa) was obtained using a vacuum pump. The condenser was designed in an efficient manner in which the water vapor was transferred and drawn through the membrane pores to the condenser and then condensed in a condenser jacket using cooling water. The cooling water was fed and recycled continuously using a peristaltic pump into the condenser jacket with a constant cooling temperature of 5°C. The permeate was collected downstream of the condenser.

2.3. Experimental Procedures. Two commercial hydrophobic microporous flat sheet PTFE and PVDF membranes (Fluoropore, Millipore) were used in this experiment. Their

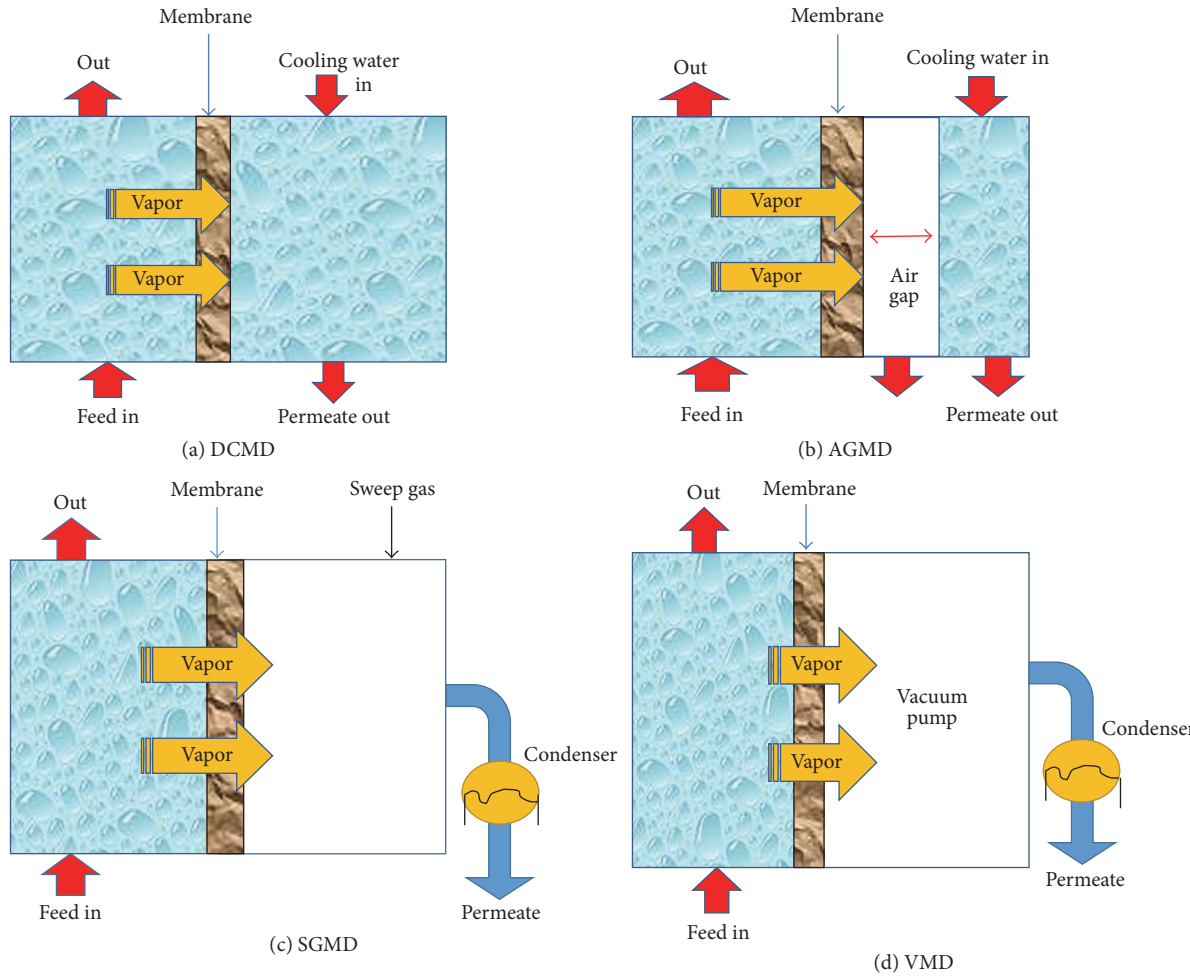

Figure 2: The membrane distillation configurations.

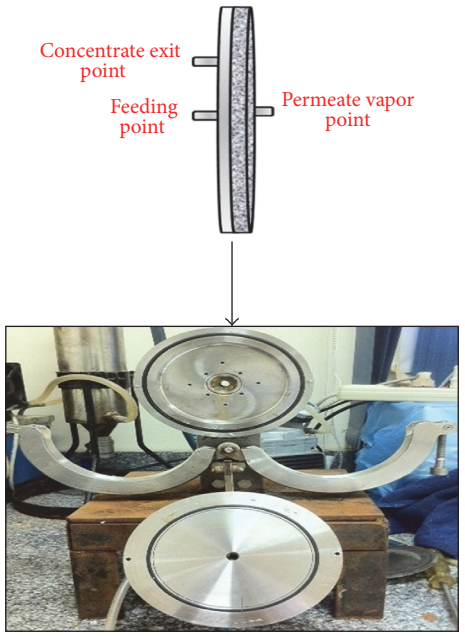

Figure 3: O-ring membrane module.

characteristics are shown in Table 1. The membrane effective area was 117 cm^2. A synthetic salt solution was prepared at different concentrations using commercial sodium chloride (NaCl). Cold water was used to cool the condenser. The feed solutions and permeate solutions were measured using a conductivity meter. The performance of the VMD process in terms of the water flux and salt rejection was investigated for both membranes at different feed temperatures (28, 45, 55, and 65°C), feed flow rates (27.7, 58.7, 97.2, and 110.2 L/h), feed concentrations (10,000, 20,000, and 35,000 mg/L), and vacuum degrees (92, 94, 96, and 97 kPa). During the experiments, the water flux was measured every 15 minutes, where each run lasted for 3 hours and the water flux for each experimental run was the mean value of the fluxes computed in steady state operation with an experimental error of less than 5%. The water flux was calculated using the following formula:

$$J_m = \frac{V}{(A_m t)}, \quad (1)$$

where J_m is the water flux (kg/m^2 h), V is the collected sample volume (L), A_m is the membrane effective area (m^2), and t is the running time (h).

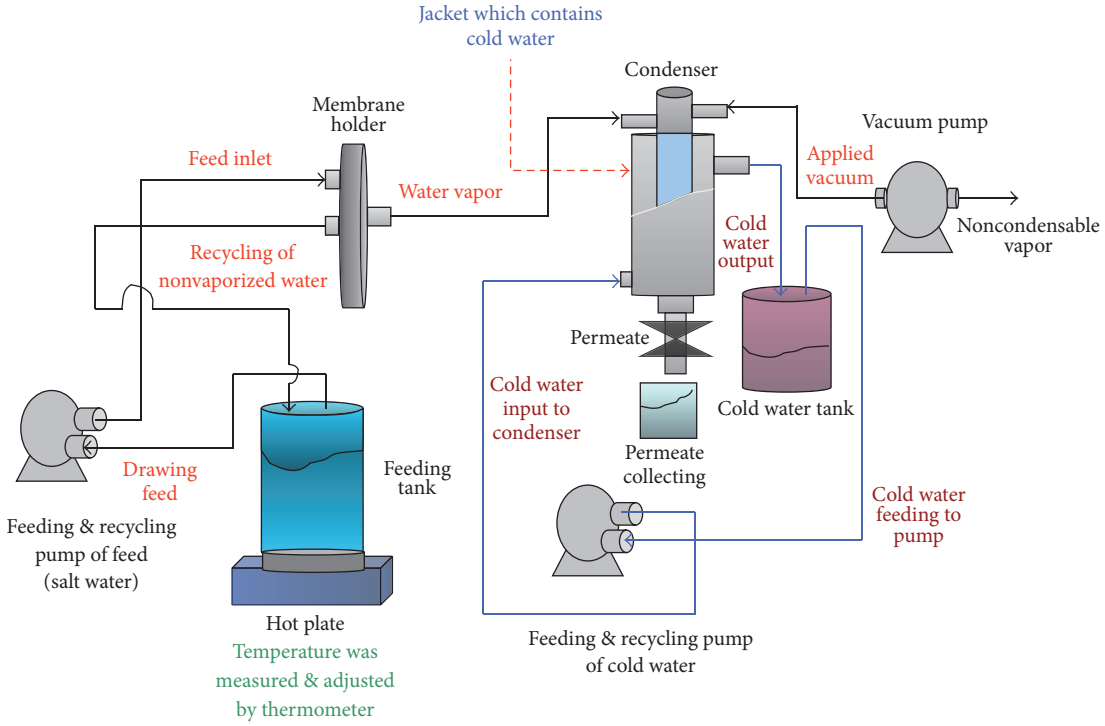

Figure 4: VMD experimental set-up.

Table 1: Membrane properties.

Membrane type	PTFE	PVDF
Pore size (μm)	0.2	0.22
Porosity %	75	75
Thickness (μm)	120	200
Thermal conductivity (W/m·K)	0.28	0.20

3. Results and Discussion

3.1. VMD Experiments for Pure and Saline Water. A series of pure water and saline water (35,000 mg/L) VMD experiments were conducted using two commercial PTFE and PVDF hydrophobic membranes to evaluate the fluid dynamics at the feed boundary layer, where the experimental results were used to evaluate the constant parameters (a and b) of the heat and mass transfer analogy. Pure and saline water were kept in turbulent flow in the membrane module to calculate the heat (h_f) and mass (k_f) transfer coefficients, respectively, from the obtained correlations. A dimensionless Nusselt number (Nu) is commonly used to relate h_f to other factors that affect heat transfer in the feed boundary layer, as illustrated in the equation below:

$$\mathrm{Nu} = \frac{h_f d}{k} = a\,\mathrm{Re}^b\,\mathrm{Pr}^c. \tag{2}$$

$$\log\frac{\mathrm{Nu}}{\mathrm{Pr}^c} = \log a + b\log \mathrm{Re}. \tag{3}$$

The exponent of the Prandtl number (Pr) c is usually equal to 1/3. Therefore, to determine a and b, some of the experimental results with pure water for the two membranes are listed in Table 2. The water flux J_m was measured under various feed flow rates F_f (27.7 to 110.2 L/h), a constant feed temperature T_f (65°C), and vacuum degree levels (92 kPa). As shown in Table 2, the Reynolds number within the membrane module lies in the turbulent flow region, and the Prandtl number is constant (2.77) at 65°C. Figures 5(a) and 5(b) show the results of a straight line equation plotted as $\log \mathrm{Nu}/\mathrm{Pr}^{1/3}$ versus $\log \mathrm{Re}$ for pure and saline water, respectively, where the intercept is equal to $\log a$ and the slope is equal to b, as shown in (3). It is obvious from Figures 5(a) and 5(b) that the value of intercept b is equal to 0.81 and 0.82 and the values of a are $10^{-1.7184}$ and $10^{-1.7277}$, which are equal to 0.0191 and 0.0187, respectively. Therefore, (2) and (3) can be written as shown in (4) and (5). Consider

$$\mathrm{Nu} = \frac{h_f k}{d} = 0.0191\,\mathrm{Re}^{0.81}\,\mathrm{Pr}^{(1/3)}\ \text{Pure water}. \tag{4}$$

$$\mathrm{Nu} = \frac{h_f k}{d} = 0.0187\,\mathrm{Re}^{0.82}\,\mathrm{Pr}^{(1/3)}\ \text{saline water}\,(35{,}000\ \mathrm{mg/L}). \tag{5}$$

Therefore, using (3) and (4), the heat transfer coefficient h_f can be obtained, and because the heat and mass transfer are involved simultaneously in VMD, the mass transfer coefficient k_f on the feed side can be calculated using the equation shown below:

$$\frac{h_f}{k_f} = \frac{k_L}{D_{\mathrm{AB}}\,(\mathrm{Pr}/\mathrm{Sc})^{1/3}}. \tag{6}$$

Table 2: Pure water VMD experimental results for PVDF and PTFE at a 92 kPa vacuum degree.

Run	T_f (°C)	v_f (m/s)	J_m (kg/m^2 h)		h_f (W/m^2 K)	$k_f \times 10^{-2}$	Re	Nu	Pr
			PVDF	PTFE					
1	65	0.32	17.7	19.4	1553.8	3.97	86711.31	288.2	2.77
2	65	0.67	35.7	37.7	2821.6	7.23	183557.7	523.2	2.77
3	65	1.11	53.1	58.9	4225.0	10.83	304052.6	783.5	2.77
4	65	1.25	55.2	63.8	4670.0	11.97	344593.0	866.0	2.77

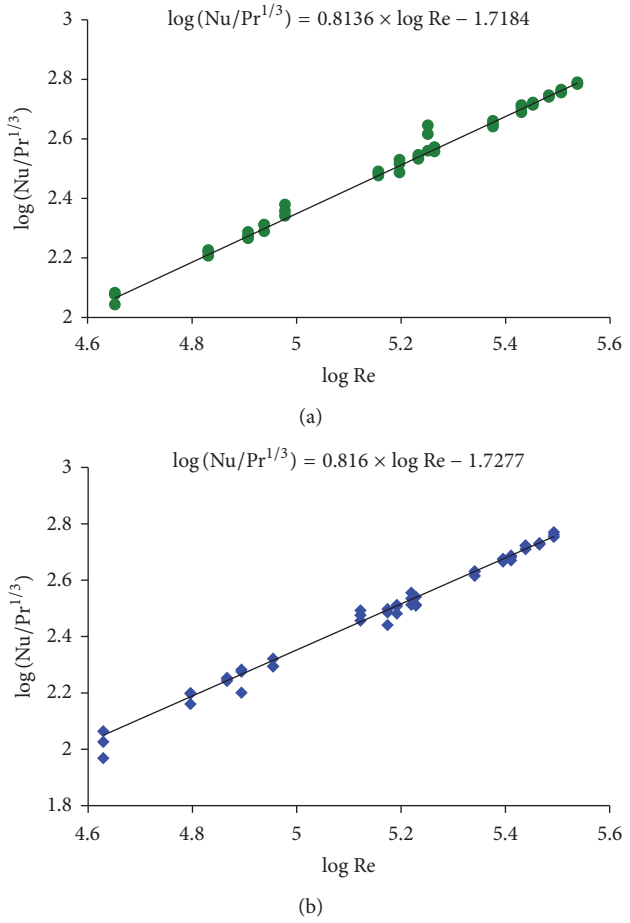

Figure 5: The linear relationship of log(Nu/Pr$^{1/3}$) versus log(Re) for the (a) pure and (b) saline water.

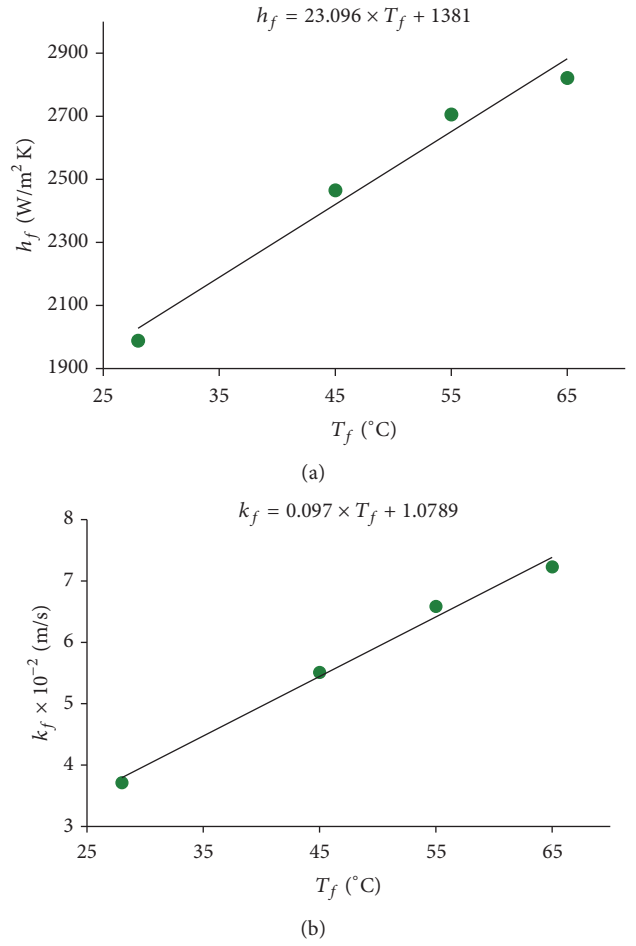

Figure 6: The pure water (a) heat (h_f) and (b) mass (k_f) transfer coefficients versus the feed temperature at a flow rate of 58.7 L/h.

The linear relationship of the heat (h_f) and mass (k_f) transfer coefficients of the membrane module versus the feed temperature T_f for pure and saline water at 58.7 L/h is shown in Figures 6(a) and 6(b) and Table 3, respectively.

Table 3: Derived heat and mass transfer coefficients of saline water.

NaCl concentration, C_f (mg/L)	h_f (W/m^2 K)	$k_f \times 10^{-2}$ (m/s)
10,000	$22.335T_f + 1396.9$	$0.0936T_f + 1.130$
20,000	$21.656T_f + 1398.9$	$0.0903T_f + 1.177$
35,000	$20.679T_f + 1400.8$	$0.0856T_f + 1.242$

3.1.1. VMD Performance. The performance of VMD in terms of its water flux and salt rejection has been studied experimentally by investigating the effects of various operating parameters, such as the feed temperature, feed flow rate, vacuum degree, and NaCl concentration in the feed.

(1) Effect of Feed Temperature. The effect of the feed temperature on the permeate flux of the PVDF and PTFE membranes was studied under different feed flow rate conditions (27.7, 58.7, 97.2, and 110.2 L/h) and a constant vacuum degree (97 kPa) and feed concentration (35,000 mg/L). As shown in Figures 7(a) and 7(b), the feed temperature had a remarkable

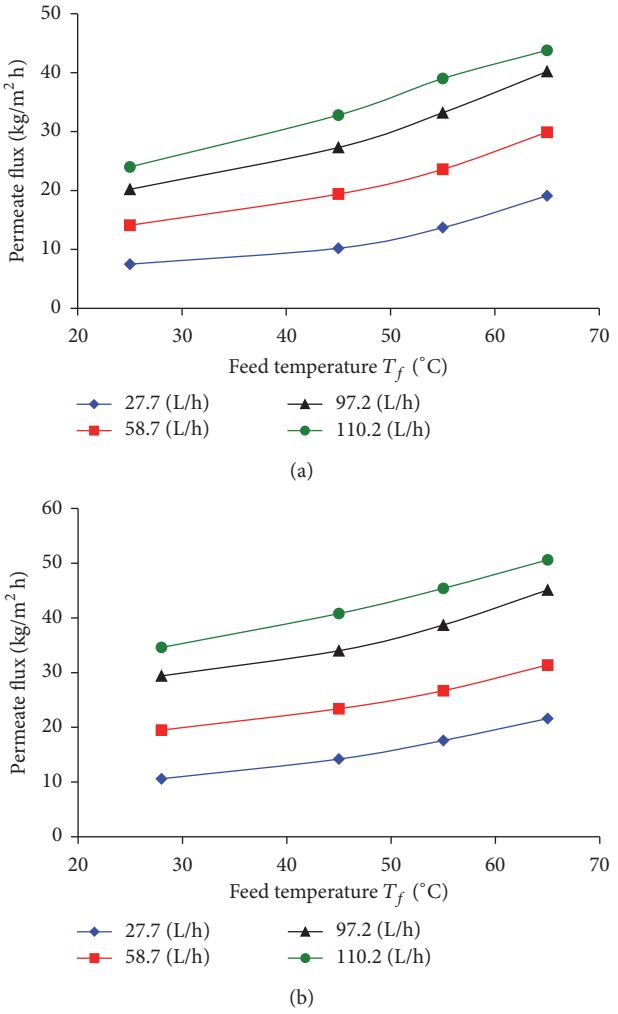

FIGURE 7: The effect of the feed temperature on the permeate flux through (a) PVDF and (b) PTFE membranes at different feed flow rates, with 97 kPa vacuum degree and feed concentration of 35,000 mg/L.

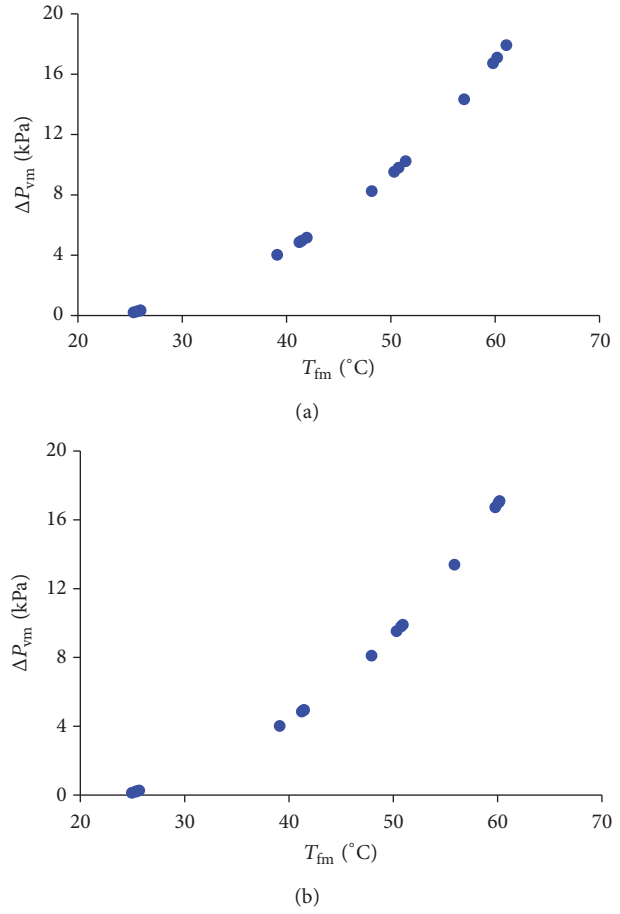

FIGURE 8: The variations in the membrane surface temperature T_{fm} with the vapor pressure difference ΔP_{vm} for the (a) PVDF and (b) PTFE membranes.

influence on the water flux of VMD. As expected, the water flux of VMD for both membranes increases exponentially with the feed temperature. This is due to the major effect of temperature on the water vapor pressure according to the exponential Antoine equation [2, 8, 34]. Increasing the feed temperature decreases the feed viscosity and the thickness of the boundary layer, which significantly enhances the mass transfer coefficient. Furthermore, as shown in Figures 8(a) and 8(b), increasing the feed temperature (T_f) can significantly increase the membrane surface temperature (T_{fm}), which consequently increases the vapor pressure difference ΔP_{vm} across the membrane module and therefore enhances the water flux of VMD, where the feed surface temperature T_{fm} and vapor pressure difference ΔP_{vm} are calculated based on the experimental data for different feed temperatures, feed flow rates, and vacuum levels. For instance, increasing the feed temperature from 28 to 65°C at 110.2 (L/h) increases the VMD water flux from 24 to 45.8 (kg/m^2 h) for PVDF and 34.6 to 52.6 (kg/m^2 h) for PTFE. It is clear that the PTFE membrane provides a much higher water flux than the PVDF membrane. This is mainly due to the difference in membrane thickness (200 μm for PVDF and 120 μm for PTFE) where the thin membrane has a lower resistance to mass transfer across it.

(2) Effect of the Feed Flow Rate. The feed flow rate is also one of the most important parameters that affect the performance of the VMD process. The effect of the feed flow rate on the water flux was investigated for the PVDF and PTFE membranes by changing it from 27.7 to 110.2 (L/h) for different vacuum levels (92, 94, 96, and 97 kPa) at a constant feed concentration of 35,000 mg/L and feed temperature of 65°C. The changes in the VMD water flux for both membranes with respect to the various feed flow rates are shown in Figures 9(a) and 9(b), respectively. It is obvious that the permeate flux of VMD increases rapidly for both membranes with an increasing feed flow rate. This increase is due to the increase in Reynolds number, which causes enhanced mixing of the flow in the channels due to the turbulence. In other words, the enhanced turbulent flow reduces the thickness of the boundary layers for both the temperature and concentration

Table 4: The effect of the feed flow rate on the heat transfer coefficient, surface temperature, and temperature polarization coefficient at 55 and 65°C and a constant vacuum level of 92 kPa.

Feed flow rate (F_f) (mL/s)	Re	55°C			65°C		
		h_f (W/m^2 K)	T_{fm} (°C)	TPC	h_f (W/m^2 K)	T_{fm} (°C)	TPC
7.7	78315	1420.1	51.7	0.94	1475.6	60.7	0.93
16.6	165784	2587.5	52.3	0.95	2688.6	61.3	0.94
27	274612	3874.5	52.7	0.96	4026.0	61.6	0.95
30.3	311226	4282.5	53.2	0.97	4450.0	62.0	0.96

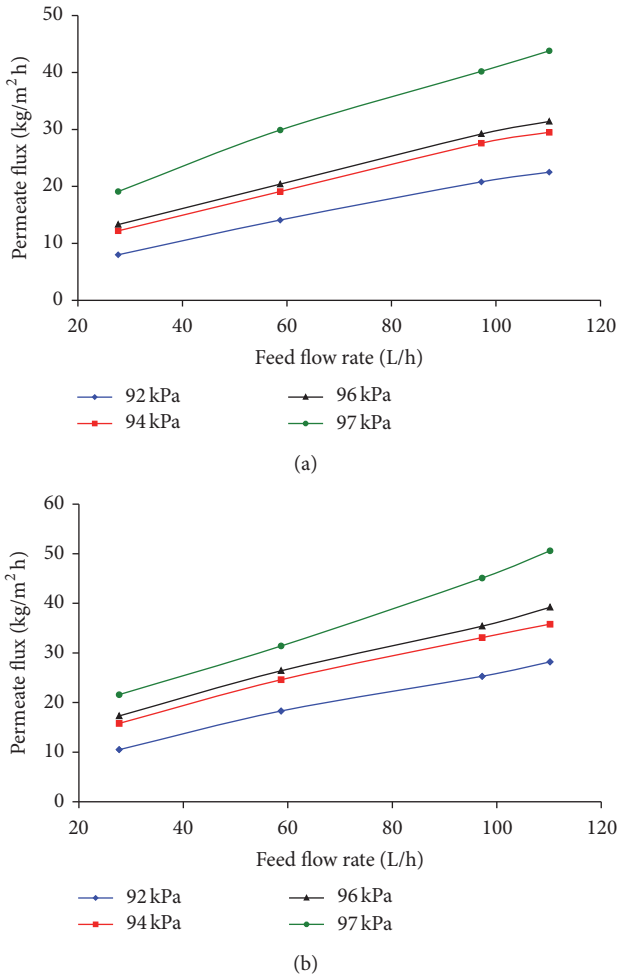

Figure 9: The effect of the feed flow rate on the permeate flux of (a) PVDF and (b) PTFE membranes at different vacuum degrees, with a feed temperature of 65°C and feed concentration of 35,000 mg/L.

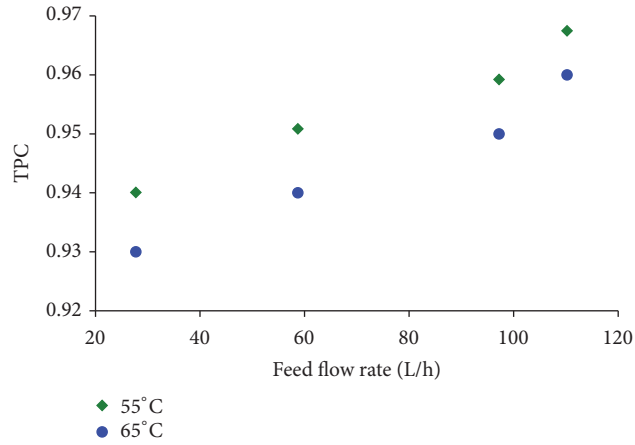

Figure 10: The effect of the feed flow rate on the temperature polarization coefficient at a constant 92 kPa vacuum degree and feed temperatures of 55 and 65°C.

(i.e., the boundary layer resistance), which consequently increases the driving force for evaporation. Moreover, the turbulence increases the convective heat transfer coefficient h_f at the feed boundary layer. This is clear from (3) and (4), where h_f is directly proportional to $\mathrm{Re}^{0.8}$, which consequently speeds up the heat transfer process from the bulk feed to the membrane surface [20, 38, 39]. This consequently increases the feed membrane surface temperature T_{fm} and temperature polarization coefficient (TPC), as seen in Table 4 and Figure 10, respectively. The TPC clearly increases with the increasing feed flow rate; this is due to the reduction of the heat transfer resistance within the boundary layers. However, the feed temperature has a negative influence on the TPC. This is attributed to the increased heat flux through the thermal boundary layer, which leads to a decrease in the membrane surface temperature T_{fm} [40]. Thus, increasing the feed flow rate is one way to mitigate the temperature polarization effect in VMD. Additionally, the increase in water flux seemed to approach the maximum values asymptotically with a higher feed flow rate [41–43]; for example, in Figure 9(a), the percentage increase in the water flux from 27.7 to 58.7 (L/h) was 57%, while it decreased to 9% from 97.2 to 110.2 (L/h). Therefore, a further increase in Reynolds number has less effect on the water flux so that the effective method is to optimize the feed flow rate to reach a high water flux [41, 44]. The results from Figures 9(a) and 9(b) show that the PTFE membrane provides a higher flux compared to the PVDF membrane, where the PTFE membrane reached a permeate flux of 50.6 (kg/m^2 h) at 65°C and 97 kPa vacuum degree, while the flux was 43.8 (kg/m^2 h) for the PVDF membrane under the same conditions.

(3) Effect of the Vacuum Degree. Based on some studies [35, 45], the vacuum degree on the permeate side was one of the most significant factors, along with the feed temperature and feed flow, which affect the performance of the VMD

Table 5: Heat flux for evaporation at different vacuum degrees for the PVDF and PTFE membranes.

Feed flow rate (F_f) (mL/s)	Heat flux, Q (W), PVDF vacuum degree kPa at 65°C				Heat flux, Q (W), PTFE vacuum degree kPa at 65°C			
	92	94	96	97	92	94	96	97
7.7	74.2	64.5	103.2	125.8	80.6	122.5	132.2	161.2
16.3	116.0	116.0	163.8	184.3	136.5	191.2	204.8	245.7
27.0	158.3	158.3	226.1	260.1	192.2	260.1	271.4	328.0
30.6	153.8	179.4	294.7	346.0	217.8	333.2	346.0	410.1

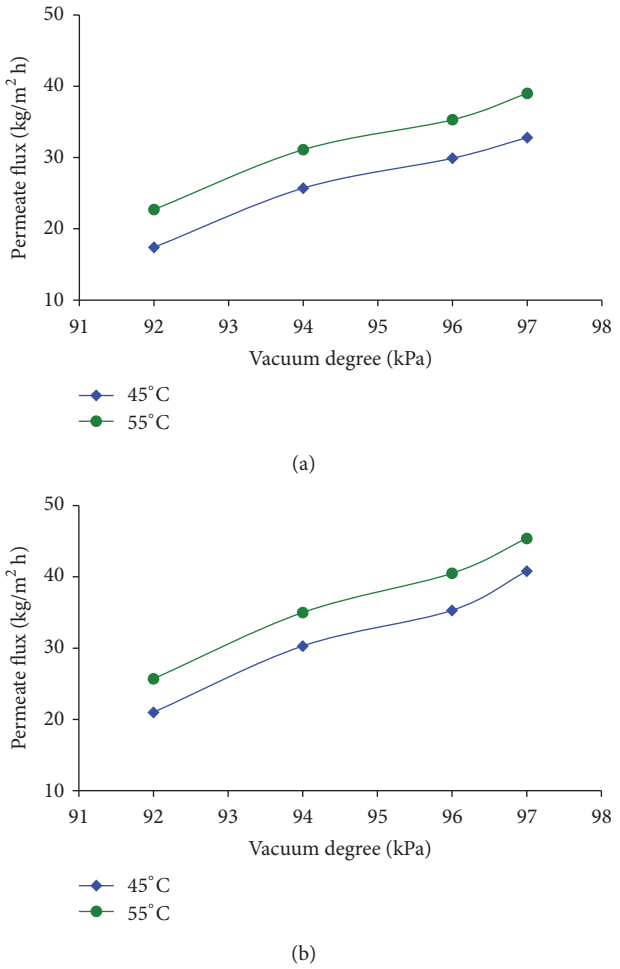

Figure 11: The effect of the vacuum degree on the permeate flux at 45 and 55°C feed temperatures; 110.2 (L/h) feed flow rate and 35,000 mg/L of NaCl for (a) PVDF and (b) PTFE membranes.

process. In Figures 11(a), 11(b), 12(a), and 12(b), the water flux was plotted as a function of the vacuum degree at a 35,000 mg/L feed concentration, different feed temperatures, and feed flow rates. As shown in Figures 11(a), 11(b), 12(a), and 12(b), increasing the vacuum degree, while varying the feed temperature and feed flow rate, causes the water flux to increase linearly. This is attributed to the significant decrease in water vapor pressure on the permeate side, consequently enhancing the vapor pressure difference (i.e., the driving force) through the membrane; it is clear from the curve behavior that the effect of the feed temperature with the vacuum degree is more significant than the effect of the feed flow rate with the vacuum [26, 29, 46–48]. This is because the vapor pressure difference across the membrane is induced by the temperature at the feed side and the high vacuum applied to the permeate side. In addition, the percentage increase in the water flux when the vacuum level was first changed (i.e., from 92 to 94 kPa) increases dramatically at various feed temperature and feed flow rates, but the percentage increase is reduced as the vacuum level increases from 96 to 97 kPa. For example, at 27.7 (L/h) and 55°C, the water flux increased from 5.6 to 9.8 (kg/m^2 h), that is, by more than 75%, while the percentage increase was 15% for a change in the vacuum degree from 96 to 97 kPa. This means that the increase in water flux is reduced as the vacuum degree increases with the feed temperature and feed flow rate. Therefore, there is a trade-off between all of these variables in their effect on VMD performance; therefore, optimizing all of them is the best way to achieve a high water flux. Moreover, as shown in Table 5, increasing the vacuum level increases the amount of heat flux required for evaporation, which is consequently necessary for increasing the performance of the VMD process. For example, the increase in the heat flux for the PVDF membrane from a 92 kPa vacuum degree to that of 97 kPa at a feed flow rate of 110.2 (L/h) and feed temperature of 65°C is greater than a twofold increase. The water flux of the PTFE membrane is higher than that of the PVDF membrane under the same operating conditions of the feed temperature and feed flow rate, where the water flux through the PTFE membrane is 13–16% greater than that for the PVDF membrane.

(4) Effect of the Feed Concentration. The effect of the feed concentration of the NaCl salt in aqueous solutions on the water flux and percentage rejection was investigated in VMD. The experiments were performed for different feed concentrations (10,000, 20,000, and 35,000 mg/L) where the feed temperature, the feed flow rate, and the vacuum degree were kept constant at 65°C, 58.7 (L/h), and 97 kPa, respectively. From Figure 13, the effect of the feed concentration of NaCl on the water flux may be noted. The results show that the water flux decreases as the NaCl concentration increases due to the reduction of the vapor pressure difference, which decreases the amount of water vapor flowing across the membrane. Furthermore, Alhathal et al. and Mericq et al. [8, 21] attributed the decline in the permeate flux to the variation in the NaCl thermodynamic properties (i.e., the water activity coefficient). Moreover, the temperature and

Table 6: Comparison of the PVDF and PTFE membranes at 65°C, 110.2 (L/h), and 97 kPa for 35 g/L.

Membrane	Permeate flux (kg/m^2 h)	Permeate concentration (mg/L)	Permeate conductivity (μS/cm)	% of rejection
PVDF	43.8	175	8.1	99.5
PTFE	52.6	280	10.2	99.2

Table 7: Comparison of the permeate fluxes at different operating conditions in MD for different NaCl solutions.

MD type	Membrane	d_p (μm)	T_f (°C)	Vacuum (kPa)	F_f (mL/s)	C_f (g/L)	Flux (kg/m^2 h)	Ref.
VMD	PTFE	0.1	65	100	2280	35	66	[19]
VMD	PP 50/200	0.1	90	87	5 cm/s	3.5	15	[29]
VMD	PES/TiO_2NTs	—	65	70	11	35	5.5	[34]
VMD	PP	0.2	55	97	30	100	14.4	[35]
VMD	PP	0.074	60	93	42	35	3	[36]
VMD	PVDF	0.2	60	14.5	25	3.5	4	[37]
VMD	PVDF	0.22	65	97	30.6	35	43.8	This study
VMD	PTFE	0.22	65	97	30.6	35	52.6	This study

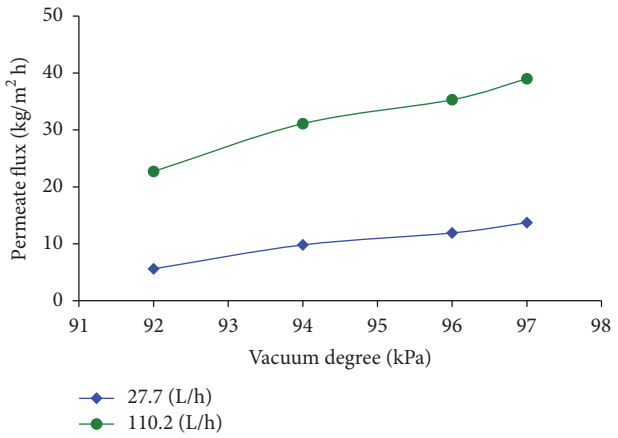

Figure 12: The effect of the vacuum degree on the permeate flux at 27.7 and 110.2 (L/h) feed flow rates; a 55°C feed temperature and 35,000 mg/L of NaCl for the (a) PVDF and (b) PTFE membranes.

concentration polarization effects reduce the evaporation driving force where the thickness of the boundary layer is increased. As the concentration increases from 10,000 mg/L to 35,000 mg/L, the decline in flux is 14% for PTFE and 15%

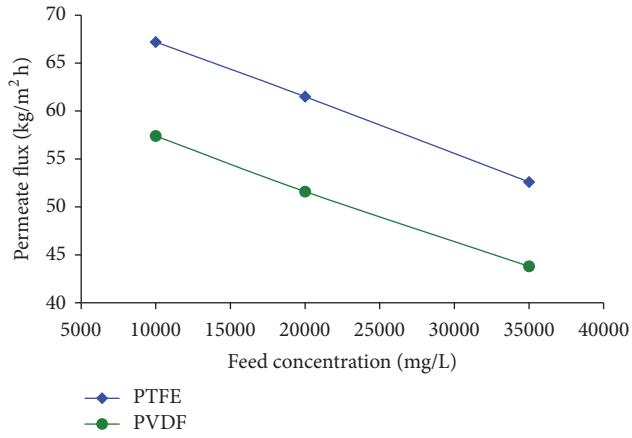

Figure 13: The effect of the feed concentration of NaCl on the permeate flux for PTFE and PVDF membranes at a 65°C feed temperature, 110.2 (L/h) feed flow rate, and 97 kPa vacuum degree.

for PVDF, while the percentage rejection of salt shows more than 99% for both membranes. Based on previous studies [13, 34], MD process can treat a highly saline water at a feed concentration of 35,000 to 180,000 (mg/L), with a decline in water flux from 13 to 35%, while the salt rejection is not affected by the feed concentration.

(5) Comparison of the PVDF and PTFE Membranes. Within the investigation, a range of experimental operating conditions of a 65°C feed temperature, 110.2 (L/h) feed flow rate, and 97 kPa vacuum degree at a feed concentration of 35,000 (mg/L) was chosen for comparison with previous studies of VMD in terms of water flux, water quality, and salt rejection, as shown in Tables 6 and 7. It is clear that the water fluxes and salt rejection were 43.8 (kg/m^2 h) and 99.5% for PVDF and 52.6 (kg/m^2 h) and 99.2% for PTFE. In terms of water quality, the average electrical conductivities of the permeates are 8.1 and 10.2 μS/cm for the PVDF and PTFE membranes, respectively.

4. Conclusions

An O-ring membrane module was constructed and specially designed to investigate the performance of the VMD process using PTFE and PVDF membranes. Pure water experiments were conducted to measure the heat and mass transfer coefficients within the membrane module. The results were used to reevaluate the constant parameters of the heat and mass transfer analogy. Therefore, the obtained equations were used to calculate the heat and mass transfer coefficients. The results showed that the membrane module design proved its applicability for achieving a high heat transfer coefficient h_f of the order of 10^3 (W/m^2 K) and high Reynolds number (Re). The effect of process parameters, namely, the feed temperature, feed flow rate, vacuum degree, and feed concentration, on the performance of VMD process in terms of water flux and salt rejection has been discussed. The results showed that the water flux increased exponentially with feed temperature. Additionally, the water flux increased with the increasing feed flow rate and seemed to approach maximum values asymptotically at higher flow rates. The degree of vacuum plays an important role in increasing the process performance, where the water flux increases linearly with an increasing vacuum degree. Therefore, there is a trade-off between these three variables on the effect of the VMD performance, so optimizing all of them is the best way to achieve a high permeate flux. As expected, the feed concentration of 10,000 to 35,000 mg/L of NaCl decreased the water flux, where the percentage decline was approximately 13 and 14% for PTFE and PVDF, respectively. It was concluded that, at operating conditions of a 65°C feed temperature, 110.2 (L/h) feed flow rate, and 97 kPa vacuum degree for a 35,000 (mg/L) feed concentration, the water flux reached 43.8 and 52.6 (kg/m^2 h) for PVDF and PTFE, respectively, and the salt rejection of NaCl was higher than 99% for both membranes. Within the investigation range of the experimental operating conditions, the obtained water fluxes were relatively high compared to those reported in the literature, and these results might be attributed to the unique design of O-ring membrane module and the condenser.

Competing Interests

The authors declare that they have no competing interests.

Acknowledgments

The authors wish to express their sincere thanks to the Public Authority of Applied Education and Training (PAAET) in Kuwait for funding this research.

References

[1] A. Altaee, "Forward osmosis: potential use in desalination and water reuse," *Journal of Membrane and Separation Technology*, vol. 1, pp. 79–93, 2012.

[2] A. AlHathal Al-Anezi, A. O. Sharif, M. I. Sanduk, and A. R. Khan, "Potential of membrane distillation—a comprehensive review," *International Journal of Water*, vol. 7, no. 4, pp. 317–346, 2013.

[3] A. A. Alanezi and A.O. Sharif, "Membrane distillation: an attractive alternative," *Arab Water World*, vol. 36, no. 5, pp. 1–77, 2012.

[4] H. T. El-Dessouky and H. M. Ettouney, *Fundamentals of Salt Water Desalination, Department of Chemical Engineering, College of Engineering and Petroleum, Kuwait University*, Elsevier, Amsterdam, Netherlands, 2002.

[5] A. Ahmad, F. Jamshed, T. Riaz et al., "Self-sterilized composite membranes of cellulose acetate/polyethylene glycol for water desalination," *Carbohydrate Polymers*, vol. 149, pp. 207–216, 2016.

[6] R. Gemma Raluy, R. Schwantes, V. J. Subiela, B. Peñate, G. Melián, and J. R. Betancort, "Operational experience of a solar membrane distillation demonstration plant in Pozo Izquierdo-Gran Canaria Island (Spain)," *Desalination*, vol. 290, pp. 1–13, 2012.

[7] M. A. Eltawil, Z. Zhengming, and L. Yuan, "A review of renewable energy technologies integrated with desalination systems," *Renewable and Sustainable Energy Reviews*, vol. 13, no. 9, pp. 2245–2262, 2009.

[8] A. A. Al-Anezi, A. O. Sharif, M. I. Sanduk, and A. R. Khan, "Experimental investigation of heat and mass transfer in tubular membrane distillation module for desalination," *ISRN Chemical Engineering*, vol. 2012, Article ID 738731, 8 pages, 2012.

[9] M. Khayet, "Solar desalination by membrane distillation: dispersion in energy consumption analysis and water production costs (a review)," *Desalination*, vol. 308, pp. 89–101, 2013.

[10] M. M. A. Shirazi, A. Kargari, and M. Tabatabaei, "Evaluation of commercial PTFE membranes in desalination by direct contact membrane distillation," *Chemical Engineering and Processing: Process Intensification*, vol. 76, pp. 16–25, 2014.

[11] L. Martínez, "Comparison of membrane distillation performance using different feeds," *Desalination*, vol. 168, no. 1–3, pp. 359–365, 2004.

[12] L. M. Camacho, L. Dumée, J. Zhang et al., "Advances in membrane distillation for water desalination and purification applications," *Water*, vol. 5, no. 1, pp. 94–196, 2013.

[13] A. Alkhudhiri, N. Darwish, and N. Hilal, "Produced water treatment: application of air gap membrane distillation," *Desalination*, vol. 309, pp. 46–51, 2013.

[14] H. C. Duong, A. R. Chivas, B. Nelemans et al., "Treatment of RO brine from CSG produced water by spiral-wound air gap membrane distillation—a pilot study," *Desalination*, vol. 366, pp. 121–129, 2015.

[15] A. S. Alsaadi, N. Ghaffour, J.-D. Li et al., "Modeling of air-gap membrane distillation process: a theoretical and experimental study," *Journal of Membrane Science*, vol. 445, pp. 53–65, 2013.

[16] S. Al-Obaidani, E. Curcio, F. Macedonio, G. Di Profio, H. Al-Hinai, and E. Drioli, "Potential of membrane distillation in seawater desalination: thermal efficiency, sensitivity study and cost estimation," *Journal of Membrane Science*, vol. 323, no. 1, pp. 85–98, 2008.

[17] P. Wang and T.-S. Chung, "Recent advances in membrane distillation processes: membrane development, configuration design and application exploring," *Journal of Membrane Science*, vol. 474, pp. 39–56, 2015.

[18] E. Curcio and E. Drioli, "Membrane distillation and related operations—a review," *Separation and Purification Reviews*, vol. 34, no. 1, pp. 35–86, 2005.

[19] J. P. Mericq, S. Laborie, and C. Cabassud, "Vacuum membrane distillation for an integrated seawater desalination process," *Desalination and Water Treatment*, vol. 9, no. 1–3, pp. 293–302, 2009.

[20] M. S. El-Bourawi, Z. Ding, R. Ma, and M. Khayet, "A framework for better understanding membrane distillation separation process," *Journal of Membrane Science*, vol. 285, no. 1-2, pp. 4–29, 2006.

[21] J.-P. Mericq, S. Laborie, and C. Cabassud, "Vacuum membrane distillation of seawater reverse osmosis brines," *Water Research*, vol. 44, no. 18, pp. 5260–5273, 2010.

[22] S. Cerneaux, I. Struzyńska, W. M. Kujawski, M. Persin, and A. Larbot, "Comparison of various membrane distillation methods for desalination using hydrophobic ceramic membranes," *Journal of Membrane Science*, vol. 337, no. 1-2, pp. 55–60, 2009.

[23] Z. Jin, D. L. Yang, S. H. Zhang, and X. G. Jian, "Hydrophobic modification of poly(phthalazinone ether sulfone ketone) hollow fiber membrane for vacuum membrane distillation," *Journal of Membrane Science*, vol. 310, no. 1-2, pp. 20–27, 2008.

[24] D. E. Suk, T. Matsuura, H. B. Park, and Y. M. Lee, "Development of novel surface modified phase inversion membranes having hydrophobic surface-modifying macromolecule (nSMM) for vacuum membrane distillations," *Desalination*, vol. 261, no. 3, pp. 300–312, 2010.

[25] N. Tang, Q. Jia, H. Zhang, J. Li, and S. Cao, "Preparation and morphological characterization of narrow pore size distributed polypropylene hydrophobic membranes for vacuum membrane distillation via thermally induced phase separation," *Desalination*, vol. 256, no. 1–3, pp. 27–36, 2010.

[26] B. Wu, K. Li, and W. K. Teo, "Preparation and characterization of poly(vinylidene fluoride) hollow fiber membranes for vacuum membrane distillation," *Journal of Applied Polymer Science*, vol. 106, no. 3, pp. 1482–1495, 2007.

[27] Z. Jin, D. L. Yang, S. H. Zhang, and X. G. Jian, "Removal of 2,4-dichlorophenol from wasterwater by vacuum membrane distillation using hydrophobic PPESK hollow hiber membrane," *Chinese Chemical Letters*, vol. 18, no. 12, pp. 1543–1547, 2007.

[28] B. Wu, X. Tan, K. Li, and W. K. Teo, "Removal of 1,1,1-trichloroethane from water using a polyvinylidene fluoride hollow fiber membrane module: vacuum membrane distillation operation," *Separation and Purification Technology*, vol. 52, no. 2, pp. 301–309, 2006.

[29] B. Li and K. K. Sirkar, "Novel membrane and device for vacuum membrane distillation-based desalination process," *Journal of Membrane Science*, vol. 257, no. 1-2, pp. 60–75, 2005.

[30] M. Khayet and T. Matsuura, "Pervaporation and vacuum membrane distillation processes: modeling and experiments," *AIChE Journal*, vol. 50, no. 8, pp. 1697–1712, 2004.

[31] M. Khayet, K. C. Khulbe, and T. Matsuura, "Characterization of membranes for membrane distillation by atomic force microscopy and estimation of their water vapor transfer coefficients in vacuum membrane distillation process," *Journal of Membrane Science*, vol. 238, no. 1-2, pp. 199–211, 2004.

[32] J.-M. Li, Z.-K. Xu, Z.-M. Liu et al., "Microporous polypropylene and polyethylene hollow fiber membranes—part 3: experimental studies on membrane distillation for desalination," *Desalination*, vol. 155, no. 2, pp. 153–156, 2003.

[33] M. Khayet and T. Matsuura, "Preparation and characterization of polyvinylidene fluoride membranes for membrane distillation," *Industrial and Engineering Chemistry Research*, vol. 40, no. 24, pp. 5710–5718, 2001.

[34] H. Abdallah, A. F. Moustafa, A. A. AlAnezi, and H. E. M. El-Sayed, "Performance of a newly developed titanium oxide nanotubes/polyethersulfone blend membrane for water desalination using vacuum membrane distillation," *Desalination*, vol. 346, pp. 30–36, 2014.

[35] M. Safavi and T. Mohammadi, "High-salinity water desalination using VMD," *Chemical Engineering Journal*, vol. 149, no. 1–3, pp. 191–195, 2009.

[36] J.-M. Li, Z.-K. Xu, Z.-M. Liu et al., "Microporous polypropylene and polyethylene hollow fiber membranes. Part 3. Experimental studies on membrane distillation for desalination," *Desalination*, vol. 155, no. 2, pp. 153–156, 2003.

[37] C.-K. Chiam, A. Ibrahim, and R. Sarbatly, "Desalination in cross-flow vacuum membrane distillation under the negative membrane pressure difference," *Journal of Applied Sciences*, vol. 14, no. 12, pp. 1259–1264, 2014.

[38] S. Srisurichan, R. Jiraratananon, and A. G. Fane, "Mass transfer mechanisms and transport resistances in direct contact membrane distillation process," *Journal of Membrane Science*, vol. 277, no. 1-2, pp. 186–194, 2006.

[39] J. Phattaranawik and R. Jiraratananon, "Direct contact membrane distillation: effect of mass transfer on heat transfer," *Journal of Membrane Science*, vol. 188, no. 1, pp. 137–143, 2001.

[40] M. Khayet, A. O. Imdakm, and T. Matsuura, "Monte Carlo simulation and experimental heat and mass transfer in direct contact membrane distillation," *International Journal of Heat and Mass Transfer*, vol. 53, no. 7-8, pp. 1249–1259, 2010.

[41] A. M. Alklaibi and N. Lior, "Membrane-distillation desalination: status and potential," *Desalination*, vol. 171, no. 2, pp. 111–131, 2005.

[42] L. Martínez-Díez, M. I. Vázquez-González, and F. J. Florido-Díaz, "Study of membrane distillation using channel spacers," *Journal of Membrane Science*, vol. 144, no. 1-2, pp. 45–56, 1998.

[43] M. Khayet, "Membrane distillation," in *Advanced Membrane Technology and Applications*, N. N. Li, A. G. Fane, W. S. W. Ho, and T. Matsuura, Eds., pp. 297–370, John Wiley & Sons, Inc, New York, NY, USA, 2008.

[44] M. Sudoh, K. Takuwa, H. Iizuka, and K. Nagamatsuya, "Effects of thermal and concentration boundary layers on vapor permeation in membrane distillation of aqueous lithium bromide solution," *Journal of Membrane Science*, vol. 131, no. 1-2, pp. 1–7, 1997.

[45] T. Mohammadi and M. A. Safavi, "Application of Taguchi method in optimization of desalination by vacuum membrane distillation," *Desalination*, vol. 249, no. 1, pp. 83–89, 2009.

[46] S. Bandini, C. Gostoli, and G. C. Sarti, "Separation efficiency in vacuum membrane distillation," *Journal of Membrane Science*, vol. 73, no. 2-3, pp. 217–229, 1992.

[47] S. Al-Asheh, F. Banat, M. Qtaishat, and M. Al-Khateeb, "Concentration of sucrose solutions via vacuum membrane distillation," *Desalination*, vol. 195, no. 1–3, pp. 60–68, 2006.

[48] R. Bagger-Jørgensen, A. S. Meyer, C. Varming, and G. Jonsson, "Recovery of volatile aroma compounds from black currant juice by vacuum membrane distillation," *Journal of Food Engineering*, vol. 64, no. 1, pp. 23–31, 2004.

Hindawi Publishing Corporation
Journal of Chemistry
Volume 2016, Article ID 2391576, 11 pages
http://dx.doi.org/10.1155/2016/2391576

Research Article

Preparation of Cathode-Anode Integrated Ceramic Filler and Application in a Coupled ME-EGSB-SBR System for Chlortetracycline Industrial Wastewater Systematic Treatment

Yuanfeng Qi,[1,2] Suqing Wu,[1] Fei Xi,[2] Shengbing He,[1] Chunzhen Fan,[1] Bibo Dai,[2] Jungchen Huang,[1] Meng Meng,[2] Xiangguo Zhu,[2,3] and Lei Wang[2,4]

[1]*School of Environmental Science and Engineering, Shanghai Jiaotong University, Shanghai 200240, China*
[2]*Shandong ATK Environmental Engineering Company Limited, Jinan 250101, China*
[3]*Shandong Kenli Petrochemical Group, Dongying 257500, China*
[4]*Shandong Wonfull Petrochemical Group Co., Ltd., Zibo 256410, China*

Correspondence should be addressed to Shengbing He; shengbing_he@163.com

Received 28 June 2016; Revised 6 September 2016; Accepted 20 September 2016

Academic Editor: Manuel A. R. Rodrigo

Chlortetracycline (CTC) contamination of aquatic systems has seriously threatened the environmental and human health throughout the world. Conventional biological treatments could not effectively treat the CTC industrial wastewater and few studies have been focused on the wastewater systematic treatment. Firstly, 40.0 wt% of clay, 30.0 wt% of dewatered sewage sludge (DSS), and 30.0 wt% of scrap iron (SI) were added to sinter the new media (cathode-anode integrated ceramic filler, CAICF). Subsequently, the nontoxic CAICF with rough surface and porous interior packed into ME reactor, severing as a pretreatment step, was effective in removing CTC residue and improving the wastewater biodegradability. Secondly, expanded granular sludge bed (EGSB) and sequencing batch reactor (SBR), serving as the secondary biological treatment, were mainly focusing on chemical oxygen demand (COD) and ammonia nitrogen (NH_3-N) removal. The coupled ME-EGSB-SBR system removed about 98.0% of CODcr and 95.0% of NH_3-N and the final effluent met the national discharged standard (C standard of CJ 343-2010, China). Therefore, the CTC industrial wastewater could be effectively treated by the coupled ME-EGSB-SBR system, which has significant implications for a cost-efficient system in CTC industrial systematic treatment and solid wastes (DSS and SI) treatment.

1. Introduction

As a biological wastewater treatment process, activated sludge technology has been widely used in municipal and industrial wastewater treatment. However, large amounts of excess sludge, generated as by-product during the process, usually contain organic and mineral components [1] and pathogenic and toxic substances [2, 3], which has hindered application of activated sludge process. Generally, disposal of excess sludge might account for more than 60% of the total operating expenditure in a wastewater treatment plant [4]. Various methods have been applied in excess sludge treatment, including incineration, land application, land filling, road surfacing, and conversion to fertilizer [5]. Although these studies achieved some desired effect in treating excess sludge, these methods were uneconomical, unsafe, or insanitary. Therefore, eco-friendly and economical methods for safe handling, disposal, and recycling of excess sludge are of great significance.

As a kind of solid waste, large quantity of scrap iron might be generated and discarded by machinery plants, resulting in waste of resources. In recent years, scrap iron has been utilized in many manners, mainly including hexavalent chromium reduction [6], sulfur dioxide removal [7], azo dyes wastewater pretreatment [8], and antibiotics residue removal [9]. These methods are insufficient for scrap iron reusing; therefore, more economical and effective methods are essential for recycling scrap iron.

In the past several decades, excess sewage sludge and scrap iron have been utilized to prepare ceramics, which have

been widely used in construction industry, chemical industry, metallurgy, agriculture, and environmental protection [10], resulting in reusing these solid wastes and reducing clay consumption during ceramics production.

CTC, as a broad-spectrum antibiotic, has been widely used in disease control and animal growth [11, 12]. Large amounts of wastewater are generated from fermentation process during CTC production, mainly containing fermentation medium residue, mycelium, and various complicated metabolites (carbohydrates, proteins, organic acids, etc.). In addition, CTC extraction process also generates some wastewater, mainly containing organic solvent, acid, alkali, and antibiotic residue. Therefore, CTC industrial wastewater is difficultly degraded by biological methods and it will accumulate constantly [13]. So far, lots of methods have been utilized to treat the CTC industrial wastewater, including photodegradation [14–17], advanced oxidation/reduction [18, 19], manganese oxidation [20], and sorption [21–24]. Although these studies obtained some desired effect, very few of them could be applied in practical project due to their rigorous reaction conditions and expensive operating cost. Consequently, it is important to develop economical and easily applicable methods for real CTC industrial wastewater treatment.

In our previous study [25], a coupled ME-EGSB-A/O system was utilized for oxytetracycline (OTC) production wastewater treatment. In this study, a similar coupled system (ME-EGSB-SBR) was applied to treat CTC production wastewater. Although similar treatment system was used in the two studies, different fillers were prepared and applied in ME reactor, cathode fillers (CCF) and anode fillers (ACF) in different particle bodies were sintered separately in the previous study while cathode and anode fillers were incorporated in the same particle body, and the incorporate fillers (CAICF) were prepared in the present study, which could simplify preparation process of the fillers and enhance the treatment efficiency of the ME reactor. Therefore, in this study, a coupled ME-EGSB-SBR system was utilized for CTC industrial wastewater treatment.

Firstly, new media (CAICF) were prepared from DSS, SI, and clay and subsequently applied as fillers for ME reactor. Microelectrolysis technology, developed on the basis of electrochemistry, was first applied in Europe during the 1960s [26]. Its principles are very similar to electrochemical methods, and the electrons are supplied from the galvanic corrosion of many microscale sacrificial anodes without external power supply. Numerous microscopic galvanic cells are formed between the iron and carbon particles when contacted with wastewater (electrolyte solution). The half-cell reactions can be represented as follows [27, 28]:

$$\text{Anode (oxidation)}: 2\text{Fe} \longrightarrow 2\text{Fe}^{2+} + 4\text{e}^{-}, \quad E^{\theta}\left(\text{Fe}^{2+}/\text{Fe}\right) = -0.44\,\text{V}$$

$$\text{Cathode (reduction)}: \text{Acidic } 2\text{H}^{+} + 2\text{e}^{-} \longrightarrow \text{H}_2\uparrow, \quad E^{\theta}\left(\text{H}^{+}/\text{H}_2\right) = 0\,\text{V}$$

$$\text{O}_2 + 4\text{H}^{+} + 4\text{e}^{-} \longrightarrow 2\text{H}_2\text{O}, \quad E^{\theta}\left(\text{O}_2/\text{H}_2\text{O}\right) = +1.23\,\text{V}$$

$$\text{Neutral to alkaline}: \text{O}_2 + 2\text{H}_2\text{O} + 4\text{e}^{-} \longrightarrow 4\text{OH}^{-}, \quad E^{\theta}\left(\text{O}_2/\text{OH}^{-}\right) = +0.40\,\text{V}. \tag{1}$$

In recent years, ME has been widely used to treat refractory wastewaters, including landfill leachate [29], pharmaceutical wastewater [30], palm oil mill wastewater [31], ionic liquids wastewater [32], coking wastewater [33], and dyeing wastewater [26, 34]. In this research, ME was used as the wastewater pretreatment, mainly focusing on CTC residue removal and improvement of the wastewater biodegradability, which could facilitate subsequent biological treatments.

Secondly, EGSB followed by SBR was utilized as the secondary biological treatment for the CTC wastewater. EGSB, as a representative kind of anaerobic bioreactors, was mainly based on the mechanisms about anaerobic biological degradation of organic contaminants. When influent wastewater flowed through the anaerobic bioreactor, the contained organic contaminants were biologically degraded by the anaerobic microorganisms in granule sludge with COD removal and methane generation. Therefore, EGSB has been applied to disposal of high concentrated organic wastewaters, including brewing industry wastewater [35, 36], starch extracting wastewater [37], trichloroethylene-contaminated wastewater [38], and industrial oil wastewater [39]. SBR systems have been remarkably employed in industrial and municipal wastewater treatment for many years [40], such as wastewater containing p-nitrophenol [41], dairy effluents [42], and soybean-processing wastewater [43]. The secondary treatment was mainly used to remove majority of CODcr and NH_3-N in the wastewater.

2. Materials and Methods

2.1. Materials. DSS, SI, and clay, utilized as raw materials to prepare CAICF, were obtained from Jinan wastewater treatment plant, a machinery plant in Jinan city (Shandong Province, China), and a brickyard in Zibo city (Shandong Province, China), respectively. The components of DSS and clay were shown in Table 1 and the raw materials were dried at 105°C for 4 h, crushed in a ball mill, sieved through a 0.154 mm mesh, and then stored in polyethylene vessels to avoid humidification before utilization.

The utilized CTC industrial wastewater, obtained from a CTC manufacturing factory in Hohhot city (Inner Mongolia Autonomous Region, China), was mainly generated from separation and extraction processes of CTC, equipment rinsing process. The main water quality of the raw wastewater and the national discharged standard (wastewater quality standards for discharge to municipal sewers, C standard of CJ 343-2010, China) are shown in Table 2, revealing that the wastewater quality was not stable and all indexes of the wastewater did not meet the national discharged standard. In the wastewater treatment plant of this enterprise, the utilized wastewater treatment system mainly contained flocculation and precipitation, upflow anaerobic sludge blanket (UASB) (two anaerobic reactors were connected in series), cyclic activated sludge system (CASS), anoxic/oxic activated sludge

Table 1: Chemical components of clay and DSS (wt%).

	SiO_2	Al_2O_3	Fe_2O_3	CaO	K_2O	Na_2O	Sulfate	Phosphate	Others
DSS	29.94	18.50	9.48	21.42	1.78	—	9.43	5.37	4.08
Clay	63.28	18.75	7.72	1.23	2.14	2.07	—	—	4.81

Table 2: The components of the raw CTC industrial wastewater and the national standard.

Indexes	Unit	Concentration range	CJ 343-2010, C standard
CODcr	$mg\,L^{-1}$	10474–16855	≤300
NH_3-N	$mg\,L^{-1}$	358.5–840.2	≤25
Suspended solid (SS)	$mg\,L^{-1}$	847.5–1049	≤300
Chroma	—	210.5–332.3	≤60
pH	—	4.60–6.52	6.50–9.50
CTC residue	$mg\,L^{-1}$	72.8–102.6	—
BOD_5	$mg\,L^{-1}$	1124.3–1532.5	≤150

process (A/O), and Fenton oxidation. However, this complicated system had several problems: (1) the two anaerobic reactors could not operate stably and granule sludge in the reactors disintegrated greatly and must be renewed every three months; (2) the system required high operating cost, mainly resulting from the renewal of granule sludge and operation of the Fenton process; (3) the final effluent of the system (CODcr of 586–673 $mg\,L^{-1}$, NH_3-N of 21.5–26.8 $mg\,L^{-1}$, SS of 97.5–113.8 $mg\,L^{-1}$, chroma of 200–300) did not meet the discharged national standard (CODcr ≤ 300 $mg\,L^{-1}$, NH_3-N ≤ 25 $mg\,L^{-1}$, SS ≤ 300 $mg\,L^{-1}$, chroma ≤ 60). Therefore, it is necessary to improve the system or develop new system for the CTC wastewater treatment.

According to our previous study [28], CAICF was prepared according to the following three steps.

Step 1 (dosing, mixing, pelleting, screening, and drying). Clay, DSS, and SI (4 : 3 : 3, w/w/w) were completely mixed and poured into a pelletizer (DZ-20) to produce raw pellets (about 7.00 wt% of water was added). Then, the raw pellets were sieved (the diameters were 5.0–6.0 mm) and stored in draught cupboard at room temperature (22°C) for about 24 h before thermal treatment.

Step 2 (sintering treatment). The dried raw pellets were rapidly transferred into electric tube rotary furnace (KSY-4D-16) and sintered at 400°C for 20 min in anoxic conditions.

Step 3 (cooling treatment). After the sintering treatment, the pellets were transferred to draught cupboard until they cooled down to room temperature (22°C).

2.2. Starting and Operating of the Wastewater Treatment System. In this study, a coupled ME-EGSB-SBR system was utilized for the CTC industrial wastewater treatment. A pilot-scale experiment was set up for the wastewater treatment as shown Figure 1; all units were made of stainless steel to prevent possible corrosion caused by the wastewater and to eliminate potential photodegradation by the light.

Firstly, flocculation and precipitation processes were used to remove SS in the raw wastewater and prevent blockage of the ME reactor. Then the wastewater was introduced into the regulating reservoir 1 (cylinder, 1.0 m in diameter and 1.5 m tall) to adjust pH of the wastewater by adding hydrochloric acid (HCl) solution. Seven initial pH values (1.0, 2.0, 3.0, 4.0, 5.0, 6.0, and 7.0) and eight hydraulic retention times (HRTs, 1.0, 2.0, 3.0, 4.0, 5.0, 6.0, 7.0, and 8.0 h) were selected to determine the optimum conditions of ME reactor according to the removal rate of CTC residue and CODcr. 30 cm of cobble stone was packed as supporting layer at the bottom of ME reactor (cylinder, 1.0 m diameter and 2.0 m height) with 1.0 m of CAICF as media layer on the top, leaving a bottom space of 20 cm for water and air distribution and a headspace of 30 cm to retain fillers during backwashing. The wastewater was pumped into the reactor through the inlet at the bottom and discharged to the regulating reservoir 2 (cylinder, 1.0 m in diameter and 1.5 m tall) from the upper outlet.

Secondly, calcium hydroxide ($Ca(OH)_2$) solution was added to adjust and keep pH of the wastewater to about 7.0 before being introduced into EGSB tank. At start-up stage, the up-flow EGSB tank (cylinder, 1.2 m in diameter and 5.0 m tall) with an effective volume of approximately 3.96 m^3 was inoculated with granule sludge (approximately 1.2 m^3) from a local starch factory at a concentration of approximately 15.9 g VSS L^{-1}, and the starting organic loading rate (OLR) was about 0.5 $kg\,m^{-3}\,d^{-1}$. During the operation, OLR was increased gradually until the optimum OLR was determined by the CODcr removal efficiency. Other conditions including temperature and pH were kept at about 35.0°C and 7.0, respectively. The effluent was discharged into sludge precipitation reservoir (cylinder, 1.0 m in diameter and 1.5 m tall) and excess sludge was returned to the EGSB tank via a reflux sludge pump.

Thirdly, the supernatant of sludge precipitating reservoir was pumped into SBR reactor (cuboid, 1.2 m × 0.6 m × 0.65 m) with an effective volume of approximately 0.43 m^3. At the start-up stage, the reactor was inoculated with activated sludge obtained from the same starch factory at a solids concentration of approximately 5.4 g MLSS L^{-1}. During the operation, the time for influent feeding, aerating, precipitating, and effluent discharging was 1.0 h, 4.0 h, 2.0 h, and 1.0 h, respectively. Additionally, temperature and pH of the

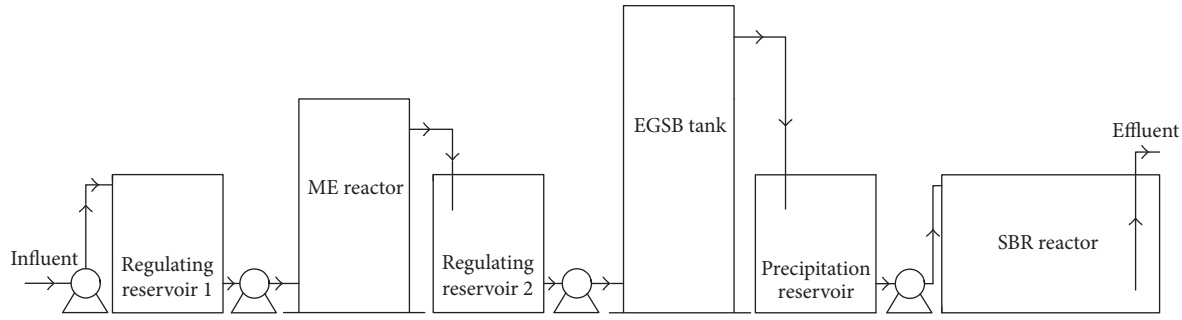

Figure 1: The treatment system of CTC wastewater.

wastewater were controlled at about 30.0°C and 7.0 by adding $NaHCO_3$ solution. Finally, the effluent was discharged from the wastewater treatment system into urban sewage pipe network.

All pumping and mixing cycles in the system were operated via four metering pumps (JsbasenGM500/0.3, Beijing, China) and a sludge pump (LanshenQJB-W4, Nanjing, China). The dissolved oxygen (DO) concentration in the SBR reactor was controlled at 2.0–4.0 mg L^{-1} using a Roots blower (FengyuanFRMG350, Shandong, China).

2.3. Analytical Methods

2.3.1. Properties of CAICF. According to our previous study [44], water absorption and bulk density were measured by the national standard (lightweight aggregates and the test methods-part 2, test methods for lightweight aggregate, GB/T 17431.2-2010, China) and grain density was calculated according to Archimedes' principle. The above-mentioned physical properties were calculated as follows:

$$\begin{aligned}
\text{Bulk density} &= \frac{\text{mass of ceramic bodies}}{\text{bulk volume of ceramic bodies}}\ \text{kg·m}^{-3} \\
\text{Grain density} &= \frac{\text{mass of ceramic bodies}}{\text{volume of ceramic bodies}}\ \text{kg·m}^{-3} \\
\text{Water absorption} &= \frac{\text{1 h saturated mass of ceramic bodies} - \text{mass dry of ceramic bodies}}{\text{mass of dry ceramic bodies}} \times 100\%.
\end{aligned} \tag{2}$$

Structural and morphological analysis was conducted by scanning electron microscopy (SEM, Hitachi S-520, Japan) both in the surface and in the cross section (Au coated).

1000.00 g of CAICF was soaked into 1.00 L of HCl (0.20 mol L^{-1}) for 24 h. 1.00 mL of leach solution obtained from the supernatant was collected for leaching test of the toxic metal elements. Toxic metal concentrations (Cu, Zn, Pb, Cr, Cd, Hg, Ba, Ni, and As) of 1000.00 g of CAICF were determined by ICP-AES (IRIS Intrepid II XSP equipment, Thermo Electron, USA) and were compared with national standard (identification standards for hazardous wastes, identification for extraction toxicity, GB 5085.3-2007, China).

2.3.2. Characterization of Wastewater. CODcr, NH_3-N, SS, BOD_5, chroma, and pH of the wastewater were measured according to national standard methods (State Environmental Protection Administration of China, Monitoring and Analysis Methods of Water and Wastewater, fourth ed., China Environmental Science Press, Beijing), and volatile fatty acid (VFA) of the wastewater in the EGSB tank was measured by titrimetry [45]. CTC residue in the wastewater was detected by High Performance Liquid Chromatography (HPLC) analysis (Shimadzu LC-2010A, Japan) equipped with a UV absorbance detector, and the analytical method for the CTC analysis was shown in Table 3. Dissolved oxygen (DO) and temperature were monitored with DO meter (HQ 30d 53LED™ HACH, USA). All measurements were conducted in five replicates.

3. Results and Discussion

3.1. Properties of CAICF. Firstly, physical properties of CAICF as shown in Table 4 revealed that the fillers had low bulk density and grain density. The low bulk density implied abundant void, which could enhance mass transfer and prevent short-circuiting. The low grain density might improve backwashing process and SS intercepted by the fillers could be easily removed during backwashing process. Therefore, utilization of CAICF as fillers could ensure the reliability of ME reactor.

Secondly, Figure 2 showed the appearance and microstructure of CAICF ((a) surface, (b) fracture surface). Figure 2(a) demonstrated a few small and large apertures distributed on the rough surface of CAICF, mainly caused by the escaped gas from interior of CAICF during the sintering treatment. As mentioned in our previous study [28], the

Table 3: Analytical methods for CTC analysis with a HPLC.

	Column stationary phase	Injection volume (μL)	Flow rate (mL min^{-1})	UV detection (nm)	Eluent
CTC	C8[b]	50	1.0	355	0.01 M oxalic acid : methanol : acetonitrile (72 : 8 : 20)

[b]Luna 5μ C8(2) 100 A (Phenomenex, Torrance, CA, USA): 150 mm (L) × 4.6 mm (ϕ).

Table 4: Physical properties of CAICF.

Ceramics	Bulk density (kg m^{-3})	Grain density (kg m^{-3})	Water absorption (wt%)
CAICF	918.5	1318.2	13.6

Table 5: Toxic metal leaching tests of CAICF.

Toxic metal	Contents (mg kg^{-1} of CAICF)	Threshold (mg kg^{-1} of hazardous waste)
Total Cu	0.08	100.00
Total Zn	0.02	100.00
Total Cd	0.01	1.00
Total Pb	0.06	5.00
Total Cr	0.02	15.00
Total Hg	—	0.10
Total Ba	0.05	100.00
Total Ni	—	5.00
Total As	0.02	5.00

rough surface could make fillers contact with wastewater more easily and the apertures on surface could promote the wastewater flow into the interior of CAICF, resulting in enhancement of treating effect. Figure 2(b) revealed lots of small and large apertures distributed inside of CAICF, meaning that the wastewater could flow through inside of the fillers. Consequently, the wastewater could be treated sufficiently inside of the fillers and the interior might not be easily blocked by SS. Therefore, utilization of CAICF as fillers might be satisfactory according to the microstructure analysis.

Thirdly, results of the toxic metal leaching test of CAICF were shown in Table 5, revealing that all the nine metal concentrations (Cu, Zn, Pb, Cr, Cd, Hg, Ba, Ni, and As) in lixivium were much lower than the limits of the national standard (GB 5085.3-2007). The results suggested that CAICF utilized as fillers would not lead to secondary pollution to water environment. Additionally, comparing with the detection for DSS [44], all the toxic metal leaching concentrations of CAICF were far lower than those of DSS, especially for total Cu, Zn, Cr, Pb, and Ba. This result showed that utilization of DSS to prepare CAICF could immobilize the toxic metals in DSS and consequently decrease the pollution of DSS.

Overall, it could be deduced that CAICF used as fillers of ME reactor might be feasible, safe, and reasonable according to the properties test.

3.2. CTC Wastewater Pretreatment Effect by ME

3.2.1. Initial pH of the Wastewater. pH is an important parameter for ME reaction and may affect the treatment effect of ME reactor. Therefore, seven pH values were selected to study the influence of initial pH on ME reactor. During this experiment, CAICF was applied as fillers in the ME reactor; HRT was kept at 8.0 h under aerating condition.

The influence of initial pH on CTC and CODcr removal was shown in Figure 3(a). The results revealed that the removal efficiency of CODcr and CTC decreased rapidly when initial pH increased from about 3.0 to 7.0, and the removal efficiency decreased slightly as initial pH increased from about 1.0 to 3.0. It was likely that corrosion and dissolution of Fe^0 in the fillers were more easily proceeded under acidic condition; therefore, more reducing agents (Fe^0, Fe^{2+}, and active radical ([H])) could be generated, resulting in destruction and reduction of CTC in the wastewater [28, 46]. Moreover, hydroxyl radical ($^{\bullet}OH$), as a strong oxidizing agent, might be easily generated during ME reactions under aerating conditions, resulting in oxidation of CTC and COD residue in the wastewater. However, when the wastewater reached neutral and alkaline condition, iron oxides and hydroxides were easily formed on the surface of the fillers, resulting in slow iron corrosion and surface passivation, consequently leading to the weakening of reduction and oxidation effect by the ME reactor. Therefore, higher CTC removal efficiency by the ME reactor was obtained on acidic condition than that on neutral and alkaline condition, and the CTC removal efficiency increased when pH decreased gradually, probably due to the acceleration of Fe corrosion, which could strengthen the reduction and oxidation effect by the ME reactor. However, when pH in the wastewater was too low, dissolution of Fe was accelerated drastically, which would greatly decrease service life of the sintered fillers. Therefore, 3.0 should be the optimum pH for the ME reactor in order to obtain high CTC removal efficiency and long service life of the sintered fillers.

3.2.2. HRT of the Wastewater. HRT is also a crucial parameter for ME reaction. Therefore, eight HRTs were selected to study the influence of HRT on CODcr and CTC removal of ME reactor. During this experiment, initial pH was kept at about 3.0 under aerating condition.

Figure 3(b) showed the influence of HRT on the removal efficiency of CODcr and CTC by ME reactor, revealing that the removal efficiency increased quickly when HRT was increased from 1.0 h to 4.0 h, and it varied slightly as HRT was increased from 4.0 h to 8.0 h. It could be deduced that ME reaction could not be accomplished with short HRT, which might be confirmed by abnormally low pH in

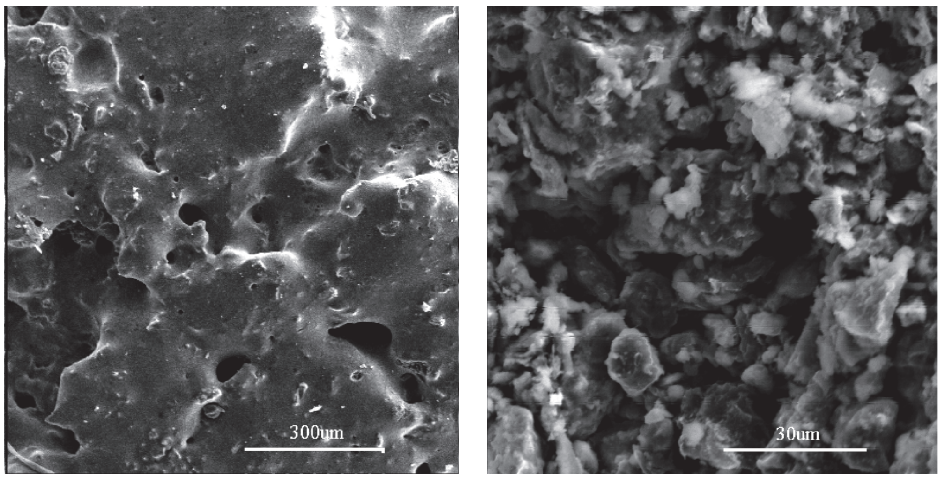

(a) (b)

Figure 2: The appearance and microstructure of CAICF (SEM): (a) surface, (b) fracture surface.

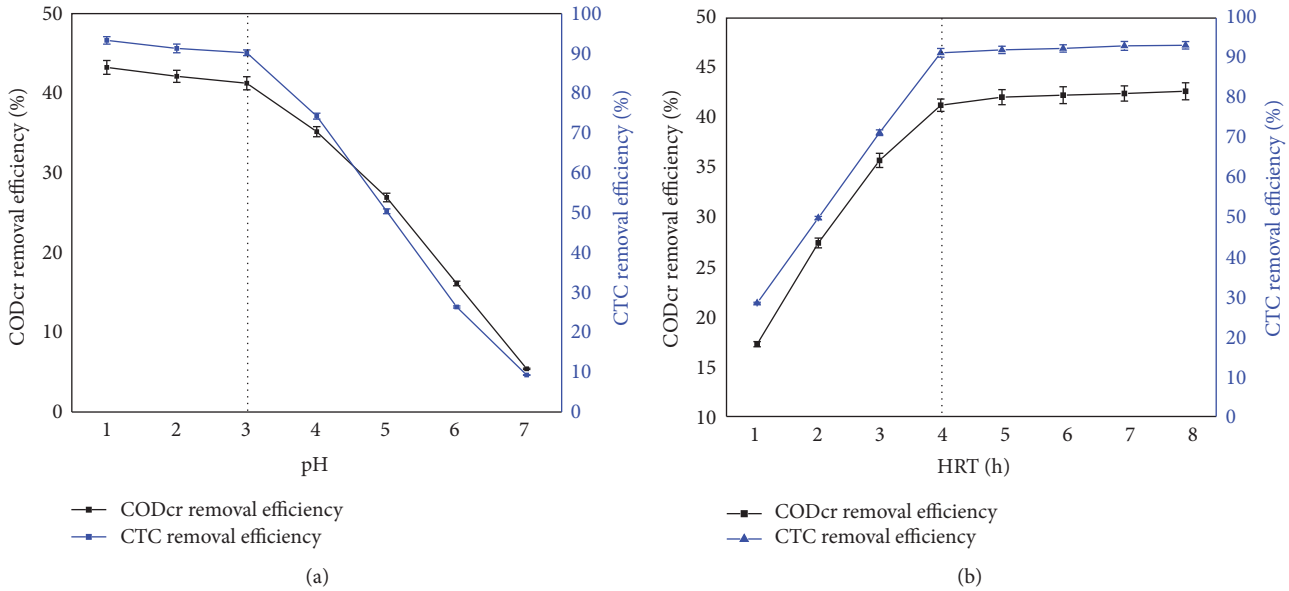

(a) (b)

Figure 3: Influence of initial pH and HRT on ME treatment effect ((a) pH, (b) HRT).

effluent, resulting in low removal efficiency of CODcr and CTC. Consequently, the removal efficiency increased quickly when HRT was increased from 1.0 h to 4.0 h. However, when HRT exceeded 4.0 h, the reaction time was enough for accomplishing ME reaction sufficiently. Additionally, pH in the effluent (about 6.50) varied slightly as HRT was increased from 4.0 h to 8.0 h, probably leading to the slight variation of removal efficiency. In all, the optimum HRT for the ME reactor should be 4.0 h determined by the CODcr and CTC removal efficiency.

3.2.3. Mechanisms for CTC and CODcr Removal. In ME reactor, several reaction mechanisms are involved in ME reactions for CTC removal. Firstly, the residual CTC might be reduced by the reduction effect, which was derived from active radical ([H]), Fe^0, and Fe^{2+} under acidic conditions [47]. It was known that when contacted with wastewater under acidic conditions, Fe^0 could react with H^+ and generated active radical ([H]), which was a strong reducing agent to reduce CTC. Additionally, Fe^0 and its corrosion product (Fe^{2+}) were also reducing agents, which could also reduce CTC. Secondly, H^+ was consumed during ME reactions and pH reached neutral and alkaline conditions gradually, resulting in the generation of iron hydroxide ($Fe(OH)_2$ and $Fe(OH)_3$), which could remove the residual CTC and CODcr by flocculation effect [48, 49]. Thirdly, the electrode voltage under acidic and aerating conditions (+1.67 V) was higher than that under acidic and anaerobic conditions (+0.40 V), which could enhance ME reactions and accelerate corrosion of Fe, resulting in the improvement of CTC removal [46]. Additionally, as a strong oxidizing agent, hydroxyl radical ($^{\bullet}OH$) might be generated during ME reactions under

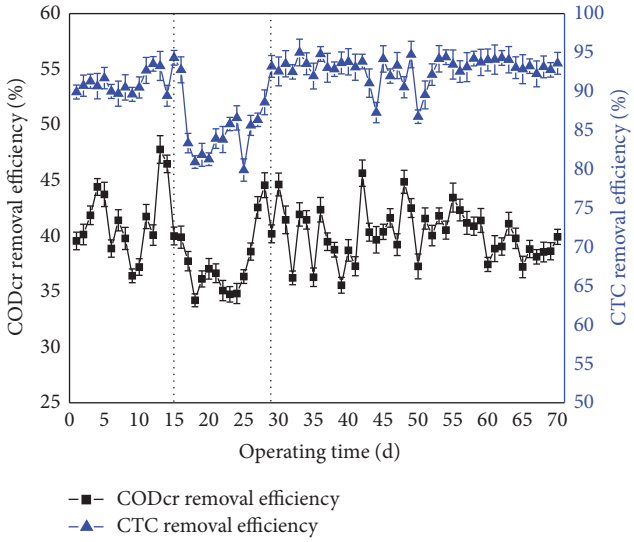

Figure 4: Operating effect of the ME reactor.

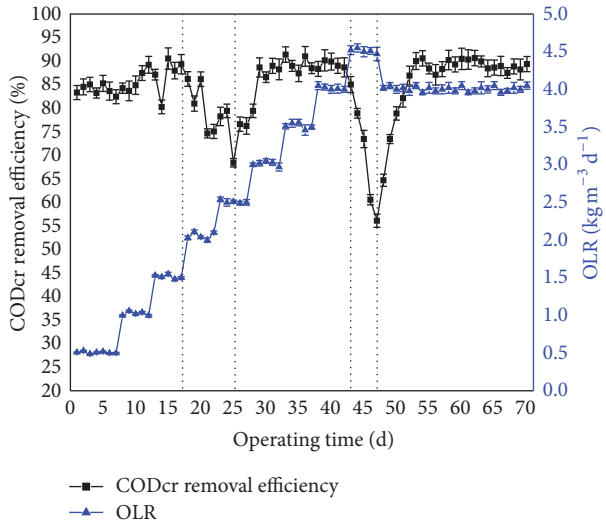

Figure 5: The effect of EGSB tank.

aerating conditions, which has been demonstrated by some researchers [50, 51]. $^{\bullet}$OH might oxidize the residual CTC and remove some CODcr in the wastewater. Overall, CTC and CODcr in the wastewater were mainly removed by reducing, oxidizing, and flocculation effects.

3.2.4. Operating Effect of ME Reactor. According to the above experiments, the optimum initial pH (about 3.0) and HRT (4.0 h) were applied in the pilot-scale experiment and the ME reactor was packed with CAICF.

Figure 4 showed the operating results of the ME reactor in the whole experiment. It could be seen that the ME reactor could get stable CODcr and CTC removal efficiency (40.0% and 90.0%, resp.). It was noted that the removal efficiency decreased appreciably (about 5.0%) from 15 d to 29 d, probably due to the blockage of the reactor by SS in the wastewater. Consequently, the mass transfer of wastewater was inhibited, resulting in the decrease of removal efficiency. After the backwash for the reactor, the removal efficiency was recovered. Therefore, the reactor was backwashed regularly (the backwashing cycle was about 15 d) and the reactor operated stably during the later experiment.

From the operating effect, it could be deduced that the molecular structure of CTC might be destroyed by the ME reactor and the majority of CTC residue in the wastewater might be decomposed or inactivated, and biotoxicity of the wastewater might be decreased according to the high removal efficiency of the ME reactor and the operating effect of later biological treatment. Therefore, it could be deduced that utilization of this ME reactor for CTC wastewater pretreatment was feasible and satisfactory.

3.3. Anaerobic Biological Treatment by EGSB. After the ME pretreatment, EGSB tank was used as the following anaerobic biological treatment for the wastewater, in order to remove the majority of CODcr in the wastewater and further enhance biodegradability of the wastewater.

CODcr removal efficiency of the EGSB tank was shown in Figure 5. The results showed that the operating effect fluctuated occasionally during the microbial acclimation stage and CODcr removal efficiency could reach 85.0% to 90.0% after microbial acclimation was accomplished. During the whole experiment, it could be observed that CODcr removal efficiency decreased obviously on two stages. The first stage appeared from 17 d to 25 d, it was likely that dominant bacteria in the EGSB tank have not been greatly reproduced, and it could not bear high OLR (2.0 kg m^{-3} d^{-1}), resulting in insufficient degradation of organic substances by dominant bacteria. Meanwhile, granule sludge in the tank was recombined and some bacteria that could not adapt to the wastewater would be eliminated, resulting in the discharge of some eliminated flocculent sludge. When the tank was operated after 25 d, the CODcr removal efficiency trended to stability, suggesting that dominant bacteria might reproduce gradually in the tank.

On the second stage (43 to 47 d), when OLR reached about 4.5 kg m^{-3} d^{-1}, the CODcr removal efficiency decreased rapidly with the rapid increase of VFA (from 2.59 to 10.08 mmol L^{-1}). It was likely that the present OLR has exceeded endurance limit of dominant bacteria, resulting in insufficient degradation of organic substances. It could be deduced that CTC loading rate was enhanced as OLR increased due to small amount of CTC residue in the wastewater, resulting in the inhibition of dominant bacteria. It is well known that methane and carbon dioxide are the end-products of anaerobic biological treatment. Two groups of bacteria play the major roles in this process: acetoclastic methanogens and hydrogenotrophic methanogens; the former transform acetate to methane and carbon dioxide, and the latter can produce methane and carbon dioxide by utilizing hydrogen produced during anaerobic oxidation of soluble organics. Moreover, about 75% of the methane produced during anaerobic biological treatment is caused by the acetoclastic methanogen activity [52]. CTC could inhibit both homoacetogenic bacteria and acetoclastic methanogens,

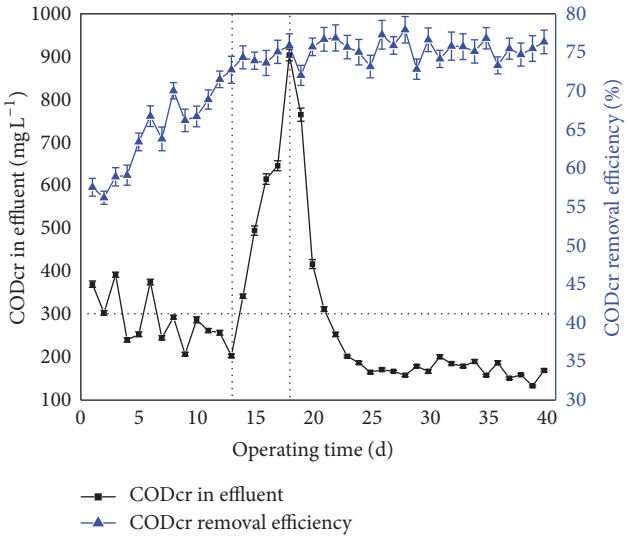

Figure 6: The effect of SBR reactor.

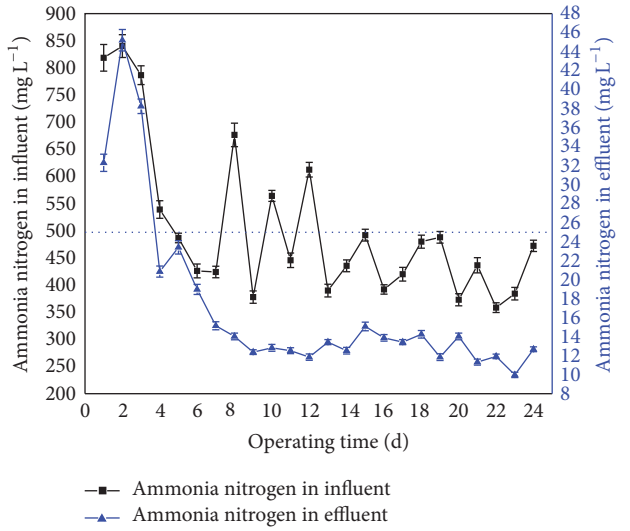

Figure 7: NH_3-N removal effect of the system.

which could utilize acetate, and consequently affect methane production by these microorganisms [53]. Moreover, acetogenic bacteria could also be inhibited by CTC, resulting in accumulation of VFA in the tank. After this stage, OLR was reduced to 4.0 kg m^{-3} d^{-1} and the tank was recovered to normal stage gradually, resulting in the increase of the CODcr removal efficiency.

To sum up, the optimum OLR of the EGSB tank was about 4.0 kg m^{-3} d^{-1} with 85.0% to 90.0% of CODcr removal efficiency, and the anaerobic treatment effect demonstrated that biotoxicity of the wastewater could be reduced by the ME reactor.

3.4. Aerobic Biological Treatment by SBR. Subsequently, SBR was utilized for the aerobic biological treatment, mainly focusing on CODcr residue and majority of NH_3-N removal, and SBR reactor was started after EGSB has been operated for 30 d.

CODcr removal efficiency of SBR reactor was shown in Figure 6, revealing that the reactor could reach stable stage easily (about 23 d) and it operated stably after 23 d with the stable CODcr removal efficiency (about 75.0%). From 1 to 13 d, it could be observed that CODcr in effluent was decreased gradually with the increase of CODcr removal efficiency, suggesting that quantity of aerobic heterotrophic bacteria might grow and reproduce gradually. From 13 to 18 d, CODcr in the effluent increased rapidly, probably due to the increase of influent CODcr in SBR, mainly caused by the overload operating of EGSB tank. However, the CODcr removal was affected slightly in this stage, mainly due to the sufficient aerobic heterotrophic bacteria and effective degradation of organic substance, resulting in high CODcr removal efficiency. Meanwhile, the results suggested that the SBR reactor had strong shock resistance ability. After 18 d, CODcr in effluent decreased gradually and subsequently trended to stability, and the reactor entered into the stable stage on 23 d.

Overall, after the SBR reactor reached stability, about 75.0% of influent CODcr could be removed and the effluent CODcr could be always lower than 300 mg L^{-1} on the basis of stable operation of EGSB tank. Moreover, this SBR reactor had strong shock resistance ability.

3.5. Nitrogen Removal Effect by the Whole System. NH_3-N removal effect by the whole system was investigated when the SBR reactor has been operated for about 16 d. The results were shown in Figure 7. It could be observed that the effluent NH_3-N was higher in the first three days than that in later time, mainly caused by the high influent NH_3-N of the system. From 1 to 7 d, the effluent NH_3-N was decreased gradually, mainly due to the growth and reproduction of nitrifying bacteria in the SBR reactor. After this stage, the system entered into the stable stage, resulting in the stable NH_3-N in the effluent of the system. Additionally, NH_3-N in the wastewater was mainly removed by the SBR reactor, demonstrating the great NH_3-N removal ability of SBR reactor [54–56].

Finally, it could be concluded that the whole system could remove about 95.0% of NH_3-N in the wastewater, and NH_3-N in the final effluent of the system could be always lower than 25.0 mg L^{-1}.

4. Conclusions

In this study, conclusions were shown as follows:

(1) Utilization of solid waste (DSS and SI) to prepare new media CAICF was feasible and satisfactory according to the physical properties, microstructure analysis, and toxic metal leaching test of CAICF.

(2) CAICF applied as filler in ME reactor for CTC wastewater pretreatment was effective, approximately 40.0% of CODcr and 90.0% of CTC residue in the wastewater were removed, and biodegradability of the raw wastewater was enhanced effectively.

(3) The coupled ME-EGSB-SBR system could treat the CTC wastewater effectively, approximately 98.0% of

CODcr and 95.0% of NH_3-N could be removed, and the final effluent met the requirement of national standard (CODcr ≤ 300 mg L^{-1}, NH_3-N ≤ 25 mg L^{-1}).

Nomenclature

CTC: Chlortetracycline
OTC: Oxytetracycline
DSS: Dewatered sewage sludge
SI: Scrap iron
CAICF: Cathode-anode integrated ceramic filler
CCF: Cathode fillers
ACF: Anode fillers
EGSB: Expanded granular sludge bed
ME: Microelectrolysis
SBR: Sequencing batch reactor
UASB: Upflow anaerobic sludge blanket
CASS: Cyclic activated sludge system
A/O: Anoxic/oxic activated sludge process
SS: Suspended solid (mg L^{-1})
COD: Chemical oxygen demand (mg L^{-1})
NH_3-N: Ammonia nitrogen (mg L^{-1})
BOD: Biochemical oxygen demand (mg L^{-1})
VFA: Volatile fatty acid (mg L^{-1})
OLR: Organic loading rate (kg m^{-3} d^{-1})
HRT: Hydraulic retention time (h)
DO: Dissolved oxygen (mg L^{-1}).

Competing Interests

The authors declare that they have no competing interests.

Acknowledgments

The study was supported by Program for New Century Excellent Talents in University (NCET-11-0320); the National Natural Science Foundation of China (51378306); Shanghai Jiaotong University "Chenxing Plan (SMC-B)"; and Shandong Provincial Environmental Protection Industry Projects for Technology Research and Development (SDHBYF-2012-12).

References

[1] E. Neyens, J. Baeyens, M. Weemaes, and B. De Heyder, "Hot acid hydrolysis as a potential treatment of thickened sewage sludge," *Journal of Hazardous Materials*, vol. 98, no. 1–3, pp. 275–293, 2003.

[2] S. Werle and R. K. Wilk, "A review of methods for the thermal utilization of sewage sludge: the Polish perspective," *Renewable Energy*, vol. 35, no. 9, pp. 1914–1919, 2010.

[3] J. Werthera and T. Ogadab, "Sewage sludge combustion," *Progress in Energy and Combustion Science*, vol. 25, no. 1, pp. 55–116, 1999.

[4] S.-T. Yan, H. Zheng, A. Li et al., "Systematic analysis of biochemical performance and the microbial community of an activated sludge process using ozone-treated sludge for sludge reduction," *Bioresource Technology*, vol. 100, no. 21, pp. 5002–5009, 2009.

[5] M. R. Salsabil, J. Laurent, M. Casellas, and C. Dagot, "Techno-economic evaluation of thermal treatment, ozonation and sonication for the reduction of wastewater biomass volume before aerobic or anaerobic digestion," *Journal of Hazardous Materials*, vol. 174, no. 1–3, pp. 323–333, 2010.

[6] M. Gheju and I. Balcu, "Removal of chromium from Cr(VI) polluted wastewaters by reduction with scrap iron and subsequent precipitation of resulted cations," *Journal of Hazardous Materials*, vol. 196, pp. 131–138, 2011.

[7] J.-H. Jiang, Y.-H. Li, and W.-M. Cai, "Experimental and mechanism research of SO_2removal by cast iron scraps in a magnetically fixed bed," *Journal of Hazardous Materials*, vol. 153, no. 1-2, pp. 508–513, 2008.

[8] J. R. Perey, P. C. Chiu, C.-P. Huang, and D. K. Cha, "Zero-valent iron pretreatment for enhancing the biodegradability," *Water Environment Research*, vol. 74, no. 3, pp. 221–225, 2002.

[9] Ö. Hanay, B. Yildiz, S. Aslan, and H. Hasar, "Removal of tetracycline and oxytetracycline by microscale zerovalent iron and formation of transformation products," *Environmental Science and Pollution Research*, vol. 21, no. 5, pp. 3774–3782, 2014.

[10] S. Wu, Q. Yue, Y. Qi, B. Gao, S. Han, and M. Yue, "Preparation of ultra-lightweight sludge ceramics (ULSC) and application for pharmaceutical advanced wastewater treatment in a biological aerobic filter (BAF)," *Bioresource Technology*, vol. 102, no. 3, pp. 2296–2300, 2011.

[11] W.-R. Chen and C.-H. Huang, "Adsorption and transformation of tetracycline antibiotics with aluminum oxide," *Chemosphere*, vol. 79, no. 8, pp. 779–785, 2010.

[12] Z. R. Hopkins and L. Blaney, "A novel approach to modeling the reaction kinetics of tetracycline antibiotics with aqueous ozone," *Science of the Total Environment*, vol. 468-469, pp. 337–344, 2013.

[13] N. Kemper, "Veterinary antibiotics in the aquatic and terrestrial environment," *Ecological Indicators*, vol. 8, no. 1, pp. 1–13, 2008.

[14] M. Hammad Khan, H.-S. Jung, W. Lee, and J.-Y. Jung, "Chlortetracycline degradation by photocatalytic ozonation in the aqueous phase: mineralization and the effects on biodegradability," *Environmental Technology*, vol. 34, no. 4, pp. 495–502, 2013.

[15] I. Kim and H. Tanaka, "Photodegradation characteristics of PPCPs in water with UV treatment," *Environment International*, vol. 35, no. 5, pp. 793–802, 2009.

[16] R. Daghrir, P. Drogui, and M. A. El Khakani, "Photoelectrocatalytic oxidation of chlortetracycline using Ti/TiO_2 photo-anode with simultaneous H_2O_2 production," *Electrochimica Acta*, vol. 87, pp. 18–31, 2013.

[17] J. J. López-Peñalver, M. Sánchez-Polo, C. V. Gómez-Pacheco, and J. Rivera-Utrilla, "Photodegradation of tetracyclines in aqueous solution by using UV and UV/H_2O_2 oxidation processes," *Journal of Chemical Technology and Biotechnology*, vol. 85, no. 10, pp. 1325–1333, 2010.

[18] J. J. López Peñalver, C. V. Gómez Pacheco, M. Sánchez Polo, and J. Rivera Utrilla, "Degradation of tetracyclines in different water matrices by advanced oxidation/reduction processes based on gamma radiation," *Journal of Chemical Technology and Biotechnology*, vol. 88, no. 6, pp. 1096–1108, 2013.

[19] J. Jeong, W. Song, W. J. Cooper, J. Jung, and J. Greaves, "Degradation of tetracycline antibiotics: mechanisms and kinetic studies for advanced oxidation/reduction processes," *Chemosphere*, vol. 78, no. 5, pp. 533–540, 2010.

[20] H. C. Zhang, W.-R. Chen, and C.-H. Huang, "Kinetic modeling of oxidation of antibacterial agents by manganese oxide,"

Environmental Science and Technology, vol. 42, no. 15, pp. 5548–5554, 2008.

[21] X. L. Bao, Z. M. Qiang, W. C. Ling, and J.-H. Chang, "Sono-hydrothermal synthesis of MFe_2O_4 magnetic nanoparticles for adsorptive removal of tetracyclines from water," *Separation and Purification Technology*, vol. 117, pp. 104–110, 2013.

[22] S. E. Allaire, J. Del Castillo, and V. Juneau, "Sorption kinetics of chlortetracyline and tylosin on sandy loam and heavy clay soils," *Journal of Environmental Quality*, vol. 35, no. 4, pp. 969–972, 2006.

[23] R. V. P. Jutta and L. David, "Sorption of tetracycline and chlortetracycline on K^- and Ca^- saturated soil clays, humic substances, and clay-humic complexes," *Environmental Science & Technology*, vol. 41, no. 6, pp. 1928–1933, 2007.

[24] J. Rivera-Utrilla, C. V. Gómez-Pacheco, M. Sánchez-Polo, J. J. López-Peñalver, and R. Ocampo-Pérez, "Tetracycline removal from water by adsorption/bioadsorption on activated carbons and sludge-derived adsorbents," *Journal of Environmental Management*, vol. 131, pp. 16–24, 2013.

[25] Y. Qi, S. Wu, F. Xi et al., "Performance of a coupled micro-electrolysis, anaerobic and aerobic system for oxytetracycline (OTC) production wastewater treatment," *Journal of Chemical Technology & Biotechnology*, vol. 91, no. 5, pp. 1290–1298, 2016.

[26] X.-C. Ruan, M.-Y. Liu, Q.-F. Zeng, and Y.-H. Ding, "Degradation and decolorization of reactive red X-3B aqueous solution by ozone integrated with internal micro-electrolysis," *Separation and Purification Technology*, vol. 74, no. 2, pp. 195–201, 2010.

[27] H. Cheng, W. Xu, J. Liu, H. Wang, Y. He, and G. Chen, "Pretreatment of wastewater from triazine manufacturing by coagulation, electrolysis, and internal microelectrolysis," *Journal of Hazardous Materials*, vol. 146, no. 1-2, pp. 385–392, 2007.

[28] S. Wu, Y. Qi, Y. Gao et al., "Preparation of ceramic-corrosion-cell fillers and application for cyclohexanone industry wastewater treatment in electrobath reactor," *Journal of Hazardous Materials*, vol. 196, pp. 139–144, 2011.

[29] D. Ying, J. Peng, X. Xu, K. Li, Y. Wang, and J. Jia, "Treatment of mature landfill leachate by internal micro-electrolysis integrated with coagulation: a comparative study on a novel sequencing batch reactor based on zero valent iron," *Journal of Hazardous Materials*, vol. 229-230, pp. 426–433, 2012.

[30] I. Sirés and E. Brillas, "Remediation of water pollution caused by pharmaceutical residues based on electrochemical separation and degradation technologies: a review," *Environment International*, vol. 40, no. 1, pp. 212–229, 2012.

[31] J. Cheng, X. Zhu, J. Ni, and A. Borthwick, "Palm oil mill effluent treatment using a two-stage microbial fuel cells system integrated with immobilized biological aerated filters," *Bioresource Technology*, vol. 101, no. 8, pp. 2729–2734, 2010.

[32] H. Zhou, P. Lv, Y. Shen, J. Wang, and J. Fan, "Identification of degradation products of ionic liquids in an ultrasound assisted zero-valent iron activated carbon micro-electrolysis system and their degradation mechanism," *Water Research*, vol. 47, no. 10, pp. 3514–3522, 2013.

[33] W.-W. Liu, X.-Y. Tu, X.-P. Wang, F.-Q. Wang, and W. Li, "Pretreatment of coking wastewater by acid out, micro-electrolysis process with in situ electrochemical peroxidation reaction," *Chemical Engineering Journal*, vol. 200–202, pp. 720–728, 2012.

[34] L. Huang, G. Sun, T. Yang, B. Zhang, Y. He, and X. Wang, "A preliminary study of anaerobic treatment coupled with micro-electrolysis for anthraquinone dye wastewater," *Desalination*, vol. 309, pp. 91–96, 2013.

[35] I. Colussi, A. Cortesi, L. D. Vedova, V. Gallo, and F. K. C. Robles, "Start-up procedures and analysis of heavy metals inhibition on methanogenic activity in EGSB reactor," *Bioresource Technology*, vol. 100, no. 24, pp. 6290–6294, 2009.

[36] S. Connaughton, G. Collins, and V. O'Flaherty, "Psychrophilic and mesophilic anaerobic digestion of brewery effluent: a comparative study," *Water Research*, vol. 40, no. 13, pp. 2503–2510, 2006.

[37] W.-Q. Guo, N.-Q. Ren, Z.-B. Chen et al., "Simultaneous biohydrogen production and starch wastewater treatment in an acidogenic expanded granular sludge bed reactor by mixed culture for long-term operation," *International Journal of Hydrogen Energy*, vol. 33, no. 24, pp. 7397–7404, 2008.

[38] A. Siggins, A.-M. Enright, and V. O'Flaherty, "Methanogenic community development in anaerobic granular bioreactors treating trichloroethylene (TCE)-contaminated wastewater at 37°C and 15°C," *Water Research*, vol. 45, no. 8, pp. 2452–2462, 2011.

[39] N. Garcia-Mancha, D. Puyol, V. M. Monsalvo, H. Rajhi, A. F. Mohedano, and J. J. Rodriguez, "Anaerobic treatment of wastewater from used industrial oil recovery," *Journal of Chemical Technology and Biotechnology*, vol. 87, no. 9, pp. 1320–1328, 2012.

[40] Y. J. Chan, M. F. Chong, C. L. Law, and D. G. Hassell, "A review on anaerobic–aerobic treatment of industrial and municipal wastewater," *Chemical Engineering Journal*, vol. 155, no. 1-2, pp. 1–18, 2009.

[41] S. Yi, W.-Q. Zhuang, B. Wu, S. T.-L. Tay, and J.-H. Tay, "Biodegradation of p-nitrophenol by aerobic granules in a sequencing batch reactor," *Environmental Science and Technology*, vol. 40, no. 7, pp. 2396–2401, 2006.

[42] N. Schwarzenbeck, J. M. Borges, and P. A. Wilderer, "Treatment of dairy effluents in an aerobic granular sludge sequencing batch reactor," *Applied Microbiology and Biotechnology*, vol. 66, no. 6, pp. 711–718, 2005.

[43] K.-Z. Su and H.-Q. Yu, "Formation and characterization of aerobic granules in a sequencing batch reactor treating soybean-processing wastewater," *Environmental Science and Technology*, vol. 39, no. 8, pp. 2818–2827, 2005.

[44] Y. Qi, Q. Yue, S. Han et al., "Preparation and mechanism of ultra-lightweight ceramics produced from sewage sludge," *Journal of Hazardous Materials*, vol. 176, no. 1–3, pp. 76–84, 2010.

[45] Y. L. He, *Anaerobic Biological Treatment of Wastewater*, China Light Industry Press, Beijing, China, 1998.

[46] F. Ju and Y. Hu, "Removal of EDTA-chelated copper from aqueous solution by interior microelectrolysis," *Separation and Purification Technology*, vol. 78, no. 1, pp. 33–41, 2011.

[47] M. Stieber, A. Putschew, and M. Jekel, "Treatment of pharmaceuticals and diagnostic agents using zero-valent iron—kinetic studies and assessment of transformation products assay," *Environmental Science and Technology*, vol. 45, no. 11, pp. 4944–4950, 2011.

[48] J.-H. Fan and L.-M. Ma, "The pretreatment by the Fe-Cu process for enhancing biological degradability of the mixed wastewater," *Journal of Hazardous Materials*, vol. 164, no. 2-3, pp. 1392–1397, 2009.

[49] T. B. Hofstetter, C. G. Heijman, S. B. Haderlein, C. Holliger, and R. P. Schwarzenbach, "Complete reduction of TNT and other (poly)nitroaromatic compounds under iron-reducing subsurface conditions," *Environmental Science and Technology*, vol. 33, no. 9, pp. 1479–1487, 1999.

[50] Y. Segura, F. Martínez, and J. A. Melero, "Effective pharmaceutical wastewater degradation by Fenton oxidation with zero-valent iron," *Applied Catalysis B: Environmental*, vol. 136-137, pp. 64–69, 2013.

[51] R. C. Martins, D. V. Lopes, M. J. Quina, and R. M. Quinta-Ferreira, "Treatment improvement of urban landfill leachates by Fenton-like process using ZVI," *Chemical Engineering Journal*, vol. 192, pp. 219–225, 2012.

[52] J. J. Stone, S. A. Clay, Z. Zhu, K. L. Wong, L. R. Porath, and G. M. Spellman, "Effect of antimicrobial compounds tylosin and chlortetracycline during batch anaerobic swine manure digestion," *Water Research*, vol. 43, no. 18, pp. 4740–4750, 2009.

[53] T. M. Dreher, H. V. Mott, C. D. Lupo, A. S. Oswald, S. A. Clay, and J. J. Stone, "Effects of chlortetracycline amended feed on anaerobic sequencing batch reactor performance of swine manure digestion," *Bioresource Technology*, vol. 125, pp. 65–74, 2012.

[54] J. Adriano, S. David, E. Jack et al., "Full-scale nitrogen removal from digester liquid with partial nitritation and anammox in one SBR," *Environmental Science & Technology*, vol. 43, no. 14, pp. 5301–5306, 2009.

[55] M. K. De Kreuk, J. J. Heijnen, and M. C. M. Van Loosdrecht, "Simultaneous COD, nitrogen, and phosphate removal by aerobic granular sludge," *Biotechnology and Bioengineering*, vol. 90, no. 6, pp. 761–769, 2005.

[56] S. Tsuneda, T. Ohno, K. Soejima, and A. Hirata, "Simultaneous nitrogen and phosphorus removal using denitrifying phosphate-accumulating organisms in a sequencing batch reactor," *Biochemical Engineering Journal*, vol. 27, no. 3, pp. 191–196, 2006.

Hindawi Publishing Corporation
Journal of Chemistry
Volume 2016, Article ID 5347154, 10 pages
http://dx.doi.org/10.1155/2016/5347154

Research Article

Winter Maintenance Wash-Water Heavy Metal Removal Pilot Scale Evaluation

Christopher M. Miller, William H. Schneider IV, Mufuta J. Tshimanga, and Philip Custer

University of Akron, 244 Sumner Street, Akron, OH 44325, USA

Correspondence should be addressed to Christopher M. Miller; cmmiller@uakron.edu

Received 6 June 2016; Revised 22 August 2016; Accepted 4 September 2016

Academic Editor: Manuel A. R. Rodrigo

To encourage sustainable engineering practices, departments of transportation are interested in reusing winter maintenance truck wash water as part of their brine production and future road application. Traffic-related metals in the wash water, however, could limit this option. The objective of this work was to conduct a pilot scale evaluation of heavy metal (copper, zinc, iron, and lead) removal in a filtration unit (maximum flow rate of 45 L/minute) containing proprietary (MAR Systems Sorbster®) media. Three different trials were conducted and approximately 10,000 L of wash water collected from a winter maintenance facility in Ohio was treated with the pilot unit. Lab studies were also performed on six wash-water samples from multiple facilities to assess particle size removal and estimate settling time as a potential removal mechanism during wash-water storage. Pilot unit total metal removal efficiencies were 79%, 77%, 63%, and 94% for copper, zinc, iron, and lead, respectively. Particle settling calculation estimates for copper and zinc show that 10 hours in storage can also effectively reduce heavy metal concentrations in winter maintenance wash water in excess of 70%. These pilot scale results show promise for reducing heavy metal concentrations to an acceptable level for reuse.

1. Introduction

During the winter months of the year, snow events can interfere significantly with car and truck based transportation systems. To minimize the effects of these events, the application of anti-icing, pretreatment, and deicing liquids alongside snow plowing is practiced. Anti-icing agents such as calcium acetate, magnesium acetate, and calcium chloride are occasionally applied to roadways. In Ohio, approximately $50 million is spent on snow and ice removal annually, accounting for almost half of the annual operating budget. An average of 600,000 tons of salt is used to maintain Ohio's 43,000 lane miles each year [1]. Due to the corrosive nature of salt, trucks are washed frequently during winter months at garages across the state. At garages with sanitary sewer access, truck wash water is disposed of through the sewer system after treatment by an oil/water separator. Garages without sewer access must find an alternative method of managing truck wash water which falls in line with disposal guidelines. Alternatively, based on the concentrations of suspended solids, oil and grease, and dissolved solids in truck wash water, previous researchers have shown that truck wash water could be reused for the production of brine after a treatment process including an oil/water separator and settling tank [2, 3].

However, the main restrictive elements to winter maintenance wash-water reuse as brine are posed by heavy traffic-related metals that are in violation of EPA set standards and regulations. The traffic heavy metals of concern were observed during a study of water quality parameters of wash water taken during wash cycles at 24 ODOT garages during the winter of 2012-2013. Of all samples tested, 59% were above the reuse limitations for total copper and 66% were found to be above in total zinc [4]. Considering both metal concentrations, only 28% of all samples were found to be reusable according to the Ohio Administrative Code (OAC) aquatic, agricultural, and wildlife standards based on the characteristic hardness of receiving water bodies. The presence of heavy metals above threshold potentially creates a toxic environment, and accumulation over a prolonged period of time can harm receiving water environment by affecting the health of the aquatic ecosystem [5]. Many heavy metals, especially lead and zinc, have been recognized as traffic-related pollutants [6–8]. Specific sources of heavy metals include tire treads for which zinc oxide is an activator during the vulcanizing

process, resulting in a composition of between 0.4% and 4.3% [9]. Other heavy metals in tire tread include manganese, iron, cobalt, nickel, copper, zinc, cadmium, and lead [10]. Brake dust has been recognized as a significant pollutant for copper, antimony, and barium [11]. 47% of the total loading for copper in urban runoff is also contributed by brake dust [12]. Additional sources of heavy metals in urban areas include corrosion of buildings and their fittings, atmospheric deposition, transport, and other industrial activities [12, 13]. Most heavy metals in urban storm water runoff are attached to suspended solids [6, 14] with metal concentrations generally increasing with decreasing particle size [15, 16] due to the relatively large surface area of fine sediments and higher exchange capacity [6]. Furthermore, particles smaller than 50 μm can be a significant component in runoff, contributing to as much as three-quarters of the weight of total solids [17].

The treatment of contaminants in wash water can be achieved using various conventional and emerging methods including ion exchange, electrolyte or liquid extraction, precipitation, and reverse osmosis [18]. However, most of the physiochemical techniques are either economically unfavorable [19] or simply too technically complicated. As an alternative, other studies investigated the removal of storm water contaminants through different media such as calcite, zeolite, iron fillings, and sand through column and batch experiments [20, 21]. These studies found that no single filter medium was capable of removing all contaminants.

There are few options for removing heavy metals in wash water which include the aforementioned physiochemical techniques. For application at DOT garages, there is a need for any technology selected to be simple to use, to be cost-effective, and to require low maintenance, thus negating the options listed above. Therefore, there is a need for pilot evaluation of media particular to traffic-related heavy metals which allows for heavy metal removal from DOT garage wash water. This study investigates the efficiency of MAR Sorbster media, proprietary media for the removal of heavy traffic-related metals (copper, zinc, lead, and iron) from winter maintenance wash water. Experiments were conducted on the MAR Sorbster media testing metal removal efficiency using wash water from actual maintenance events as well as spiked wash water synthesized using actual winter maintenance wash water. The experiments and gradation examinations allowed insights to be made regarding removal efficiency of the traffic-related heavy metals in addition to the effects of particles size distribution of traffic-related heavy metals.

2. Materials and Methods

2.1. Filtration Unit. The filtration unit consisted of two 1,136-liter vessels in series with a continuous downflow configuration. A pair of 5 μm filters was installed immediately after the inlet of the filtration pilot unit but prior to the inlet of the vessels. These filters were arranged in a parallel configuration with the water entering the filtration unit split by a splitter so that it can be treated by either one of the filters. At the outlet of the vessels, a pair of 1 μm filters was installed in a parallel configuration as well. The filters help reduce the amount of suspended solids in the wash water entering the filtration pilot unit as well as in the effluent of treated wash water, improving the life of the media. The wash water was pushed through the filtration pilot unit using a model MCS close coupled, end suction, centrifugal pump with a threaded shaft extension.

2.2. Filter Media. MAR Sorbster media were selected for this study following a series of batch experiments with four different media types in which MAR Sorbster had the most efficient heavy metal removal characteristics [4]. MAR Sorbster is a proprietary medium that removes metal contaminants from water. It is an enriched alumina medium. Each vessel was filled with 102 kg of gravel constituting the bottom layer and 495 kg of MAR Sorbster media as the overlying layer. The moisture content of the media was <10%. The physical properties of the media were obtained from the manufacturer. The specific gravity was 3-4. The grain size of the MAR Sorbster media was 0.0048 m which was assumed to be uniform. The physical state of the media was as free flowing granules. Before use on the wash water, the media were dry loaded into the pilot unit and then backwashed at a flow rate of 35–45 L/minute which resulted in a bed expansion of approximately 15%. Backwashing was done to avoid plugging of the media by any debris as well as reduce the amount of total suspended solids in the treated wash water through particulates in the media and gravel. In between experimental runs, the media were kept in a damp state in order to maintain an optimal removal state. The hydraulic time was controlled through the flow rate. The optimal contact time for heavy metal removal by the MAR Sorbster media is 30 minutes. The flow rate was adjusted to 38 L/minute such that the contact time in each vessel was 15 minutes.

2.3. Wash-Water Pilot Testing Procedures. Wash water for all experimental runs was collected from the oil/water separator at the Stark County garage in Canton, Ohio, and pumped directly from the swap truck using a sump pump into the filtration unit. To observe the variability and characteristics of the wash water, a 3-hour wash cycle study was conducted at the Stark County garage oil/water separator in Canton, Ohio. During this 3-hour study, samples were collected every 15 minutes at a consistent depth below the oil layer. Each sample was placed in 0.5 L high density polyethylene bottle; 125 mL of the sample was preserved with (1 + 1) reagent grade nitric acid at pH < 2. The rest of the sample was left unpreserved. During this study, particles below 5 μm in diameter were assumed to be in the dissolved state. The individual average values of the nonmetal parameters for the wash water were measured using a minimum of 9 samples from different time intervals. Three experimental runs were conducted on the MAR Sorbster media. Stark 1, the first trial, was a 3,255 L run of wash water. Stark 2, the second trial, was a 2,650 L run of wash water spiked with 1.92 grams of $CuSO_4 \cdot 5H_2O$, 2.03 grams of ZnO, and 3.99 grams of $PbCO_3$. Stark 3, the third trial, was a 4,164 L run of wash water spiked with 1.82 grams of $CuSO_4 \cdot 5H_2O$, 3.35 grams of ZnO, and 3.98 grams of $PbCO_3$. Stark 2 and Stark 3 were spiked in order to elevate the concentration of dissolved target metals in the untreated wash water to assess the removal capabilities of the media with higher concentrations of dissolved metals.

During each experimental run, samples were taken at the following locations on the pilot unit: influent (C_o), after the 5 μm filters, after the first filtration unit vessel, after the second filtration unit vessel, and after the 1 μm filters (C_e). For Stark 2 and Stark 3, the 1 μm filters were removed which effectively made the effluent the same as the location after the second pilot unit vessel. Samples were collected every 15 minutes, characteristic of the water-to-media contact time for a single filtration unit vessel. Each sample was placed in 0.5 L high density polyethylene bottle; 125 mL of the sample was preserved with (1 + 1) reagent grade nitric acid at pH < 2. The difference between the influent and the effluent concentrations was used to calculate the percent removal by the media. The equation is listed below:

$$\text{heavy metal removal } (\%) = \frac{(C_o - C_e)}{C_o} \times 100, \quad (1)$$

where heavy metal removal signifies the amount of heavy metals removed from the wash water by the MAR Sorbster media. C_e is the average concentration of the effluent and C_o is the average concentration of the influent.

In order to assess the proportion of the particles greater than 4 μm contributing to the total metal concentration, a Whatman filter paper procedure was used. Five ODOT county garages, namely, Allen, Stark, Fairfield, Guernsey, and Cuyahoga county garages, were selected for sampling using the same samples that were initially collected for the wash-water analysis. These garages were selected because they represented garages at which the metals of concern exceeded reuse limits consistently during the previous study in the 24 ODOT garages which was conducted in the winter of 2012-2013 [4]. Three size fractions were selected, <4 μm, 4 μm < size < 5 μm, and >5 μm. The wash-water samples from the six garages were separated into three size fractions using 4 μm and 5 μm filter paper. Each sample was placed in 0.5 L high density polyethylene bottle; 125 mL of the sample was preserved with (1+1) reagent grade nitric acid at pH < 2. This procedure analyzed the dissolved metal concentration, the total metal concentration, and concentration between 4 μm and 5 μm. The fractions of each size fraction's contribution to the total metal concentration were used to assess settling as a viable option to total metal concentration reduction in ODOT winter maintenance wash water.

2.4. Settling Calculations. Settling could be a crucial mechanism in heavy metal removal. Settling rates are dependent on several different variables. The primary variables are the physical properties of both the settling particle and the fluid in which the particle is settling. The behavior of the fluid is related to two intrinsic properties of the fluid: density and viscosity. The density of a fluid is its mass per unit volume. The density of a fluid is affected by changes in temperature and pressure. The viscosity of a fluid is the measure of the internal resistance. The viscosity of Newtonian fluids is affected by temperature, pressure, and, in the case of solutions and mixtures, composition. For the case of this study, it will be assumed that pressure will remain constant at atmospheric pressure. The composition of winter maintenance wash water varies greatly based on the characteristics of the roadways being maintained. Of the variances, salinity would have the greatest effect on the settling times of particles.

Settling calculations were conducted for various sized particles of the metals copper, zinc, lead, and iron. Equation (2), Stokes law, was used to calculate the settling velocity for the above stated metals. Stokes equation is listed below:

$$V_s = \frac{gd^2\left(\rho_p - \rho_m\right)}{18\mu}, \quad (2)$$

where V_s is the settling velocity, g is the acceleration due to gravity, d is the diameter of particle, ρ_p is the density of particle, ρ_m is the density of medium, and μ is the dynamic viscosity. The acceleration due to gravity was assumed to be 9.81 m/s^2, and the diameter of the particles ranged from 1 μm to 5 μm in 1 μm increments. The density of copper was 8,960 kg/m^3, of zinc was 7,140 kg/m^3, of lead was 11,340 kg/m^3, and of iron was 7,874 kg/m^3; the density of water was 1000 kg/m^3. It was assumed that since the settling tank would be housed indoors but without any climate control, the temperature during the settling process would be 4.4°C.

The viscosity of liquids decreases with increasing temperature. The relationship between temperature and viscosity is expressed as an Arrhenius equation as follows:

$$\mu = \mu_o \frac{E_\mu}{e^{RT}}, \quad (3)$$

where μ_o is the viscosity at a reference temperature (4.4°C), E_μ is the temperature coefficient for viscosity, R is the gas constant, and T is the temperature in Kelvin. Therefore, the dynamic viscosity was 0.001519 kg/m-s at the specified temperature of 4.4°C. The viscosity of wash water based on the above equation ranged from 0.00091 kg/m-s to 0.00179 kg/m-s as the temperature was varied from 0°C to 21.1°C. The density of water also varied as the temperature changed from 0°C to 21.1°C with values ranging between 998 kg/m^3 and 1,000 kg/m^3.

2.5. Analytical Methods. The heavy metals selected for wash-water analysis were aluminum (Al), arsenic (As), boron (B), beryllium (Be), cadmium (Cd), cobalt (Co), chromium (Cr), copper (Cu), iron (Fe), lithium (Li), manganese (Mn), molybdenum (Mo), nickel (Ni), lead (Pb), selenium (Se), vanadium (V), and zinc (Zn). Each sample was placed in 1 L high density polyethylene bottle; 125 mL of the sample was preserved with (1 + 1) reagent grade nitric acid at pH < 2. The rest of the sample was left unpreserved. 25 mL of the sample was preserved with (1 + 1) reagent grade nitric acid at pH < 2 and then filtered with a 5 μm filter. The preserved samples were digested according to EPA 200.7 and analyzed by Inductively Coupled Plasma-Optical Emission Spectrometry (ICP-OES) that used an Agilent 720/730 series spectrometer. ICP-OES can be used to determine dissolved analytes in aqueous samples after suitable filtration and acid preservation. For the determination of total recoverable analytes in aqueous and solid samples, digestion/extraction is required prior to analysis. The traffic metals were analyzed

for their total concentration as well for the dissolved metal concentrations. The calibration, detection limits, and linear ranges were determined according to EPA 200.7. Dissolved analytes were filtered with a 0.45 μm filter before analysis through ICP-OES. Unpreserved samples were analyzed for the following: conductivity (HACH CO150 Conductivity Meter), pH (Fisher Scientific AB15 pH Meter), and total dissolved solids (Shimadzu TOC-5000A TOC Analyzer).

3. Results and Discussion

3.1. Pilot Unit Heavy Metal Removal. This section characterizes the attributes of the wash water from Stark County garage, which was the location that all the wash water was collected from throughout the duration of the study. In order to characterize the wash water, a 3-hour wash study was performed at the Stark County garage. In characterizing the wash water, the traffic metals of concern in this study were highlighted. Analysis of any observable trends in heavy metal concentrations during the 3-hour sampling duration was made and any probable causes were discussed. Finally, in the characterization, the nonmetal attributes of the wash water were quantified. The heavy metal removal efficiency from the wash water by the pilot unit was then analyzed. This was accomplished through analyzing the removal mechanisms in two distinct stages. The first stage of the analysis was the physical removal of any particulate species greater than the 5 μm size. The second stage of the analysis was the removal of any species less than 5 μm in size including not only metals in the dissolved phase but also metals in the particulate form less than 5 μm in size. Although three experimental trials were run on the filtration unit, trial Stark 1 was not studied extensively because the dissolved constituent (below 5 μm) of the heavy metal concentrations of the wash water was frequently below the detection limit. The percentage of copper samples below the detection limit was 83% with the percentage of lead samples below the detection limit at 35%. This meant that observations of any significant changes in dissolved heavy metal concentrations through treatment by the MAR Sorbster media could not be made. Trials Stark 2 and Stark 3 had a measurable dissolved metal concentration range that allowed for observations of trends through the different filtration unit locations, although monitoring was carried out only for two of the heavy metals, zinc and iron.

3.2. Wash-Water Characteristics. Table 1 represents the total metal concentrations during the 3-hour study with the traffic heavy metals of concern highlighted for ease of identification. The traffic heavy metals of concern were observed during a study of water quality parameters of wash water taken during wash cycles at 24 ODOT garages during the winter of 2012-2013. Of all samples tested, 59% were above the reuse limitations for total copper and 66% were found to be above in total zinc [4]. Considering both metal concentrations, only 28% of all samples were found to be reusable according to the Ohio Administrative Code (OAC) aquatic, agricultural, and wildlife standards based on the characteristic hardness of receiving water bodies. The variability of the metals in Table 1 was observed, which can be accounted for by several factors based on the conditions of the wash including varying hose pressure during the wash as well as any initial flushes towards the beginning of the wash. Another possible cause for the variation in metal concentrations during the 3-hour study could be attributed to inconsistent depths at which the samples were collected. The nonmetal parameters were also characterized with the characteristic pH of the wash water between 6.5 and 7. The conductivity of the wash water was on average 73.9 mS/cm. The turbidity of the wash water was on average 42,788 NTU.

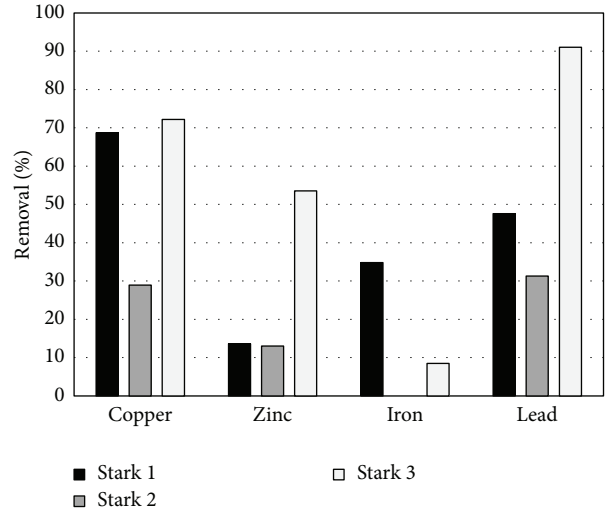

Figure 1: Total metal removal due to the 5 μm filter located directly after the inlet of the filtration unit. Removal percentage was calculated based on the average concentration after the 5 μm filter across all time periods. Refer to Table 2.

3.3. Filtration Unit Heavy Metals Removal by Filters. A portion of the total metal removal is attributed to the 5 μm filters only which are located immediately after the inlet of the pilot unit and directly before the vessels containing the MAR Sorbster media. Figure 1 summarizes the removal of each metal for each of the three Stark County filtration unit runs by these initial 5 μm filters. The average metal removal of total copper, zinc, iron, and lead by just the 5 μm filter is 57%, 27%, 8%, and 57%, respectively, across all 3 experimental runs. Removal percentages were calculated based on the initial concentrations of the influent wash water which are given in Table 2 and the average metal concentrations after the 5 μm filter across all time periods; that is, the metal concentration of every sample taken throughout the duration of each filtration run at the location after the 5 μm filter was averaged to attain the removal percentage.

When total metal concentrations are evaluated, a clear and consistent pattern is observed for the three pilot unit runs from the Stark County garage. Figures 1 and 2 display the cumulative removal of copper and zinc as the wash water passes through each stage in the pilot unit. The removal percentage for each location was calculated based on the average concentration across all time periods tested at that location. A similar pattern is found for iron and lead. After treatment

Table 1: Metal concentrations from the 3-hour oil/water separator study that was conducted at the Stark County garage on April 3, 2013. All samples below the detection limit have been identified with the less than sign and the detection limit. For the computation of the average, standard deviation, and median, all values below the detection limit were replaced with half the detection limit. Arsenic, cobalt, and selenium values are not shown below because more than half of the samples were below the detection limit. All units are μg/L (ppb).

Time	Al	B	Be	Cd	Cr	Cu	Fe	Li	Mn	Mo	Ni	Pb	V	Zn
7:00	4463	206	0.3	1	79	**100**	**16828**	13	1283	15	59	**45**	13	**929**
7:15	4106	170	0.4	1	132	**93**	**19733**	10	1185	14	69	**44**	14	**1095**
7:30	4940	182	0.5	3	158	**324**	**23329**	13	1366	15	112	**140**	16	**2278**
7:45	3322	168	0.3	1	145	**111**	**17741**	14	1056	12	57	**33**	11	**1579**
8:00	3114	175	0.3	2	152	**142**	**21929**	6	944	10	63	**60**	11	**2105**
8:15	546	134	<0.1	1	22	**57**	**3752**	6	288	7	28	**<21**	<1	**423**
8:30	2768	181	0.2	1	103	**120**	**18571**	11	711	11	54	**42**	10	**913**
8:45	2058	169	0.2	<0.9	70	**108**	**12740**	12	529	9	45	**32**	5	**460**
9:00	4723	205	0.3	2	125	**269**	**26345**	5	863	11	64	**62**	14	**756**
9:15	3784	185	0.3	2	106	**257**	**18805**	11	886	11	68	**76**	10	**591**
9:30	3418	201	0.2	2	118	**179**	**27431**	11	861	10	65	**41**	10	**699**
9:45	2749	190	0.2	1	90	**136**	**18547**	10	667	8	62	**30**	8	**771**
10:00	1358	178	0.1	<0.9	41	**64**	**8667**	9	400	6	37	**<21**	4	**307**
Average ± std. dev.	3181 ± 1250	180 ± 18	0.2 ± 0.1	1 ± 1	103 ± 40	**151 ± 80**	**18032 ± 6360**	10 ± 3	849 ± 315	11 ± 3	60 ± 19	**48 ± 32**	10 ± 4	**993 ± 600**
Median	3322	181	0.3	1	106	**120**	**18571**	11	863	11	62	**42**	10	**771**

Table 2: Initial total metal concentrations for experimental runs Stark 1, Stark 2, and Stark 3 measured at the inlet of the filtration unit. All samples below the detection limit were given the value of half the detection limit. Only the traffic metals that are of concern regarding the violation of reuse and disposal guidelines are listed. All units are μg/L (ppb).

Heavy metal species	Experimental run		
	Stark 1	Stark 2	Stark 3
Copper	197	277	236
Iron	8033	2667	2684
Lead	23	747	364
Zinc	564	827	690

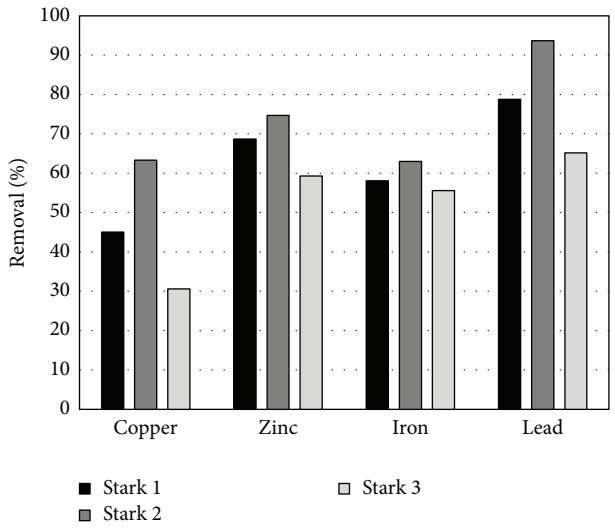

Figure 2: Percent removal of total metals by MAR media on all metals less than 5 μm in diameter, that is, the percent removal of total metals in the vessels of the filtration unit by the MAR media. Removal percentage was calculated based on the average concentration after vessel 2 for all time periods and the average concentration after the 5 μm filter for all time periods.

with the pilot unit, the average total copper removal for all three experiments was 79%. For total zinc, the average removal is 77%. For total iron, the average removal is 63%. For total lead, the average removal is 94%. For the influent concentration, an initial sample was taken at the beginning of each trial and used throughout the trial; therefore, there was no resampling of the influent concentration at the different time periods. This was done in order to maintain a baseline with which to analyze heavy metal removal across the time periods and locations.

Analyzing Figure 1 which illustrates the heavy metal removal percentages by the 5 μm filter located immediately after the inlet of the filtration unit and directly before the media vessels, there is relatively high heavy metal removal by the 5 μm filters. What can also be observed as well is that, for the metals of concern, copper and zinc, a significantly higher average percentage, 57%, of copper was removed by the 5 μm filters as compared to 27% removal of zinc. This may be indicative of the notion that higher toxicity of copper is in

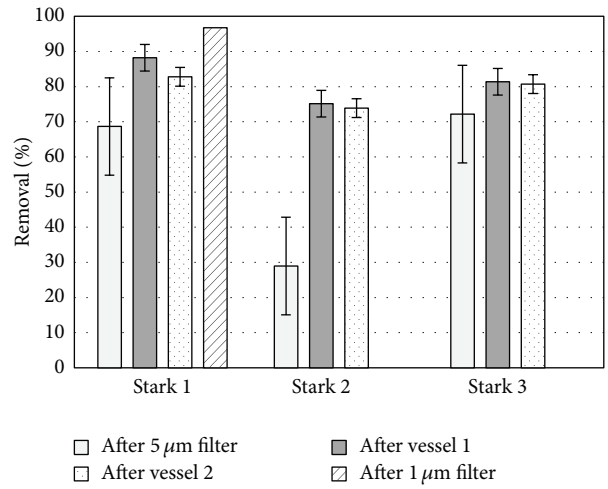

Figure 3: Cumulative removal of total copper at each stage of the Stark County garage trials. The removal percentage for each location was calculated based on the average concentration across all time periods tested at that location. The second and third trials did not have the optional 1 μm filter attached at the end of the unit. The error bars are indicative of the standard error.

the particulate form, whereas zinc toxicity is predominantly characterized by particles less than 5 μm in size.

3.4. Filtration Unit Heavy Metals Removal by MAR Media. After the 5 μm filter, the reduction in the metal concentrations is attributed solely to MAR Systems Sorbster media. As exhibited in Figure 2, the media within vessels 1 and 2 remove between 30% and 94% of metal particles less than 5 μm depending on the experimental run and the type of metal. For copper, average metal removal of 46% is found for particles less than 5 μm. For zinc, the removal percentage is even better at 68%. For iron and lead, the removal percentages are 59% and 79%, respectively. Removal percentages were calculated based on the average concentration after vessel 2 for all time periods and the average concentration after the 5 μm filter for all time periods.

For trial Stark 2, the concentration of dissolved zinc was reduced from an initial concentration of 88 μg/L to 15 μg/L. For trial Stark 3, the trend was similar as the dissolved zinc concentration was reduced from 78 μg/L to 6 μg/L. For trial Stark 2, the dissolved iron concentration increased from 110 μg/L to 288 μg/L. For trial Stark 3, the dissolved iron concentration increased from 148 μg/L to 235 μg/L. The increase of the dissolved iron could be attributed to the makeup of the MAR Sorbster media. Sorbster media however are effective in dissolved zinc removal. Analyzing Figure 2, the metal removal by the Sorbster media is greater for zinc at 68% than it is for the other metal of concern, copper, at 46%. This solidifies what is shown in Figure 1 that the dominant constituent form of zinc contributing to its toxicity is dissolved and particulate below the 5 μm size fraction whereas copper is found in greater concentrations in the particulate (greater than 5 μm) size fraction. Figures 3 and 4 can further illustrate removal trends by isolating each of the metals of concern and

Table 3: Percent total metal removal by a 4 μm and 5 μm filter for each of the six wash-water samples.

County garage	Copper		Zinc		Iron		Lead	
	>5 μm	>4 μm	>5 μm	>4 μm	>5 μm	>4 μm	>5 μm	>4 μm
Allen	98	99	82	86	94	95	96	98
Stark 1	98	98	93	95	99	100	96	95
Stark 2	82	73	72	84	98	99	93	64
Fairfield	40	46	25	28	87	96	93	87
Guernsey	99	99	81	82	99	99	99	99
Cuyahoga	72	73	9	10	44	43	11	17

See (2).

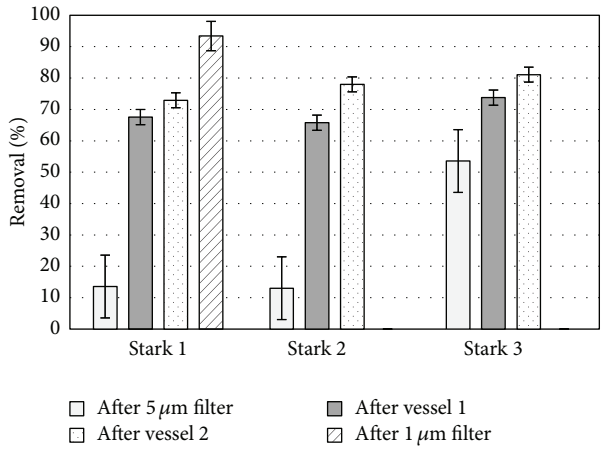

Figure 4: Cumulative removal of total zinc at each stage of the Stark County garage trials. The removal percentage for each location was calculated based on the average concentration across all time periods tested at that location. The second and third trials did not have the optional 1 μm filter attached at the end of the unit. The error bars are indicative of the standard error.

assessing the metal removal rate at each stage of the filtration unit. Analyzing copper in Figure 3, for each of the experimental trials, there was initial physical metal removal by the 5 μm filters on the filtration unit. There was a continued increase in the cumulative removal rate of copper from the wash water through vessel 1 which contained the Sorbster media, which indicated that both physical removal of particulates below the 5 μm size and adsorption of dissolved copper by the Sorbster media were the mechanisms of removal. After vessel 1, the cumulative copper removal did not continue to increase but it statistically did not change from vessel 1 to vessel 2.

This, as observed earlier, indicates that, of the two forms in which copper was found in the wash water, the particulate (greater than 5 μm) form contributes more to the toxicity of copper in wash water. In contrast, analyzing Figure 4 particularly trials Stark 1 and Stark 2, although there was removal of zinc by the 5 μm filters, the majority of the removal was observed after the wash water was treated in vessel 1 with an average increase in the cumulative removal in excess of 50%. There was a continued increase in the cumulative removal through vessel 2 as well. This showed that the Sorbster media were the primary mode of removal for zinc, further indicating that the zinc in the wash water was most toxic in particle sizes below the 5 μm size.

3.5. Particle Settling Heavy Metal Removal Evaluation. The result of effect of the size of particles on heavy metal toxicity was then further explored through a size gradation experiment. Wash water for the size gradation experiment was collected from five garages distributed across the state of Ohio. The selection criteria for each garage were dependent on whether the traffic metals of concern in this study exceeded reuse limits at that particular garage. If a garage exceeded the reuse limits, it becomes a candidate for selection for the gradation experiment which graded the wash water in three distinct size gradations. After this, results of the analysis of settling times for the particle sizes with significant contributions towards heavy metal toxicity are discussed. Settling depths typical of settling basin depths at Ohio Department of Transport garages were used in the analysis and varying temperature ranges were used to mimic different garage conditions and settings. Finally, any beneficial applications and implementation methods are discussed.

This section analyzes the results of the particle size evaluation procedure that was conducted. Table 3 summarizes the percentage total metal removal by the 4 μm and 5 μm Whatman filter paper particle size evaluation procedure. For copper, the average removal by the 4 μm filter was 81% while that of the 5 μm filter was 82%. For zinc, the average removal by the 4 μm filter was 64% while that of the 5 μm filter was 60%. For iron, the average removal by the 4 μm filter was 89% while that of the 5 μm filter was 87%. For lead, the average removal by the 4 μm filter was 76% while that of the 5 μm filter was 76%. This indicates that there is a significant portion of the total metal concentration that is present in the particulate form greater than 4 μm. Looking at the 5 μm and 4 μm sizes overall average total metal removal also indicates that there is not much difference in total metal removal between the two size fractions. Again, it can be observed that for the two metals of concern copper is more predominantly toxic in the particle size range greater than the 5 μm size. Although the reduction in zinc toxicity was reduced by 60%, there is still a significant metal concentration of zinc in the dissolved phase and particulate form below the 5 μm size fraction. Using this, along with the clogging of filters due to particulate metals, the merit of allowing the wash water to settle in order to allow for removal of colloidal metals became a viable and efficient

Table 4: Summarization of settling times for the significant particle sizes of copper and zinc for depths most similar to settling tanks located at ODOT garages (2 m-3 m). Times are computed using Stokes law and the dynamic viscosity of water is assumed to be 0.001519 kg/m-s (4.4°C). Settling times are in hours.

Metal	5 μm		3 μm	
	2 m	3 m	2 m	3 m
Copper	7.8	11.7	21.6	32.4
Zinc	10.1	15.1	28.0	42.0

option to reduce total metal concentrations worthy of further study.

Settling calculations were conducted at depths ranging from 0 meters to depths of 3 meters with major emphasis put on the depth ranges of 2 meters-3 meters which is characteristic of ODOT settling basins and tanks. The significance of this is that at this depth ODOT garages capacity to work on a day-to-day basis would not be jeopardized by overfilling or overflow due to multiple wash events before any existing wash water is allowed to settle. The summary of the settling of copper is shown in Table 4. The size fractions analyzed were 1 μm–5 μm. The settling times for 1 μm size fraction ranged from 97.3 hours to 486.3 hours with the depth increasing from 1 m to 5 m, whereas the settling times for the 5 μm size ranged from 3.9 hours to 19.5 hours with the depth increasing from 1 m to 5 m. The settling times were varied by depth. For the 1 μm size fraction of zinc, the settling times ranged from 126.1 hours to 630.5 hours as the depth increased from 1 m to 5 m. For the 5 μm size fraction of zinc, the settling times ranged from 5.0 hours to 25.2 hours as the depth increased from 1 m to 5 m. The 1 μm size fraction of lead had settling times that varied from 74.9 hours to 374.4 hours as the depth increased from 1 m to 5 m; the 5 μm size fraction of lead varied from 3.0 hours to 15.0 hours as the depth increased from 1 m to 5 m. The 1 μm size fraction of iron had settling times that varied from 112.6 hours to 563.1 hours as the depth increased from 1 m to 5 m; the 5 μm size fraction of iron varied from 4.5 hours to 22.5 hours as the depth increased from 1 m to 5 m. Table 4 shows the settling times for copper and zinc for depths of 2 m and 3 m for the size fractions 3 μm and 5 μm. Figure 5 illustrates the settling time for the zinc particle at a fixed temperature of 4.4°C which is typical of a housed settling basin during the winter months at ODOT garages. Zinc was chosen because it is the metal with the smallest density among the metals of concern; therefore, all the other metals would take a shorter time frame to settle than zinc, thus making the overall critical settling time depend more on the critical zinc settling times.

Figure 6 shows the settling times for copper, iron, and lead at the same temperature of 4.4°C at depths ranging from 0 m to 3 m. The temperature of the water has a great effect on the settling time as well. In order to grasp what the effect was, the settling times based on temperatures ranging from 0°C to 21.1°C were plotted against depths ranging from 0 m to 3 m. This temperature range was chosen as it represented the different extreme conditions that a settling basin would be subjected to if it were located indoors or outdoors during

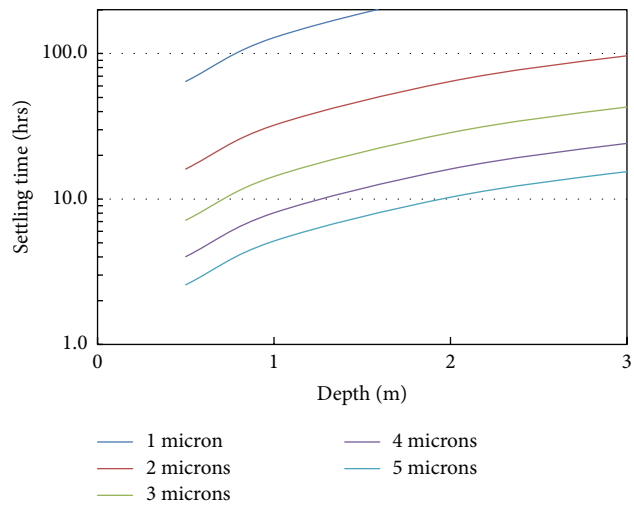

Figure 5: Settling times for zinc particles based on Stokes law. The assumed dynamic viscosity of water for the equation is 0.001519 kg/m-s (4.4°C). The settling times vary by depth with the different size fraction.

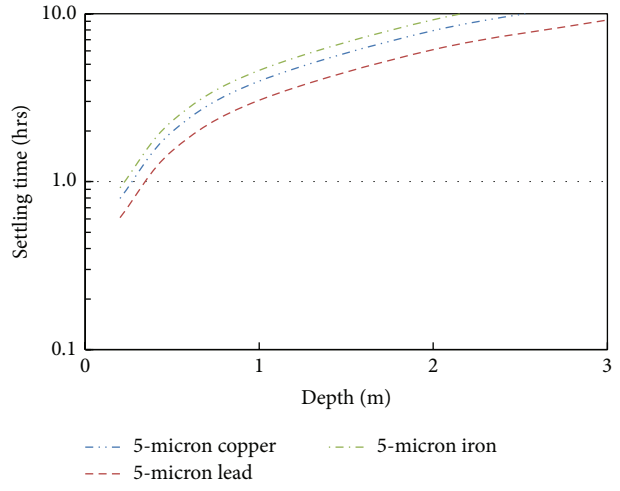

Figure 6: Settling time for copper, iron, and lead particles based on Stokes law. The assumed dynamic viscosity of water for the equation is 0.001519 kg/m-s (4.4°C). The settling times vary by depth, size, and material.

the winter months when winter maintenance was conducted. This is illustrated by both Figure 7 and Table 5. Both show that, for instance, keeping the depth fixed at 2 m and a temperature of 0°C and a temperature of 5°C, the resultant settling time difference was 2 hours. These subtle changes can help improve treatment times of wash water through settling by finding an optimal temperature at which to allow the wash water to settle.

3.6. Application and Implementation. Owing to the variability in the heavy metal constituents of the winter maintenance wash water used throughout the duration of this study, recommendations for a single treatment train for winter maintenance wash water cannot be made with any confidence. It has been shown that the form (particulate or

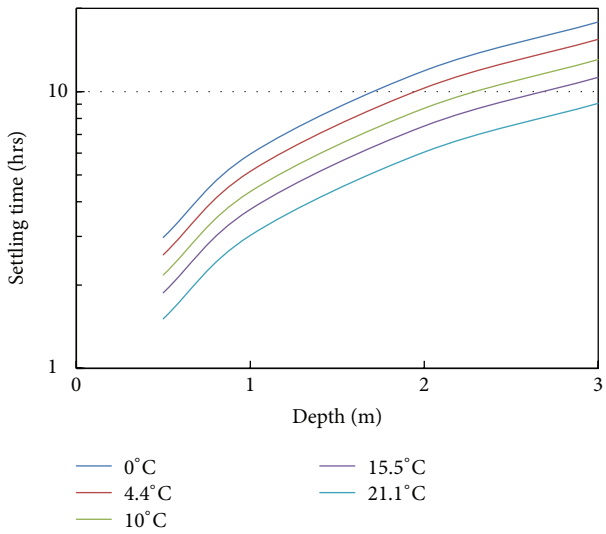

Figure 7: Settling times for zinc particles based on Stokes law. The assumed dynamic viscosity of water for the equation is determined based on the temperature of the water. The settling times vary by the different water temperatures and the depth to which particles are settling.

Table 5: Settling times in hours for zinc particles based on Stokes law. The assumed dynamic viscosity of water for the Stokes law equation is determined by the temperature of the water. The particle settling times vary based on water temperature and the depth to which the particles are settling.

Depth (m)	Temperature (°C)				
	0	5	10	16	21
1	6	5	4	4	3
2	12	10	9	8	6
3	18	15	13	11	9

dissolved) or particle size range in which the heavy metal is most toxic would allow a choice of either media filtration or settling. By retrofitting an ODOT garage with both settling tanks and a filtrations unit, the majority of the particulate metals can be removed through allowing the wash water to sit for a prescribed period of time, before running the wash water through the filtration system to remove any remaining particulates and the majority of the dissolved constituent as well. The study has shown that MAR Sorbster media are effective in reducing heavy metals concentration in wash water. The study also showed that, allowing the wash water to settle for a prescribed amount of time at an optimal temperature, the majority of the particulate constituent of heavy metals can be eliminated and, for heavy metal species that are more toxic in larger particle size ranges, this can be a viable treatment option if used in isolation. Understanding the nature of the wash water allows for a more appropriate treatment regime to be applied.

4. Conclusions

The study assessed the heavy traffic metal reduction in winter maintenance wash water by MAR Sorbster media as well as the impact of particle size on heavy metal concentration. A pilot unit filled with the media was used to run a series of continuous flow experiments to assess heavy metal removal on winter maintenance wash water. The wash water was taken from ODOT's Stark County garage in Northeast Ohio. The total and dissolved metal concentrations were assessed. The metals assessed were copper, zinc, lead, and iron. The effect of particle size on heavy metal toxicity was analyzed and theoretical settling calculations using Stokes law were applied to assess viable heavy metal removal mechanisms. The following conclusions can be drawn:

(i) Particulate metal concentrations are typically higher than dissolved metal concentrations for the traffic metals.

(ii) The pilot unit removal efficiency for copper and zinc removal in the wash water exceeded 70% of the influent concentration.

(iii) The 5 μm filters removal efficiency for copper exceeded 25%, for zinc exceeded 10%, and for lead exceeded 30%.

(iv) For all the trials, MAR Sorbster media average removal efficiency for copper exceeded 30%, for zinc exceeded 55%, for lead exceeded 50%, and for iron exceeded 60% for particles <5 μm.

(v) Of the two heavy metals of concern, copper was found predominantly more in the particulate form, and this contributed a greater percentage of the overall toxicity of copper. Zinc alternatively was found to be in the dissolved phase and particulates below the 5 μm size range.

(vi) Allowing the wash water to settle for a minimum of 10 hours would allow removal of particulates larger than 5 μm resulting in heavy metals removal rates exceeding 70%. In addition, adjusting the temperature to an optimal temperature can reduce settling times in excess of a few hours based on settling depths.

(vii) Overall MAR Sorbster media are an effective option to remove heavy metals in winter maintenance wash water, particularly zinc whose cumulative removal increased in excess of 50% by the end of treatment by just a single filtration media vessel.

(viii) Alternatively, allowing the wash water to settle results in a significant reduction in heavy metal concentration in winter maintenance wash water which was equal to or close to the filtration pilot heavy metal reduction.

Competing Interests

The authors declare that they have no competing interests.

References

[1] Ohio Department of Transportation, *Snow and Ice Practices*, Division of Operations, Office of Maintenance Administration, 2011.

[2] J. E. Alleman, B. K. Partridge, and L. Yeung, "Innovative environmental management of winter salt runoff problems at INDOT maintenance yards," 2004.

[3] V. Craver, G. Fitch, and J. Smith, "Recycling of salt-contaminated stormwater runoff for brine production at Virginia Department of Transportation Road-Salt Storage Facilities," Tech. Rep. VTRC 08-R17, Virginia Transportation Research Council, Charlottesville, Va, USA, 2008.

[4] C. M. Miller, W. H. Schneider IV, M. Kennedy, H. Parker, and S. Sullivan, "Snow removal waste water disposal alternatives," State Job PS-2012-06, Ohio Department of Transportation, Office of Research and Development, Columbus, Ohio, USA, 2012.

[5] Q. Zhou, J. Zhang, J. Fu, J. Shi, and G. Jiang, "Biomonitoring: an appealing tool for assessment of metal pollution in the aquatic ecosystem," *Analytica Chimica Acta*, vol. 606, no. 2, pp. 135–150, 2008.

[6] A. Dong, G. Chesters, and G. V. Simsiman, "Metal composition of soil, sediments, and urban dust and dirt samples from the Menomonee River Watershed, Wisconsin, USA," *Water, Air, and Soil Pollution*, vol. 22, no. 3, pp. 257–275, 1984.

[7] W. G. Wilber and J. V. Hunter, "Distribution of metals in street sweepings, stormwater solids, and urban aquatic sediments," *Journal of the Water Pollution Control Federation*, vol. 51, no. 12, pp. 2810–2822, 1979.

[8] J. J. Sansalone and S. G. Buchberger, "Partitioning and first flush of metals in urban roadway storm water," *Journal of Environmental Engineering*, vol. 123, no. 2, pp. 134–143, 1997.

[9] E. Smolders and F. Degryse, "Fate and effect of zinc from tire debris in soil," *Environmental Science and Technology*, vol. 36, no. 17, pp. 3706–3710, 2002.

[10] N. Fukuzaki, T. Yanaka, and Y. Urushiyama, "Effects of studded tires on roadside airborne dust pollution in Niigata, Japan," *Atmospheric Environment*, vol. 20, no. 2, pp. 377–386, 1986.

[11] J. Sternbeck, Å. Sjödin, and K. Andréasson, "Metal emissions from road traffic and the influence of resuspension—results from two tunnel studies," *Atmospheric Environment*, vol. 36, no. 30, pp. 4735–4744, 2002.

[12] A. P. Davis, M. Shokouhian, and S. Ni, "Loading estimates of lead, copper, cadmium, and zinc in urban runoff from specific sources," *Chemosphere*, vol. 44, no. 5, pp. 997–1009, 2001.

[13] E. J. Christensen, C. E. Olney, and T. F. Bidleman, "Comparison of dry and wet surfaces for collecting organochlorine dry deposition," *Bulletin of Environmental Contamination and Toxicology*, vol. 23, no. 1, pp. 196–202, 1979.

[14] B. A. Bodo, "Heavy metals in water and suspended particulates from an urban basin impacting Lake Ontario," *Science of The Total Environment*, vol. 87-88, pp. 329–344, 1989.

[15] J. Liebens, "Heavy metal contamination of sediments in stormwater management systems: the effect of land use, particle size, and age," *Environmental Geology*, vol. 41, no. 3-4, pp. 341–351, 2002.

[16] M. Ujevic and P. S. Letelier, "Acceleration, streamlines and potential flows in general relativity: analytical and numerical results," *Classical and Quantum Gravity*, vol. 18, no. 15, p. 2917, 2001.

[17] M. C. Andral, S. Roger, M. Montréjaud-Vignoles, and L. Herremans, "Particle size distribution and hydrodynamic characteristics of solid matter carried by runoff from motorways," *Water Environment Research*, vol. 71, no. 4, pp. 398–407, 1999.

[18] B. Kus, M. Johir, J. Kandasamy et al., "Performance of granular medium filtration and membrane filtration in treating stormwater for harvesting and reuse," *Desalination and Water Treatment*, vol. 45, no. 1–3, pp. 120–127, 2012.

[19] J. Q. Jiang and B. Lloyd, "Progress in the development and use of ferrate(VI) salt as an oxidant and coagulant for water and wastewater treatment," *Water Research*, vol. 36, no. 6, pp. 1397–1408, 2002.

[20] S. Dastgheibi, *Stormwater treatment using in-ground permeable reactive filter systems: batch test evaluation of media [Ph.D. dissertation]*, University of Illinois at Chicago, Chicago, Ill, USA, 2012.

[21] K. R. Reddy, T. Xie, and S. Dastgheibi, "PAHs removal from urban storm water runoff by different filter materials," *Journal of Hazardous, Toxic, and Radioactive Waste*, vol. 18, no. 2, Article ID 04014008, 2014.

Hindawi Publishing Corporation
Journal of Chemistry
Volume 2016, Article ID 9312952, 13 pages
http://dx.doi.org/10.1155/2016/9312952

Research Article

Use of *Moringa oleifera* (Moringa) Seed Pods and *Sclerocarya birrea* (Morula) Nut Shells for Removal of Heavy Metals from Wastewater and Borehole Water

Irene Wangari Maina, Veronica Obuseng, and Florence Nareetsile

Department of Chemistry, University of Botswana, Private Bag UB 00704, Gaborone, Botswana

Correspondence should be addressed to Irene Wangari Maina; slyrish35@gmail.com

Received 7 June 2016; Revised 27 July 2016; Accepted 31 July 2016

Academic Editor: Rosa Maria Gomez Espinosa

Use of nonedible seed pods of *Moringa oleifera* (Moringa) tree and nutshells of *Sclerocarya birrea* (Morula) tree for removal of selected metal ions (lead, cadmium, copper, manganese, iron, zinc, and magnesium) from wastewater and borehole water samples was investigated. Removal parameters such as contact time, pH, temperature, particle size, sorbent dose, and initial metal concentration were optimized. Determination of residual metal ions after employing sorbent was done using flame atomic absorption spectroscopy (FAAS). Using 200 ng synthetic metal ion mixture in 50 mL of water sample, the optimized parameters for Moringa seed pods were 60 min contact time, 1.0 g of sorbent dose, pH 8, 100 μm sorbent particle size, and extraction temp 35°C. While using Morula nutshells, the optimized conditions were 120 min contact time, 2.0 g sorbent dose, pH 8, 100 μm sorbent particle size, and extraction temp of 35°C. The removal efficiency of acid treated sorbents was compared to that of untreated sorbents and it was found to be higher for acid treated sorbents. These nonedible plant parts for Morula and Moringa plants are proposed as a cheap, simple, and an effective alternative for purification of water contaminated with heavy metals.

1. Introduction

Demands on water resources for households, commercial, industrial, and agricultural activities are increasing on daily basis. Agriculture and domestic sectors account for more than 70% of global freshwater withdrawals [1]. Wastewater resulting from homes and industries is often discharged into rivers after treatment. Recycling and reuse of wastewater can be a supplementary source to already existing water sources, especially in arid and semiarid regions where water is scarce. Municipal wastewater comes mainly from sewage treatment plants, which may contain pathogens and potentially toxic elements and organic compounds. Before discharge into rivers, removal of most pollutants can be achieved by treatment technologies such as screening, primary treatment, and secondary and tertiary treatment in wastewater treatment plants. Despite the usage of treated wastewater in several parts of the world, the safety and quality of wastewater reuse still remain a problem [2]. Trace inorganic compounds such as heavy metals could be present in treated water due to treatment failure or inability to remove them [3]. Besides occurring naturally, heavy metals may leach from industrial and consumer waste into the groundwater. Therefore, there is a high probability that the water discharged to the rivers after treatment in oxidation ponds and potable and ground water as well could contain heavy metals not benign to the environment.

Therefore, the biggest predicament is to optimize the benefits of wastewater as water sources and the nutrients it contains while minimizing negative impacts on human health. Fu and Wang [4] reported that the trend in heavy metals pollution in the ecosystem was increasing consistently throughout the world especially among developing countries. Hence, there is a need to come up with a way of purifying water, which is effective and also cost effective even at very low metal concentrations. Removal of heavy metals from wastewaters has been achieved through chemical precipitation [4, 5], ion exchange [6, 7], ion flotation [8, 9],

Table 1: Metal concentration (mgg^{-1}) in Moringa seed pods and Morula nut shells.

	Concentration of metal (mgg^{-1}) and ± standard deviation						
	Pb	Cu	Cd	Fe	Zn	Mn	Mg
Moringa seed pods	0.018 ± 0.002	0.012 ± 0.009	Not detected	0.111 ± 0.026	0.036 ± 0.015	0.047 ± 0.007	2.578 ± 0.041
Morula nut shells	0.015 ± 0.004	0.012 ± 0.005	Not detected	0.088 ± 0.031	0.026 ± 0.033	0.029 ± 0.007	2.274 ± 0.006

adsorption [5, 10–12], reverse osmosis [13–17], and membrane filtration [8–10, 18]. Although these conventional methods have higher capacity for the removal of toxic heavy metals, their utilization may require several pretreatments as well as additional treatments, thereby incurring high installation and operating cost [19, 20]. Due to these challenges, there is need for safer, economical, and effective ways for elimination of heavy metals from waters.

Recently, use of low cost sorbents has focused attention on use of biological materials as a considerable potential solution for removal and recovery of pollutants from industrial effluents [21–27]. These materials have the following advantages: they (i) are readily available, (ii) require little or no processing, (iii) possess good adsorption capacity even for low-level metal concentrations, (iv) have got selective adsorption for heavy metal ions, and (v) can be easily regenerated [28–30]. Such materials include use of plant parts from indigenous trees like *Moringa Oleifera* and *Sclerocarya birrea*. These tropical multipurpose trees can be easily cultivated and adaptable in semiarid climates; hence, they can be beneficial to developing world. Most parts of these trees are edible and very beneficial to human beings and have a lot of applications. Essential oils and essential minerals are extracted from Morula kernel [31] while Moringa biomass has been used as coagulant agent in water purification [32], for heavy metal removal [33] and removal of organic pollutants from aqueous solutions [34]. However, some parts of these trees that are not edible are normally considered as waste material and often thrown away: for example, seed pods from Moringa and nut shells from Morula. However, limited work has been done on the application of *Moringa oleifera* seed pods (MSP) and *Sclerocarya birrea* nut shells (MNS) since these parts are often taken to be useless.

The work reported here seeks to explore the unexploited property of Moringa seed pod (MSP) and Morula nut shells (MNS) as a bioremedial approach for removal of metals (copper, zinc, lead, manganese, cadmium, magnesium, and iron) from wastewater and borehole water. The removal efficiency of the two materials is compared. Metal removal by employing acid treated MSP and MNS sorbents was also investigated.

2. Materials and Methods

2.1. Materials. All reagents were of analytical grade. Acids were used for digesting and adjusting pH. HNO_3 (69%, Skylabs), HCl (32%), Minema Chemicals, and double deionized water (Millipore-Q Millipore 18.2 MΩ/cm resistivity) were also used for dilutions of samples to be analyzed with FAAS. Elemental standards solutions used for calibration were prepared from 1000 ppm of stock solutions supplied by Minema Chemicals (Pb and Fe), Merck Pty Ltd. (Cu, Mn, Mg, and Zn), and Sumitomo Metal Mining Instruments (pty) Ltd, (Cd). NaOH (≥97.0%, Rochelle Chemicals) was used to adjust pH, (Hanna Instruments HI 991001 pH); orbital shaker (Scigenics), agate pestle, and mortar were also used for reducing the particles further. 100 μm, 200 μm, and 500 μm stainless steel sieves were used for sieving the sorbents. The filter papers used were ashless Whatman filter paper number 1 from England. The filter papers were used to filter the mixtures of sorbents and solution.

2.2. Preparation and Characterization of MSP and MNS. The *Moringa oleifera* (Moringa) seed pods (deseeded) and *Sclerocarya birrea* (Morula) nut shells were obtained from various sampling points in Artesia, Botswana. Dried Moringa seed pods (MSP) and Morula nut shells (MNS) were washed with double deionized water, further dried in an oven at 65°C for 24 hrs. The dried samples were ground and then sieved to different mesh sizes (100, 200, and 500 μm) and stored in glass bottles until further analysis. The MNS and MSP powder were also characterized by Fourier Transform Infrared (FTIR) spectroscopy and Scanning Electron Microscope (SEM) as described in Section 2.5.

2.3. Determination of Metal Concentration in Sorbent Material. About 2 g of each ground sorbent was weighed and then digested with an aqua regia solution of HCl : HNO_3 in a ratio of 3 : 1 v/v. Each mixture was placed in 100 mL conical flasks and heated at 85°C until the volume was reduced to 1 mL. The resulting volume was filtered using a Whatman number 1 filter paper and put into 50 mL volumetric flasks. Deionized water was added to the flasks and filled up to the mark. The samples were analyzed using FAAS following a modified method [35]. Table 1 reflects the concentration of the selected metals.

2.4. Acid Treatment of MSP and MNS Sorbents. 15 g of each sorbent was weighed and put in a conical flask, 200 mL of 0.1 M HNO_3 was added, and the mixture was soaked for 24 hrs. The mixture was then filtered and the sorbent was washed several times with deionized water until the pH of the sorbent was neutral (around pH 7). The sorbent was then dried in an oven at 50°C overnight and then put in glass bottle until further use.

Using the optimized sorption parameters (Section 2.6), the ability to remove heavy metals from waste water samples by the acid treated and untreated sorbents were compared.

Table 2: Concentration (mgL^{-1}) of selected metals in water samples.

	Average concentration (mgL^{-1}) of selected metals in water samples and ± standard deviations.						
	Fe	Zn	Cu	Cd	Pb	Mn	Mg
Inlet	1.361 ± 0.020	0.251 ± 0.010	0.086 ± 0.005	0.013 ± 0.001	0.285 ± 0.021	0.309 ± 0.001	12.867 ± 0.009
Primary	1.074 ± 0.023	0.206 ± 0.012	0.078 ± 0.001	0.013 ± 0.001	0.245 ± 0.007	0.304 ± 0.001	11.596 ± 0.003
Secondary	0.288 ± 0.046	0.142 ± 0.063	0.029 ± 0.002	0.015 ± 0.001	0.230 ± 0.042	0.222 ± 0.001	13.487 ± 0.002
Aeration	2.432 ± 0.045	0.405 ± 0.087	0.127 ± 0.012	0.016 ± 0.001	0.390 ± 0.003	0.380 ± 0.001	13.478 ± 0.001
Effluent	0.255 ± 0.028	0.116 ± 0.018	0.028 ± 0.002	0.015 ± 0.001	0.265 ± 0.021	0.211 ± 0.005	13.671 ± 0.003
Borehole	0.334 ± 0.004	0.011 ± 0.002	0.012 ± 0.001	0.002 ± 0.001	0.113 ± 0.008	0.002 ± 0.000	1.288 ± 0.032

2.5. Instrumental Analysis. A Varian 220FS atomic absorption spectrometer operated with air/acetylene was used for determination of seven selected metal ions which included lead (Pb), manganese (Mn), iron (Fe), zinc (Zn), copper (Cu), magnesium (Mg), and cadmium (Cd). Varian hollow cathode lamps for each of the analyzed metals were used as radiation source. 1000 mgL^{-1} ppm stock solutions of metals were used to prepare working standards (in the range 0.0 to 5.0 mgL^{-1}) in deionized water. The instrument was calibrated manually by aspirating the prepared working standards of the cations of interest one by one into the flame. The samples were also aspirated manually into the flame for atomization. The instrumental conditions applied were according to AAS manual.

FTIR spectroscopy was used to characterize the sorbents to determine the functional groups responsible for metal removal. The FTIR spectra were recorded in the wavenumber range 400–4000 cm^{-1} on a Perkin Elmer system 2000 FTIR. The sorbents were kept at ambient temperature. 1 mg seed powder per 200 mg of KBr was weighed. The powder was pressed into pellets by using a 15 ton hydraulic press. The data were collected at 2.0 cm^{-1} resolution, and each spectrum was a result of 256 scans.

In order to observe the surface morphology of the sorbents, a Philips XL 30 ESEM model environmental scanning electron microscope (ESEM) was used.

2.6. Biosorption of Heavy Metal Ions. Batch experiments were used for the biosorption of Cd, Cu, Fe, Zn, Mg, Mn, and Pb. Stock solutions at various concentrations were prepared from 1000 mgL^{-1} of each metal standard. Solution of known metal ion concentration was prepared and known amount of sorbent (MSP or MNS) was added. The mixture was shaken with a controlled orbital shaker and the concentrations of the unadsorbed metal ions in solutions were determined after separation of the sorbent by filtration using Whatman paper number1 filter papers. The effects of contact time (0–240 min), initial metal concentration (1–20 mgL^{-1}), pH (2.0–10.0), sorbent dose (0.5–2.5 g, in 50 mL^{-1}), particle size (100–500 μm), and temperature (298–333 K) were studied as shown in Figure 1. Analysis and instrumentation were done using FAAS with air/acetylene. The amount of the metal adsorbed (% removal) by the sorbent was calculated using

$$\%\ \text{Removal} = \frac{C_i - C_f}{C_i} \times 100, \quad (1)$$

where C_i is the initial concentration before adsorption and C_f is the concentration after adsorption of metal ions. All experiments were done in replicates and reported as the average of the experiments.

2.7. Sampling and Storage of Water Samples. Water samples were obtained from Gaborone waste water treatment plant, Gaborone, Botswana. At the treatment plant five sampling sites were identified (inlet point, primary settling, secondary settling point, aeration point, and effluent point). Grab sampling technique was employed to obtain the water samples from individual sampling sites. Each sample was put in labelled brown glass bottle and acidified to pH < 2 in order to prevent further microbial activity which could eventually affect the composition of metal in the sample. Also acidifying the samples ensured that all metals were dissolved.

The water samples were placed in the cold room at 4°C; this was to help immobilize any microbial activity or degradation of the sample. Samples were stored for seven days until analysis.

2.8. Determination of Metal Concentration in the Wastewater and Borehole Samples. 50 mL of waste water from inlet, primary, secondary, aeration, effluent points, and borehole samples was put in six different 250 mL conical flasks. The samples were digested by adding 1.0 mL of 55% HNO_3 and 0.5 mL of 37% HCl was added to each flask. The mixture was heated until the initial volume reduced to approximately 0.5 mL. The mixture was then filtered into a 50 mL volumetric flask and deionized water added to the mark. The sample was then analyzed with AAS to determine the concentration of seven selected metals (Pb, Zn, Fe, Cu, Mg, Mn, and Cd). Table 2 shows the concentrations of the metals.

2.9. Application of the Optimized Biosorption Method to Real Samples. The extraction efficiency for the acid treated sorbents and the untreated sorbents was compared by applying the optimized parameters (Section 2.6) to water samples collected from sewage treatment plant and borehole water collected from a borehole in Artesia, Botswana. Both Moringa seed pods and Morula nut shells biomass were used for the metal removal in the samples. 50 mL of water samples was used and the optimized conditions were applied to both water samples. The analysis was done in triplicate, and the analytes remaining in the water sample after sorption were determined with FAAS.

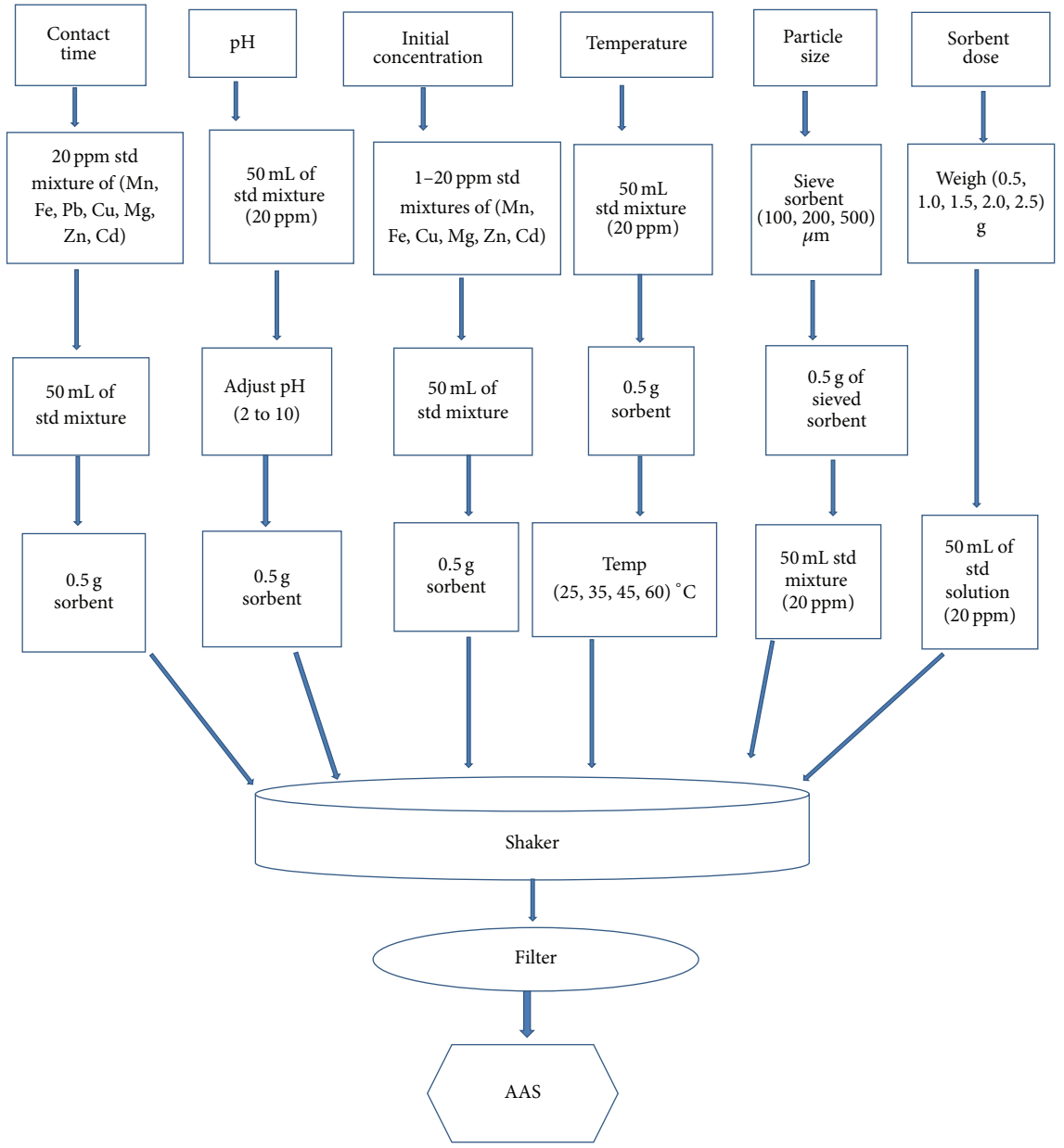

Figure 1: Summary of the optimization procedures for biosorption of metals on Morula nut shells and Moringa seed pods.

3. Results and Discussion

3.1. Characterization of the Sorbents. The SEM images (Figures 2(a) and 2(b)) reveal the surface texture and morphology of the sorbents. The micrographs of MSP (Figure 2(a)) reveal mesoporous structures with different pore sizes. These surface characteristics would result in high metal binding due to available binding cavities for the metal ions. MNS micrographs also show that the structures consist of different shapes and have pores on the surface offering binding sites for higher adsorption capacity of metal on the sorbent.

Other sorbents have shown similar characteristics, for example, almond shells [36], *Moringa oleifera* wood [37], and fruit peels [22]. However, the efficiency of the sorbent can be increased by increasing the number of pores and the surface area. This is done by treating the sorbents with acids or activated with carbons [33, 34].

3.1.1. Fourier Transform Infrared (FTIR) Spectroscopy. The IR spectra of MSP as shown on Figure 3(a) show broad bands around 3333 cm^{-1} attributed to the surface hydroxyl group. The bands at 2917 and 2849 cm^{-1} are due to C-H group of the alkenes, at 1741 cm^{-1} the C=O from esters, at 1593 cm^{-1} the C=C aromatics, and C-O from carboxylic acids at 1104 to 1027 cm^{-1}. Decrease in intensity and shift of the above-mentioned peaks as shown in Figure 3(b) could be due to interaction of the metal with the specific functional groups.

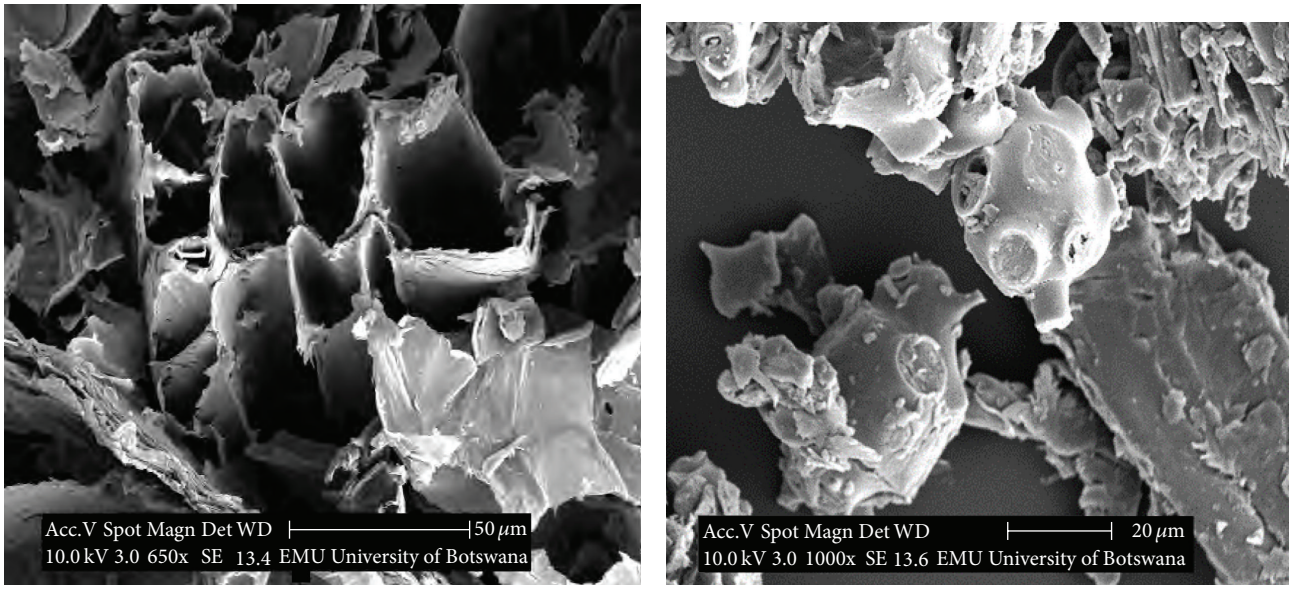

(a) (b)

Figure 2: SEM micrographs: (a) Moringa seed pods and (b) Morula nut shells.

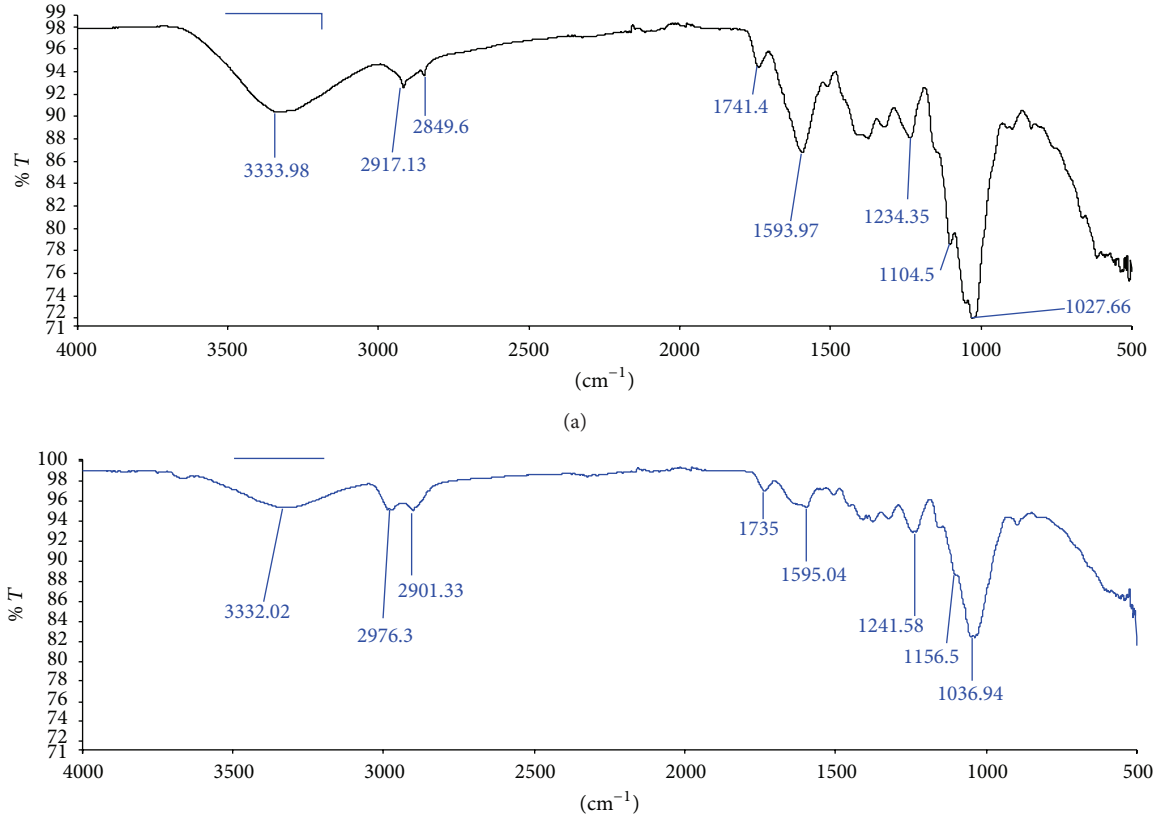

Figure 3: Unnormalized spectra of MSP (a) before metal ion removal and (b) after metal ion removal.

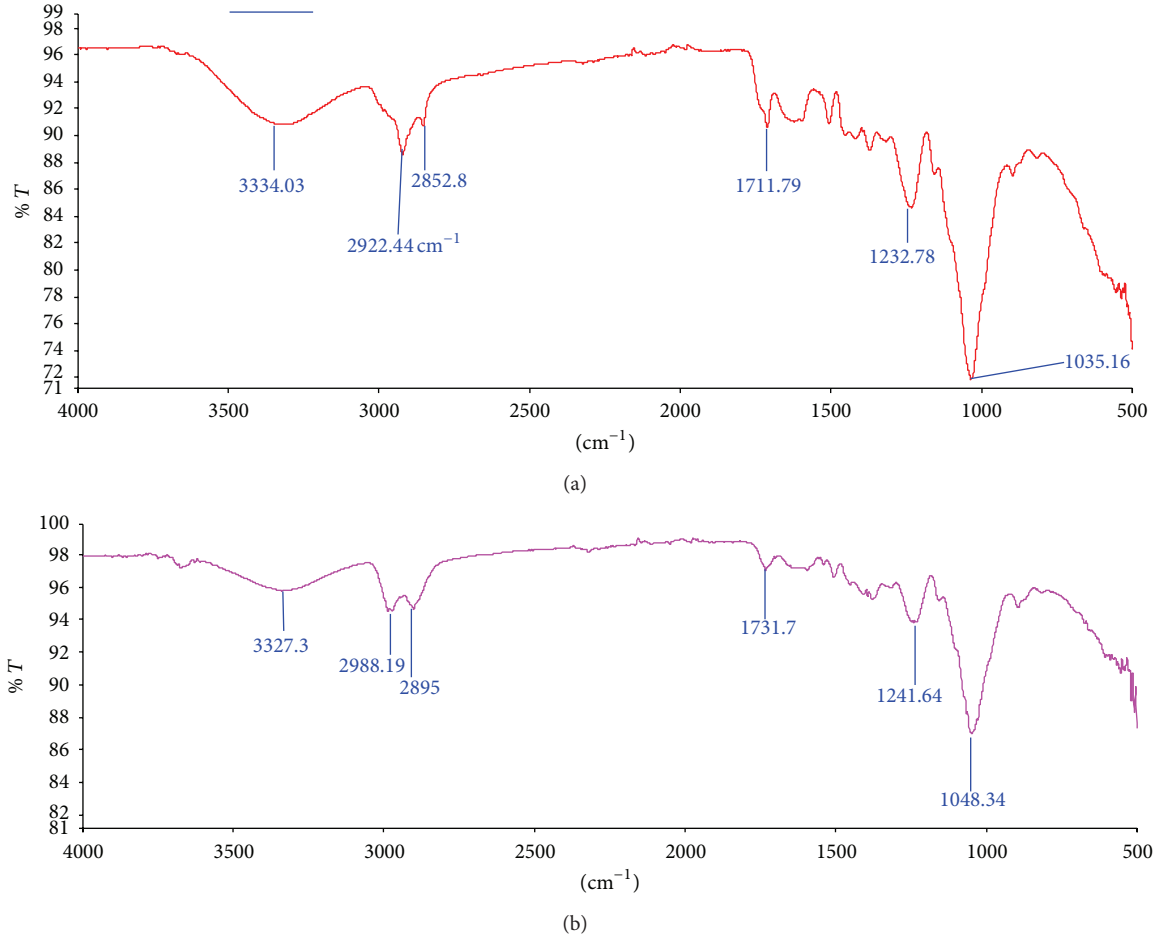

Figure 4: Unnormalized spectra of MNS (a) before metal sorption and (b) after metal sorption from water sample.

The metal adsorption capacity is influenced strongly by the surface structures of carbon-oxygen and surface behavior of carbon [38]. Studies done with other biomass sorbents have shown similar functional groups responsible for metal removal [36, 37, 39]. The functional groups responsible for metal removal in MSP are therefore hydroxyl (OH), C-H of the alkenes, C=C alkenes, and C-O from the carboxylic acids.

Morula nut shell (MNS) IR spectra are shown in Figures 4(a) and 4(b). Figure 4(a) is for MNS before sorption while Figure 4(b) is after sorption of metals. The observed peaks on Figure 4(a) were identified as hydroxyl (O-H) broad group at 3334 cm^{-1}, C-H from alkenes at 2922–2852 cm^{-1}, carbonyls (C=O) at 1711 cm^{-1}, amines at 1232 cm^{-1}, and C-O from either carboxylic acid, esters, or ethers at 1035 cm^{-1}.

Figure 4(b) shows FTIR spectra of metal loaded MNS. The shift and reduction of the peaks such as O-H (3327 cm^{-1}), C-H (2895–2988 cm^{-1}), C=O (1735 cm^{-1}), C-N (1241 cm^{-1}), and C-O (1048 cm^{-1}) are due to interaction of the functional group with the metal ions. The functional groups such as amines, carboxylic, hydroxyl, and carbonyls form anionic sites as pH is raised from acidic to basic conditions. The anionic sites could be responsible for binding with the metal cations. It can be speculated that combination of the following could be the principal mechanism for metal removal [40]: (i) electrostatic interactions between the conjugate base of either carboxyl group or amine group (at pH 8) reacting with metal ions, (ii) coordination or complex formation (using empty d-orbitals of metal ions) to interact with the electron pairs from the oxygen in the carboxyl, hydroxyl, and nitrogen of the amine groups, (iii) ion exchange processes in which the ionizable hydrogen on the carboxyl and amine groups exchange with metal cations, (iv) microprecipitation (especially at higher pH) where the OH- ions form insoluble hydroxides with the metal ions and the sorbent here then acts as a filter, (v) acid-base interactions (most of these metal ions are hard acids and interact with atoms on the functional groups such as oxygen on the carboxyl and hydroxyl group and nitrogen on the amine groups), and (vi) adsorption: for example, with the presence of alkenes, the concentration of electron density on them actually creates dipole moments with negative dipole moment concentrated on the center of the double bond and the positively charged metal ions will sit on these areas with high electron density.

It can be concluded that, in the MSP, the functional groups significant for metal removal are the carbonyl, alcohol, and alkenes groups, while with MNS, the active groups for metal removal are the alcohols, carbonyls, alkenes, amines, and carboxylic acids.

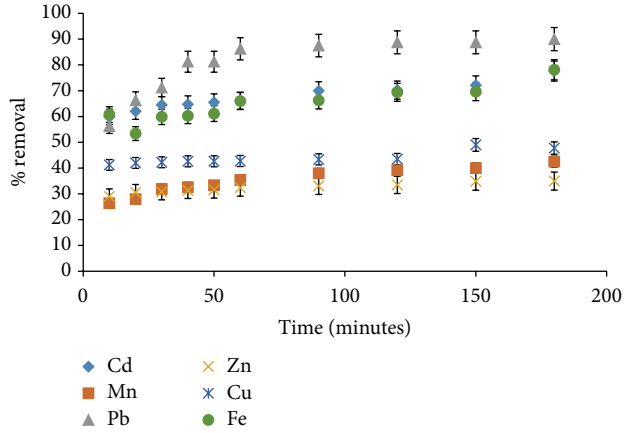

Figure 5: Effect of contact time on metal removal using MSP (all other variables in Section 2.6 constant).

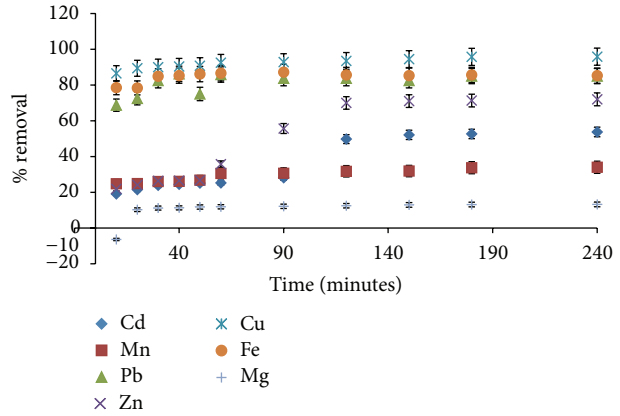

Figure 6: Effect of contact time on selected metal removal using Morula nut (MNS) sorbent (all other variables constant).

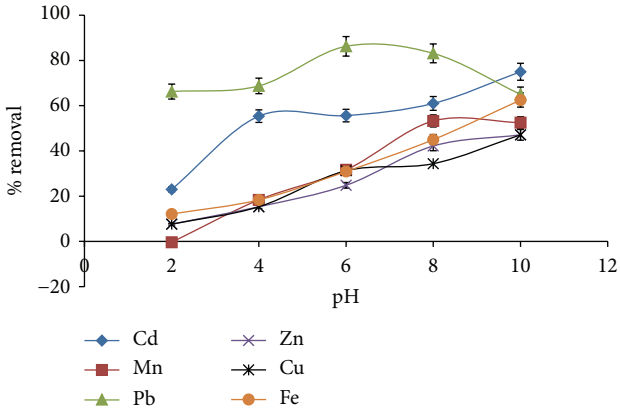

Figure 7: Effect of adjusting pH on metal removal by Moringa seed pods (MSP). Other conditions kept constant.

3.2. Effect of Operating Variables

3.2.1. Effect of Contact Time. Contact time is an important parameter for determining the equilibrium time required for the sorption of metal ions on a sorbent as it is directly proportional to amount of metal ions removed from aqueous solution. It was observed that when MSP sorbent was used for metal removal, the highest removal was reached within 60 minutes (Figure 5) and for MNS sorbent it was 120 minutes (Figure 6), the equilibrium was reached, and further increase in time did not show any significant change. The extraction efficiency of the selected metals by MSP was directly proportional to the sizes of the metal ions: that is, the order was Pb > Cd > Fe > Cu > Mn > Zn > Mg (largest to smallest), with exception of copper and magnesium. This trend could be attributed to the fact that the sorbents have pores of different sizes as seen from SEM micrographs and therefore offer different binding sites to the different metal ions [41]. However, larger metal ions were removed efficiently compared to smaller ions. Similar trend has been observed in previous studies [33]. The trend in metals removal by MNS from the aqueous samples was in the order Cu > Fe > Pb > Zn > Cd > Mn > Mg. Percentage removal of the metal ions on the MNS increases with increase in contact time. More time allows the adsorbent particle to interact with the metal ion and increase chances of more adsorption [42]. MNS has greater affinity for the metal with higher electronegative values [43], that is, Cu (2.00 Pauling), Fe (1.91 Pauling), Pb (2.33 Pauling), Zn (1.65 Pauling), Cd (1.69), Mn (1.55 Pauling), and Mg (1.31 Pauling). Higher biosorption of the metals on the sorbents can also be explained by hard-soft-base theory [44]. Metals belonging to hard acid like Fe may be removed effectively.

3.2.2. Effect of pH. The pH of aqueous solution is very important in sorption processes since it affects the solubility of metal ions, concentration of the counter ions on the functional groups of the adsorbent, and the degree of ionization of the sorbate during the reaction [45]. An increase in pH of solution while keeping all other factors (time, temperature, metal concentration, sorbent dose, and particle size) constant increased the percentage removal of the selected metal ions using the MSP (Figure 7) and MNS (Figure 8). This could be due to the surface charge on the sorbents. At low pH, the cations compete with the hydrogen ion in the solution for the active sites and therefore lower adsorption. But at higher pH, the surface of the adsorbent has a higher negative charge which attracts more cations [37]. At pH > 8, precipitation of metal hydroxide is likely to occur and hence could enhance metal removal, resulting in the sorbents acting like filtering materials. Removal of Pb was highest at pH 6; however, ANOVA showed that there was an insignificant decrease in percentage removal as the pH was increased to pH 8. Therefore, the optimum pH was taken to be 8 for all metals using both sorbents since there was highest percentage removal before the precipitates could form.

3.2.3. Effect of Initial Metal Concentration. The initial concentration provides essential driving force to overcome all mass transfer resistance of metal ions between the aqueous and the solid sorbent. As the initial metal concentration is increased, the removal efficiency is increased and after saturation, the

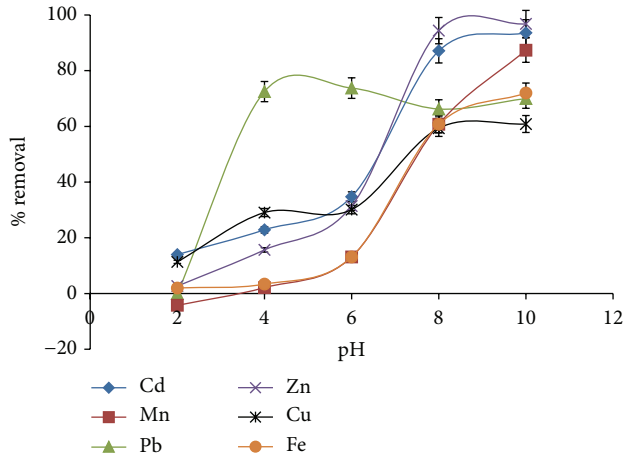

Figure 8: Effect of pH on metal removal using morula nut shells (MNS) while keeping other conditions constant.

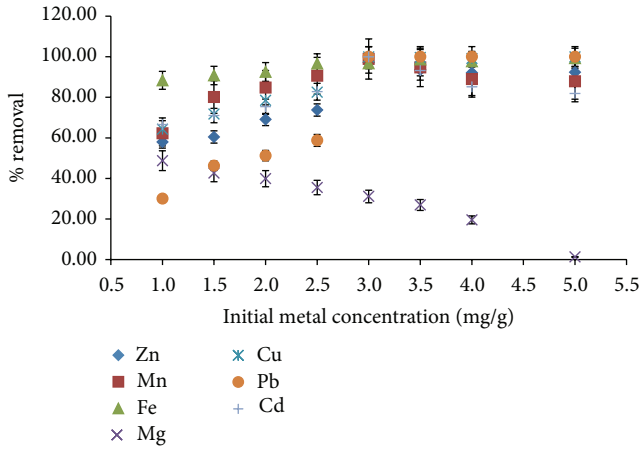

Figure 9: Effect of initial metal concentration on metal removal by MNS.

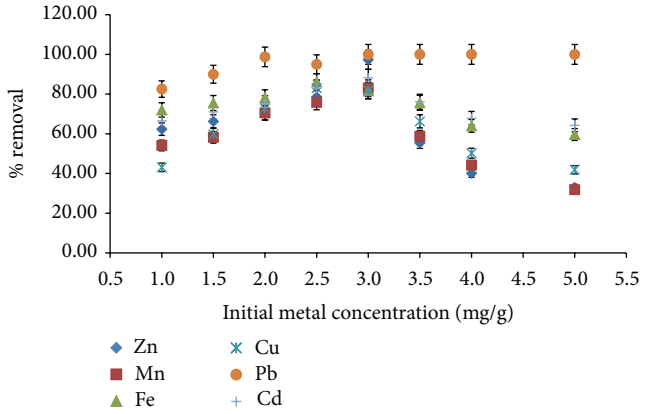

Figure 10: Effect of initial metal concentration on metal removal by MSP.

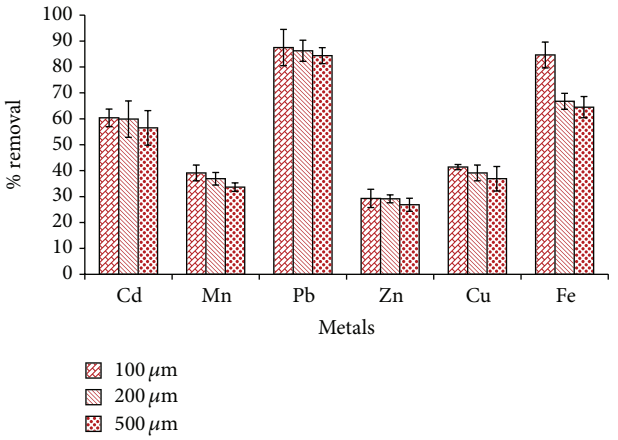

Figure 11: Effect of particle size on metal removal using MSP.

percentage removal is constant as shown in Figure 9 while using MNS. This could also be attributed to the saturation of the binding sites as more ions are added in the solution. As the concentration of metal ion increases, the number of metal ions competing for available binding sites on the sorbent increases. Therefore, binding sites become quickly saturated as the biomass amount remained constant [38, 46]. The same was observed using MSP; at lower concentration there was an increase in removal efficiency; however, after a threshold (different for each metal) any further increase in the metal concentration resulted in reduced removal efficiency for Zn, Mn, Fe, Cu, and Cd (see Figure 10). Removal of magnesium by both sorbents was poor and this was attributed to limited loading capacity of the sorbents due to saturation of magnesium binding sites. This is because the concentration of magnesium ions in the sorbent was higher (see Table 1) in comparison to the other metals. Therefore, increase in initial concentration led to a decrease in percentage removal of magnesium.

3.2.4. Effect of Particle Size. Surface area of the sorbent is significant for sorption process. Exposure of the sorbent sites for solid-metal ion interaction is high if the surface area of the sorbent is high. As shown in Figures 11 and 12 using MSP and MNS, respectively, the percentage removal of the metal was effective at sorbent particles size less than 100 μm as compared to larger particles. The smaller the particle size the higher the surface area per unit weight of sorbent and hence higher percentage removal is expected [47]. Similar trends have been observed by other researchers [45, 48]. An exception was the magnesium that showed higher removal at 500 μm while using MNS (Figure 12) and this may be attributed to the fact that magnesium may prefer to adsorb internally as opposed to external adsorption. Beside adsorption at the outer surface of the sorbent, there is a possibility of intraparticle diffusion from the outer surface into the internal surface of the sorbent [40]. A large particle size has larger internal surface area than a small one, and hence magnesium showed higher removal at 500 μm than at 100 μm. However, ANOVA significant test was conducted and showed that using 100 μm had no significant difference, hence resulting in using 100 μm to be the optimum particle

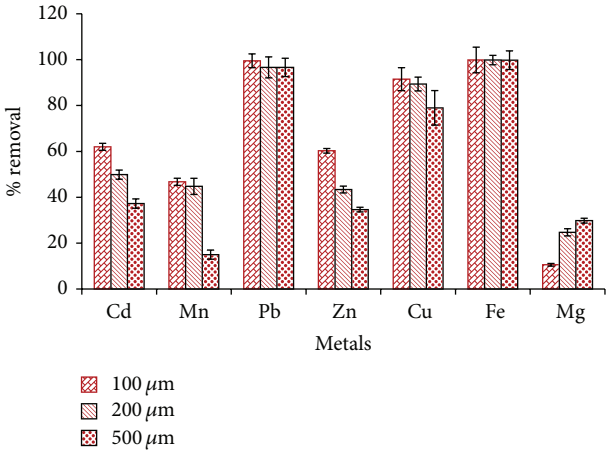

Figure 12: Effect of particle size on metal removal using MNS.

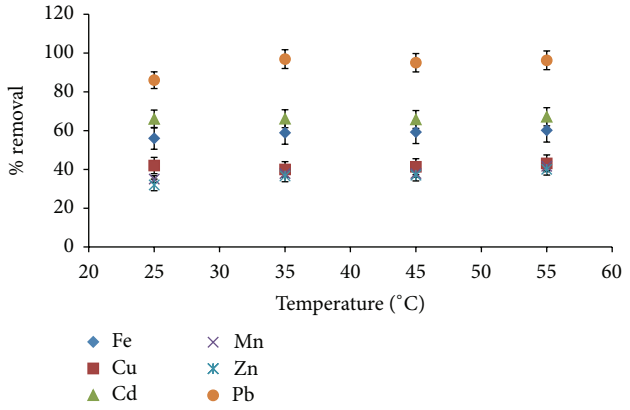

Figure 13: Effect of temperature on metal removal using MSP.

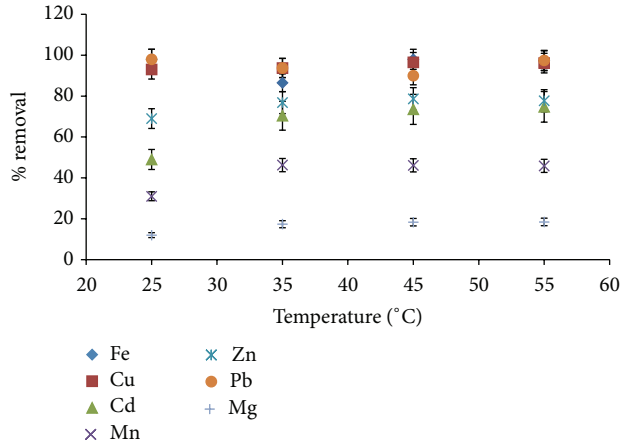

Figure 14: Effect of temperature on metal removal using MNS.

size using both sorbents. It was also observed that while using MSP, there was no removal of magnesium due to the fact that MSP had higher amounts of magnesium (see Table 1) and therefore the adsorbing sites for magnesium were saturated.

The ionic sizes trend of the metals is Pb > Cd > Zn > Cu > Mg > Fe > Mn for divalent cations. The larger ions are expected to be removed first and the order of removal should decrease from Pb to Mn [49], but in some case it will be different depending on the environment of the interacting sites. This trend was not observed completely and this could be attributed to the fact that the metals were interacting differently with the MNS and MSP adsorbing sites.

3.2.5. Effect of Temperature. An increase of removal efficiency with increase in temperature has been attributed to two factors. Increase in temperature increases the mobility of the metal ions towards the sorbent and also it may cause a swelling effect within the internal structure of the sorbents and therefore enabling the metal ions to penetrate further or increases the surface area for the binding of the metal ions [48]. Temperature effect on metal removal by the sorbents was investigated using batch experiments conducted in water bath with temperature range from 25°C to 60°C. There was no significant change in percentage removal for other metals except for lead where there was increase at 35°C as depicted in Figure 13 when using MSP. It was also observed that there was no significant change when higher temperatures up to 60°C were used; hence, 35°C was used as optimum temperature. Araújo et al. [50] discussed that use of Moringa seed pods for removal of Zn and Pb worked well at a temperature of 30°C to 35°C. Figure 14 shows an increase in percentage removal from 25°C up to 35°C for removal of Zn, Cd, Mn, and Mg using MNS. When removing Fe, Cu, and Pb, there was no significant difference even when temperature was altered. Hence, 35∘C was taken to be the optimum extraction temperature.

3.2.6. Effect of Sorbent Dose. It is expected that, as the sorbent amount increases, the number of sorbent particles surrounding the metal ion or ratio of sorbent particle to metal ion increases [51]. This increases the surface area on which the metal ions bind to the surface of the sorbents, hence increasing the removal efficiency. However, a further increase beyond the optimum sorbent dose decreases the percentage removal and this is attributed to the fact that there is possibility of the particle overlapping and overcrowding resulting in a reduction of the total adsorbent surface area and hence decreases the percentage removal [38]. Figure 15 shows that as the sorbent dose was increased from 0.5 g to 1.0 g of MSP sorbent, the percentage removal of metal ions increased and the optimum sorbent dose for the removal of Cd, Mn, Zn, Cu, and Fe was 1 g except Pb which had its highest removal using 1.5 g sorbent. However, ANOVA showed that there was no significant difference when 1 g was used to remove Pb ions. The results for metal removal using MNS adsorbent at different dosing levels (0.5 g to 2.5 g) showed a slight increase for cadmium, manganese, and zinc up to 2 g dosing level (Figure 16), but no significant difference was observed for copper, lead, and iron at all dosing levels. Similar studies have been reported with other low cost sorbents [29, 43]. Therefore, 1 g of MSP and 2.0 g of MNS was taken to be the optimum sorbent dose for the experiments.

Table 3: Summary of the optimized parameters.

Material	Contact time (min)	PH	Temp (°C)	Adsorbent dose (g)	Particle size (μm)
Morula nut shells	120	8	35	2	100
Moringa seed pods	60	8	35	1	100

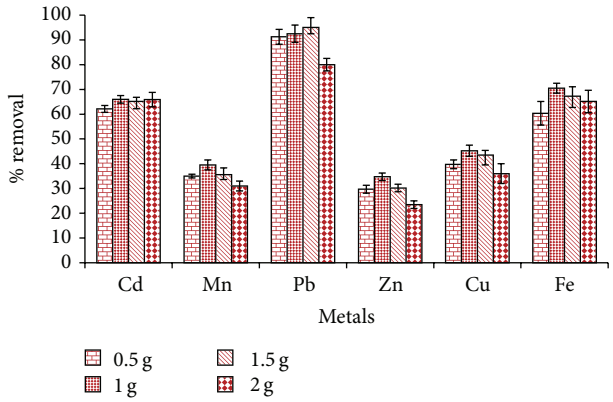

Figure 15: Effect of adsorbent dose on metal removal using Moringa seed pods.

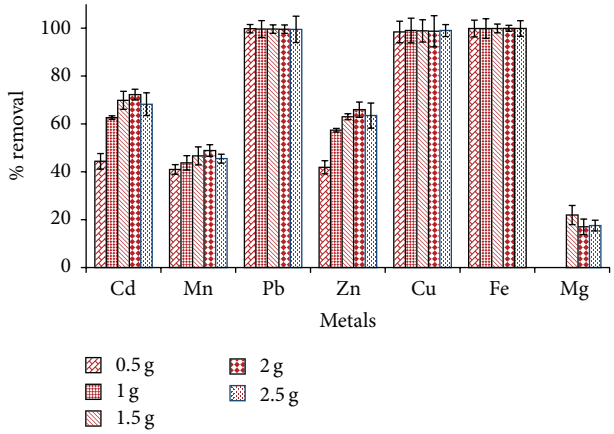

Figure 16: Effect of adsorbent dose on metal removal using MNS.

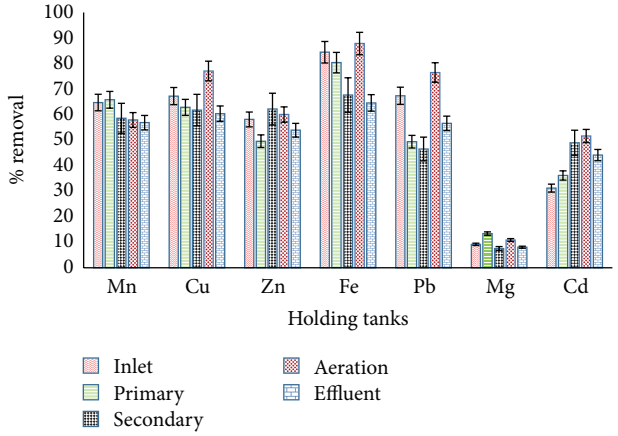

Figure 17: Percentage removal of metals from wastewater using MNS.

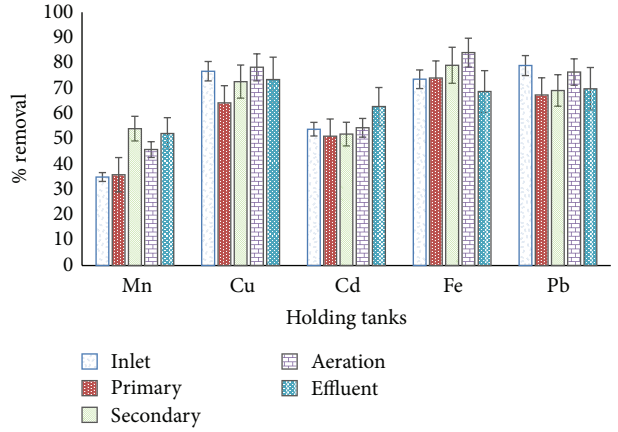

Figure 18: Percentage removal of metals from wastewater using MSP.

Table 3 shows the summary of the optimized parameters. They were then applied in real samples (wastewater and borehole water) as discussed in Section 3.3.

3.3. Metal Removal from Wastewater and Borehole Water. Figures 17 and 18 show the percentage removal of metals from wastewater holding tanks using Morula nutshells and Moringa seed pods, respectively.

The metals were removed from the wastewater efficiently using MNS as shown in Figure 17. At effluent tanks the percentage trend was Fe > Cu > Pb > Mn > Zn > Cd > Mg. This was a little different from optimization process and this could be attributed to the fact that in real samples there are other competitive ions competing for the same binding sites and reducing and altering the removal efficiency. MSP also removed five elements Mn, Cu, Cd, Fe, and Pb. The trend was Cu > Pb > Fe > Cd > Mn. However, MSP could not remove Zn and Mg due to desorption of the ions from sorbent into the sample solution and probably due to saturation of binding sites on the sorbent.

Removal efficiency was also investigated in borehole samples as shown in Figures 19 and 20. MSP removed Pb > Cd > Cu > Fe efficiently in that order. However, for the reason stated above, Zn, Mg, and Mn were not removed. However, MNS removed all the metal efficiently with an exception of Zn as shown in Figure 20.

Due to poor removal efficiency of some metals, sorbents were chemically treated to determine if the removal efficiency can be increased as discussed in Section 3.4.

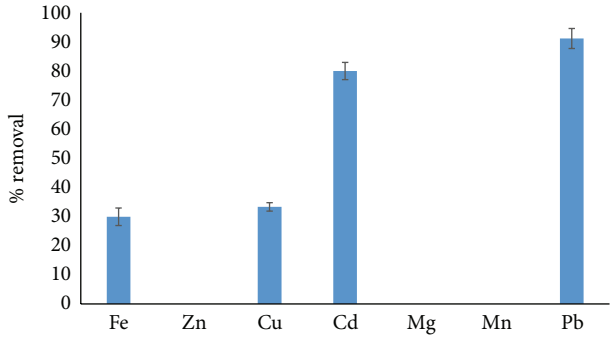

Figure 19: Percentage removal of metals from borehole water using MSP.

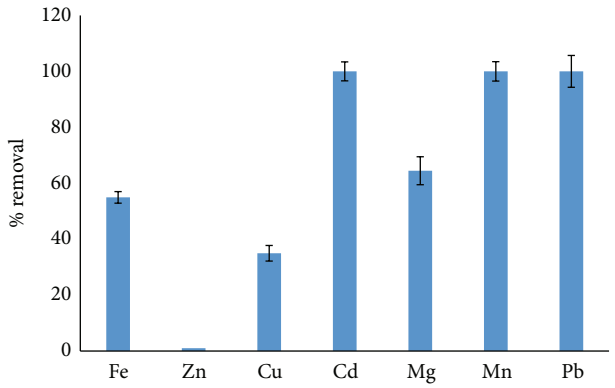

Figure 20: Percentage removal of metals from borehole water using MNS.

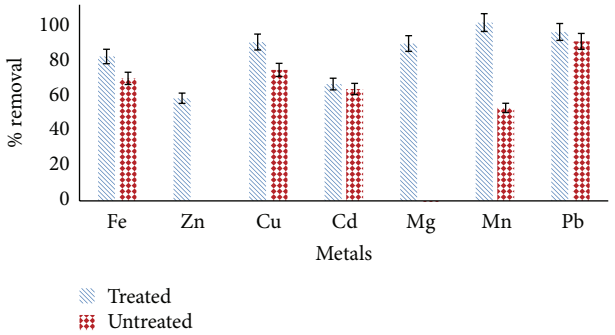

Figure 21: Comparison of treated and untreated MSP for removal of metal from wastewaters at final effluent point.

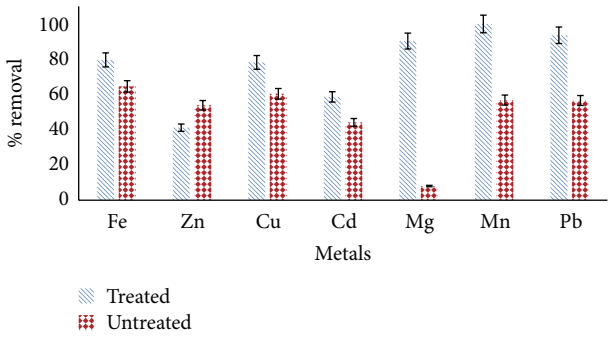

Figure 22: Comparison of treated and untreated MNS for removal of metal from wastewaters at final effluent point.

3.4. Use of Treated MNS and MSP for Metal Removal from Wastewater Samples. Use of untreated plant biomass is capable of directly removing metal ionic species from aqueous solutions. This has been confirmed in this work. To further enhance metal removal efficiency, sorbents can be chemically pretreated before metal sorption. Commonly employed treatments include using alkaline solutions and acids. This treatment normally removes organic and inorganic matter from the sorbent surface [27]. Treating the sorbents with acid helps to extract any metal cations on the sorbents, thereby creating new sorption sites and increasing the surface area of the sorbent and hence increasing the metal removal efficiency. In this current work, acid (0.4 M of HNO_3) and untreated MNS and MSP sorbents were compared in terms of extraction of heavy metals from the inlet and effluent wastewater samples. It was observed that treated sorbents showed better removal efficiency as compared to the untreated sorbents as shown by Figures 21 and 22 using treated MSP and MNS, respectively.

The percentage removal of Fe, Zn, Cu, Cd, Mg, Mn, and Pb from water samples using treated MNS was 79.6, 52.9, 78.2, 58.6, 90.3, 100.0, and 93.4 while using treated MSP it was 80.9, 57.6, 89.0, 65.5, 88.2, 100.0, and 94.7, respectively.

Other sorbent materials have been used to effectively remove heavy metals from aqueous solution, for example, use of carbon materials for removal of metals from aqueous solutions [45, 48, 52, 53]. The removal efficiencies were reported to be in the range of 65% to 90%. However, some of the disadvantages associated with use of such sorbents are the high costs and cannot be regenerated and the adsorption efficiency of carbon materials also depends on the nature of carbon used. Synthetic adsorbents such as zeolites have been reported to remove metals effectively. However, it was demonstrated that the capability of these minerals depends on the pretreatment method and that conditioning improves the ion exchange ability and removal efficiency [54]. Low cost sorbents have been reported to effectively remove heavy metals such as soybean hulls [55], tea waste [24], fruit peels [22], egg shells [56], and other agricultural wastes [57, 58].

3.5. Method Validation. The linearity of the method was tested by using standards in the range of 0.0 mgL^{-1} to 5.0 mgL^{-1} of the selected metal (Pb, Mn, Fe, Zn, Mg, Cu, and Cd). The developed method was validated and the % metal removal by sorbents was between 86.49 ± 4.33 and 99.63 ± 3.36%. The method indicated good linearity (R^2 > 0.99) for all selected metals and also proved to be sensitive as low LODs were achieved ranging from 0.010 ± 0.003 to 0.067 ± 0.02 mgL^{-1}. Equation (2) below was used to calculate for the % removal:

$$\%\,\text{Removal} = \frac{\text{amount added} - \text{amount found}}{\text{amount added}} \times 100. \quad (2)$$

4. Conclusion

Moringa oleifera seed pods and *Sclerocarya birrea* nut shells were used to successfully remove selected heavy metals from water samples. This work explored the possibility of adding value to waste material by recycling and reusing for purification of contaminated water. FTIR analysis of the sorbents showed different functional groups indicating complex nature and capability of the sorbents. The pH, initial metal concentration, sorbent dose, particle size, and temperature were found to affect the sorption process. Removal efficiencies were improved after treating sorbents with acids. The developed method was found to be simple, cheap, environmental friendly, and does not need trained personnel to use it. Hence, it can be a remedial solution for water scarcity in rural areas where there are no resources to obtain the expensive conventional techniques.

Competing Interests

The authors declare that they have no competing interests.

References

[1] Fao, *The State of Food Insecurity in the World 2012*, 2012.

[2] T. A. Ternes, "Occurrence of drugs in German sewage treatment plants and rivers1Dedicated to Professor Dr. Klaus Haberer on the occasion of his 70th birthday.1," *Water Research*, vol. 32, no. 11, pp. 3245–3260, 1998.

[3] S. Toze, "Reuse of effluent water—benefits and risks," *Agricultural Water Management*, vol. 80, no. 1–3, pp. 147–159, 2006.

[4] F. Fu and Q. Wang, "Removal of heavy metal ions from wastewaters: a review," *Journal of Environmental Management*, vol. 92, no. 3, pp. 407–418, 2011.

[5] M. M. Matlock, B. S. Howerton, and D. A. Atwood, "Chemical precipitation of heavy metals from acid mine drainage," *Water Research*, vol. 36, no. 19, pp. 4757–4764, 2002.

[6] H. Cho, D. Oh, and K. Kim, "A study on removal characteristics of heavy metals from aqueous solution by fly ash," *Journal of Hazardous Materials*, vol. 127, no. 1–3, pp. 187–195, 2005.

[7] L. D. Nichols and M. B. Allen, "Reuse of industrial wastewaters by electrodialytic extraction of heavy metals through Poroplastic bound liquid ion exchange membranes," *Proceedings of the Water Reuse Symposium*, vol. 2, pp. 1433–1435, 1982.

[8] A. Dabrowski, Z. Hubicki, P. Podkościelny, and E. Robens, "Selective removal of the heavy metal ions from waters and industrial wastewaters by ion-exchange method," *Chemosphere*, vol. 56, no. 2, pp. 91–106, 2004.

[9] E. N. Peleka and K. A. Matis, "Application of flotation as a pretreatment process during desalination," *Desalination*, vol. 222, no. 1–3, pp. 1–8, 2008.

[10] K. A. Matis, A. I. Zouboulis, G. P. Gallios, T. Erwe, and C. Blöcher, "Application of flotation for the separation of metal-loaded zeolites," *Chemosphere*, vol. 55, no. 1, pp. 65–72, 2004.

[11] S. Wang and H. Wu, "Environmental-benign utilisation of fly ash as low-cost adsorbents," *Journal of Hazardous Materials*, vol. 136, no. 3, pp. 482–501, 2006.

[12] I. J. Alinnor, "Adsorption of heavy metal ions from aqueous solution by fly ash," *Fuel*, vol. 86, no. 5-6, pp. 853–857, 2007.

[13] H. A. Qdais and H. Moussa, "Removal of heavy metals from wastewater by membrane processes: a comparative study," *Desalination*, vol. 164, no. 2, pp. 105–110, 2004.

[14] B. K. C. Chan and A. W. L. Dudeney, "Reverse osmosis removal of arsenic residues from bioleaching of refractory gold concentrates," *Minerals Engineering*, vol. 21, no. 4, pp. 272–278, 2008.

[15] L. Song and S. Yu, "Concentration polarization in cross-flow reverse osmosis," *AIChE Journal*, vol. 45, no. 5, pp. 921–928, 1999.

[16] C. S. Slater, R. C. Ahlert, and C. G. Uchrin, "Treatment of landfill leachates by reverse osmosis," *Environmental Progress*, vol. 2, no. 4, pp. 251–256, 1983.

[17] W. Jian, A. Kitanaka, W. Nishijima, A. U. Baes, and M. Okada, "Removal of oil pollutants in seawater as pretreatment of reverse osmosis desalination process," *Water Research*, vol. 33, no. 8, pp. 1857–1863, 1999.

[18] K. Uosaki, "Removal of heavy metals from waste water by electrodialysis," 1974.

[19] S.-O. Kim, S.-H. Moon, K.-W. Kim, and S.-T. Yun, "Pilot scale study on the ex situ electrokinetic removal of heavy metals from municipal wastewater sludges," *Water Research*, vol. 36, no. 19, pp. 4765–4774, 2002.

[20] U. Farooq, J. A. Kozinski, M. A. Khan, and M. Athar, "Biosorption of heavy metal ions using wheat based biosorbents—a review of the recent literature," *Bioresource Technology*, vol. 101, no. 14, pp. 5043–5053, 2010.

[21] H. M. Zwain, M. Vakili, and I. Dahlan, "Waste material adsorbents for zinc removal from wastewater: a comprehensive review," *International Journal of Chemical Engineering*, vol. 2014, Article ID 347912, 13 pages, 2014.

[22] G. Annadurai, R. S. Juang, and D. J. Lee, "Adsorption of heavy metals from water using banana and orange peels," *Water Science and Technology*, vol. 47, no. 1, pp. 185–190, 2003.

[23] K. K. Singh, R. Rastogi, and S. H. Hasan, "Removal of Cr(VI) from wastewater using rice bran," *Journal of Colloid and Interface Science*, vol. 290, no. 1, pp. 61–68, 2005.

[24] A. H. Mahvi, D. Naghipour, F. Vaezi, and S. Nazmara, "Teawaste as an adsorbent for heavy metal removal from industrial wastewaters," *American Journal of Applied Sciences*, vol. 2, no. 1, pp. 372–375, 2005.

[25] K. K. Singh, M. Talat, and S. H. Hasan, "Removal of lead from aqueous solutions by agricultural waste maize bran," *Bioresource Technology*, vol. 97, no. 16, pp. 2124–2130, 2006.

[26] V. Sarin and K. K. Pant, "Removal of chromium from industrial waste by using eucalyptus bark," *Bioresource Technology*, vol. 97, no. 1, pp. 15–20, 2006.

[27] G. Yan and T. Viraraghavan, "Effect of pretreatment on the bioadsorption of heavy metals on Mucor rouxii," *Water SA*, vol. 26, no. 1, pp. 119–123, 2000.

[28] W. S. Wan Ngah and M. A. K. M. Hanafiah, "Removal of heavy metal ions from wastewater by chemically modified plant wastes as adsorbents: a review," *Bioresource Technology*, vol. 99, no. 10, pp. 3935–3948, 2008.

[29] M. Nasiruddin Khan and M. Farooq Wahab, "Characterization of chemically modified corncobs and its application in the removal of metal ions from aqueous solution," *Journal of Hazardous Materials*, vol. 141, no. 1, pp. 237–244, 2007.

[30] S. Gupta and B. V. Babu, "Removal of toxic metal Cr(VI) from aqueous solutions using sawdust as adsorbent: equilibrium, kinetics and regeneration studies," *Chemical Engineering Journal*, vol. 150, no. 2-3, pp. 352–365, 2009.

[31] O. G. Moatshe, V. E. Emongor, and O. Oagile, "Effect of benzyladenine (BA) on fruit set and mineral nutrition of morula (*Sclerocarya birrea* subspecies caffra)," *African Journal of Plant Science*, vol. 5, no. 4, pp. 268–272, 2011.

[32] K. A. Ghebremichael, K. R. Gunaratna, H. Henriksson, H. Brumer, and G. Dalhammar, "A simple purification and activity assay of the coagulant protein from *Moringa oleifera* seed," *Water Research*, vol. 39, no. 11, pp. 2338–2344, 2005.

[33] V. Obuseng, F. Nareetsile, and H. M. Kwaambwa, "A study of the removal of heavy metals from aqueous solutions by Moringa oleifera seeds and amine-based ligand 1,4-bis[N,N-bis(2-picoyl)amino]butane," *Analytica Chimica Acta*, vol. 730, pp. 87–92, 2012.

[34] M. Akhtar, S. Moosa Hasany, M. I. Bhanger, and S. Iqbal, "Sorption potential of Moringa oleifera pods for the removal of organic pollutants from aqueous solutions," *Journal of Hazardous Materials*, vol. 141, no. 3, pp. 546–556, 2007.

[35] M. Tüzen, "Determination of heavy metals in soil, mushroom and plant samples by atomic absorption spectrometry," *Microchemical Journal*, vol. 74, no. 3, pp. 289–297, 2003.

[36] E. Demirbas, M. Kobya, E. Senturk, and T. Ozkan, "Adsorption kinetics for the removal of chromium (VI) from aqueous solutions on the activated carbons prepared from agricultural wastes," *Water SA*, vol. 30, no. 4, pp. 533–539, 2004.

[37] M. Helen Kalavathy and L. R. Miranda, "Moringa oleifera—a solid phase extractant for the removal of copper, nickel and zinc from aqueous solutions," *Chemical Engineering Journal*, vol. 158, no. 2, pp. 188–199, 2010.

[38] M. S. Rahman and M. R. Islam, "Effects of pH on isotherms modeling for Cu(II) ions adsorption using maple wood sawdust," *Chemical Engineering Journal*, vol. 149, no. 1–3, pp. 273–280, 2009.

[39] V. K. Gupta, A. Rastogi, and A. Nayak, "Adsorption studies on the removal of hexavalent chromium from aqueous solution using a low cost fertilizer industry waste material," *Journal of Colloid and Interface Science*, vol. 342, no. 1, pp. 135–141, 2010.

[40] A. Shukla, Y.-H. Zhang, P. Dubey, J. L. Margrave, and S. S. Shukla, "The role of sawdust in the removal of unwanted materials from water," *Journal of Hazardous Materials*, vol. 95, no. 1-2, pp. 137–152, 2002.

[41] L. V. A. Gurgel and L. F. Gil, "Adsorption of Cu(II), Cd(II) and Pb(II) from aqueous single metal solutions by succinylated twice-mercerized sugarcane bagasse functionalized with triethylenetetramine," *Water Research*, vol. 43, no. 18, pp. 4479–4488, 2009.

[42] T. O. Jimoh, "Utilization of Blighia sapida (Akee apple) pod in the removal of lead, cadmium and cobalt ions from aqueous solution," *Journal of Environmental Chemistry and Ecotoxicology*, vol. 4, no. 10, pp. 178–187, 2012.

[43] S. J. Allen and P. A. Brown, "Isotherm analyses for single component and multi-component metal sorption onto lignite," *Journal of Chemical Technology and Biotechnology*, vol. 62, no. 1, pp. 17–24, 1995.

[44] E. Fouresta, A. Serreb, and J. C. Roux, "Contribution of carboxyl groups to heavy metal binding sites in fungal wall," *Toxicological & Environmental Chemistry*, vol. 54, no. 1–4, pp. 1–10, 1992.

[45] O. S. Amuda, A. A. Giwa, and I. A. Bello, "Removal of heavy metal from industrial wastewater using modified activated coconut shell carbon," *Biochemical Engineering Journal*, vol. 36, no. 2, pp. 174–181, 2007.

[46] P. Sharma, P. Kumari, M. M. Srivastava, and S. Srivastava, "Removal of cadmium from aqueous system by shelled *Moringa oleifera* Lam. seed powder," *Bioresource Technology*, vol. 97, no. 2, pp. 299–305, 2006.

[47] H. N. Bhatti, B. Mumtaz, M. A. Hanif, and R. Nadeem, "Removal of Zn(II) ions from aqueous solution using *Moringa oleifera* Lam. (horseradish tree) biomass," *Process Biochemistry*, vol. 42, no. 4, pp. 547–553, 2007.

[48] M. Nadeem, A. Mahmood, S. A. Shahid, S. S. Shah, A. M. Khalid, and G. McKay, "Sorption of lead from aqueous solution by chemically modified carbon adsorbents," *Journal of Hazardous Materials*, vol. 138, no. 3, pp. 604–613, 2006.

[49] J. D. Lee, *Concise Inorganic Chemistry*, Oxford University Press, New York, NY, USA, 5th edition, 2008.

[50] C. S. T. Araújo, D. C. Carvalho, H. C. Rezende et al., "Bioremediation of waters contaminated with heavy metals using moringa oleifera seeds as biosorbent," in *Applied Bioremediation—Active and Passive Approaches*, Y. B. Patil and P. Rao, Eds., chapter 10, InTech, Rijeka, Croatia, 2013.

[51] A. R. Iftikhar, H. N. Bhatti, M. A. Hanif, and R. Nadeem, "Kinetic and thermodynamic aspects of Cu(II) and Cr(III) removal from aqueous solutions using rose waste biomass," *Journal of Hazardous Materials*, vol. 161, no. 2-3, pp. 941–947, 2009.

[52] N. Ozbek and S. Akman, "Microwave plasma atomic emission spectrometric determination of Ca, K and Mg in various cheese varieties," *Food Chemistry*, vol. 192, pp. 295–298, 2016.

[53] M. Kazemipour, M. Ansari, S. Tajrobehkar, M. Majdzadeh, and H. R. Kermani, "Removal of lead, cadmium, zinc, and copper from industrial wastewater by carbon developed from walnut, hazelnut, almond, pistachio shell, and apricot stone," *Journal of Hazardous Materials*, vol. 150, no. 2, pp. 322–327, 2008.

[54] M. A. Barakat, "New trends in removing heavy metals from industrial wastewater," *Arabian Journal of Chemistry*, vol. 4, no. 4, pp. 361–377, 2011.

[55] J. S. Yadav, M. Soni, S. Verma, and J. K. Srivastava, "Removal of copper ion (Cu^{2+}) using soybean hulls," *Pollution Research*, vol. 27, no. 2, pp. 323–326, 2008.

[56] C. Arunlertaree, W. Kaewsomboon, A. Kumsopa, P. Pokethitiyook, and P. Panyawathanakit, "Removal of lead from battery manufacturing wastewater by egg shell," *Songklanakarin Journal of Science and Technology*, vol. 29, no. 3, pp. 857–868, 2007.

[57] K. M. S. Surchi, "Agricultural wastes as low cost adsorbents for Pb removal: kinetics, equilibrium and thermodynamics," *International Journal of Chemistry*, vol. 3, no. 3, pp. 103–112, 2011.

[58] C. Saka, Ö. Şahin, and M. M. Küçük, "Applications on agricultural and forest waste adsorbents for the removal of lead (II) from contaminated waters," *International Journal of Environmental Science and Technology*, vol. 9, no. 2, pp. 379–394, 2012.

Hindawi Publishing Corporation
Journal of Chemistry
Volume 2016, Article ID 2742013, 11 pages
http://dx.doi.org/10.1155/2016/2742013

Research Article

Surface Modification of Polypropylene Membrane Using Biopolymers with Potential Applications for Metal Ion Removal

Omar Alberto Hernández-Aguirre,[1] Alejandra Núñez-Pineda,[2] Melina Tapia-Tapia,[2] and Rosa María Gómez Espinosa[1]

[1]*Facultad de Química, UAEM and Centro Conjunto de Investigación en Química Sustentable UAEM-UNAM, km 14.5 Carretera Toluca-Atlacomulco, San Cayetano, 50200 Toluca, MEX, Mexico*
[2]*Instituto de Química, UNAM and Centro Conjunto de Investigación en Química Sustentable UAEM-UNAM, km 14.5 Carretera Toluca-Atlacomulco, San Cayetano, 50200 Toluca, MEX, Mexico*

Correspondence should be addressed to Rosa María Gómez Espinosa; rosamarigo@gmail.com

Received 7 April 2016; Revised 2 June 2016; Accepted 7 June 2016

Academic Editor: João Paulo Leal

This work aims to present the modification of polypropylene (PP) membranes using three different biopolymers, chitosan (CHI), potato starch (PS), and cellulose (CEL), in order to obtain three new materials. The modified membranes may be degraded easier than polypropylene ones and could be used as selective membranes for metal ions removal, among other applications. For this purpose, the UV energy induced graft copolymerization reaction among polypropylene membrane, acrylic acid, benzophenone (as photoinitiator), and the biopolymer (CHI, PS, or CEL) was conducted. The results of FT-IR-ATR, XRD, TGA, DSC, SEM, BET, and AFM analyses and mechanical properties clearly indicate the successful modification of the membrane surface. The change of surface wettability was monitored by contact angle. The grafting reaction depends on natural polymer, reaction time, and concentration. In order to prove the potential application of the modified membranes, a preliminary study of sorption of metal ion was carried out. For this purpose, the PP-CHI membrane was chosen because of the high hydrophilicity, proportionate to -OH and NH_2; these groups could act as ligands of metal ions, provoking the interaction between PP-CHI and M+ (PP-CHI-M^+) and therefore the metal ion removal from water.

1. Introduction

Polypropylene (PP) is widely used in a variety of industrial applications such as wastewater treatment and separation process because of its low cost, good mechanical and thermal properties, and chemical stability. In the membrane field, PP is also considered for biomedical applications, namely, hemodialysis, plasmapheresis, blood oxygenation, and leukodepletion process [1]. However, the hydrophobicity of PP material limits its applications and consequently many compounds have been used to modify the PP surface [2–4], in order to change its properties and increase their applications. The surface of PP films has been grafted with polar groups [5, 6] to modify its permeability coefficient and hydrophilicity. Grafting modification with specific functional groups is one of the approaches to synthesize adsorbent PP that can be used for metal removal from wastewater [7], where the selectivity depends on the specific interactions between the grafted monomer and the metal ions.

The surface modification of membranes is a promising approach to confer new properties to the membranes, different from those of the original material. Surface chemistry and morphology of membranes play an important role in the efficiency of the membrane modification process [8]. Generally, the objective of the modification is not only to increase the flux and/or selectivity, but also to improve the chemical resistance [9]. A monomer could be introduced within a polymeric matrix using blend or immobilization processes, such as other several ways [10]. However, the compatibility of the monomer with the polymeric matrix becomes a prime constraint to develop the required material [11]. In this context, several methods have been used to

modify the chemistry of membranes. These include surface grafting [12], pore-filled grafting [13], and dip coating [14]. The UV-induced graft polymerization of a monomer into the polymer matrix is an adequate route to modify the surface; it changes its properties such as wettability or permeability. The attractive feature of the grafting process is that the extent of modification can be precisely controlled by the proper selection of the irradiation and reaction conditions [10]. In addition, the graft polymerization is initiating without prior modification of a surface. The procedure is relatively simple, energy-efficient, cost-effective, and well-suited for integration with other technologies [15]. The matrix can be modified with different functional groups such as carboxylic acid, amine, hydroxyl, and sulfonic acid groups. These groups attached onto the polymeric networks can be tailored for a specific application [16]. Owing to higher adsorption rate and adsorption capacity, the modified polymer can provide many advantages as new-type, fast-responsive, and high-capacity adsorbent materials for the removal of pollutants from aqueous solutions [17, 18].

Biopolymers are good candidates to modify the surface properties of PP, due to their properties such as water binding capacity, nontoxicity, biocompatibility, selectivity, and biodegradability. Therefore, it is reasonable to combine the advantages of UV-induced graft polymerization with the versatile characteristics of natural polymers like potato starch (PS), cellulose (CEL), and chitosan (CHI), which occur abundantly in nature [19–22]. The present work is concerned with the use of the natural polymers as grafting compounds to modify PP using UV energy source to obtain new membranes with capabilities of water affinity, metal removal, and potential biodegradability after use. It was decided to functionalize the polypropylene membrane with acrylic acid, taking advantage of the polar groups (C=O, -OH) to anchor the biopolymer (Figure 1).

2. Materials and Methods

Polypropylene microporous membrane with pore size of 0.45 μm, thickness of 114 μm, and porosity of 84.6% was supplied by 3M Company. Chitosan (448877-medium molecular weight, deacetylated chitin), cellulose (α-cellulose), phosphoric acid, acrylic acid, and benzophenone (radical photoinitiator) were from Sigma-Aldrich and were used without prior treatment. Potato starch was obtained by the method reported by BeMiller and Whistler [19].

2.1. Preparation of Biopolymers Solutions for Membrane Surface Modification. Solutions of 1% w/v of each biopolymer were prepared: potato starch (in water), chitosan (in 2% acetic acid solution), and cellulose (in phosphoric acid). In addition, solutions of acrylic acid (1 : 1 in deionized water) and benzophenone (0.05 M in acetone) were also prepared.

2.2. Grafting of Biopolymers into Polypropylene Surface. The polypropylene membrane was cut into square-shaped pieces (5 × 5 cm) and impregnated with corresponding biopolymer solution, acrylic acid, and benzophenone. The so-prepared membranes were put in between two liners, placed in squeeze rollers, and transferred to a glass plate and another glass plate was put on top of it. Membranes were irradiated with UV radiation (300 nm) during 8 h. After this time, the samples were washed in Soxhlet equipment for 24 h to remove nongrafted biopolymer. The grafted membranes were dried under vacuum until constant weight.

2.3. Graft Polymerization for Kinetics Analysis

2.3.1. Determination of Grafting Degree. The grafting degree (Gd) was calculated from the equation

$$\text{Gd}\,(\%) = \frac{(W_1 - W_0)}{W_0} \times 100, \tag{1}$$

where W_0 and W_1 are the mass of the PP membrane and the modified membrane, respectively.

2.3.2. Effect of the Irradiation Time. The effect of irradiation time was evaluated by the grafting degree determined at 1 to 8 hours of exposure to UV energy.

2.3.3. Effect of the Biopolymer Concentration. The effect of biopolymer concentration was evaluated at 0.25, 0.5, 1, and 2% in solution.

2.4. Methods of Characterization. The modified membranes of polypropylene have been characterized using the following methods.

2.4.1. Wettability and Contact Angle Test. To determine the equilibrium water absorption, the modified membranes were subjected to swelling test. The samples were immersed in deionized water during different periods. Excess of water on the surface of the samples was removed with filter paper and the swollen samples were weighted. The swelling was determined by the following equation:

$$\text{Swelling}\,(\%) = \frac{(W_s - W_i)}{W_i} \times 100, \tag{2}$$

where W_s and W_i are the weights of swollen and dry membranes, respectively.

Contact angle measurements were conducted in a Krüss model G-1 apparatus.

2.4.2. Fourier Transform Infrared Spectroscopy (FT-IR). FT-IR-ATR spectra were acquired by an infrared spectrometer Bruker Tensor 27; the ATR accessory contained a diamond crystal. The spectra acquisition conditions were 25°C, 64 scans, and 500–4000 cm^{-1} and 2 cm^{-1} resolution, with respect to the appropriate background spectra.

2.4.3. Scanning Electronic Microscopy (SEM). Scanning Electronic Microscopy was performed in JEOL JSM-6510LV equipment. For this analysis the membranes were first dried until constant weight and then covered with gold to improve images quality.

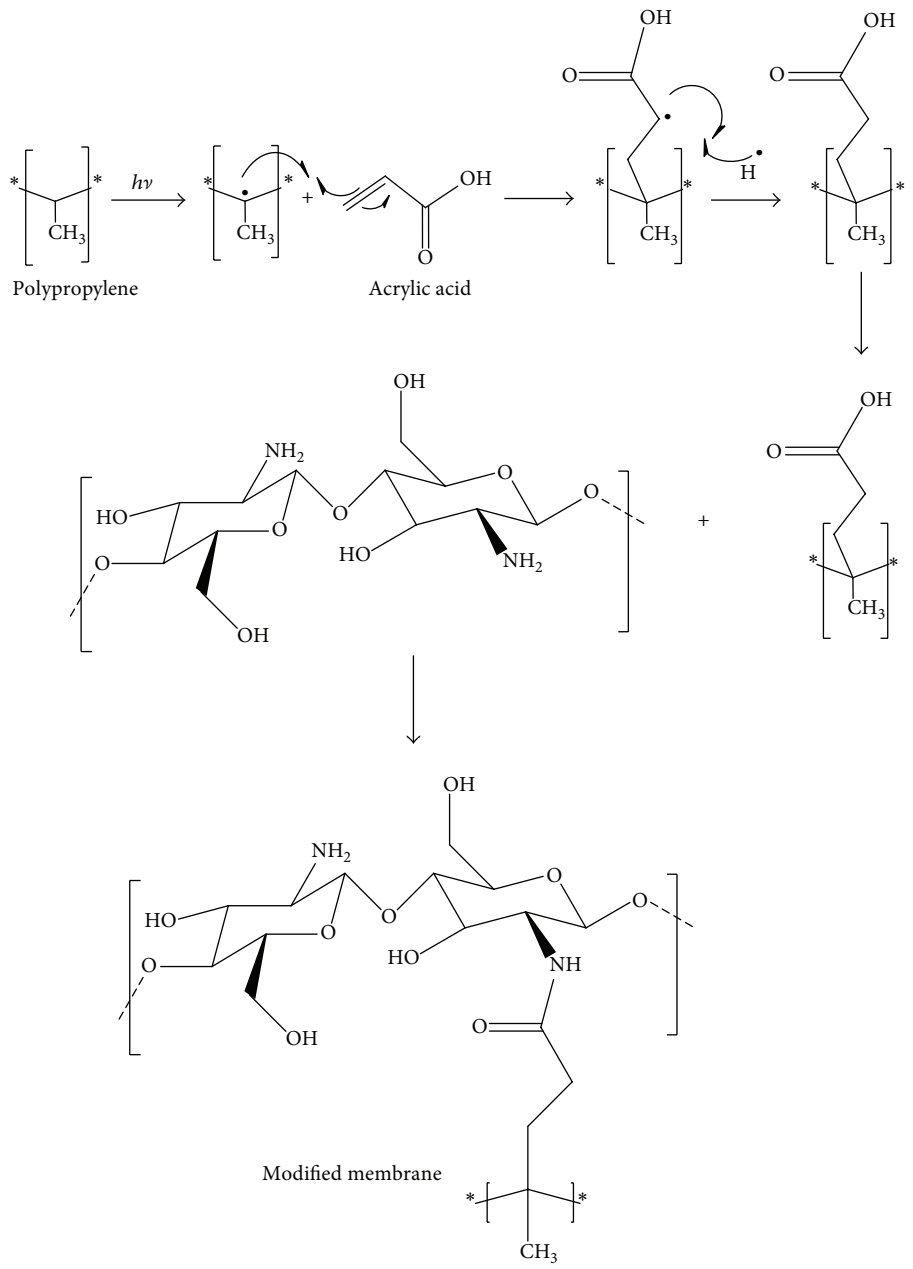

Figure 1: Schematic proposal of grafting of each biopolymer on the surface of PP membrane using radiation UV. (Chitosan was used for this example.)

2.4.4. Atomic Force Microscopy (AFM). AFM was performed with the noncontact mode using a MFP-3D Origin AFM apparatus equipped with Igor Pro 6.34A. The sample was attached to a glass slide using a double-sided tape, followed by scanning of the surface by a silicon nitride probe in air at ambient conditions. The scanning was performed at a speed of 0.24 Hz and scan sizes of 90, 60, 30, and 15 μm. Sampling resolution of 448 points per line was selected.

2.4.5. Thermogravimetric Analysis (TGA) and Differential Scanning Calorimetry (DSC). TGA and DSC studies were carried out in a thermal analyzer Netzsch STA 449 F3 Jupiter, with a heating ramp of 10°C/min, in a nitrogen atmosphere at a flow rate of 20 mL/min. Samples were heated from room temperature to 560°C. Aluminum crucibles of 5 mm diameter were used. Savitzky-Golay's smoothing algorithm was employed for TGA curves.

2.4.6. Specific Surface Area (Using BET). The specific surface area of the modified membrane was determined by N_2 adsorption using the multipoint Brunauer-Emmett-Teller isotherm (BET) in Autosorb iQ equipment of Quantachrome Instruments at 77 K.

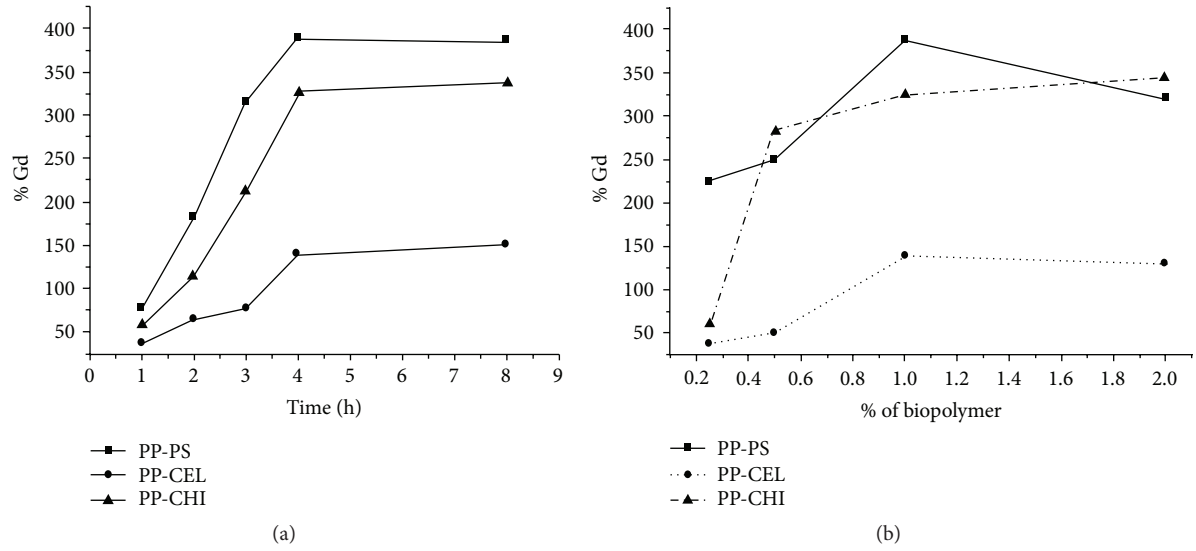

Figure 2: (a) Grafting yield of biopolymer as function of the reaction time. (b) Effect of biopolymer concentration on grafting degree.

2.4.7. X-Ray Diffraction (XRD). The diffraction patterns were obtained using Bruker D8 Advance, Cu-kα to 1.5404 Å at 2θ (5–60°) at 30 kV and 20 mA. The scanning electron microscopy SEM-EDS was performed in JEOL JSM-6510LV. Elemental analysis was performed in an Elementar Vario Micro Cube analyzer.

2.4.8. Mechanical Test. Tensile modulus and ultimate load-to-failure strength were determined on separate strips of 1 × 5 cm by a tensile test in TA Instruments DMA-Q800.

2.5. Sorption Test. A sorption test was conducted with a variable flow peristaltic pump (Pump Low Speed Flow Control Company), latex connections, a 20 mg/L copper solution prepared from copper pentahydrate sulfate ($CuSO_4 * 5H_2O$), and deionized water (DI). The system was conditioned at a flow rate of 2 mL/min.

3. Results and Discussion

3.1. Grafting of Biopolymers onto Polypropylene Surface. The reaction was carried out by free radical polymerization of acrylic acid, benzophenone (as photoinitiator), and biopolymers (CEL, PS, and CHI, separately). In previous experiments by our group, the need of acrylic acid addition to achieve the biopolymers grafting has been established. The reaction results in the formation of the interpolymer network where biopolymer molecules are grafted into the macromolecular lattice acrylic acid-polypropylene [25, 26]. Thus, once the PP was functionalized, the modification using biopolymer is feasible.

3.1.1. Determination of Grafting Degree, Concentration, and Irradiation Time. The dependence of the reaction time and biopolymer concentration on the grafting degree was evidenced in Figure 2. It is worth pointing out that the acrylic acid provides the reactive sites for the grafting of the biopolymer; otherwise the reaction does not occur [27]. In Figure 2(a) the graft copolymerization is proportional to the reaction time, where the modified membranes presented the highest grafting yields at 4 hours. The observed behavior for the grafting yield of the biopolymers was as follows: PS (388%), CHI (240%), and CEL (140%). Figure 2(b) shows the dependence of the grafting degree on biopolymer concentration. The grafting yield of the reaction system could change with the different reactant concentrations. It can be seen that an increase of the biopolymer concentration leads to a Gd enhancement. However, the biopolymer concentration increased to a maximum of 1% and then decreased. The initial positive slope of the plot is explained by an increase of the grafting reaction due to a greater concentration of the reactant. When the biopolymer concentration further increased, an increase in the viscosity of the grafting mixture was observed producing a difficult diffusion of the biopolymer into the PP [25, 27]. It is often reported that the grafting efficiency increases with monomer concentration up to a certain limit and then decreases with higher concentrations [28–30]. These results indicated that the optimal conditions for this study were 4 hours of reaction time and 1% of the biopolymer concentration to modify polypropylene surface.

3.2. Characterization of Modified Membranes. To evaluate the hydrophilic character of the modified membrane, the contact angle and the kinetics of swelling were studied.

3.2.1. Wettability Test of Membrane. The kinetics of swelling of the modified membrane at room temperature in water was followed by gravimetry. Figure 3 shows the swelling process of each modified membrane. The equilibrium was observed after 20 minutes for each new membrane with a maximum absorption as follows: PP-PS (247%), then PP-CEL (177%), and PP-CHI (164%). The unmodified polypropylene

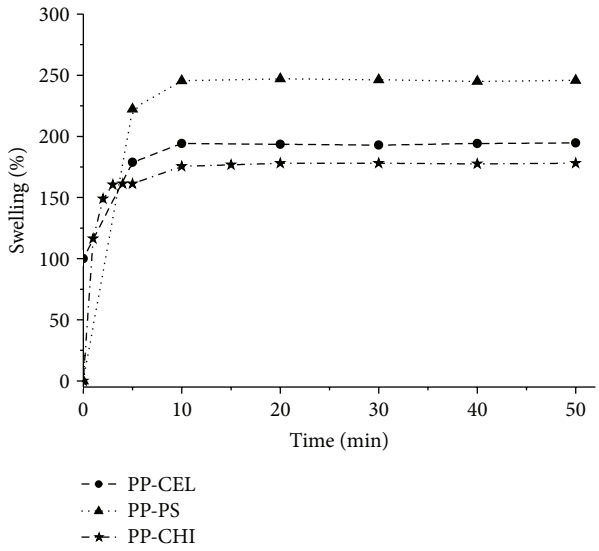

Figure 3: Swelling process of modified membranes.

membrane did not present swelling ability. The grafted polar groups provoked a radical change in the hydrophobic character of the membrane [31, 32].

3.2.2. Contact Angle. The interfacial properties between a liquid and a polymer component are characterized by the surface energies of each phase and the contact angle between them [33]. Contact angle measurements have been commonly used to characterize the hydrophilicity of membrane surfaces [15]; the unmodified membrane had a 90° water contact angle, while modified membranes decreased the angle depending on the grafted biopolymer on PP surface. The PP-CEL membrane showed an angle of 25°; the PP-CHI membrane presented 16°; when it comes to the PP-PS, the contact angle was 0°, and this indicates a dramatic change in its hydrophobic character, having complete wetting. These results show that the modified membranes changed the hydrophobicity of the polypropylene membrane, due to the presence of polar groups from the biopolymers, which enhances the surface energy and the hydrophilicity of modified membranes [34]. The hydrophilicity will influence the permeation and surface properties of the PP membranes, thus widening their applications in biomedical and environmental fields [35].

3.2.3. FT-IR-ATR Analysis. The FT-IR spectroscopy can confirm that each biopolymer was grafted onto the PP membrane surface. Figure 4 shows the FT-IR-ATR analysis of modified membranes compared with PP, as reference. The PP spectrum shows the absorbency peaks at 2918 cm^{-1} (CH_2 stretching asymmetrical vibration), 2848 cm^{-1} (CH_2 stretching symmetrical vibration), and 1455 cm^{-1} and 1380 cm^{-1} (CH_2 scissor vibration), and other low frequency -C-C- stretching vibration modes are also observed. The spectra of modified membranes PP-PS and PP-CEL showed characteristic signals at 3159 and 3367 cm^{-1} corresponding at stretching

Table 1: Elemental analysis of modified membranes.

Membrane	% Gd	Carbon	Hydrogen	Oxygen	Nitrogen
PP	—	85.50	13.92	—	—
PP-PS	388	67.68	10.14	22.18	—
PP-CEL	140	68.24	10.68	21.08	—
PP-CHI	240	54.55	7.64	37.7	0.11

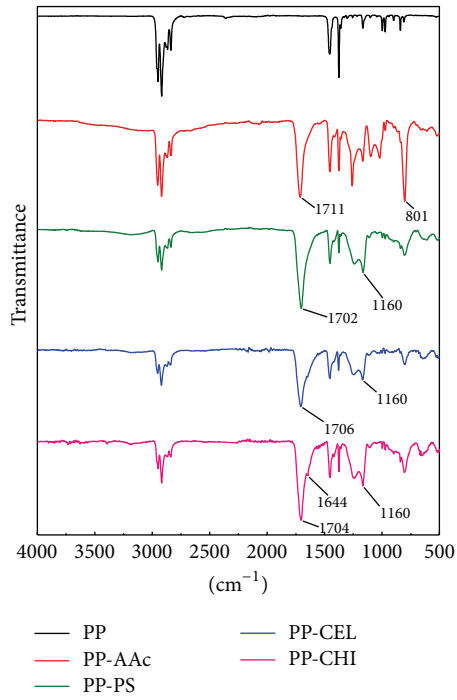

Figure 4: FT-IR-ATR spectra of modified membranes (PP-CHI, PP-CEL, and PP-PS) and PP.

vibration of -OH, respectively. PP-CHI spectrum showed a broad band at 3161 cm^{-1} of stretching vibration of N-H and O-H; the signal in 1644 cm^{-1} corroborates the bending vibration of N-H. The C=O vibration had a different shift depending on the biopolymer grafted; for example, the PP-PS was observed at 1702 cm^{-1}, the PP-CEL at 1706 cm^{-1}, and the PP-CHI at 1704 cm^{-1}. The spectra of PP-PS, PP-CEL, and PP-CHI showed the same pattern around 1200–1160 cm^{-1} corresponding to the glycosidic bond (C-O-C stretching vibration) of the biopolymers. It is important to mention that the carbonyl group of the acrylic acid grafted to polypropylene membrane (PP-AAc) showed a different shift at 1711 cm^{-1}.

3.2.4. Elemental Analysis of the Modified Membranes. This analysis showed that the results are consistent with the empirical equation of PP (C_3H_6) that is calculated as 85.71% of carbon and 14.29% of hydrogen. According to the elemental analysis results for PP-PS, PP-CEL, and PP-CHI (Table 1), there is a significant amount of oxygen caused by the presence of acrylic acid and biopolymer. The analyses of the composition of the modified membrane of PP-PS and

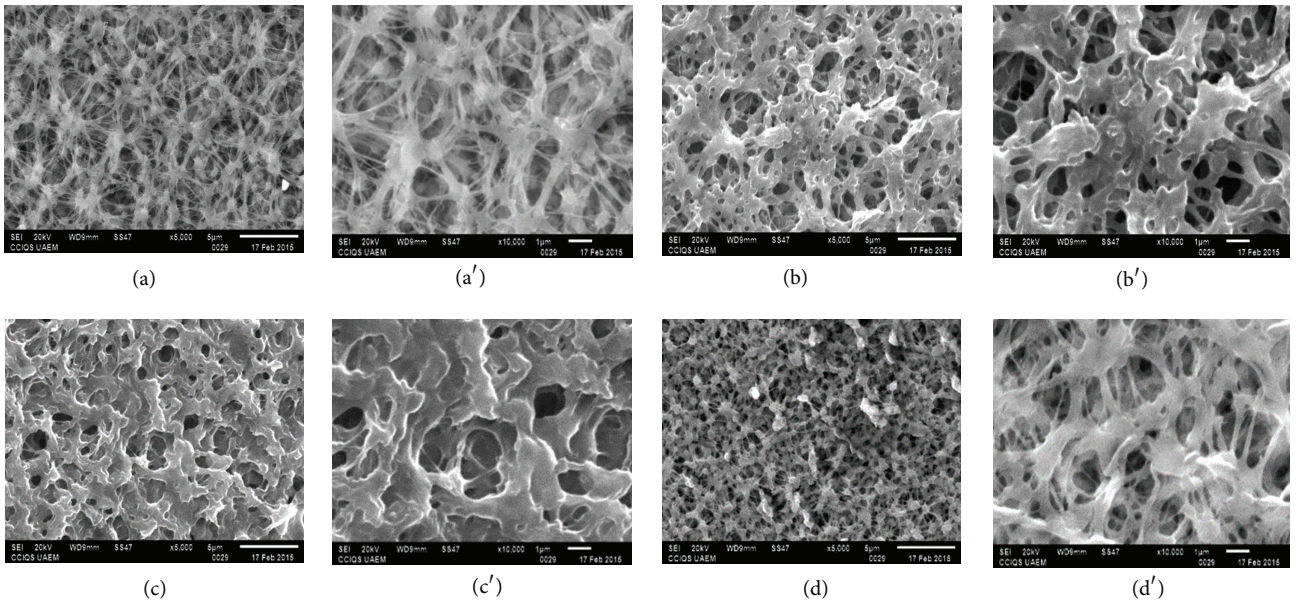

Figure 5: SEM images of membranes: unmodified PP, (a) ×5000 and (a′) ×10000; PP-PS, (b) ×5000 and (b′) ×10000; PP-CEL, (c) ×5000 and (c′) ×10000; and PP-CHI, (d) ×5000 and (d′) ×10000.

PP-CEL have the same empirical equation ($C_6H_{10}O_5$), unlike chitosan ($C_6H_{11}O_4N$) that showed the presence of nitrogen from the amine group. These results are similar to the sum of PP + AAc + biopolymer, for example. In the case of PP-CHI the theoretical composition was 52.36% of carbon, 7.6% of hydrogen, 32.98% of oxygen, and 5.1% of nitrogen for $C_{12}H_{21}O_6N$. Certainly, these results clearly indicate the presence of the biopolymer in the PP grafted membrane.

3.2.5. Scanning Electron Microscopy (SEM). Scanning electron microscopy (SEM) was used to examine the morphology of the different modified membranes. It can be observed in Figure 5 that the surface of the modified membranes is considerably different from the starting membrane. The PP unmodified membrane (Figures 5(a) and 5(a′)) shows well-defined fibers forming pores of heterogeneous size. The changes in the morphology are evident depending on the grafted biopolymer, observing a greater increase in the thickness of the fibers in the modified membrane: PP-PS (Figures 5(b) and 5(b′)), followed by PP-CEL (Figures 5(c) and 5(c′)), and PP-CHI (Figures 5(d) and 5(d′)). We attributed the different thickness to the chemical structure of each biopolymer and to their different molecular weight.

3.2.6. BET Assay. The BET analysis was used as a complementary assay. The specific surface area of the modified membrane was determined by the physical adsorption of nitrogen on the surface of the membrane and by calculating the amount of adsorbate gas corresponding to a layer on the surface. The results show that the addition of the biopolymer reduces the total area and the pore diameter. This is in agreement with the SEM images. The diminished porosity of the modified membrane can be ascribed to the biopolymer grafted in the surface, causing more resistance to the lamellar separation [34]. The BET surface area of the PP membrane was 922.3 m^2/g and is characteristic of a microporous material. However, the modified membranes exhibit surface areas in the following order: PP-CHI > PP-CEL > PP-PS (48.6, 46.6, and 42.6 m^2/g, resp.). This indicates that the biopolymer has penetrated into the support pores, which changes the characteristic of the PP membrane from microporous membrane to a mesoporous material.

3.2.7. Topographical Analysis (Using AFM). Determination of the surface roughness by AFM is crucial to confirm the grafted reaction. PP and modified membranes were analyzed by AFM. The PP has a nodular mesh organized in a framework in which between 5 and 6 fibers converge, allowing the formation of holes with different diameters, and an ovoid geometry was observed. Figure 6 represents (2D) the morphological changes between the PP and the modified membranes (PP-CEL, PP-PS, and PP-CHI). The lightest areas represent the highest regions of the structure and the darkest the deepest. The maximum heights shown for the modified membranes were in the following order: PP-CEL samples ≈ 600 nm, PP-CHI ≈ 400 nm, and PP-PS ≈ 300 nm.

The morphology of PP-CEL, likewise PP-PS, showed flakes with a semiradial growth from nodular regions of the PP; these flakes have 54% more volume. The presence of chitosan promotes the formation of thicker layers, and an amorphous morphology with a soft texture was presented [36]. AFM analysis suggests that the penetration, as well as infiltration of the hybrid materials, is favored in the following order: PP-PS (800 nm), PP-CEL (600 nm), and PP-CHI (300 nm) [37–39].

(1) Surface Roughness. Surface roughness is an important structural property of polymeric membranes. It has been

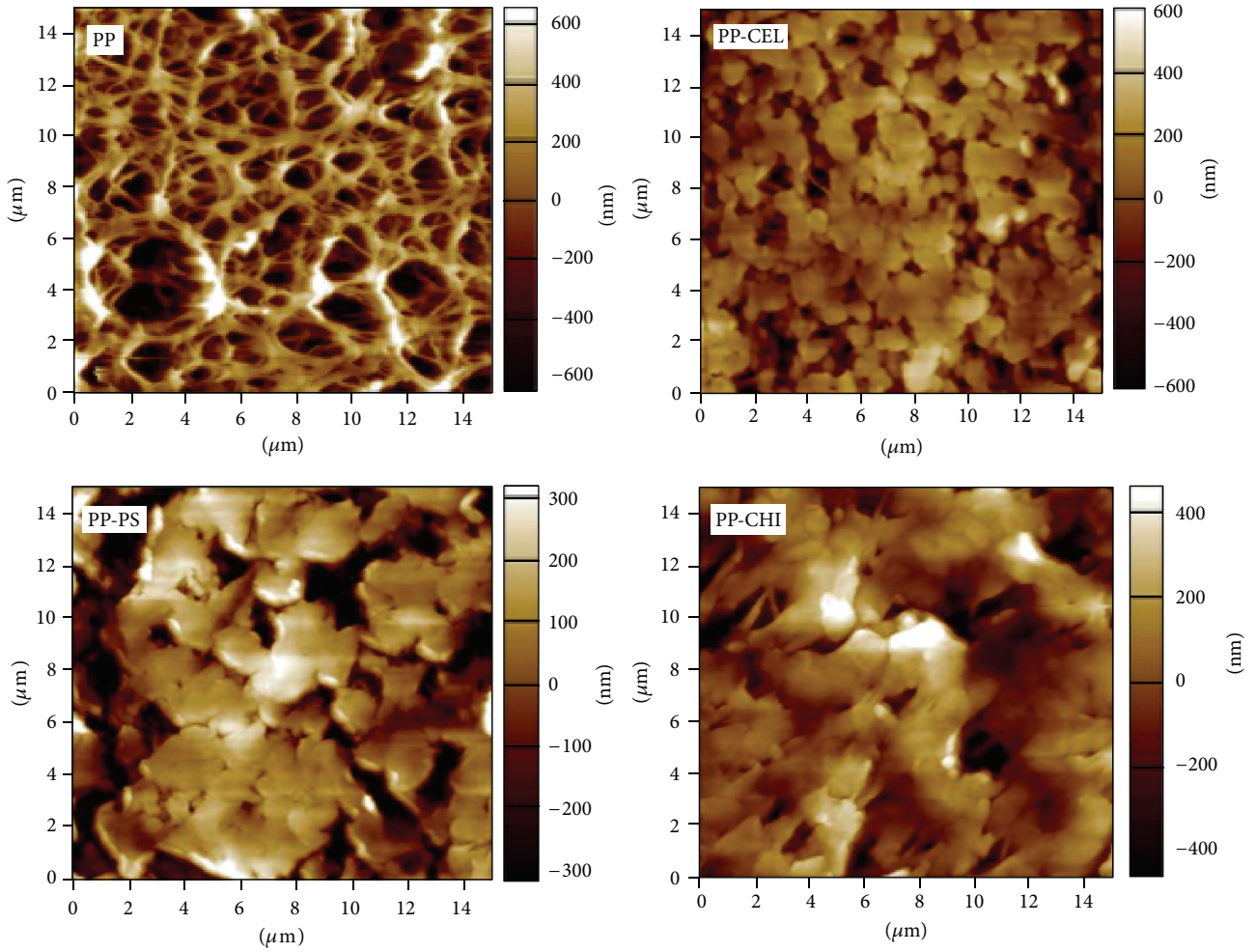

Figure 6: AFM topographical image of 15 × 15 microns for PP, PP-CEL, PP-PS, and PP-CHI.

Table 2: Surface roughness.

Membrane	Roughness (Ra) Nm	Z max (nm)
PP	263.01	1700
PP-PS	212.70	1000
PP-CEL	256.80	1400
PP-CHI	242.59	1200

Table 3: Tensile test of PP and modified membranes.

Membrane	% Gd	Stress (MPa)	Strain (%)
PP	—	14.1	18
PP-CEL	140	56	7
PP-PS	388	Max. limit	—
PP-CHI	240	77.5	30

shown that this parameter could be influenced by various membrane fabrication parameters.

Table 2 shows the average of the values of the roughness (Ra) which are related to the penetration and infiltration capability. PP-PS exhibits the lowest roughness; the morphology of the flake has a greater surface and slightly irregular homogeneous characteristics that generate the formation of a film in the regions of greater depth, and the Z values decrease. The PP-CHI presents an intermediate roughness between PP and PP-CEL; the reason is that chitosan film was a hard film and was difficult to penetrate.

3.2.8. Mechanical Properties Evaluation. The tensile strength and elongation at break for the modified membranes were analyzed [40]. This test determines the main mechanical characteristics of the material and thus indicates its mechanical durability and its plausible application. Table 3 shows the differences in the mechanical properties of each membrane and direct correlation between grafted degree and stress. For the PP-PS membrane the strength at break exceeds 85 MPa. This fact indicates that PS gives mechanical stability to PP. The PP-CEL and PP-CHI show an increase of the tensile strength of more than 4 and 5.5 times, respectively, with respect to PP. These results indicate that the modified membranes may be exposed to greater stress. However, the

Table 4: Thermal parameters of PP and modified membranes.

Membrane	T_m (°C)	ΔH_m (J/g)	% biopolymer[1]	ΔH_{d2} (J/g)	ΔH_{d3} (J/g)
PP	153.2	97.2	ND	ND	680.4
PP-PS	152.9	27.6	11.4	165.1	195.7
PP-CEL	152.6	23.2	16.0	187.7	191.9
PP-CHI	151.8	16.9	22.6	196.9	149.3

[1]Values were obtained from thermogravimetric analysis in a range of 120–300°C.

percentage of elongation of PP-CEL membrane shows a significant reduction, whereas, for the PP-CHI membrane, this property increases approximately 12%. Therefore, the PP-CHI membranes show significant improvements on their mechanical durability, which potentiate their applications. Not all the surface modifications of the materials improve the mechanical properties. In fact, other reports about the modification of polypropylene, using different methods, showed that the polypropylene decreased its mechanical properties [41].

The improved strength for the three modified membranes confirms that the biopolymer chains were strongly attached to the PP membrane [42] and showed that they could be used in processes that require high resistance to mechanical stress, but with a small elastic capacity.

3.2.9. Thermal Properties and Decomposition Profile. Thermal properties and decomposition profiles of the PP and modified membranes were determined using DSC and TGA. The analysis of the changes in stability and thermal properties of modified membranes is important for their application, as well as the characterization and determination of their chemical and physical changes.

The melting temperatures of grafted membranes and PP were determined from peak onset (Figure 7, peak 1). Heat of melting (ΔH_m) and heat of decomposition (ΔH_{d2}, ΔH_{d3}) of the polymers were determined from the peak area of its corresponding transition in DSC (Figure 7, peaks 2 and 3).

(1) Change in T_m and ΔH_m. Table 4 shows the values of T_m for PP and modified membranes. Fusion temperature was slightly lower for modified membranes than the one of the unmodified PP membrane. This change in T_m could be attributed to the crystal arrangement in modified membranes and depends on the grafted biopolymer. The heat of melting (ΔH_m) for modified membranes decreases with the increase of the total content of biopolymer (% biopolymer). It has been reported that the thermodynamic melting temperature of semicrystalline biopolymers decreases as the molecular weight decreases and/or as the number of defects increases, that is, with an increase in branching and/or crosslinking [43].

(2) Heat of Decomposition and Natural Polymer Content in Grafted Membranes. In Figure 7, peak 2 refers to an endothermic process associated with decomposition of grafted biopolymer, which was not observed in PP curve. This process was also observed in TGA curves (Figure 8) with evident mass loss in modified membranes at 120–290°C,

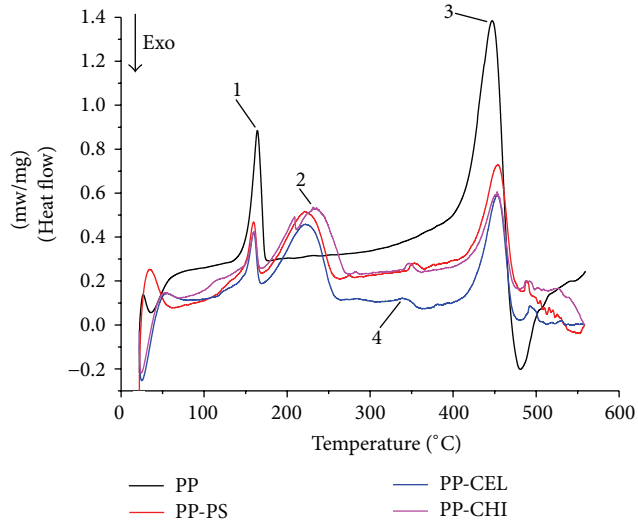

Figure 7: DSC curves of PP and modified membranes.

which was associated with a complex process, including dehydration of the biopolymer rings and breaking of the C-O-C glycosidic bonds, present in the main chain of the biopolymer [44]. In addition, Table 4 shows that the largest increase in ΔH_{d2} occurs for PP-CHI. It is worth pointing out that this is directly related to the total molar amount of the biopolymer in the membrane and indicates that crosslinking or branching of grafts was greater in PP-CHI.

The second decomposition stage (peak 3 in Figure 7) was related to the PP decomposition, and this peak was observed in the modified membranes as well. The most important characteristic for modified membranes is heat decomposition, ΔH_{d3}. The energy in modified membranes was lower than that in the PP membrane, and this behavior was observed for the three modified membranes, therefore indicating that grafted polymers require less quantity of energy for decomposition, which would favor their degradation. This process of decomposition was also observed in TGA curves (Figure 8) in 380–480°C range. Modified membranes showed a mass loss around 300–380°C that can be related to acrylic acid fragments, corroborated by peak 4 in DSC curves (Figure 7).

3.2.10. X-Ray Diffraction Analysis (XRD). In this work the evaluation of the degree of crystallinity of the modified membranes was performed by X-ray diffraction (XRD) [45]. XRD patterns were collected at 2θ (5–60°), though the most significant differences in the diffraction pattern of the

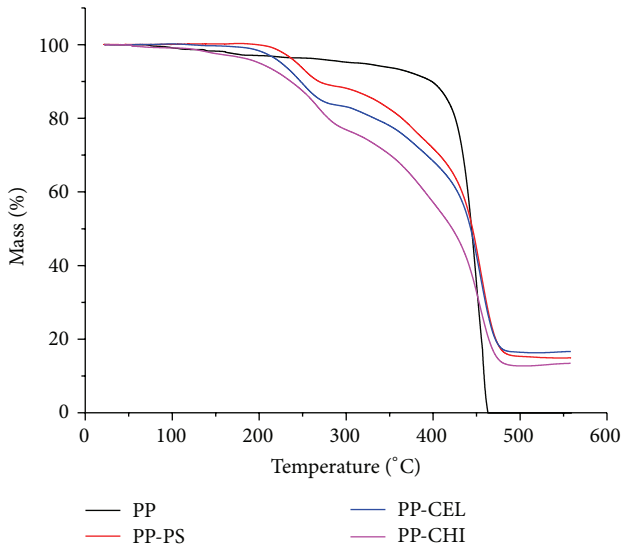

Figure 8: TGA curves of polypropylene and modified membranes.

respective phases appear in the range of $10^{\circ} < 2\theta < 15^{\circ}$, which directly depends on the grafted biopolymer and was related to the loss of crystallinity in the following order: PP-CEL > PP-PS > PP-CHI (Figure 9). This behavior is probably due to the random arrangement of each grafted biopolymer [46] and the branches formed by graft copolymerization reaction.

3.3. Preliminary Test of Sorption of Copper. The major challenge for the adsorption field is to select the most promising types of sorbent from an extremely large pool of readily available materials. In order to evaluate the capability of removing metal ions of the modified membranes, the PP-CHI membrane was selected; it contains polar functional groups such as -OH and $-NH_2$. These groups can be involved in chemical bonding and are responsible for the capacity for metal ions removal. With this in mind, a preliminary test of sorption process was carried out. A Cu^{+2} solution passed through the PP-CHI for 1 hour of operation time and 12 aliquots were collected every 5 min. Experiments were conducted in triplicate. The breakthrough curve shows a tendency to equilibrium after 10 minutes with a value of C_e/C_i (effluent concentration/initial concentration) equal to 0.8, indicating that the 80 percent was removed (Figure 10). However, the membrane has not reached saturation point, since the value of C_e/C_i is different than 1.0.

The copper sorption capacity for the membrane PP-CHI was 35.2 mg Cu/g; this result indicates that the modified membrane still has active groups for the metal removal. Table 5 shows that the PP-CHI is an excellent alternative for the metal ion removal such as copper comparing with chitosan in different presentation and process conditions [23, 24].

The performed test of copper ions sorption suggests that the modified materials prepared in this work find a potential application in the removal of metal ions.

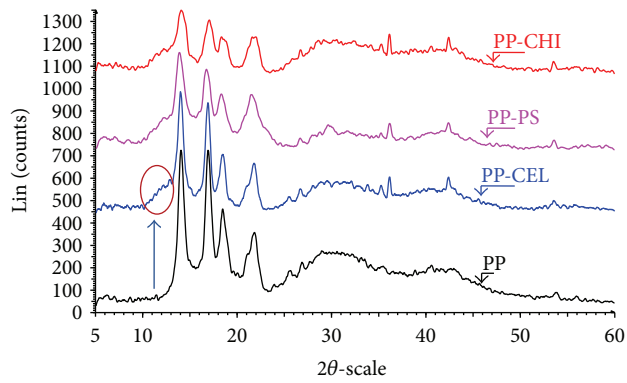

Figure 9: X-ray diffraction analysis of polypropylene (PP) and modified membranes.

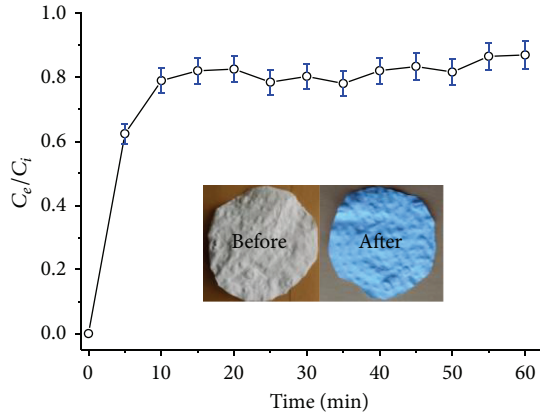

Figure 10: Breakthrough curve for sorption of Cu^{+2} using PP-CHI membrane.

4. Conclusions

Three new modified materials were obtained using UV radiation induced graft copolymerization reaction. The use of biopolymers such as potato starch, cellulose, and chitosan resulted in a very good alternative to modify the polypropylene membrane, changing its physical and chemical properties and therefore expanding its applications. The acrylic acid was a good option to functionalize the polypropylene membrane and graft the biopolymers. The grafting reaction depends on natural polymer, reaction time, and concentration. FT-IR-ATR, XRD, TGA, DSC, SEM, BET, and AFM analyses showed that the grafting reaction occurred. The mechanical properties of these membranes were improved. The kinetics of swelling of modified membranes and their water contact angles indicate a complete change to hydrophilic material. The modified membranes could be used for the metal ions removal, due to the affinity of the metal ions with the polar groups present in the modified membranes.

Table 5: Comparative sorbent material for metal ion removal.

Sorbent material	Sorption capacity (mg de Cu^{2+}/g)	Process condition	Author
Chitosan pearls	40–200	Batch	Flores et al., 2005 [23]
Chitosan	<150	Batch	Flores et al., 2005 [23]
Chitosan membrane	0.63	Continuous	Mora Molina et al., 2012 [24]
PP-CHI membrane	35.2	Continuous	This work

Competing Interests

The authors declare that they have no competing interests.

Acknowledgments

The authors would like to thank the Centro Conjunto de Investigación en Química Sustentable UAEM-UNAM and 3M Company for providing the propylene membrane, Lizbeth Triana Cruz and María Citlalit Martínez Soto for technical assistance, and A. R. Vilchis Nestor for SEM microscopy. Finally, the financial support of SIyEA of UAEMex through Project 3719/2014 and CONACYT through Project 220392 is also acknowledged.

References

[1] M. Ulbricht, "Advanced functional polymer membranes," *Polymer*, vol. 47, no. 7, pp. 2217–2262, 2006.

[2] L. H. Sperling and C. E. Carraher Jr., "Renewable resource monomers and polymers," in *Polymer Applications of Renewable-Resource Materials*, L. H. Sperling and C. E. Carraher Jr., Eds., pp. 1–26, Springer, New York, NY, USA, 1983.

[3] I. Frischinger and S. Dirlikov, "Toughening of epoxy resins by epoxidized soybean oil," in *Toughened plastics i*, vol. 233, pp. 451–489, American Chemical Society, Washington, DC, USA, 1993.

[4] J. Rösch and R. Mülhaupt, "Toughened polypropylene-polyamide 6 blends prepared by reactive blending," in *Toughened Plastics II*, vol. 252, pp. 291–302, American Chemical Society, Washington, DC, USA, 1996.

[5] V. Costamagna, M. Strumia, M. López-González, and E. Riande, "Gas transport in surface grafted polypropylene films with poly(acrylic acid) chains," *Journal of Polymer Science Part B: Polymer Physics*, vol. 45, no. 17, pp. 2421–2431, 2007.

[6] N. H. Taher, A. M. Dessouki, and F. H. Khalil, "Radiation grafting of acrylic acid onto polypropylene films," *International Journal of Radiation Applications and Instrumentation Part C: Radiation Physics and Chemistry*, vol. 36, no. 6, pp. 785–790, 1990.

[7] M. M. Nasef and E.-S. A. Hegazy, "Preparation and applications of ion exchange membranes by radiation-induced graft copolymerization of polar monomers onto non-polar films," *Progress in Polymer Science*, vol. 29, no. 6, pp. 499–561, 2004.

[8] I. Pinnau and B. D. Freeman, "Formation and modification of polymeric membranes: overview," in *Membrane Formation and Modification*, vol. 744 of *ACS Symposium Series*, chapter 1, pp. 1–22, American Chemical Society, 1999.

[9] T. Matsuura, *Synthetic Membranes and Membrane Separation Processes*, Taylor & Francis, New York, NY, USA, 1993.

[10] S. Saxena, A. R. Ray, and B. Gupta, "Chitosan immobilization on polyacrylic acid grafted polypropylene monofilament," *Carbohydrate Polymers*, vol. 82, no. 4, pp. 1315–1322, 2010.

[11] D. S. Kumar, M. Fujioka, K. Asano, A. Shoji, A. Jayakrishnan, and Y. Yoshida, "Surface modification of poly(ethylene terephthalate) by plasma polymerization of poly(ethylene glycol)," *Journal of Materials Science: Materials in Medicine*, vol. 18, no. 9, pp. 1831–1835, 2007.

[12] Y. Ogiwara, K. Torikoshi, and H. Kubota, "Vapor phase photografting of acrylic acid on polymer films: effects of solvent mixed with monomer," *Journal of Polymer Science: Polymer Letters Edition*, vol. 20, no. 1, pp. 17–21, 1982.

[13] A. M. Mika, R. F. Childs, J. M. Dickson, B. E. McCarry, and D. R. Gagnon, "A new class of polyelectrolyte-filled microfiltration membranes with environmentally controlled porosity," *Journal of Membrane Science*, vol. 108, no. 1-2, pp. 37–56, 1995.

[14] M. E. Cohen, M. A. Grable, and B. M. Riggleman, *Second Report on Development of Improved Cellulose Acetate Membranes for Reverse Osmosis*, U.S. Dept. of the Interior, Office of Saline Water, Washington, DC, USA, 1970.

[15] M.-X. Hu, Q. Yang, and Z.-K. Xu, "Enhancing the hydrophilicity of polypropylene microporous membranes by the grafting of 2-hydroxyethyl methacrylate via a synergistic effect of photoinitiators," *Journal of Membrane Science*, vol. 285, no. 1-2, pp. 196–205, 2006.

[16] Z. Xu, J. Wang, L. Shen, D. Men, and Y. Xu, "Microporous polypropylene hollow fiber membrane: part I. Surface modification by the graft polymerization of acrylic acid," *Journal of Membrane Science*, vol. 196, no. 2, pp. 221–229, 2002.

[17] A. T. Paulino, M. R. Guilherme, A. V. Reis, G. M. Campese, E. C. Muniz, and J. Nozaki, "Removal of methylene blue dye from an aqueous media using superabsorbent hydrogel supported on modified polysaccharide," *Journal of Colloid and Interface Science*, vol. 301, no. 1, pp. 55–62, 2006.

[18] Y. Zheng, D. Huang, and A. Wang, "Chitosan-g-poly(acrylic acid) hydrogel with crosslinked polymeric networks for Ni^{2+} recovery," *Analytica Chimica Acta*, vol. 687, no. 2, pp. 193–200, 2011.

[19] J. N. BeMiller and R. L. Whistler, *Starch: Chemistry and Technology*, Elsevier Science, 2009.

[20] P. Jolles and R. A. A. Muzzarelli, *Chitin and Chitinases*, Springer, Berlin, Germany, 1999.

[21] J. F. Kennedy and L. Quinton, "Column handbook for size exclusion chromatography: Chi-San Wu (Ed.); Academic Press, New York, 1999, 637 pages, ISBN 0-12-765555-7, US$140.00," *Carbohydrate Polymers*, vol. 43, no. 2, pp. 205–206, 1999.

[22] R. Lapasin, *Rheology of Industrial Polysaccharides: Theory and Applications*, Springer US, 2012.

[23] J. A. Flores, A. E. Navarro, K. P. Ramos et al., "Adsorción de CU(II) por quitosano en polvo y perlas de gel," *Revista de la Sociedad Química del Perú*, vol. 71, pp. 17–25, 2005.

[24] J. Mora Molina, L. Chaves Barquero, M. Araya Marchena, and R. Starbird Perez, "Chitosan membrane development and design of equipment for the removal of heavy metals from water," *Tecnologia en Marcha*, vol. 25, no. 3, pp. 3–18, 2012.

[25] C. A. B. Nava-Ortiz, G. Burillo, E. Bucio, and C. Alvarez-Lorenzo, "Modification of polyethylene films by radiation grafting of glycidyl methacrylate and immobilization of β-cyclodextrin," *Radiation Physics and Chemistry*, vol. 78, no. 1, pp. 19–24, 2009.

[26] M. L. Palacios-Jaimes, F. Cortes-Guzman, D. A. González-Martínez, and R. M. Gómez-Espinosa, "Surface modification of polypropylene membrane by acrylate epoxidized soybean oil to be used in water treatment," *Journal of Applied Polymer Science*, vol. 124, no. 1, pp. E147–E153, 2012.

[27] P. A. Dworjanyn and J. L. Garnett, "Synergistic effects of urea with polyfunctional acrylates for enhancing the photografting of styrene to polypropylene," *Journal of Polymer Science Part C: Polymer letters*, vol. 26, no. 3, pp. 135–138, 1988.

[28] A. S. Singha, A. Shama, and V. K. Thakur, "Pressure induced graft-co-polymerization of acrylonitrile onto Saccharum cilliare fibre and evaluation of some properties of grafted fibre," *Bulletin of Materials Science*, vol. 31, no. 1, pp. 7–13, 2008.

[29] S. D. Bhattacharya and M. S. Inamdar, "Polyacrylic acid grafting onto isotactic polypropylene fiber: methods, characterization, and properties," *Journal of Applied Polymer Science*, vol. 103, no. 2, pp. 1152–1165, 2007.

[30] A. Bhattacharya and B. N. Misra, "Grafting: a versatile means to modify polymers: techniques, factors and applications," *Progress in Polymer Science*, vol. 29, no. 8, pp. 767–814, 2004.

[31] Z. Xu, L. Wan, and X. Huang, "Techniques for membrane surface characterization," in *Surface Engineering of Polymer Membranes*, Advanced Topics in Science and Technology in China, chapter 2, pp. 5–63, Springer, Berlin, Germany, 2009.

[32] Z.-K. Xu, X.-J. Huang, and L.-S. Wan, *Surface Engineering of Polymer Membranes*, Advanced Topics in Science and Technology in China, Springer, Berlin, Germany, 2009.

[33] N. Hameed, S. P. Thomas, R. Abraham, and S. Thomas, "Morphology and contact angle studies of poly(styrene-co-acrylonitrile) modified epoxy resin blends and their glass fibre reinforced composites," *eXPRESS Polymer Letters*, vol. 1, no. 6, pp. 345–355, 2007.

[34] A. Saffar, P. J. Carreau, A. Ajji, and M. R. Kamal, "Development of polypropylene microporous hydrophilic membranes by blending with PP-g-MA and PP-g-AA," *Journal of Membrane Science*, vol. 462, pp. 50–61, 2014.

[35] R. Jayakumar, M. Prabaharan, R. L. Reis, and J. F. Mano, "Graft copolymerized chitosan—present status and applications," *Carbohydrate Polymers*, vol. 62, no. 2, pp. 142–158, 2005.

[36] J. M. Bennett, "Recent developments in surface roughness characterization," *Measurement Science and Technology*, vol. 3, no. 12, pp. 1119–1127, 1992.

[37] L. Palacio, P. Prádanos, A. Hernández, M. J. Ariza, J. Benavente, and M. Nyström, "Phase-contrast scanning force microscopy and chemical heterogeneity of GR polysulfone ultrafiltration membranes," *Applied Physics A: Materials Science & Processing*, vol. 73, no. 5, pp. 555–560, 2001.

[38] S. Lowell, J. E. Shields, M. A. Thomas, and M. Thommes, *Characterization of Porous Solids and Powders: Surface Area, Pore Size and Density*, Springer, Rotterdam, Netherlands, 2012.

[39] M. J. Esplandiu, "Scanning probe microscopies for analytical studies at the nanometer scale," *Contributions to Science*, vol. 3, pp. 33–46, 2005.

[40] H. Habibi, R. Amrollahi, and M. Alavi, "Polymerization of acrylic acid by a 4kj plasma focus device," in *Proceedings of the 13th International Conference on Plasma Surface Engineering (PSE '12)*, pp. 270–273, Linköping University Electronic Press, Garmisch-Partenkirchen, Germany, September 2012.

[41] H.-Y. Yu, Z.-K. Xu, H. Lei, M.-X. Hu, and Q. Yang, "Photoinduced graft polymerization of acrylamide on polypropylene microporous membranes for the improvement of antifouling characteristics in a submerged membrane-bioreactor," *Separation and Purification Technology*, vol. 53, no. 1, pp. 119–125, 2007.

[42] L. A. Fasce, V. Costamagna, V. Pettarin, M. Strumia, and P. M. Frontini, "Poly(acrylic acid) surface grafted polypropylene films: near surface and bulk mechanical response," *eXPRESS Polymer Letters*, vol. 2, no. 11, pp. 779–790, 2008.

[43] E.-S. A. Hegazy, H. A. A. El-Rehim, and H. A. Shawky, "Investigations and characterization of radiation grafted copolymers for possible practical use in waste water treatment," *Radiation Physics and Chemistry*, vol. 57, no. 1, pp. 85–95, 2000.

[44] Y. Chen and H.-M. Tan, "Crosslinked carboxymethylchitosan-g-poly(acrylic acid) copolymer as a novel superabsorbent polymer," *Carbohydrate Research*, vol. 341, no. 7, pp. 887–896, 2006.

[45] S. Kavesh and J. M. Schultz, "Meaning and measurement of crystallinity in polymers: a review," *Polymer Engineering & Science*, vol. 9, no. 6, pp. 452–460, 1969.

[46] P. Zugenmaier, *Crystalline Cellulose and Derivatives: Characterization and Structures*, Springer, Berlin, Germany, 2008.